



The University of
Nottingham

UNITED KINGDOM • CHINA • MALAYSIA

THE RISE OF TAYLOR BUBBLES IN VERTICAL PIPES

Stephen Ambrose

Thesis submitted to the University of Nottingham for the
degree of Doctor of Philosophy

July 2015

Abstract

Elongated bubbles which are constrained by the walls of a pipe are commonly known as Taylor bubbles. Taylor bubbles are prevalent in industrial gas-liquid flow, where they are commonly found in buoyancy driven fermenters, the production and transportation of hydrocarbons in the oil and gas industry, the boiling and condensing process in thermal power plants, and the emergency cooling of nuclear reactors. These bubbles also exist in the natural world, and are the driving force behind certain types of volcanic eruption. An analysis of the literature identified a paucity of experimental or numerical studies investigating the rise of Taylor bubbles in pipes with a diameter in excess of 0.12 m or in pipes which contain a change in geometry.

The aim of this thesis was to gain a better understanding of the behaviour of Taylor bubbles in flow conditions which have not previously been studied. To achieve this, a CFD model was used to simulate the rise of single Taylor bubbles and a set of experiments conducted. The CFD model was validated against the results of published experimental studies, empirical correlations and theoretical predictions.

Further validation was conducted using the results of the experimental study which investigated the rise of Taylor bubbles in a pipe of diameter 0.29 m. These experiments confirmed that the theoretically predicted stability and rise rate of the bubble were correct. Bubbles were also shown to exhibit oscillatory behaviour. Sets of parametric simulations replicated the behaviour observed in the experiments and predicted by theoretical models for a wide range of conditions.

The qualitative and quantitative experimental behaviour of a Taylor bubble rising through an expansion in pipe geometry was replicated by the CFD model. Bubbles of sufficient length were observed split as they rose through the expansion in diameter, which produced pressure oscillations. The effects of a variation in a number of parameters, including the angle of expansion, the ratio of the upper to lower pipe diameters and the liquid viscosity, were explored.

Acknowledgements

Firstly I would like to thank my supervisors, Dr Ian Lowndes and Dr David Hargreaves, for their invaluable help, support and advice throughout the past 4 years.

I am also very grateful for the input of Prof. Barry Azzopardi and Dr Alison Rust who provided a great deal of guidance over the course of my research; Dr Chris Pringle for all of his help with the experimental work; Paul and all of the technicians in the L3 Laboratories, Dr Matt Scase, Dr Jeremy Phillips and Dr Laura Pioli for their advice at various points of my research and to Dr Mike James who was most helpful with providing extra details of his experiments. I would also like to thank the research students Arianna Soldati, Diveena Danabalan and Bill Carter for all their work which has contributed to this thesis. Thanks go to the NERC, whose grant funded this research, and to Simon Lo of CD-Adapco who provided training and software.

I would also like to thank all of my friends and colleagues who have helped me throughout my time in Nottingham.

A special thanks goes to my parents Lynn and Chris and to Mark, Rob, Alison, and the rest of my family for their love and support (despite not really understanding!). Thanks also go to Dr Sam Tang for all of her support and advice over many lunchtimes!

Finally, my thanks go to Dr Selina Tang for all of her love, patience, culinary skills and grammar advice, it has been much appreciated (MFEO).

Affirmation

The work reported in this Thesis has not been published elsewhere, with the exception of the following publications

Journal Publication C.C.T. Pringle, S. Ambrose, B.J. Azzopardi, A.C. Rust, The existence and behaviour of large diameter Taylor bubbles, *International Journal of Multiphase Flow*, Article in Press, 2014. DOI: 10.1016/j.ijmultiphaseflow.2014.04.006

Contents

1	Introduction	1
1.1	Context	1
1.1.1	Multiphase Flow	1
1.1.2	Single Taylor bubbles	3
1.2	Research Aims and Objectives	5
1.3	Methodology	5
1.4	Thesis Outline	6
1.5	Highlights	8
2	Literature Review	10
2.1	Single Taylor bubbles	10
2.1.1	Non-dimensional groups	10
2.1.2	Rise speed of Taylor Bubbles	13
2.1.3	Flow fields around Taylor bubbles	16
2.1.4	Film Thickness around Taylor Bubbles	19
2.1.5	Wake behaviour of Taylor Bubbles	23

2.1.6	Other experimental methods	30
2.1.7	Stability of Taylor Bubbles	31
2.1.8	Expansions in pipe diameter	33
2.2	Taylor bubbles in Volcanic Conduits	39
2.2.1	Introduction	39
2.2.2	Background	39
2.2.3	Strombolian eruptions	43
2.2.4	Models	45
2.3	CFD studies	48
2.3.1	Modelling Multiphase Flow	48
2.3.2	Implementation	51
2.3.3	Results	53
2.3.4	Other applications	57
2.4	Conclusions	58
3	CFD Model	71
3.1	Numerical Model	71
3.1.1	Governing Equations	71
3.1.2	Turbulence Models	74
3.1.3	Mesh	78
3.1.4	Spatial Discretisation	80
3.1.5	Temporal Discretisation	81
3.1.6	Pressure-Velocity Coupling	83
3.1.7	VOF	84
3.2	Verification	92

3.2.1	Error and Uncertainty	92
3.2.2	Spatial discretisation error	93
3.2.3	Temporal discretisation error	95
3.2.4	Convergence	95
3.2.5	Computer round off error	96
3.2.6	Computer programming error	96
3.3	Validation	98
3.3.1	The base case model	98
3.3.2	Verification	101
3.3.3	Validation Study 1: White and Beardmore (1962)	105
3.3.4	Validation Study 2: van Hout et al (2002)	108
3.3.5	Validation Study 3: Viana et al, 2003	114
3.3.6	Conclusions	118
4	Rise of Taylor bubbles in vertical pipes - Experimental	119
4.1	Experimental Arrangement	119
4.1.1	Experimental Apparatus	120
4.2	Experimental Design	128
4.2.1	Objectives	128
4.2.2	Preliminary studies	128
4.3	Stability of Taylor bubbles	131
4.3.1	Experimental Design	131
4.3.2	Results and Discussion	133
4.4	Rise velocity of Taylor bubbles	135
4.4.1	Experimental Design	135

4.4.2	Results and Discussion	136
4.5	Oscillatory behaviour	139
4.5.1	Experimental design	139
4.5.2	Results and Discussion	140
4.6	Conclusions	145
5	Rise of Taylor bubbles in vertical pipes - Numerical	147
5.1	Introduction	147
5.1.1	Adaptations to Numerical Model	148
5.1.2	Domain and Mesh	149
5.1.3	Initial and Boundary Conditions	150
5.1.4	Turbulence model	151
5.2	Results	156
5.2.1	Bubble Rise and Oscillation	156
5.2.2	Pressure Oscillations	159
5.2.3	Variation of Initial Pressure	160
5.2.4	Variation of bubble size	166
5.2.5	Variation of initial bubble depth	171
5.2.6	Variation of liquid viscosity	172
5.2.7	Flow fields	177
5.2.8	Variation of Pipe Diameter	181
5.2.9	Stability of Bubbles in non- quiescent fluids	183
5.3	Conclusions	192
6	Rise of a Taylor bubble through a change in geometry	194
6.1	Introduction	194

6.2	Validation	207
6.2.1	Experimental Apparatus	207
6.2.2	Experimental Results - 0.038 to 0.08 m expansion	208
6.2.3	Simulation Set-up	211
6.2.4	Results of Validation Simulations	214
6.3	Results	217
6.3.1	Variation of curvature of expansion	217
6.3.2	Variation of angle of expansion	220
6.3.3	Variation of viscosity	237
6.3.4	Variation of pipe diameter ratio	239
6.4	Conclusions	245
7	Conclusions and Recommendations	247
7.1	Conclusions	247
7.2	Recommendations	253
	Appendices	269
A	UDF Source Code	270

List of Figures

- 1.1 A diagram showing the classification of gas-liquid flow regimes (Ghajar, 2005). 2
- 1.2 An example of a Strombolian type eruption at Stromboli, Italy (Geology.com, 2011). 3
- 1.3 Still photograph of a Taylor bubble rising through water, highlighting the bubble nose, liquid film, bubble tail and bubbly wake areas. 4

- 2.1 Crossplot of dimensionless data showing different flow regimes (White and Beardmore, 1962). 12
- 2.2 Figure showing the variation of the Froude number with the Reynolds number based on buoyancy for a collection of experimental data, (Viana et al., 2003). A clear distinction can be observed between the two flow regimes described by $Fr = 0.341$ and $Fr = 9.221 \times 10^{-3} R^{0.977}$ respectively. 14

2.3	An example of flow fields around a Taylor bubble rising in water in a vertical pipe of diameter 0.025 m which were generated using a PIV method, (van Hout et al., 2002). These flow fields are averaged from 100 experimental runs. The top image shows the flow around the nose of the Taylor bubble, the middle image shows the flow around the tail of the bubble, and the bottom image the flow further into the wake (2-4 pipe diameters below the tail).	17
2.4	A comparison of images captured by using PIV and PST and a combined method (Nogueira et al., 2003). A much clearer outline of the bubble is captured with the combined method than by using PIV alone.	18
2.5	The effects that an increased Re number has on the film thickness developed around a rising Taylor bubble, (Nogueira et al., 2006a). This Reynolds number is based on bubble velocity and pipe diameter and is varied by using aqueous glycerol solutions of different viscosities in a 0.032 m pipe.	20
2.6	The cubic Brown model proposed by Llewellyn et al. (2011), dashed line, compared to experimental data, Llewellyn et al. (2011) ,dots with error bars and Nogueira et al. (2006a), crosses.	24
2.7	(a) A Taylor bubble with $N_f < 500$ rising with a laminar wake which is closed and axisymmetric, (Campos and Carvalho, 1988) and (b) a Taylor bubble with $500 < N_f < 1500$ rising with a transitional wake which is closed but no longer axisymmetric, (Campos and Carvalho, 1988).	26
2.8	A Taylor bubble with $N_f > 1500$ rising with a turbulent wake which is open and not axisymmetric, (Campos and Carvalho, 1988).	28

2.9	A graph illustrating the dependence of the wake length on the value of N_f for a non-Newtonian CMC solution (filled line) in comparison to the results presented for Newtonian fluids (dashed line) by Campos and Carvalho (1988), (Sousa et al., 2005).	29
2.10	A photograph of a wire mesh sensor. This is an intrusive device which measures not only the total gas void fraction within a fluid, but also the void fraction distribution within the pipe.	31
2.11	A Taylor bubble rising in water in a 0.3 m pipe in an unstable manner (left) and in a stable manner (right) Pringle et al. (2014). This instability is the result of the fluid not being completely quiescent before the bubble was released.	32
2.12	A Taylor bubble rising in water in a stable manner in a pipe of diameter 0.24 m, (James et al., 2011).	34
2.13	The experimental apparatus used by James et al. (2006) to study the rise of Taylor bubbles through changes in pipe diameter. The full experimental set up is shown on the left hand side and the profiles of different expansion sections are shown on the right hand side.	36
2.14	A visual representation of the behaviour of a Taylor bubble passing through the 0.038 m to 0.08 m expansion in pipe geometry in water, (James et al., 2006). . .	37
2.15	A graphical representation of the readings by a static pressure sensor at the base of the pipe as the bubble passes through an expansion in the pipe diameter (above), and the results of a subsequent frequency analysis of these signals, (below) (James et al., 2006).	38
2.16	Examples of volcanic eruptions (left) Hawaiian at Kilauea, Hawaii. (above right) Strombolian at Stromboli, Italy. (below right) Plinian at Mt St Helens, USA. (Geology.com, 2011).	40

2.17 A diagram showing the scenario of a bubble rising into a lava lake at Erta Ale, (Bouche et al., 2010). The rising bubble encounters a sudden change in pipe diameter 40 m below the liquid surface.	44
2.18 Outline of the RSD (left) and CF (right) models (Houghton, 2008). The RSD model proposes that the formation of Taylor bubbles is caused by the coalescence of smaller bubbles during their ascent, whereas the CF model proposes that Taylor bubbles are formed by the collapse of a large foam of small bubbles at the roof of the magma chamber.	46
2.19 A diagram showing the computational domain when using a moving wall method, (Araujo et al., 2012). The walls move downwards vertically at the same velocity as the Taylor bubble.	61
2.20 Comparison of the empirical models of White and Beardmore (1962) (symbols) with the CFD results of Taha and Cui (2004) (lines).	62
2.21 Comparison of the empirical models of White and Beardmore (1962) (filled lines) with the CFD results of James et al. (2008) (dashed lines and filled circles). . . .	63
2.22 A flow map indicating the behaviour of the tail and presence of a wake behind the Taylor bubble Araujo et al. (2012).	64
2.23 Depiction of waves in the thin film of a Taylor bubble from the work of (Lu and Prosperetti, 2009). Interface shapes are plotted at a range of different times throughout one simulation.	65
2.24 The limited range of values for which the model of Kang et al. (2010) is valid, (Llewellyn et al., 2011).	66

2.25	The change in shape of a Taylor bubble for varying conditions, using a fixed initial volume, (Taha and Cui, 2004). The Taylor bubble is rising to the left. An increase in the Eötvös number gives shorter and wider bubbles and hence reduces the size of the liquid film.	67
2.26	Flow in the near wake of a Taylor bubble using a coupled VOF and mixture model (Yan and Che, 2010).	68
2.27	Streamlines around a Taylor bubble rising in an pipe inclined at 30 ° to the vertical (Taha and Cui, 2004).	69
2.28	Images showing the development of slug flow in a micro channel, with gas injected at the left hand side (Gupta, 2009). In this set of images, the gas phase is blue and the liquid phase is red.	70
3.1	Diagram of different types of structured grid, showing (a) an “O-Grid” which is often used in pipe flow simulations (b) a “C-Grid” type mesh, often used for flow around aerofoils and (c) a “H-Grid” used in many different applications where a structured grid is required.	88
3.2	Diagram illustrating different criteria of poor cell quality (a) high aspect ratio or small minimum angle cell, (b) a cell with a high growth factor and (c) a highly skewed quadrilateral cell.	89
3.3	A diagram illustrating the QUICK scheme. For face e , the face value is given by Equation 3.23	89
3.4	A diagram illustrating the steps in the NITA scheme (ANSYS FLUENT). Each set of equations is iterated to convergence individually to reduce the computation time required.	90
3.5	A diagram illustrating three cells each with a volume fraction of 0.5.	90

3.6 A diagram illustrating the results obtained by using the Geo-Reconstruct (b) and Donor-Acceptor (c) algorithms in comparison to the real solution, (a) (ANSYS FLUENT). As can be observed from this image, the Geo-reconstruct gives a much sharper interface shape than the Donor-Acceptor method. 91

3.7 An example of the residuals from the base case simulation of a bubble rising in water in a 0.3 m pipe. This image is taken while the bubble is mid way through its rise through the pipe, 4.75 s from the start of the simulation. At this time, the residuals of the continuity equation is 3.8×10^{-5} , the x , y and z momentum equations 4.5×10^{-6} , 4.45×10^{-5} and 5.5×10^{-6} respectively, the residuals for the k and ε equations are 2.4×10^{-7} and 3.9×10^{-7} , and the energy equation 7.45×10^{-8} 97

3.8 Diagram of the boundary conditions for a 2d axi-symmetric flow simulation. The x and y axes are also indicated, with gravity in the negative x direction. 99

3.9 Example of a cross section in the xy plane of a 3D O-Grid mesh used in the simulations. 100

3.10 The velocities computed on the 2D meshes of 1000 cells (average size of 0.1 D), 4000 cells (0.05 D) and 16000 cells (0.025 D) along with the extrapolated value for an infinitesimally small average cell size. 102

3.11 The velocities computed using time-steps of 0.0001 s, 0.0005 s and 0.001 s along with the extrapolated value for an infinitesimally small time-step. 103

3.12 Example of a residual graph from showing the convergence of the continuity equation, x , y and z component momentum equations as well as the k and ε equations. 104

3.13 Comparison of the results of the experiments of White and Beardmore (1962) with other experimental studies. 106

3.14 Comparison of the correlations of White and Beardmore (1962) (line) with the results from the CFD model (symbols) for various values of the Morton Number. This shows that the results of the simulations closely match the experimental correlations for higher the Morton numbers considered. However, the errors between the empirical and simulated results increase with a decrease in Morton number, particularly with a high Eötvös number. 107

3.15 Velocity vectors around a fully developed Taylor bubble. On the left, PIV results of van Hout et al. (2002) averaged over 100 experimental runs, and on the right, instantaneous CFD results. At the top, from 0.5 D above to 0.5 D below the nose of the bubble; in the middle, from the tail of bubble to 2 D below it; and at the bottom, from 2 D to 4 D below the tail of the bubble. 110

3.16 Comparison of the outline of the bubble, along with velocity measurements adjusted by position for the experimental measurements van Hout et al. (2002), filled line and filled markers, and the CFD validation case, dashed line and empty markers. The adjustment is such that a measurement read at $z/D = 2$ with a downward velocity of 1 ms^{-1} would give a reading of -3 ms^{-1} as in van Hout et al. (2002). 112

3.17 Comparison of the centreline velocity behind the tail of the bubble for the experimental measurements of van Hout et al. (2002) (*), and the CFD validation case (solid line). 113

3.18 Froude number varying with Re_B for $Re_B < 10$. The simulated and predicted Froude numbers match closely in this range of values. 116

3.19 Froude number varying with Re_B for $Re_B > 10$. The difference between the simulated Fr and the predicted F increases with increasing Re_B 116

3.20 Comparison of film thickness in CFD to the results of Llewellyn et al. (2011). The results of the CFD simulations match within 5 % of the theoretical model. 117

4.1	A 2D schematic side elevation view of the experimental apparatus. Air is supplied to the 0.29 m diameter pipe filled to a depth of 5.83 m with water via a mains air supply. The rise of the bubble is monitored using a Phantom V9.1 video camera in one of two locations and a Sanyo video camera.	121
4.2	A photograph of the air inlet injection system used in these experimental studies. The yellow lever at the inlet to the flow manifold is the mains compressed air control valve and the red rotational valves allow the fine control of the flow delivered to each batch of five injection nozzles.	122
4.3	A photograph of the mirror system used in conjunction with the high speed camera to record multiple viewing windows along the length of the pipe. This system allows two different locations of the pipe to be monitored in a single frame of the video recording.	124
4.4	An example of a still frame recorded by the Phantom. This image shows the bubble passing the marker viewable through the upper periscope. The lower marker is 1.44 m below the upper marker, and so the time taken and hence rise velocity of the bubble can be calculated.	125
4.5	An example of a still frame recorded by the Sanyo camera to determine the length of the rising bubbles.	127
4.6	Two examples of still frames taken from the Sanyo camera showing two Taylor bubbles, the left bubble is undergoing a break while the right bubble is rising smoothly. The instability causing the bubble on the left to break up is the result of the fluid not being completely quiescent before the bubble was released.	132

4.7 The probability of a Taylor bubble breaking up within a 2 m observation window in the 0.29 m pipe. If the settling period is below 50 s, all bubbles will break up. If the settling period is longer than 120 s all bubbles observed will rise in a stable manner. Between these values the bubble will break up with decreasing likelihood as the settling period increases from 50 s to 120 s. 134

4.8 The Froude numbers of the observed Taylor bubbles in the 0.29 m pipe varying with bubble length. The Froude numbers increase with increasing bubble length due to the effect of the bubble expanding as it rises. 138

4.9 Read row by row from left to right. Still frames taken at 0.05 s intervals showing the variation in surface height. The surface level decreases on the first row, remains relatively constant on the second row and increases significantly on the third row. 142

4.10 The evolution of the height of the water surface. The red line is taken from the rise of a bubble initially 0.55 m long. The green line shows the predicted mean surface rise and has been calculated by assuming the bubble expands as an ideal gas obeying $pV = nRT$. Time is measure from when the bubble bursts at the surface. 143

4.11 The frequency of oscillating bubbles as they rise up the pipe for two different mean lengths of bubble (blue is 0.55 m, red is 0.45 m). The points represent the average of experimental data taken from ten runs in the case of the longer bubble and six in the case of the shorter bubble. The lines come from the theoretical model of Pringle et al. (2014), where the polytropic exponent has been taken to be 1. Time is measured prior to the bubble bursting at the surface. 144

5.1	The numerical domain and the O-grid mesh used for simulations. The domain has a total height of 9.5 m and a diameter of 0.3 m. The mesh has a spacing of 0.0023 m at the wall rising to 0.014 m at the centre. The mesh is uniform in the vertical, z , direction.	153
5.2	Diagram showing the independence of the grid sizing in relation to rise velocity using the GCI method. From this it was concluded that the error introduced by spatial discretisation was 0.411% for the fine grid.	154
5.3	Initial conditions imposed on the numerical domain.	155
5.4	Simulated upper liquid surface rise given an initial hydrostatic pressure distribution for a Taylor bubble of length 0.64 m in a vertical, cylindrical pipe of diameter 0.3 m initially filled with 5 m of water.	157
5.5	Diagram showing the determination of the fill height in the User Defined Function.	159
5.6	Images showing, top left, a bubble mid-way through the rise given base case conditions, centre, the turbulent the turbulent kinetic energy, k , in the area surrounding the bubble at the same time, and right, the turbulent eddy dissipation, ε	160
5.7	Comparison between pressure oscillations and surface oscillations with an initial over pressure of 20 kPa. The pressure is indicated by the heavy line and the location of the surface by the lighter line. The maximum pressure in the fluid corresponds to the minimum surface height, and hence the maximum compression of the bubble.	161
5.8	Variation of water surface height with time for various initial pressures in the bubble, ranging from a 30 kPa under pressure, shown by the lowest line, to a 30 kPa over pressure, indicated by the highest line, in increments of 10 kPa.	163

5.9 (a) Surface height plot with peaks highlighted, (b) frequency of surface oscillations, (c) mean surface height and (d) comparison against experimental data from Chapter 4, (straight lines with error bars), and model (Vergnolle et al., 1996), (smooth curve) and current simulation a 0.64 m long bubble, (circles). 164

5.10 Variation in the frequency of the bubble oscillation with time for initial bubble pressures varying from -30 kPa to +30 kPa. Here the time is the time before the bubble breaks the top surface. This scale will hence be used and referred to as the “Time to burst”. 166

5.11 Frequency, f of the simulated surface oscillations plotted against $L^{-1/2}$ for bubbles of length, L , ranging from 0.28 m to 1.04 m. The lines correspond to various times to burst. 167

5.12 The variation in the simulated frequency of surface oscillations with time for 0.28, 0.44, 0.64, 0.84 and 1.04 m long bubbles. 168

5.13 Taylor bubble with 30 kPa over pressure, left, and 30 kPa under pressure, right. A clear difference in size can be seen due to the initial expansion and compression of the bubbles. Again, the colour scale here shows the gas phase in red with the liquid phase as blue. 169

5.14 The variation of non-dimensional rise velocity, Fr , with L . An extrapolation of these results gives a prediction of the Fr of a bubble with zero length, of $Fr = 0.27$. This is an under prediction of approximately 18% of the Fr observed in the experimental studies. As in the experimental studies, the rise velocity increases with increasing bubble length as the bubble expands as it rises through the pipe. 170

5.15 Frequency of surface oscillations of original simulations and predicted values based on correction for average bubble length. This shows the difference in frequency between the over and under pressured cases is due solely to difference in average length of the bubble. 171

5.16 Frequency of oscillations for bubbles at different initial depths. There is a significant difference between the frequency for bubbles released at different depths below the surface. 173

5.17 Frequency of oscillations for bubbles at different initial depths after being adjusted for initial error. This provides a much closer agreement between the different cases. 174

5.18 Oscillations of the surface for liquids of varying viscosity giving a range of Reynolds numbers of 600 to 500000. Further simulations were conducted but are not shown in this figure for clarity. 175

5.19 Frequency of oscillations for liquids of varying viscosity. The viscosity of the liquid phase does not significantly alter the frequency of oscillation as the bubble rises through the pipe. 176

5.20 Streamlines and velocity vectors in the wake of the Taylor bubble. There is little difference in the behaviour of the wake of the Taylor bubble for bubbles which are expanding and those which are in compression. 179

5.21 Streamlines and velocity vectors around the nose of the Taylor bubble. When in compression, the flow far ahead of the bubble has a negative velocity in the vertical direction, whereas the flow far ahead of the bubble has a positive velocity when the bubble is expanding. 180

5.22 Initial conditions imposed on the numerical domain of a 0.6 m pipe. The pressure conditions are shown on the left hand side and the volume fraction on the right hand side. 185

5.23	Contour plot of volume fraction of air showing the breaking of the Taylor bubble after 1 s of simulated rise.	186
5.24	The altered initial conditions imposed on the numerical domain of a 0.6 m pipe, with the same depth of water and hence initial bubble pressure as the base case which had a pipe diameter of 0.3 m.	187
5.25	Contour plot of volume fraction of air showing the breaking of the Taylor bubble subjected to the altered initial conditions after 1 s of simulated rise.	188
5.26	A bubble breaking in a pipe of diameter 0.4 m after 1 s of simulation. This break is noticeably different to the break observed for the 0.6 m pipe as the break is not axisymmetric.	189
5.27	Initial volume fraction conditions for a bubble rising into the wake of a previous bubble in a 0.3 m diameter pipe.	190
5.28	3D iso-surface images of the breaking of a Taylor bubble when rising into the wake of a previous bubble, breaking on the left, and deforming on the right.	191
6.1	A still video image extracted from Kondo et al. (2002) which shows a Taylor bubble during the necking process while passing through a sudden expansion from a pipe of diameter 0.02 m to 0.05 m in water.	196
6.2	A series of still video images extracted from Kondo et al. (2002) which show a Taylor bubble which has passed through a sudden expansion from a pipe of diameter 0.02 m to 0.05 m in water (Kondo et al., 2002).	196

6.3	Photographic sequence in 68 Pa s viscosity glucose with a 60 cm ³ bubble injected into the bowl apparatus of Danabalan (2012). The upper bowl is filled with clear glucose syrup and the lower pipe is filled with glucose syrup mixed with red dye. Images (a) to (f) show the passage of the first bubble while (g) to (l) shows secondary bubble rise (Danabalan, 2012).	199
6.4	A flow regime diagram mapping the patterns of bubble breakage tendencies observed in the expansion section for different fluid viscosities and original bubble volume. The blue diamonds represent cases whereby the bubble remained intact, the red squares where the original single bubble breaks into two separate bubbles in the cubic reservoir but did not break in the bowl-shaped reservoir, the and green circles where the original single bubble broke into two separate bubbles as it entered both of the expansion geometries (Danabalan, 2012).	200
6.5	A 3D CAD image of the experimental apparatus used in the Hele-Shaw experiments conducted at the University of Bristol to study the rise of a Taylor bubble through an expansion in geometry (Soldati, 2013).	201
6.6	A flow regime diagram mapping the patterns of Taylor bubble breakage observed for different angles of expansion (Soldati, 2013). This shows a increase in the maximum size of bubble which could pass through the expansion given a more gradually expanding section.	203
6.7	Diagrams based upon still images taken from a video recording of a Taylor bubble rising through a 75° expansion, from undisturbed rise (a) through the necking process to breakup (e) (Soldati, 2013).	204
6.8	The nose and tail positions of a typical non-breaking Taylor bubble whilst rising through an expansion in pipe diameter (Soldati, 2013).	205

6.9 Still frames extracted from a high speed video recording of a Taylor bubble rising in water through an expansion, which show the sequential the breakup mechanism. Images (a)-(d) show the Taylor bubble approaching the top of the inner tube. The next sequence of images, (e)-(j), show the bubble starting to neck as a larger volume of water begins to enter the inner pipe at a high velocity. As the bubble continues to neck a fine central film of air is maintained, shown on images (k)-(m). Between images (m) and (n), this film breaks and is catapulted through the centre of the upper bubble. This instantaneously penetrates the nose of the bubble and water jets through this opening, which is shown in the images (n) and (o). 206

6.10 The experimental apparatus used by James et al. (2006) to study the rise of Taylor bubbles through changes in pipe diameter. The full experimental set up is shown on the left hand side and the profiles of different expansion sections are shown on the right hand side. 209

6.11 Photographs of the expansion section of the pipe showing the structural supports surrounding the pipe which obscure the video recording in the study of James et al. (2006). On the left without a bubble present (a) and on the right, (b), as a bubble has passed through the expansion. 210

6.12 A photograph of the expanding glass section used in the study of James et al. (2006) which was provided via private correspondence. This photograph was used to estimate the shape of the internal shape of the expanding section. 212

6.13 Images illustrating the model generation process. (a) The point data for the expanding section. (b) A 2D plane joining the expanding section with the rest of the domain. (c) The 3D section created by rotating the 2D plane. 213

6.14 Image showing the mesh on (a) the symmetry plane (b) the outlet. 215

6.15 A comparison of the frequencies produced the bubbles passing through the (a) curved and (b) straight sided expansions. The dominant frequencies are similar for both the curved and straight expansion profiles indicating the sources of oscillation are not greatly by the curvature of the expansion. 218

6.16 A comparison of the simulated positions of the nose of the bubbles whilst rising through pipes containing a straight sided or curved expansion. The bubbles rise through the lower pipe with rise rates within 1% of each other and exhibit similar behaviour as they encounter the expansion in pipe diameter. 219

6.17 Images indicating that the critical length of bubble is bounded by lengths of $2.2L'$ (left) and $3.3L'$ (right). On the left, the only gas left in the lower pipe is that which has been shed from the tail of the bubble during the rise. On the right, the necking process has broken the longer bubble into two distinct bubbles, leaving one in the lower section of the pipe. 221

6.18 A schematic illustrating how the of angle of expansion, θ , along with other quantities, are defined. Here, r_1 is the radius of the lower pipe, r_2 is the radius of the upper pipe, r_b is the radius of the bubble, L_1 is the height of the water surface above the base of the lower pipe, L_2 is the height of the start of the expansion section above the base of the lower pipe and L_b is the length of the bubble. . . . 222

6.19 A schematic illustrating the block topology used at expanding section (above) and at the outlet (below) for the 90° expansion. An extra block was added to the topology of the mesh for the expanding section upwards. This requires the addition of extra cells in the radial direction to maintain resolution and quality of the cells in the expanding section. 224

6.20	Images showing, top left, a bubble during passage through the 90° expanding section, centre, the turbulent kinetic energy, k , in the area surrounding the bubble at the same time, and right, the turbulent eddy dissipation, ε	225
6.21	Iso-surface images indicating the location of initially identical bubbles passing through expansions with angle of expansion, $\theta = 90^\circ, 75^\circ, 60^\circ, 45^\circ, 30^\circ$ and 15° at $t=1.3$ s.	226
6.22	A comparison between the (a) 90° and (b) 15° cases. Each iso-surface indicates the location of the surface of the bubble after the neck has closed.	227
6.23	A comparison between the (a) 90° and (b) 15° cases. For each, the iso-surface indicates the location of the surface of the bubble and the vectors represent the velocity.	227
6.24	Plots showing the frequency of the signals generated by initially identical bubbles as they pass through expansions with an angle of expansion of $\theta = 90^\circ, 75^\circ, 60^\circ, 45^\circ, 30^\circ$ and 15° . The lower dominant frequency remains constant throughout while there is an increase in the higher frequencies as the angle of expansion increases.	228
6.25	3D iso-surfaces showing an example of the bubble at or above the upper bound of the critical length(left), and at or below the lower bound of the critical length (right) as they pass through a 90° expansion.	230
6.26	A plot of the upper and lower bounds of the critical length of bubble which can fully pass through the expansion before the neck closes against the angle of expanding section.	231
6.27	A plot of the upper and lower bounds of the critical length of bubble which can fully pass through the expansion before the neck closes against the cosec of angle of expanding section. This shows a linear relationship between L' and $\text{cosec}\theta$. . .	232
6.28	Schematic illustrating the definition of the angle ϕ	233

6.29 Plot showing the linear relationship between ϕ and $theta$ 234

6.30 Plot showing the relationship between v_r and $theta$ 234

6.31 The upper and lower bounds of the critical volume of bubbles which can fully pass through the expansion before the neck closes against $\text{cosec}\theta$ for the experiments performed by Soldati (2013). This also shows a linear relationship between bubble volume and $\text{cosec}\theta$ supporting the results of the simulations. 236

6.32 Plots of the Power Spectral Density of the signals generated by bubbles of identical initial length as they pass through a 90° expansion section for viscosities of 1, 0.1 and 0.001 Pa s respectively. 239

6.33 Plots of the streamlines in the wake of a Taylor bubble rising in fluids of viscosity (a) 0.001 Pa s, (b) 0.1 Pa s, (c) 1 Pa s. Image (a) demonstrates the open wake structure associated with turbulent flow regime given $\text{Re}_B > 1500$ (Nogueira et al., 2006a) and images (b) and (c) demonstrate the closed wake structure associated with the laminar flow regime with $\text{Re}_B < 500$, 240

6.34 A plot of the upper and lower bounds of the critical length of bubble against the ratio of the diameter of the upper pipe to the diameter of the lower pipe. This shows that a ratio of upper to lower pipe diameters of approximately 2.5 to 3 is required for the walls of the upper pipe to have a negligible effect on the process of Taylor bubbles passing through this expansion section. 242

6.35 3D iso-surfaces showing the simulated behaviour of the bubbles at the lower bound of the critical length as they pass through a 90° expansion with upper diameter 0.1 m (left), 0.12 m (centre) and 0.14 m (right). In the cases with an upper pipe diameters of 0.1 m and 0.12 m, there is a small difference in the shape of the bubble as the tail penetrates the nose. This is not observed when comparing the bubbles in the 0.12 and 0.14 m cases 243

6.36 3D iso-surfaces showing the simulated behaviour of the bubbles at the upper bound of the critical length as they pass through a 90° expansion with upper diameter 0.1 m (left), 0.12 m (centre) and 0.14 m (right). Although the bubble shapes in all three cases are similar, there are some minor discrepancies between the bubbles rising into pipes of diameter 0.1 m and 0.12 m which are not seen between the bubbles rising into pipes of diameter 0.12 m and 0.14 m. 244

List of Tables

2.1	Influence of water content on viscosity of magmas (Scarfe, 1973; Murase, 1962).	41
4.1	The physical properties of the fluid, the subscript L refers to the liquid phase, G to the air.	126
4.2	Table of non-dimensional parameters determined for the rise of Taylor bubbles	128
5.1	Flow conditions of the base case simulation.	151
6.1	Table of non-dimensional parameters determined for the rise of Taylor bubbles in the experiments of Danabalan (2012).	197
6.2	Table of non-dimensional parameters determined for the rise of Taylor bubbles in the experiments of Soldati (2013).	202
6.3	Table of non-dimensional parameters determined for the rise of Taylor bubbles within fluids of viscosity 0.001, 0.1 and 1 Pa.s.	238

Nomenclature

Symbol	Definition	Units
U	Bubble rise velocity	ms^{-1}
g	Gravitational acceleration	ms^{-2}
D	Pipe diameter	m
ρ_G	Gas density	kgm^{-3}
ρ_L	Liquid density	kgm^{-3}
σ	Surface tension	kgs^{-2}
μ_L	Liquid viscosity	Pa.s ($\text{kgm}^{-1}\text{s}^{-1}$)
v_t	Bubble terminal rise velocity	ms^{-1}
r	Pipe radius	m
λ	Liquid film thickness	m
v_f	Liquid film velocity	ms^{-1}
l_w	Wake length	m
v_w	Wake volume	m^3
ν	Kinematic viscosity, $\frac{\mu}{\rho}$	m^2s^{-1}
T	Temperature	$^{\circ}\text{C}$
α_c	Thermal expansion coefficient	K^{-1}
C_p	Specific heat capacity	$\text{Jkg}^{-1}\text{K}^{-1}$
μ_t	Turbulent viscosity	Pa.s ($\text{kgm}^{-1}\text{s}^{-1}$)
k	Turbulent kinetic energy	m^2s^{-2}
ε	Turbulence dissipation rate	m^2s^{-3}
S	Strain rate	s^{-1}

Symbol	Definition	Units
α_G	Volume fraction of gas	
α_L	Volume fraction of liquid	
F_s	Surface tension force	N
κ	Radius of curvature	m
p	Pressure	Pa ($\text{kgm}^{-1}\text{s}^{-2}$)
R	Universal gas constant	8.314 J mol ⁻¹ K ⁻¹
M_w	Molecular weight	gmol ⁻¹
ω	Specific turbulence dissipation rate	s ⁻¹
σ_k	Turbulent Schmidt number	
σ_ε	Turbulent Schmidt number	
σ_ω	Turbulent Schmidt number	
x, y, z	x, y, z directions	
U_x, U_y, U_z	Velocity in the x, y, z directions	ms ⁻¹
L	Bubble length	m
H	Depth of bubble	m
f	Frequency of oscillation	Hz
t	Time	s
L'	Dimensionless bubble length, L/D	
θ	Angle of expansion	°
r_b	radius of bubble	m
ϕ	Angle of velocity	°

Dimensionless Groups

Symbol	Name	Definition
M	Morton	$\frac{g\mu_L^4(\rho_L-\rho_G)}{\sigma^3\rho_L^2}$
Eo	<i>Etus</i>	$\frac{g(\rho_L-\rho_G)D^2}{\sigma}$
Fr	Froude	$\frac{U}{\sqrt{gD(\rho_L-\rho_G)/\rho_L}}$
Re _B	Buoyancy Reynolds	$\frac{(D^3g(\rho_L-\rho_g)\rho_L)^{0.5}}{\mu_L}$
N _f	Inverse viscosity	$\frac{(D^3g(\rho_L-\rho_g)\rho_L)^{0.5}}{\mu_L} = Re_B$
Re _f	Film Reynolds	$4\frac{\rho\lambda v_f}{\mu}$
Re	Reynolds	$\frac{UD\rho}{\mu}$
We	Weber	$\frac{\rho u^2 D}{\sigma}$

Acronyms

CFD	Computational Fluid Dynamics
RANS	Reynolds Averaged Navier Stokes
LES	Large Eddy Simulation
DES	Detached Eddy Simulation
AMG	Algebraic Multi-Grid
QUICK	Quadrilateral Upwind Interpolation for Convective Kinematics
SIMPLE	Semi Implicit Method for Pressure Linked Equations
PISO	Pressure Implicit with Splitting Operators
NITA	Non Iterative Time Advancement
VOF	Volume of Fluid
MFR	Moving Frame of Reference
HRIC	High Resolution Interface Capturing
RSD	Rise Speed Dependent
CF	Collapsing Foam
GCI	Grid Convergence Index
PIV	Particle Image Velocimetry
PST	Pulsed Shadow Techniques

1.1 Context

1.1.1 Multiphase Flow

The term 'multiphase flow' covers a wide variety of multi-component gas, liquid and solid flow regimes, but the sub-group of flows that are the principal focus of this thesis are two phase gas-liquid flows in a vertical pipe. There are a number of ways in which gas and liquid phases can interact in a vertical pipe. These can be categorised into four different flow regimes, shown in Figure 1.1 and are described below (Yeoh and Tu, 2010):

1. Bubbly Flow - In a bubbly flow, the gas phase is distributed into discrete bubbles in a liquid phase. As the volume of gas increases, the number of these bubbles increases. Transition from bubbly flow to slug flow is thought to occur at a gas volume fraction of between 0.25 and 0.3 (Wallis, 1969).
2. Slug Flow - Slug flow consists of large, bullet shaped gas bubbles (Taylor bubbles) rising through a liquid. Each large bubble creates a thin film of liquid flowing around the outside of it. This liquid film jets into the wake region behind the gas bubble and can cause breakup at the rear of the bubble.

3. Churn Flow - This is a highly turbulent and unstable flow regime often characterised by pulsing oscillations. A high gas flow rate is often responsible for the instability observed in this flow regime.
4. Annular Flow - This flow regime is characterised by a central core of gas. Liquid travels in an annular film close to the wall of the pipe. Waves are often observed at the interface between the phases and these this can cause liquid droplets to be entrained in the gas phase.

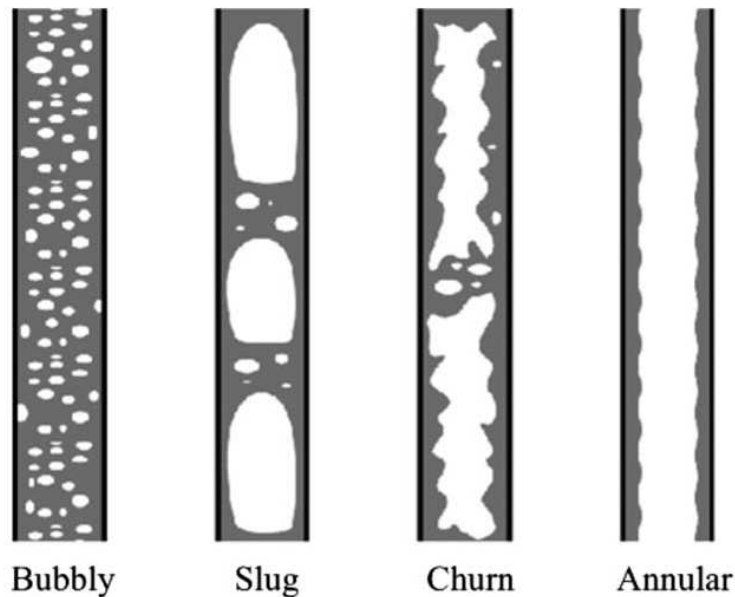


Figure 1.1: A diagram showing the classification of gas-liquid flow regimes (Ghajar, 2005).

In this thesis, the flow of Taylor bubbles, a characteristic part of the slug flow regime, has been studied. Taylor bubbles are encountered both in research and industry. From use in microfluidics and in capillary flows to a much larger scale, where Taylor bubbles are commonly found in buoyancy driven fermenters, the production and transportation of hydrocarbons in the oil and gas industry, the boiling and condensing process in thermal power plants, and emergency

cooling of nuclear reactors are a few such examples. However, the motivation for the research presented in this thesis is their existence in the natural world, and in particular the role they play in the eruption of volcanoes.

The eruption of Strombolian volcanoes is widely accepted to be caused by the rise and burst of large Taylor bubbles. These bubbles form at a great depth and rise through the conduit before bursting at the surface. The cross sectional shape of a volcanic conduit may vary as it approaches the surface, which in turn can alter the behaviour of the Taylor bubble. The most extreme example of this can be observed in the case of a lava lake, where the conduit enters a reservoir of fluid close to the surface. An example of a Strombolian eruption is shown in Figure 1.2 These topics will be discussed in greater depth in Section 2.2.



Figure 1.2: An example of a Strombolian type eruption at Stromboli, Italy (Geology.com, 2011).

1.1.2 Single Taylor bubbles

A Taylor bubble is a large, elongated gas bubble which is constrained within a fluid by the walls of a pipe. There are four main sections to a Taylor bubble: (i) the nose region ahead of the

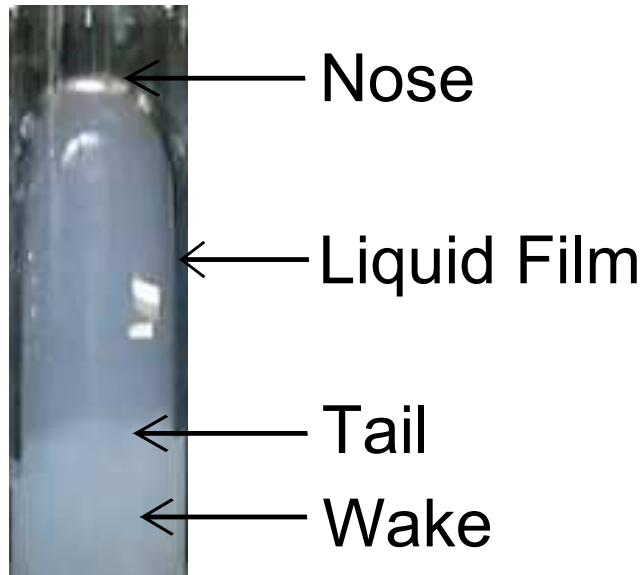


Figure 1.3: Still photograph of a Taylor bubble rising through water, highlighting the bubble nose, liquid film, bubble tail and bubbly wake areas.

bubble, (ii) the body region surrounded by a liquid film between the bubble and the wall of the pipe, (iii) the tail region and (iv) the wake region behind the bubble, these are shown in Figure 1.3. The body section may be subdivided into two sections, one in which the film is developing and one where the film is fully developed and of a constant thickness (Llewellyn et al., 2011).

Despite the large volume of research investigating the rise of Taylor bubbles, a critical analysis of the literature, presented in Chapter 2, identified number of areas lacking in published work. In particular, there is a little work that reports the rise of Taylor bubbles in pipes of diameter over 0.12 m or which investigate the behaviour of Taylor bubbles rising through pipes which contain a change in cross-section.

1.2 Research Aims and Objectives

The primary focus of this research is the modelling of the rise behaviour of single Taylor bubbles.

The research has been carried out with the aim of

Gaining a better understanding of the rise behaviour of single Taylor bubbles in flow conditions which have not previously been studied.

To achieve this aim, the following objectives have been met:

- I. Conduct experiments to confirm the rise behaviour of single Taylor bubbles in conditions which have not been previously studied.
- II. Use CFD (Computational Fluid Dynamics) to model the rise of single Taylor bubbles.
- III. Use the experimental data to validate the numerical model.
- IV. Carry out a number of parametric studies using the CFD model to investigate the behaviour of Taylor bubbles outside of the experimental parameter space.

1.3 Methodology

Numerical simulations using CFD models are used as the primary method of investigation in this research. The commercial CFD code ANSYS FLUENT 12.1 is used for the CFD modelling.

The CFD models used are both verified and validated before being used to perform parametric studies to investigate how the variation of various parameters affects the solution. The verification studies are conducted to minimize the errors introduced. In all cases, the Grid Convergence Index (GCI) method of Roache (1998), as detailed in Section 3.3.2, is used to quantify these errors for both spatial and temporal discretization and ensure mesh and time-step independence.

The models are validated against experimental data to ensure that the use of the chosen models accurately replicates the observed behaviour. This is conducted for cases using published

experimental results and empirical formulae such as those proposed by White and Beardmore (1962), Viana et al. (2003) and Llewellyn et al. (2011) in Section 3.3. More specific validation studies are conducted for the simulations to replicate the rise of air–water Taylor bubbles in a 0.29 m diameter pipe and the rise of Taylor bubbles through expansions in pipe diameter, which are reported in Chapters 5 and 6 respectively.

Once the numerical models are verified and validated, sets of parametric studies are conducted. These investigate the effects that changes in specific parameters, such as initial bubble pressure, bubble length and fluid viscosity, have on the rise behaviour. The results of these transient simulations are monitored by periodically storing values (such as the pressure at a certain location) to files which can then be subsequently analysed. Full data files recording all computed values at all locations at specific times are also stored, but with longer intervals between the recording of files. Full details of the methodology used for the parametric studies may be found in Chapters 5 and 6.

Experimental methods were also used to investigate the rise behaviour of Taylor bubbles in quiescent water in a pipe of diameter 0.29 m. The rise speed of these Taylor bubbles was calculated by determining the time taken to rise through a specific height from an analysis of video recordings. An analysis of these video recordings was also used to determine the length and stability of the rising bubbles and the change in level of the top surface of the water during the experiments. Full details of the methodology used for the experimental studies conducted are presented in Chapter 4

1.4 Thesis Outline

Chapter 1 - Introduction This initial chapter provides a brief introduction to the work that will be covered in the thesis, outlining the aims and objectives of the study, the methodology

which was used, along with the structure of the document.

Chapter 2 - Literature Review This chapter provides a detailed background into the rise of single Taylor bubbles. The flow of Taylor bubbles in volcanic systems is discussed and a critical review of the literature in this area is presented, from which a number of potential topics that could be studied are discussed.

Chapter 3 - Numerical Model In the first part of this chapter, the numerical model used is presented, together with explanations for particular choices of models. In the second part, a number of studies validating the model against published data are presented.

Chapter 4 - Bubble Rise - Experimental A set of experimental studies into the rise of Taylor bubbles were conducted in a vertical pipe filled with quiescent water and with internal diameter of 0.29 m. These experiments were conducted in collaboration with a Research Associate, Dr Chris Pringle. The stability, rise velocity and oscillatory behaviour of Taylor bubbles rising in this apparatus are examined. The methodology, results and conclusions drawn from this study are presented in this chapter.

Chapter 5 - Bubble Rise - Numerical The numerical model presented in Chapter 3 is used to model the experimental studies. The results obtained in the experimental studies are used to further validate the numerical model. A number of physical parameters, such as the initial length of the bubbles, the initial pressure of the bubble, the viscosity of the fluid and the diameter of the pipe are varied to investigate the resultant changes to the behaviour of the rising Taylor bubbles.

Chapter 6 - Expansion of pipe diameter This chapter details the results of a numerical study into the rise of a Taylor bubble through an expansion in pipe diameter. Published ex-

perimental work is discussed and other experimental studies conducted at the Universities of Nottingham and Bristol are detailed. The results of these experimental studies are used to further validate the numerical model. This numerical model is then used to explore the effects of a variation in a number of parameters, including the angle of expansion, the ratio of the upper to lower pipe diameters and the liquid viscosity.

Chapter 7 - Conclusions A summary of the outcomes and conclusions drawn from the studies reported above are presented in this chapter, along with recommendations for further work that may be conducted.

1.5 Highlights

A number of the of highlights of this research are:

- A validated (and verified) CFD model capable of replicating the rise behaviour of Taylor bubbles was created.
- Stable Taylor bubbles were shown to exist and be sustained in a pipe of internal diameter 0.29 m in the experiments of Chapter 4, which is a significantly larger diameter than had been reported in previous work.
- Taylor bubbles were also shown to exhibit oscillatory behaviour in the experiments of Chapter 4. The frequency of these oscillations was shown to be consistent with the theoretical predictions of Vergnolle et al. (1996) and Pringle et al. (2014).
- The CFD model was used to successfully replicate the oscillatory behaviour observed in the experimental studies with the frequency of oscillation within 10 % of the experimental values. The theoretical models proposed by Pringle et al. (2014) and Vergnolle et al. (1996)

predict that the frequency of bubble oscillation is proportional to $L^{-1/2}$, where L is bubble length, a relationship which is confirmed by the CFD modelling.

- The qualitative and quantitative experimental behaviour of a Taylor bubble rising through an expansion in pipe geometry was replicated by the CFD model. Bubbles are observed to expand as they encounter an expansion in pipe diameter. This causes an increase in the liquid flux in the film surrounding the bubble, which leads to a necking of the bubble. For bubbles of sufficient length, this necking process will split the bubbles into two parts. The resultant pressure oscillations generated by this splitting were validated against the results of James et al. (2006).
- An analysis of the results of the simulations confirms that there is a linear relationship between the critical length of bubble which can pass through an expansion before the neck closes and the cosec of the angle of the expansion. An analysis of the experimental results of Soldati (2013) confirms of this relationship.

2.1 Single Taylor bubbles

2.1.1 Non-dimensional groups

In Section 2.1 a Taylor bubble was described as a large, elongated gas bubble which is constrained within a fluid by the walls of a pipe. Another defining feature of single Taylor bubbles rising in a vertical pipe is that of a constant non dimensional rise rate. This was first observed by Dumitrescu (1943) and Taylor and Davies (1950) who suggested rise velocity was dependent on the square root of the pipe diameter, D . This gives rise to the non-dimensional parameter group known as the Froude number, Fr , defined by,

$$Fr = \frac{U}{\sqrt{gD(\rho_L - \rho_G)/\rho_L}}, \quad (2.1)$$

where U is the rise velocity of the bubble, g is the acceleration due to gravity, ρ_L is the liquid density and ρ_G is the gas density. The Froude number is constant for inviscid flow in a regime which is independent of surface tension. The Froude number has been both theoretically predicted and calculated from empirical data in numerous papers (Dumitrescu, 1943; Taylor and Davies, 1950; White and Beardmore, 1962; Brown, 1965; Wallis, 1969; Viana et al., 2003). Of

these, the theoretical model of Dumitrescu (1943) is widely regarded as being the most accurate for this regime (Fabre and Line, 1992).

As the effects of viscosity or surface tension become important, the Froude number will vary. To describe the effects of viscosity or surface tension, the definition of further non-dimensional parameter groups are required. Firstly, the Eötvös number,

$$E_o = \frac{g(\rho_L - \rho_G)D^2}{\sigma}, \quad (2.2)$$

where σ is the surface tension coefficient. The Eötvös number is a measure of the ratio of buoyant forces to surface forces. And secondly, the Morton number,

$$M = \frac{g\mu_L^4(\rho_L - \rho_G)}{\sigma^3\rho_L^2}, \quad (2.3)$$

which is the ratio of viscous to surface forces, where μ_L is the liquid viscosity.

Figure 2.1, taken from White and Beardmore (1962) summarizes the results of many experiments that were conducted to determine at which parameter values the observed flow regime becomes independent of inertial forces, surface tension and viscosity. In this figure, Morton number is plotted against the Eötvös number with line of constant Froude number shown. The graph is divided into regions where the results are independent of particular forces. As can be observed from this diagram, as the Eötvös number increases above 100, there is no change in Froude number. This implies that as the pipe diameter increases above a certain level, determined by the fluid properties, the rise velocity will become independent of surface tension forces. In addition, if the Eötvös number is below 3.37, then a bubble will not rise as the surface tension force matches the buoyant forces. For an air-water system this corresponds to a pipe diameter of approximately 0.005 m. As the Morton number is increased, the effects of the viscosity of the liquid in relation to the surface forces will also increase. The effects of viscosity on the rise rate of a Taylor bubble can be considered negligible provided the Morton number is less than approximately 10^{-8} given an Eötvös of less than 50. For an Eötvös number of over 50, the effects

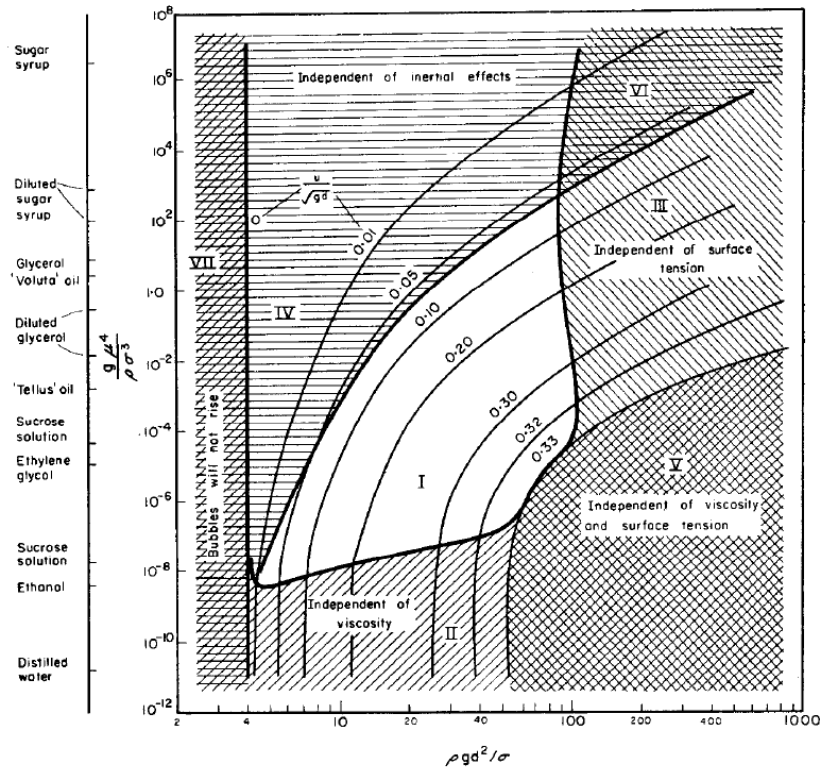


Figure 2.1: Crossplot of dimensionless data showing different flow regimes (White and Beardmore, 1962).

of viscosity may be neglected provided that the Froude number is at least 0.33, which is observed to occur in the shaded regions II and V of Figure 2.1 respectively.

2.1.2 Rise speed of Taylor Bubbles

The Froude number can be estimated using a Reynolds number based on the buoyant forces, Re_B .

$$Re_B = N_f = \frac{(D^3 g (\rho_L - \rho_g) \rho_L)^{0.5}}{\mu_L}, \quad (2.4)$$

$$\text{If, } Re_B < 10, Fr = \frac{9.494 \times 10^{-3} R^{1.026}}{(1 + (\frac{6197}{E^{3.06}}))^{0.5793}}, \quad (2.5)$$

$$\text{If, } 10 < Re_B < 200, Fr = L[R; A, B, C, G] \equiv \frac{A}{(1 + (R/B)^C)^G}, \quad (2.6)$$

where

$$A = L[EO; a, b, c, d], B = L[EO; e, f, g, h], C = L[EO; i, j, k, l], G = m/C, \quad (2.7)$$

and the parameters (a, b, \dots, m) are

$a=0.34, b=14.793, c=-3.06, d=0.58, e=31.08, f=29.868, g=-1.96, h=-0.49, i=-1.45, j=24.867, k=-9.93, l=-0.094, m=-1.0295.$

$$\text{If, } Re_B > 200, Fr = \frac{0.34}{(1 + (\frac{3805}{E^{3.05}}))^{0.58}}. \quad (2.8)$$

This is also referred to as an "inverse viscosity" in some papers and is referred to as the parameter N_f (Campos and Carvalho, 1988; Llewellyn et al., 2011). If it assumed equal to the classical Froude number, it may be arranged to yield an expression for the terminal velocity, v_t , due to the fluid properties and pipe diameter (Viana et al., 2003), (Figure 2.2). Viana et al. (2003) collated a large amount of experimental data to create empirical models to estimate the Froude number for varying Reynolds numbers. The experiments these conclusions are drawn from have an upper viscosity limit of 3.9 Pa.s, it is currently unknown whether the correlation is valid for higher viscosities.

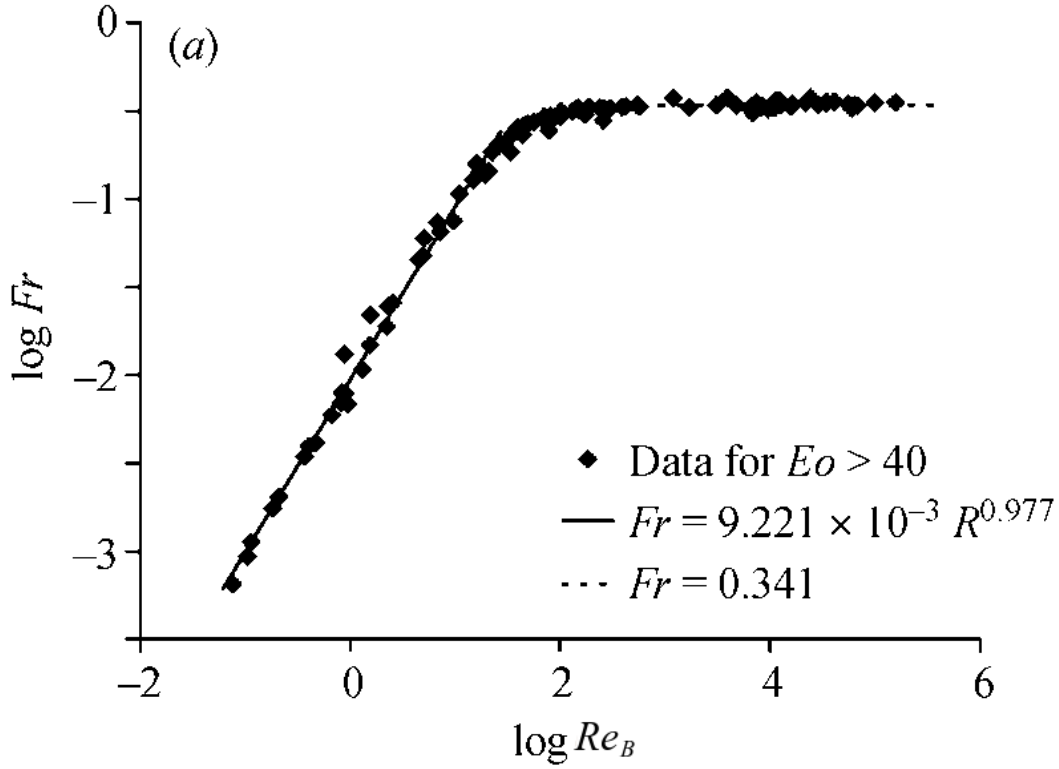


Figure 2.2: Figure showing the variation of the Froude number with the Reynolds number based on buoyancy for a collection of experimental data, (Viana et al., 2003). A clear distinction can be observed between the two flow regimes described by $Fr = 0.341$ and $Fr = 9.221 \times 10^{-3} R^{0.977}$ respectively.

The classical definition of the Froude number is given by Equation 2.1. A rearrangement of this equated to the Froude number calculated with the buoyancy Reynolds number yields the following expression for the terminal velocity of a slug.

$$v_t = Fr \sqrt{gD(\rho_L - \rho_g)/\rho_L}. \quad (2.9)$$

A Taylor bubble is defined to be fully developed when its length does not have an effect on the rise velocity. After the flow passes the top of the bubble it is squeezed into an annular gap around the bubble, forming a thin film of liquid near the wall. Once the length of the bubble

reaches a value of $1.5 D$, the flow may be assumed to be purely in vertical direction and the length of the bubble will not affect its terminal velocity (Taylor and Davies, 1950).

2.1.3 Flow fields around Taylor bubbles

A number of experimental studies have used a Particle Image Velocimetry (PIV) method to visualise the flow field around a rising Taylor bubble and obtain quantitative data from it (Polonsky et al., 1999; van Hout et al., 2002; Nogueira et al., 2003, 2006a). PIV methods are non-intrusive imaging techniques which can provide qualitative instantaneous velocity fields (Adrian, 1991).

This technique may be implemented for two phase flows by seeding the liquid phase with fluorescent particles. The PIV process uses a laser sheet which is pulsed at regular time intervals. These laser sheets illuminate the fluorescent particles. A camera is triggered at the same frequency as the time intervals to capture individual frames of the successive positions of the particles suspended in the fluid. The laser light was filtered out by a high pass filter (only light of wavelength > 550 nm is observed, the laser light typically has wavelength of 532 nm so is filtered but the particles emit light at a wavelength of 572-594 nm) and hence only the particles are observed on the final photograph frames. The images are then analysed using specialist software which compares the successive positions of the individual particles to generate instantaneous velocity fields (van Hout et al., 2002; Nogueira et al., 2003).

van Hout et al. (2002) used PIV techniques to analyse the flow field around a Taylor bubble in a 0.025 m pipe filled with stagnant water, which provided an N_f number of approximately 150. In this study, the resulting flow fields were generated for 100 single Taylor bubbles and were subsequently averaged. An example of one of these flow fields is shown in Figure 2.3. From an analysis of the results they concluded that an individual Taylor bubbles only influenced the flow ahead of their nose for one pipe diameter. This conclusion was also drawn by both Polonsky et al. (1999) and Bugg and Saad (2002) who also used PIV methods to study the flow around Taylor bubbles. A further detailed description of the study of van Hout et al. (2002) is provided in Section 3.3.4 where the results are used to validate a numerical model.

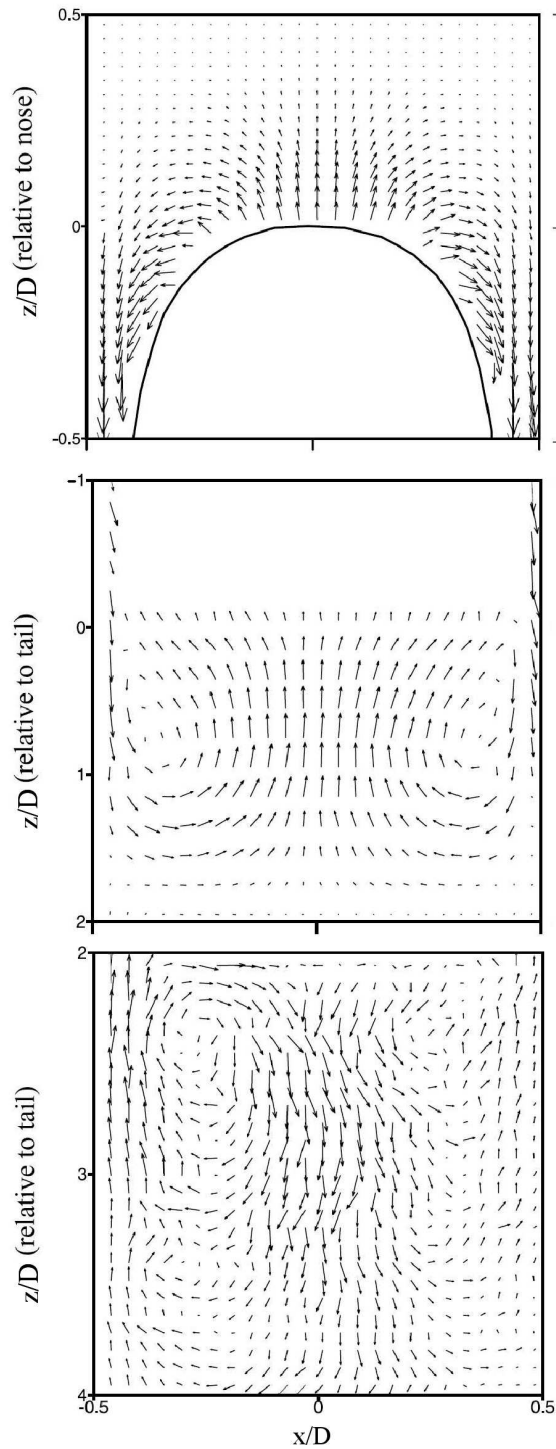


Figure 2.3: An example of flow fields around a Taylor bubble rising in water in a vertical pipe of diameter 0.025 m which were generated using a PIV method, (van Hout et al., 2002). These flow fields are averaged from 100 experimental runs. The top image shows the flow around the nose of the Taylor bubble, the middle image shows the flow around the tail of the bubble, and the bottom image the flow further into the wake (2-4 pipe diameters below the tail).

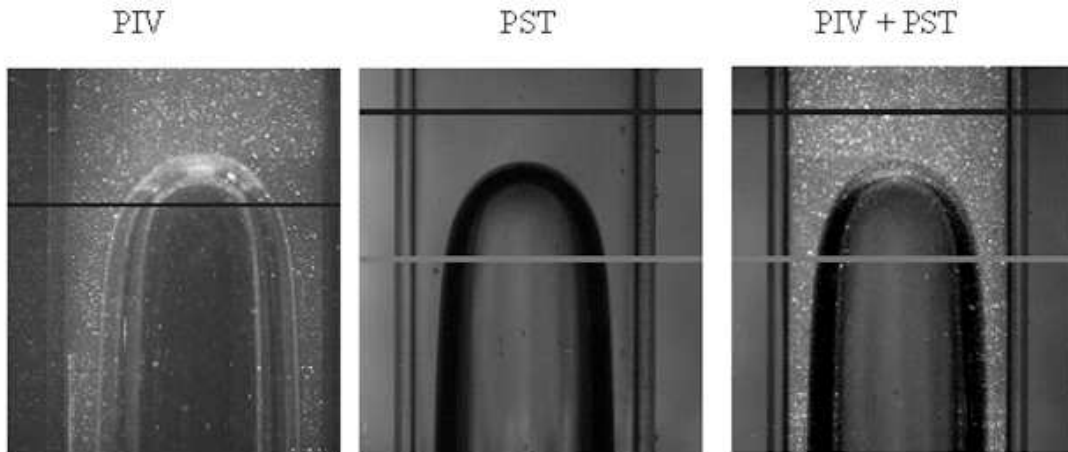


Figure 2.4: A comparison of images captured by using PIV and PST and a combined method (Nogueira et al., 2003). A much clearer outline of the bubble is captured with the combined method than by using PIV alone.

Bugg and Saad (2002) used a similar PIV method to study the flow field around Taylor bubble rising under laminar flow conditions in a 0.019 m pipe filled with olive oil. The velocity profiles observed in the lower section of the liquid film matched that expected for a viscous falling film. The flow in the wake region was also seen to fall into the laminar regime, with a N_f number of approximately 90. The shape of the bubble was sketched by hand from an examination the PIV results, which, although providing an estimate of the bubble shape, is not very accurate.

To obtain a more accurate representation of the bubble shape, a method called the Pulsed Shadow Technique (PST) may be used. This method pulses a panel of LED lights which illuminate the Taylor bubble. This produces a shadow which passes through an optical filter that may be recorded by a digital camera (Nogueira et al., 2003). An example of the images that may be created by the use of the PST method in comparison to the PIV technique is shown in Figure 2.4.

Nogueira et al. (2006a) used the results from simultaneous PIV and PST studies to determine

the flow field around single Taylor bubbles rising in both stagnant and co-current flow conditions (with a maximum viscosity of 1.5 Pa.s) contained within a vertical 0.032 m diameter pipe. An analysis of the results obtained from these studies concluded that the bubble shape and film thickness are strongly influenced by changes in the liquid viscosity. It was observed that as the viscosity increases (hence decreasing Re number), the thickness of the liquid film increases, as the bubble outlines shown on Figure 2.5 illustrate.

2.1.4 Film Thickness around Taylor Bubbles

Early research studies proposed a series of theoretical and empirical expressions to represent the ascent velocity of a Taylor bubble in terms of the observed film thickness, λ (Goldsmith and Mason, 1962; Brown, 1965; Batchelor, 1967). Goldsmith and Mason (1962) solved a mathematical model constructed using the laminar Navier-Stokes equations to represent the film flow around a Taylor bubble to derive an expression for the ascent velocity of a Taylor bubble in terms of a thin film,

$$v_t = \frac{2\rho g \lambda^3}{3\mu r}. \quad (2.10)$$

Brown (1965) and Batchelor (1967) both derived similar forms of expression for this same film thickness,

$$v_t = \frac{2\rho g \lambda^3}{3\mu r - \lambda}, \quad (2.11)$$

$$v_t = \frac{2\rho g \lambda^3}{3\mu r - 2\lambda}.$$

(2.12)

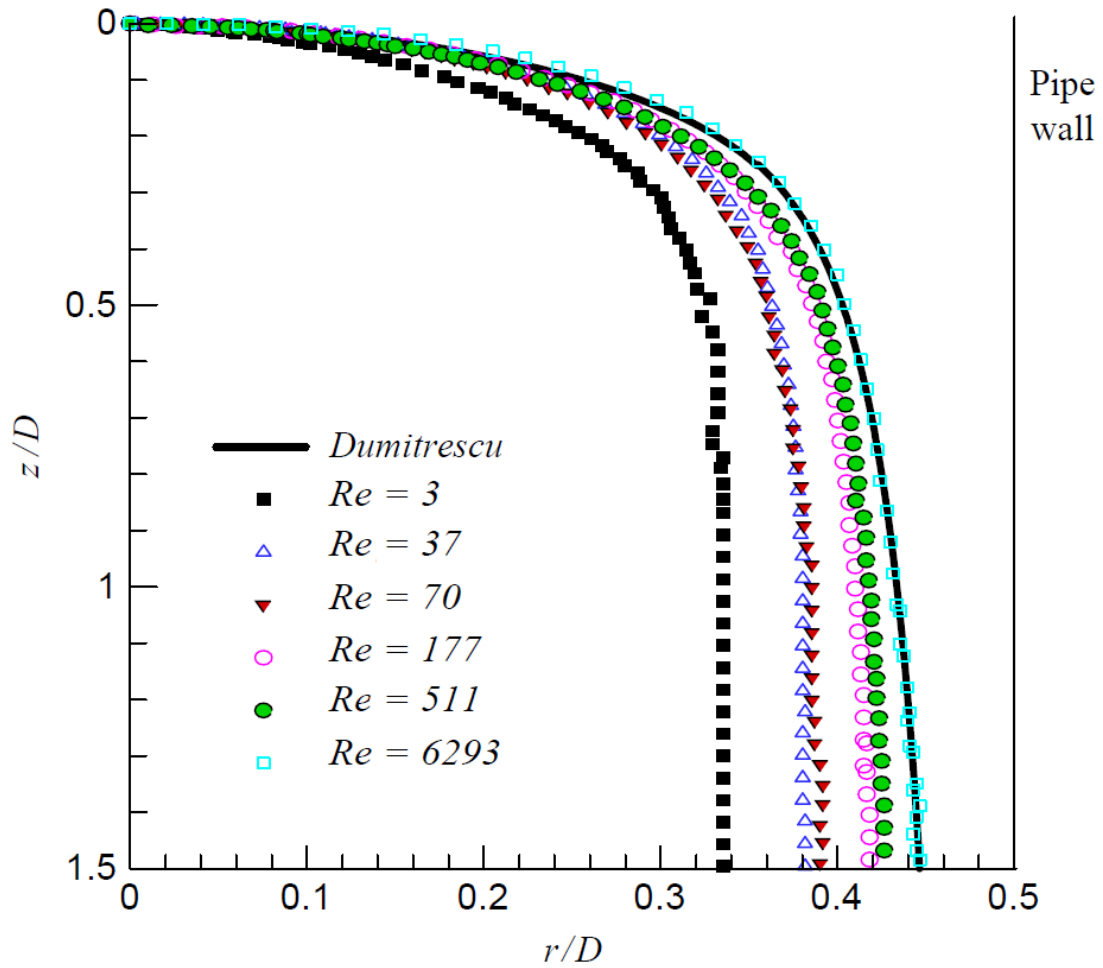


Figure 2.5: The effects that an increased Re number has on the film thickness developed around a rising Taylor bubble, (Nogueira et al., 2006a). This Reynolds number is based on bubble velocity and pipe diameter and is varied by using aqueous glycerol solutions of different viscosities in a 0.032 m pipe.

If the film is assumed to be thin (i.e. $r \gg \lambda$), both of these expressions reduce to that in Equation 2.10.

However, Brown's expression does not depend on this assumption of a thin liquid film. He instead uses an alternative definition of the Froude number, which is based on the radius of the Taylor bubble and not of the pipe radius. This leads to his formulation of film thickness,

$$\lambda = \frac{\sqrt{1 + ND_t} - 1}{N}, \quad (2.13)$$

where,

$$N = \left(14.5 \frac{\rho^2 g}{\mu^2} \right)^{1/3}, \quad (2.14)$$

where the parameter N , which relates buoyancy to viscous forces, along with the pipe diameter, D , gives an expression for the film thickness. This can then be used to provide an expression for the slug ascent velocity (Brown, 1965),

$$v_t = 0.345 \sqrt{g(D - 2\lambda)}. \quad (2.15)$$

Studies of more general liquid films, not restricted to the rise of Taylor bubbles, also provide estimates for film thickness which can be applied to Taylor bubbles. The theoretical study of Nusselt (1916) derives a value for film thickness for a viscous, laminar film falling under gravity,

$$\lambda = \left[\frac{3\mu^2}{4\rho^2 g} \text{Re}_f \right]^{1/3}, \quad (2.16)$$

where Re_f is a Reynolds number based on film velocity (Dukler and Bergelin, 1952), given by,

$$\text{Re}_f = 4 \frac{\rho \lambda v_f}{\mu}, \quad (2.17)$$

where v_f is the average velocity in the film. This theoretical model compares well to the experimental work later carried out by Dukler and Bergelin (1952) for $Re_f < 1000$. However, this model under-predicts for higher Reynolds numbers due to the laminar flow assumption. Dukler and Bergelin (1952) propose an implicit relationship for film thickness,

$$Re_f = 4\eta(3 + 2.5 \ln \eta) - 256, \quad (2.18)$$

where $\eta = \rho\sqrt{g\lambda^3}/\mu$. This theoretical model is validated by experimental work conducted over a range of Reynolds numbers, $500 < Re_f < 3000$. The thickness of the film observed in these experiments was not constant, but varied with time due to the formation of waves along the surface of the film. For this reason the mean film thickness is compared to the model in Equation 2.18, rather than the thickness at a particular time.

More recent work has sought to develop explicit, empirical models to estimate the film thickness over a wide range of Reynolds numbers (Karapantsios et al., 1989; Karapantsios and Karabelas, 1995; Lel et al., 2005; Zhou et al., 2009). The results of these studies comprise the conclusions of the analysis of a large number of experiments over a wide range of Reynolds numbers ($10 < Re_f < 15000$). Flows with Reynolds numbers below 3000 are assumed to be laminar, and turbulent above this value. For $Re_f < 3000$, the model proposed by Lel et al. (2005) was seen to best reproduce the experimental data. This model is characterised by,

$$\lambda \left[\frac{\rho^2 g}{\mu^2} \right]^{\frac{1}{3}} = 1 + 0.321 Re_f^{0.47}. \quad (2.19)$$

For turbulent flow, where $Re_f > 3000$, the model of Karapantsios and Karabelas (1995) is determined to be more accurate,

$$\lambda \left[\frac{\rho^2 g}{\mu^2} \right]^{\frac{1}{3}} = 0.214 Re_f^{0.538}. \quad (2.20)$$

A recent study by Llewellyn et al. (2011) derived a theoretical model to represent the dimensionless film thickness, $\lambda' = \frac{\lambda}{\tau}$, based on the model of Brown (1965). Instead of assuming a constant value for the Froude number, this model uses a rearrangement of Equation 2.11 in the cubic form,

$$\lambda'^3 + a\lambda' - a = 0, \quad (2.21)$$

where $a = 6\frac{Fr}{N_f}$, which has the solution,

$$\lambda' = \frac{\sqrt[3]{b^2} - \sqrt[3]{12a}}{\sqrt[3]{18b}}, \quad (2.22)$$

$$\text{where } b = 9a + \sqrt{12a^3 + 81a^2}. \quad (2.23)$$

The derivation of this result does, however, assume that the flow is laminar and hence it is only valid for $Re_f < 3000$ (Llewellyn et al., 2011). This model was validated against the experimental work of Nogueira et al. (2006a) and found to closely match the findings of the experimental work across its range of validity. This is shown in Figure 2.6.

2.1.5 Wake behaviour of Taylor Bubbles

Moissis and Griffith (1962) used a pitot tube to measure the velocity profiles of the fluid flow at various distances behind a Taylor bubble. They concluded that in the slug flow regime, the wake of the preceding bubble interacts with the dynamics of the following Taylor bubble. They proposed that slug flow may only be classed as fully developed when the wake of one bubble does not affect the flow behaviour of the next. For the rise of a single Taylor bubble, the wake of any previous bubbles must not affect the flow behaviour if it is to be considered as rising into a quiescent fluid.

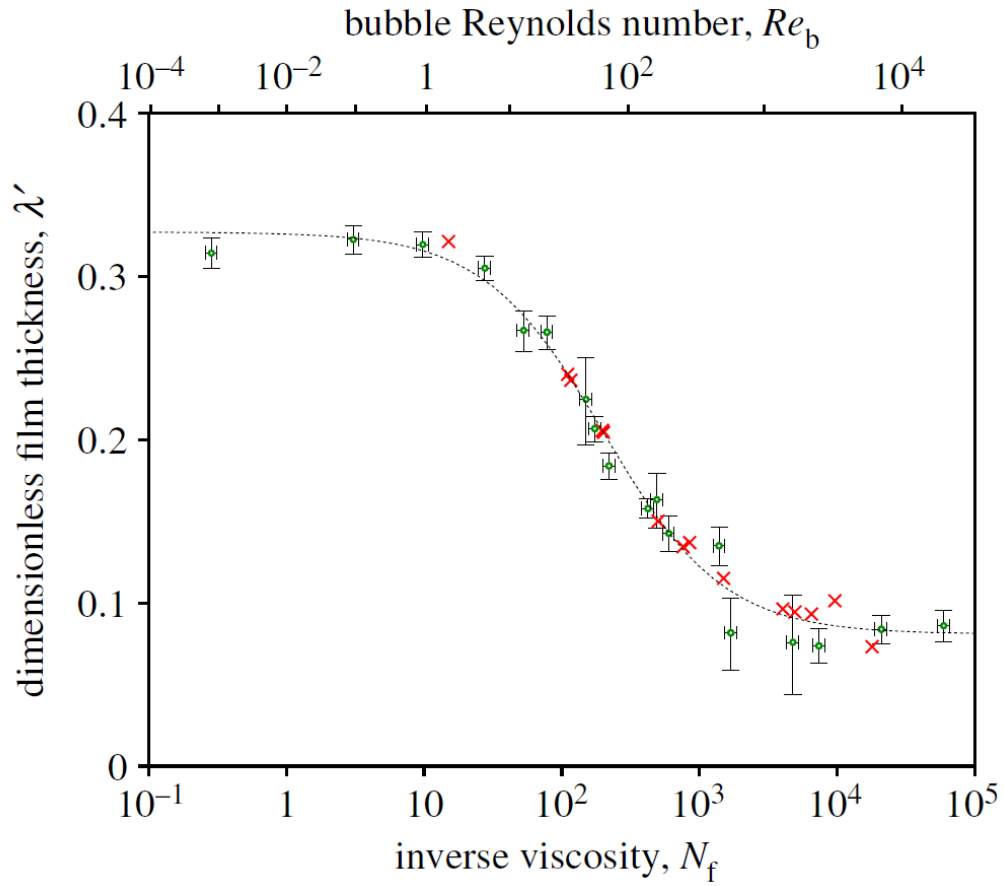


Figure 2.6: The cubic Brown model proposed by Llewellyn et al. (2011), dashed line, compared to experimental data, Llewellyn et al. (2011), dots with error bars and Nogueira et al. (2006a), crosses.

Campos and Carvalho (1988) studied the wake of individual Taylor bubbles using photographic evidence from experiments of single Taylor bubbles rising in stagnant, Newtonian liquids. Three distinct flow regimes were observed in the wake behind the bubbles. For bubbles longer than

$$Z = \frac{(gd^2/2\nu + U)^2}{2g}, \quad (2.24)$$

the flow regime of the wake is governed by the dimensionless parameter, N_f . The first of the three flow regimes observed occur at vales of $N_f < 500$ and will be referred to as a laminar wake region. The wake is observed to be closed and axisymmetrical and to rise at the same velocity as the bubble. The rear of the Taylor bubble was observed to have an oblate spheroid shape that does not oscillate. An example of such a wake is shown in Figure 2.7 (a).

Non-dimensional expressions for the length and volume of the wake for this flow regime may be empirically represented for $100 < N_f < 500$ by the expressions,

$$\frac{l_w}{D} = 0.30 + 1.22 \times 10^{-3} N_f, \quad (2.25)$$

and

$$\frac{v_w}{D} = 7.5 \times 10^{-4} N_f, \quad (2.26)$$

where l_w is the length of the wake and v_w is the volume of the wake.

Increasing the value of N_f to between 500 and 1500 defines the second regime, in which there is still a closed wake although it is no longer axisymmetric, (Figure 2.7 (b)). The rear of the bubble now has a flat shape and oscillates with a frequency which increases with an increase in the value of N_f . The use of Equation 2.25 remains valid whilst $N_f < 800$ but not if it rises above this value. This is termed a transitional wake.

For values of $N_f > 1500$ the wake behind a Taylor bubble ceases to possess clearly defined

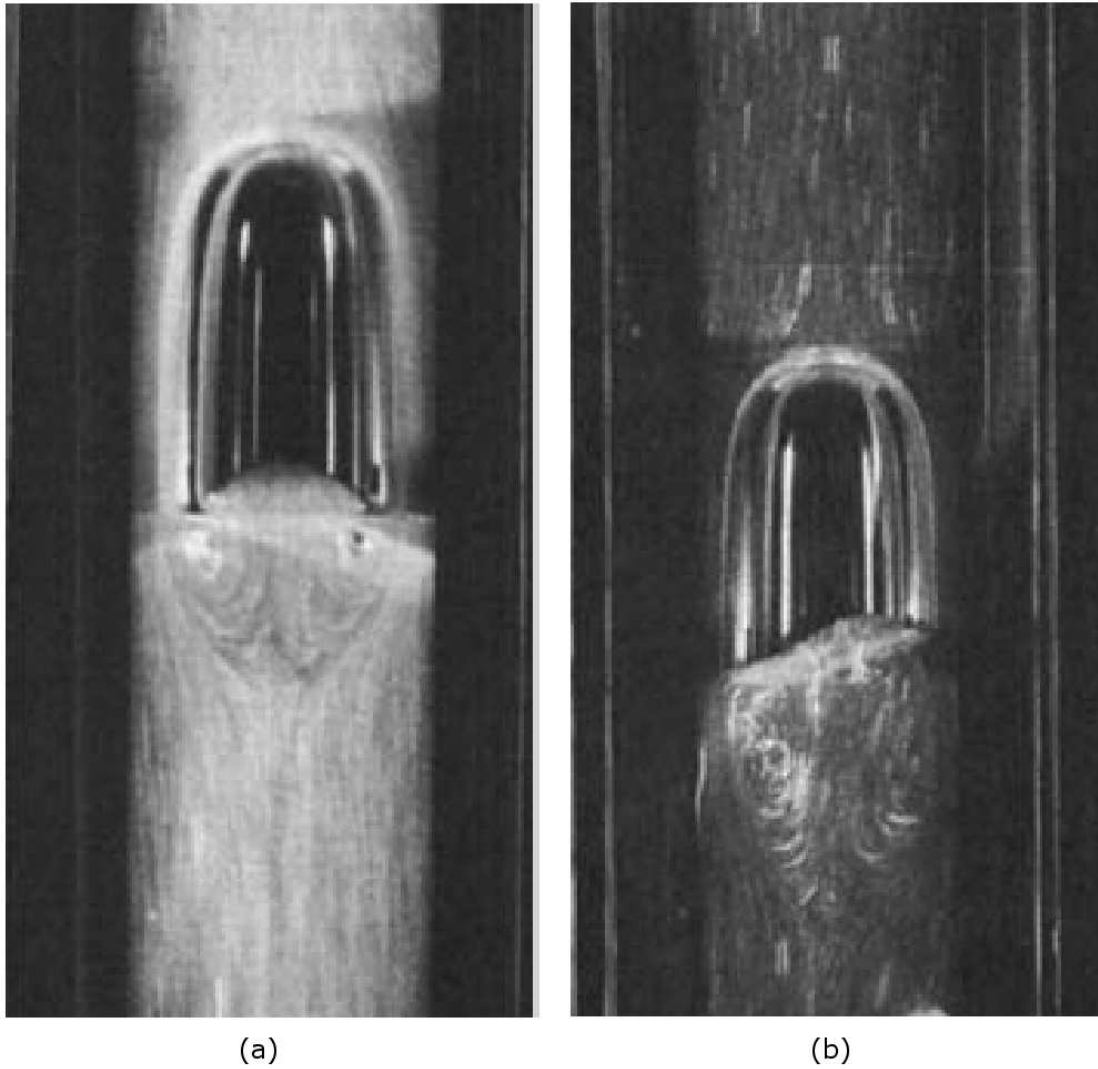


Figure 2.7: (a) A Taylor bubble with $N_f < 500$ rising with a laminar wake which is closed and axisymmetric, (Campos and Carvalho, 1988) and (b) a Taylor bubble with $500 < N_f < 1500$ rising with a transitional wake which is closed but no longer axisymmetric, (Campos and Carvalho, 1988).

boundaries. There may also be some re-circulatory regions of flow when N_f approaches 500. As the value increases, more turbulent eddies are formed which may affect the flow regime further behind the bubble. This is referred to as a turbulent wake region. An example of this phenomenon is seen in Figure 2.8

Sousa et al. (2005) used the combined PIV and PST technique described earlier to investigate the rise of Taylor bubbles in an aqueous solution of CMC polymer. This is a non-Newtonian fluid with CMC weight percentages ranging from 0.1 % to 1 %, giving a variation in N_f up to 900. Film thickness was seen to increase with an increasing weight percentage of CMC and hence an increase in the N_f . The wake behaviour observed behind these Taylor bubble was studied and compared to the work of Campos and Carvalho (1988), shown in Figure 2.9. The length of the wake is estimated to be,

$$\frac{l_w}{D} = 0.20 + 1.14 \times 10^{-3} N_f. \quad (2.27)$$

Pinto and Campos (1996) investigated the coalescence between consecutive Taylor bubbles in a stagnant liquid. They found a correlation between the minimum non-dimensional length at which bubbles would coalesce and N_f , for each of the flow patterns observed in the wake.

$$\frac{l_w}{D} = 1.46 + 4.75 \times 10^{-3} N_f, \text{ for a laminar wake, } 100 < N_f < 500 \quad (2.28)$$

$$\frac{l_w}{D} = 0.692 + 7.90 \times 10^{-3} N_f, \text{ for a transitional wake, } 500 < N_f < 1500 \quad (2.29)$$

$$\frac{l_w}{D} = 12.5, \text{ for a turbulent wake, } N_f > 1500 \quad (2.30)$$

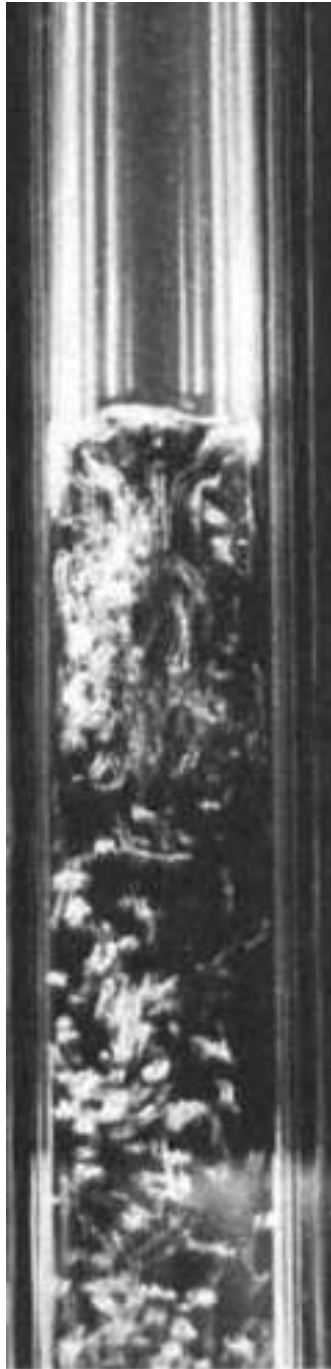


Figure 2.8: A Taylor bubble with $N_f > 1500$ rising with a turbulent wake which is open and not axisymmetric, (Campos and Carvalho, 1988).

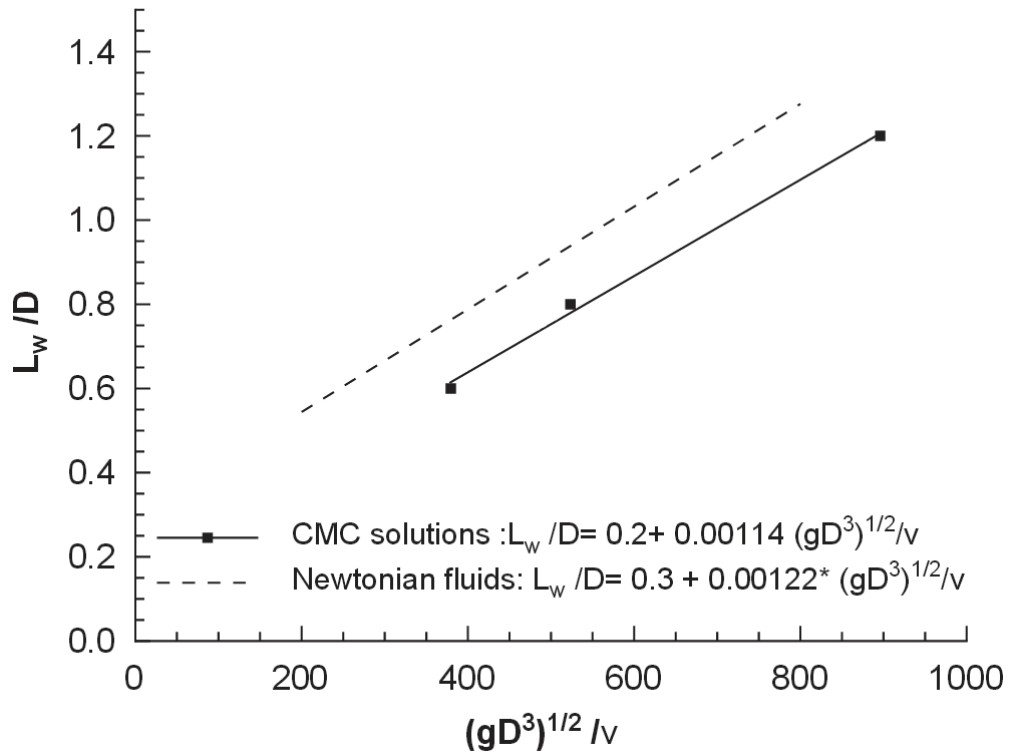


Figure 2.9: A graph illustrating the dependence of the wake length on the value of N_f for a non-Newtonian CMC solution (filled line) in comparison to the results presented for Newtonian fluids (dashed line) by Campos and Carvalho (1988), (Sousa et al., 2005).

2.1.6 Other experimental methods

There are a number of other experimental techniques which may be used to determine the various characteristic features of Taylor bubbles.

One such method to determine the shape, film thickness and rise velocity of a Taylor bubble is to use electrical capacitance tomography (ECT). This non-invasive device is formed from a number of electrodes which are externally mounted on the pipe. The capacitance of the fluid between every possible pair of electrodes is measured, and these are converted into voltage signals which are collected by a data acquisition unit, which digitalises the signal and communicates it to a computer. The computer process this data using a suitable “image reconstruction algorithm” to generate an approximate cross-sectional image, and from these a void fraction may be estimated (Huang et al., 2005). This is more common in studies investigating slug flow rather than single Taylor bubbles, as it is less accurate but capable of recording data for long periods of time.

A wire mesh sensor (WMS) is an intrusive device which measures not only the total gas void fraction within a fluid, but also the void fraction distribution within the pipe. For this reason, it can be an extremely useful sensor, although it has some severe limitations. As it is intrusive, the flow downstream of the WMS will be severely affected by its presence. At very high liquid viscosities (50–100 Pa.s) bubbles of gas may not rise through the WMS and hence it is unable to measure the void fraction in these cases. A photograph of a WMS is shown in Figure 2.10. The WMS consists of two horizontal planes of wires perpendicular to each other at slightly offset heights. The local capacitance of the liquid is measured at each of the points where these wires cross. This is achieved by pulsing the lower transmitter wire with a signal at regular intervals, and measuring the signal received at the corresponding receiving wire. From this a local void fraction can be determined and hence the distribution of the void fraction can be determined (Abdulkadir et al., 2010).

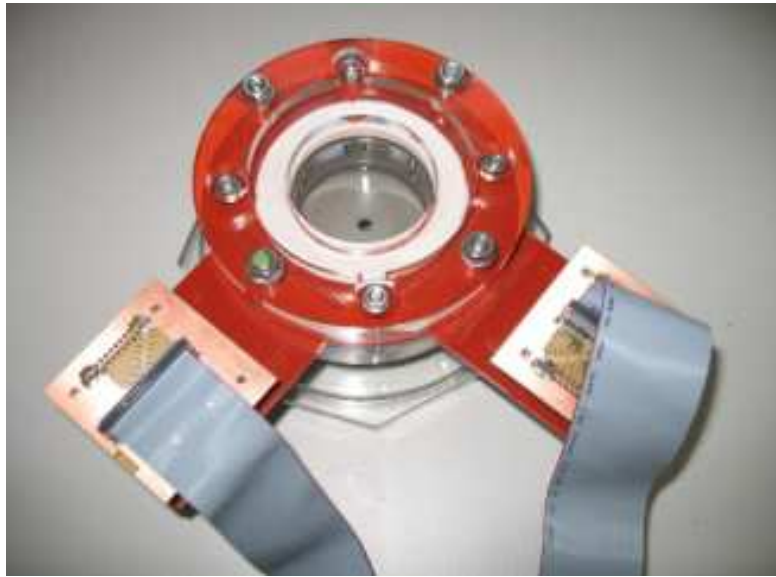


Figure 2.10: A photograph of a wire mesh sensor. This is an intrusive device which measures not only the total gas void fraction within a fluid, but also the void fraction distribution within the pipe.

2.1.7 Stability of Taylor Bubbles

The stability of Taylor bubbles is less well understood than its other characteristics. A number of previous studies have, however, attempted to theoretically determine stability criteria for Taylor bubbles, (Batchelor, 1987; Clift et al., 1978; Kitscha and Kocamustafaogullari, 1989). A bubble can be regarded as unstable if it is observed to break up as it rises. An example of an unstable Taylor bubble is shown in Figure 2.11.

It is proposed that the large difference in densities that exist between the air and water phases may cause small inter-facial disturbances around the gas-liquid interface of the bubble to grow. If these become large enough then they cause the bubble to break up. There is, however, a limited time for growth as they are simultaneously transported down the side of the bubble into the liquid film due to the upward movement of the rising bubble. Following an analysis of



Figure 2.11: A Taylor bubble rising in water in a 0.3 m pipe in an unstable manner (left) and in a stable manner (right) Pringle et al. (2014). This instability is the result of the fluid not being completely quiescent before the bubble was released.

the critical wavelengths and amplitudes of these disturbances, Batchelor (1987) predicted that a Taylor bubble could maintain a maximum diameter of 0.46 m in an air-water system.

The maximum size of a stable Taylor bubble observed in an experimental air-water system is 0.115 m (Martin, 1976). However, James et al. (2011) reports a stable Taylor bubble of air within a 0.24 m diameter pipe of water, Figure 2.12. This source is of limited use as they do not provide sufficient description of their experiment, nor define their measure of stability. An unpublished conference proceeding by Hsu and Simon (1969) also suggested the existence of stable bubbles in a 0.3 m tube.

2.1.8 Expansions in pipe diameter

Very little experimental work on the rise of single Taylor bubbles has been conducted in anything other than a straight pipe. There has been some work on both horizontal and inclined flow, although these are more commonly observed in the slug flow regime. There is a paucity of research into the effects of changes in pipe diameter on the behaviour of single Taylor bubbles in vertical pipes. However, there have been numerous investigations to the effects of expansions in pipe diameter on various co-current gas-liquid flow regimes for horizontal pipes Lottes (1961); Ahmed (b); Wang et al.; Azzopardi et al. (2014) and in vertical pipes for bubbly flow (Aloui et al., 1999; Rinne and Loth). These expansions in diameter (along with other complex geometries, such as contractions, bends, orifices and valves) are often found in processes transporting oil and gas mixtures and in heat exchangers in industry (Aloui et al., 1999; Ahmed, a).

A change in the diameter of a pipe will intuitively cause changes in the behaviour of a rising Taylor bubble. Clearly, there will be a change in the rise velocity of the bubble, as this is dependent on the diameter of the pipe. Less clear, however, are the effects that this change of velocity may have on the wider behaviour of the bubble, and in particular its stability.

A recent paper by James et al. (2006) reports the results of an experimental study that



Figure 2.12: A Taylor bubble rising in water in a stable manner in a pipe of diameter 0.24 m, (James et al., 2011).

investigated this problem. They investigate single Taylor bubbles rising through a variety of expansions and contractions (using 0.038 m, 0.05 m and 0.08 m pipe sections) through a stagnant liquid. Figure 2.13 shows an example of the experimental set up used in their study. Syrups with viscosities 0.001, 0.1 and 30 Pa.s were used to compare behaviour across a range of Froude numbers. It was observed that as the bubbles passed through an expansion they accelerated and expanded laterally. For bubbles of sufficient length this process caused the bubble to break as it rose through the expanding section. This bubble break up caused an oscillation in the static pressure readings recorded at a number of locations. The purpose of this work was to compare the pressure signals generated in the laboratory with Long Period seismic data from volcanoes, with the assertion that the pressure oscillations seen in the seismic data were caused by a gas slug rising through an expanding pipe section. Further details of this study are presented later in Chapter 6 where it is used as a validation case for the solution of a numerical model.

The only other published study that has investigated Taylor bubbles rising through expansions in pipe diameter is reported in a conference proceedings paper by Kondo et al. (2002). In this study, a Taylor bubble of air in a 0.02 m diameter pipe was observed to break up as it entered a sudden expansion, with pipe diameter increasing to 0.05 m. The focus of this study was co-current flow (resulting in a bubbly flow regime), but a case with no net liquid flow resulting in Taylor bubbles is also described. Other unpublished experimental work has been carried out as a part of a series of parallel studies associated with this NERC funded project. A research student at the University of Nottingham studied Taylor bubbles rising through a vertical 0.01 m diameter pipe into a range of larger diameter pipes (Carter, 2012). The rise of these bubbles were recorded by high speed video and the accompanying acoustic measurements detected by microphones. A research student at the University of Bristol studied the rise of Taylor bubbles in through varying angles of expansion in a series quasi-2D experiments (Soldati, 2013). Both of these studies are discussed in depth in Chapter 6.

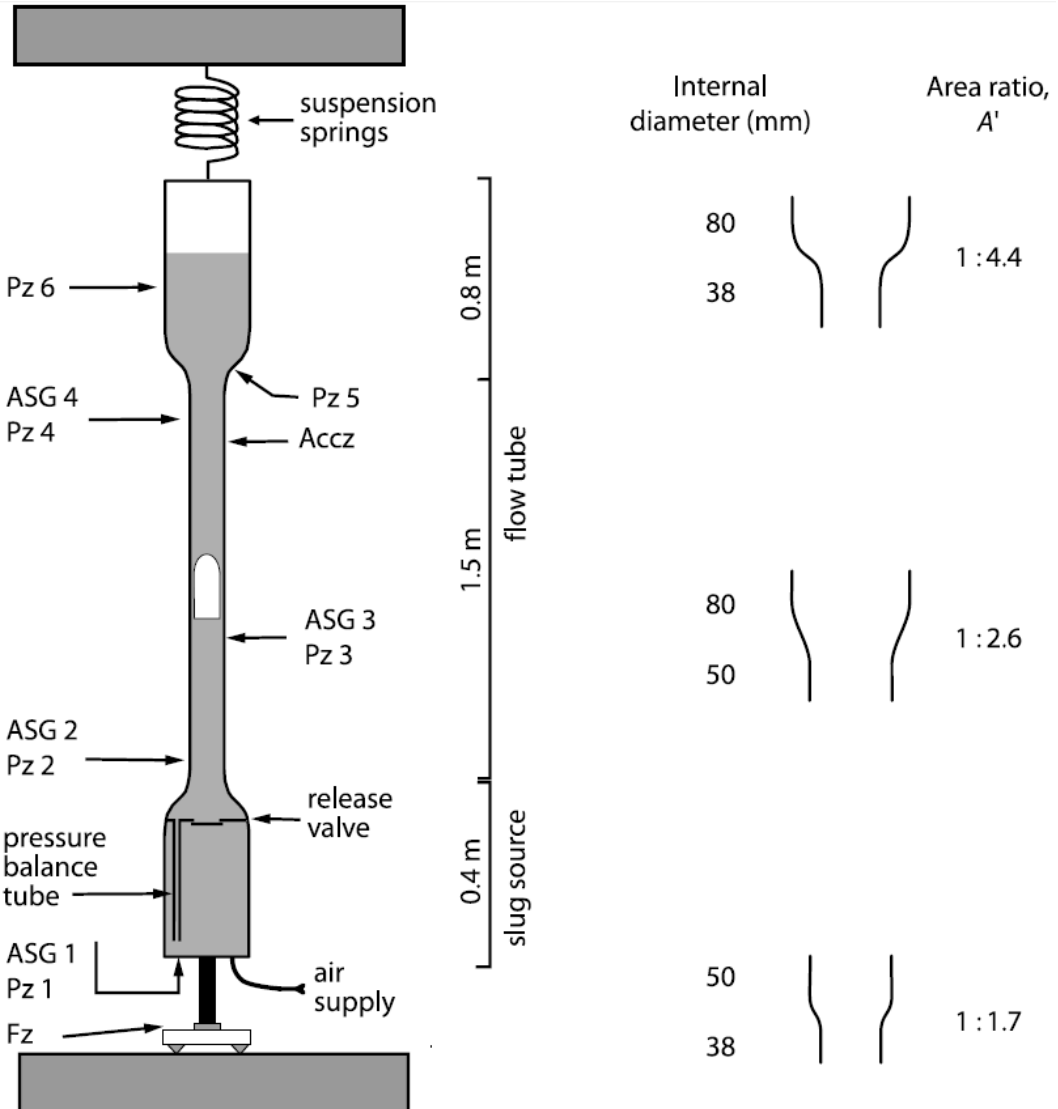


Figure 2.13: The experimental apparatus used by James et al. (2006) to study the rise of Taylor bubbles through changes in pipe diameter. The full experimental set up is shown on the left hand side and the profiles of different expansion sections are shown on the right hand side.

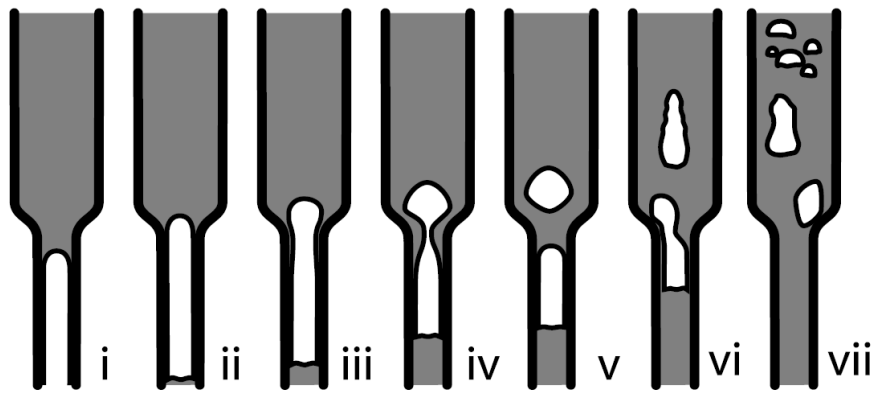


Figure 2.14: A visual representation of the behaviour of a Taylor bubble passing through the 0.038 m to 0.08 m expansion in pipe geometry in water, (James et al., 2006).

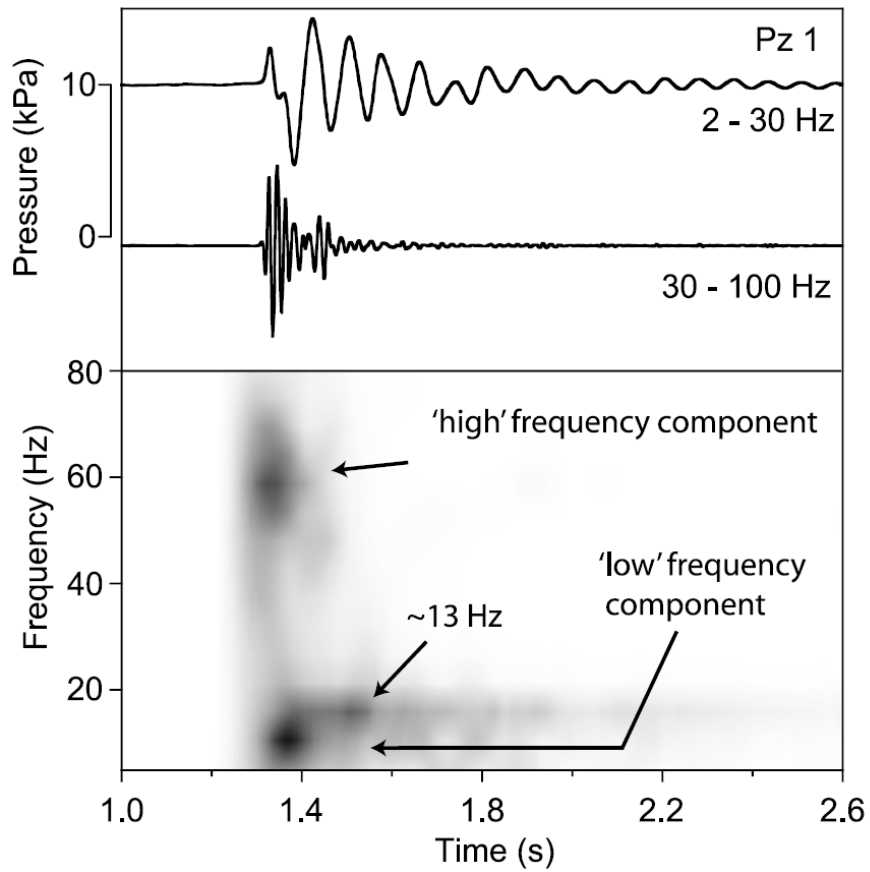


Figure 2.15: A graphical representation of the readings by a static pressure sensor at the base of the pipe as the bubble passes through an expansion in the pipe diameter (above), and the results of a subsequent frequency analysis of these signals, (below) (James et al., 2006).

2.2 Taylor bubbles in Volcanic Conduits

2.2.1 Introduction

As detailed in Section 1.1.1, the focus of this thesis is the behaviour of multiphase gas-liquid flow, and in particular Taylor bubbles. As well as being commonly found in the oil and gas, nuclear and chemical industries, Taylor bubbles are also found in the natural world; they are in fact, the driving force behind certain types of volcanic eruption. The following section provides a background and introduction to these volcanic flows. The definition of the properties of the fluids involved and the physical models used to describe these eruptions may influence the development of a computational model.

2.2.2 Background

2.2.2.1 Eruption Types

The behaviour of basaltic volcanoes acts over a wide range of differing scales and styles, not all of which can be strictly classified. These range from the smaller Hawaiian and Strombolian type eruptions through to the larger scale Plinian eruptions, with many varying types in between. Hawaiian eruptions, Figure 2.16 (a), are mainly effusive with the occasional fountaining of lava. Strombolian eruptions, Figure 2.16 (b), are driven by the rise of large gas bubbles (often referred to as slugs) which burst at the surface. This causes short periods of eruptive behaviour interspersed with effusive behaviour. Plinian eruptions, Figure 2.16 (c), are highly explosive, sustained eruptions which eject large volumes of tephra - fragmental material produced by an eruption (Williams, 1979).



Figure 2.16: Examples of volcanic eruptions (left) Hawaiian at Kilauea, Hawaii. (above right) Strombolian at Stromboli, Italy. (below right) Plinian at Mt St Helens, USA. (Geology.com, 2011).

2.2.2.2 Properties of magma

The physical properties of the fluid in this system, magma are not that well known, as there is a lack of quantitative field data. The properties and behaviour of igneous rocks in their solid state is well documented, but little reliable data is available for its molten form. However, the chemical composition of most magmas is known and this can give a good insight as to their properties. The proportion of silicon to oxygen in the magma has a strong influence on its rheological properties, and in particular, its viscosity. An increase in temperature or a decrease in silica content results in a decrease in viscosity. At temperatures below crystallisation the viscosity increases with cooling time due to the increasing proportion of crystals which raise the (effective) viscosity of the liquid.

Table 2.1: Influence of water content on viscosity of magmas (Scarfe, 1973; Murase, 1962).

Composition	T (°C)	Dry Viscosity (mPa.s ⁻¹)	Viscosity with 4% H ₂ O(mPa.s ⁻¹)
Granite	785	10 ¹²	10 ⁶
Andesite	1150	10 ⁴	10 ^{3.5}
Theolitic Basalt	1150	10 ^{3.2}	10 ³
Olivine Basalt	1250	10 ²	10 ²

The ratio of H₂O present in igneous melts also has a large influence over the viscosity of the liquid, as shown by the data contained in in Table 2.1 (Scarfe, 1973; Murase, 1962).

This data, although obtained from a very limited number of experimental studies, does give a good indication of the viscosity of the effect that water has on the physical properties on igneous melts. Other preliminary experimental work has shown that viscosity decreases with increasing pressure for basaltic magmas (Kushiro and Mysen, 1976).

As the viscosities of magmas are very large, the Reynolds number of magmatic flows will generally be low, and hence the flow may be laminar. The results of many experiments have concluded that the transition of laminar to turbulent flow in pipes to occur at the critical value of 2,000 (Taylor, 1929). This should still be the case at the scale of gas rising through the magma, despite the increase in the velocity. Magmas may also have non-Newtonian (shear thinning) characteristics that effect the flow behaviour particularly at lower temperatures (Hobiger et al., 2011). Many magmas cannot be deformed by viscous flow until a certain yield stress is exceeded (Shaw, 1969). The basaltic magma, which is the focus of this study, is clearly shown to be the least viscous type of magma, partially due to its chemical composition.

Convection may also occur in a conduit of magma provided the ratio of buoyant forces to viscous forces exceeds a critical value which is indicated by the Raleigh number

$$Ra = \frac{g\alpha_c\rho r^4\beta C_p}{\mu k}, \quad (2.31)$$

where α_c is the thermal expansion coefficient, r is the radius of conduit, k is thermal conductivity, β is the temperature gradient, C_p is the heat capacity. For Raleigh numbers above a critical value of approximately 1,700 convection is likely to occur. This implies that the majority of conduits with radii of over 10 m are likely to convect (Bartlett, 1969).

2.2.2.3 Properties of Volatiles

Gaseous volatiles are dissolved in the magma while it is in the mantle or lower crust, before it rises through volcanoes. These components are exsolved when their concentrations are greater than their solubility and this forms a gas phase in the magma. The composition of this volcanic gas differs between volcano and magma types; however, it is normally comprised mainly of H_2O , with CO_2 the next largest contributor and SO_2 the smallest of the main contributors. Other gases such as H_2S , H_2 , N_2 , CO , HCl , HF , He and Ar may also be present in very small volumes (Shinohara, 2008).

2.2.2.4 Scale

The size of volcanoes clearly differs greatly between sites and eruption types. The radius and geometry of conduits can only be estimated for volcanoes and this too can vary greatly, roughly from a radius of around 1 m to 10 m with magma rising from a number of kilometres in depth (Seyfried and Freundt, 2000). Often the idealised model of a smooth, vertical, cylindrical column is not accurate as conduits can be inclined (James et al., 2004) or may be not be entirely cylindrical, e.g. fissure shaped. The diameter of conduits may also vary, especially as the

bubbles approach the surface and in particular, in the case when a lava lake is present. A lava lake is a reservoir of magma at the top surface of a volcano. As the conduit approaches the surface, it undergoes a large expansion in diameter to form a reservoir, as shown in the diagram of Figure 2.17, (Bouche et al., 2010). Taylor bubbles rising into these reservoirs may provide hot magma from depth which is entrained in their wake and which can drive convection currents (Bouche et al., 2010; Danabalan, 2012). This change in diameter may have a large effect on the shape and behaviour of the Taylor bubbles (James et al., 2006). However, the behaviour of Taylor bubbles rising through expansions pipe diameter, as previously discussed in Section 2.1.8, has not been studied in great depth and is a topic that will be investigated in Chapter 6 of this thesis. There are a number of well studied examples of active lava lakes, including Erebus in Antarctica, Erta Ale in Ethiopia, Kilauea in Hawaii and Nyiragongo in the Democratic Republic of Congo.

2.2.3 Strombolian eruptions

Strombolian volcanoes are characterised by relatively small scale, explosive eruptions. They are more specifically characterised by extended periods of short, spontaneous explosions which can last up to tens of seconds and which eject ash and volcanic bombs (any material ejected larger than 65 mm diameter) to heights normally below 200 m. Between these short explosive periods there are normally interspersed between longer periods of effusive activity (Houghton, 2008).

Strombolian behaviour is widely accepted to be caused by bubble coalescence leading to the formation of Taylor bubbles. These bubbles rise through the column transporting magma with them, which then erupt at the surface (Parfitt, 2004). There are two main models which describe the development of these slugs, which are covered in Section 2.2.4.

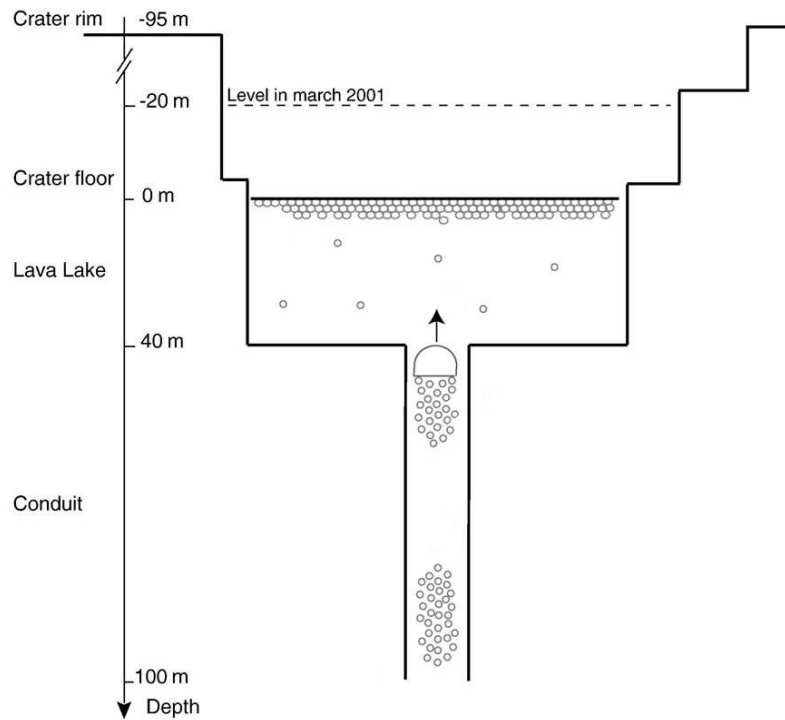


Figure 2.17: A diagram showing the scenario of a bubble rising into a lava lake at Erta Ale, (Bouche et al., 2010). The rising bubble encounters a sudden change in pipe diameter 40 m below the liquid surface.

In both of these models, the formation of slugs can be enhanced or facilitated by the geometry of the conduit system. An inclination close to that of the estimated Stromboli inclination (30° to the vertical) (Chouet et al., 2003) will lead to an increase of ascent velocity, expected due to buoyancy, of the slug by around 40%. Pressure data suggests that an inclination of the conduit enlarges the effect of inertial forces in single slug flows, however these faster and larger bubbles do occur less often with the same gas input. If consecutive bubbles are within 10-20 diameters of each other it is likely that they will coalesce (James et al., 2004).

2.2.4 Models

Basaltic eruptions can often be characterised by cyclic changes in their activity. An example of this for Strombolian type eruptions is that the activity occurs in discrete bursts. This behaviour has been widely attributed to structure of the flow inside the conduit of the volcano.

Although it is generally accepted that these discrete bursts of activity are caused by the rising of Taylor bubbles up through the magma, how these slugs form is less certain. There are currently two models to describe the way in which these gas slugs are created – the Rise Speed Dependant model (RSD) and the Collapsing Foam model (CF).

Rise Speed Dependant The RSD model proposed by Wilson (1980); Wilson and Head (1981) assumes that the gas slugs generated for Strombolian eruptions are generated by the coalescence of exsolved volatiles in the magma. If the rise velocity of these bubbles is too great they will not coalesce and the Hawaiian eruptive behaviour will be observed. The cooler magma near the top of the conduit causes a “skin” which has a finite strength, dependent on the amount of cooling which has occurred between successive bubbles arriving at the surface. If the gap between bubbles is too long, the skin will have cooled and thickened, meaning the bubble may not have the inertia to penetrate the skin. In this case, more than one bubble may be necessary to build up enough pressure to burst through the skin (Parfitt, 2004).

Collapsing Foam Figure 2.18 shows the basic principle of the collapsing foam model and RSD models (Houghton, 2008). Gas bubbles are exsolved from the liquid phase in the magma chamber. These bubbles rise through the liquid and collect in a “foam” at the roof of the chamber. The bubbles at the top of the foam are being compressed against the roof of the chamber by the buoyancy force. The force on these bubbles increases with an increase in foam thickness. When the foam reaches its critical thickness the surface tension cannot balance this buoyancy force

and the bubbles coalesce (Jaupart and Vergnolle, 1989). If the foam remains below this critical thickness, a bubbly flow regime will instead be seen in the conduit. When bubbles coalesce, the gas contained within them has to expand to maintain equilibrium with the surface tension. This thins the liquid film surrounding the pocket and hence ruptures it adding surrounding bubbles to the pocket. This is driven by capillary pressure and occurs over a characteristic time. If this characteristic time is smaller than the time it spends in the foam layer (resident time) then the foam collapses into a single pocket. For higher viscosity fluids, the characteristic time is closer to the resident time, and gas slugs are generated (Jaupart and Vergnolle, 1989).

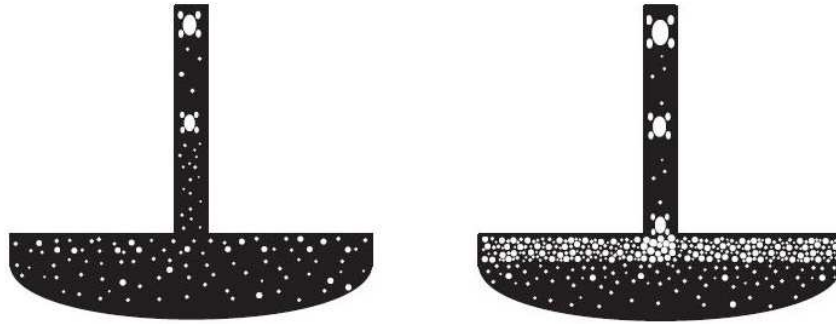


Figure 2.18: Outline of the RSD (left) and CF (right) models (Houghton, 2008). The RSD model proposes that the formation of Taylor bubbles is caused by the coalescence of smaller bubbles during their ascent, whereas the CF model proposes that Taylor bubbles are formed by the collapse of a large foam of small bubbles at the roof of the magma chamber.

The RSD model assumes that large bubbles rise faster than small ones and will overtake and coalesce with smaller bubbles. Jaupart and Vergnolle (1989) challenged this assumption as they claimed only bubbles of radius, r , at least ≈ 40 mm would coalesce while magma was rising (Jaupart and Vergnolle, 1986). So as small bubbles are typically only seen to reach sizes of 10-50 mm, they argued little coalescence would take place. More recent work has, however, shown

that bubbles with $r > 5$ mm will deform and hence enhance coalescence (Manga and Stone, 1994) and as long as the rise speed is low, gas slugs could be formed by coalescence. Physical evidence to support the idea of coalescence has been found in both lava and tephra (Mangan et al., 1993).

2.3 CFD studies

The previous sections have detailed the experimental and analytical research conducted into the behaviour of Taylor bubbles. However, the majority of real flows cannot be described by analytical expressions due to their inherent complexity. These flows can be approximated using numerical methods. Here, the partial differential equations for (PDEs) used to model fluid behaviour are discretised to difference equations which can be solved on a numerical grid using a finite volume approach. These governing equations and the techniques used to solve them will be described in detail in Chapter 3. A large body of work has been carried out analysing bubble rise using Computational Fluid Dynamics (CFD) methods, including much on the behaviour of Taylor bubbles.

2.3.1 Modelling Multiphase Flow

There are two main approaches to modelling multiphase flow, and many models within these methods. One approach is to treat both phases as continuous, and is referred to as an Euler-Euler model. The other approach is to have one continuous phase and one discrete phase, this is known as an Euler-Lagrange model, or a particle tracking method.

Euler-Euler There are many models within an Euler-Euler approach and these will often be referred to by different names, however the main models are briefly discussed below;

- VOF - The Volume of Fluid (VOF) method uses a single set of momentum equations.

The continuity equation for the volume fraction, α , is solved and for each cell the volume fraction must sum to unity. This model is most commonly used when there is a defined interface between the two phases. A separate interface reconstruction scheme is required along with this to determine the position of the phases inside (Youngs, 1982).

- **Interface tracking** - These type of methods explicitly track the location of the interface between two phases. This can be applied in a number of ways, such as using a set of points and splines Lu and Prosperetti (2009), or by using the velocity at the front of the bubble to interpolate the shape (Kang and Liu, 2000).
- **Level Set** - This method uses a level set function, $\varphi(x, t)$, to determine the location of the phases in relation to the interface. This function is zero at the interface, positive in the primary phase and negative in the secondary phase. This is more formally defined as

$$\varphi(x, t) = \begin{cases} +|d| & \text{if } x \in \text{the primary phase,} \\ 0 & \text{if } x \in \text{the interface,} \\ -|d| & \text{if } x \in \text{the secondary phase.} \end{cases} \quad (2.32)$$

- **Mixture** - This is a slightly more complex model as the two fluids can be inter-penetrating. One set of momentum equations is still used, however the phases do not have to have the same velocity and there can be momentum transfer between phases. This is often implemented in bubbly flow or particle laden flow regimes.
- **Eulerian Multiphase** - This is the most complicated Euler-Euler model as the momentum and continuity equations are solved for each phase. The phases are couple by inter-phase transfer coefficients. This model is commonly applied to bubble columns, particle suspension or fluidised beds.

Euler-Lagrange This is a particle tracking approach which has discrete models for one phase, while the other phase is continuous. The bubbles are modelled as spherical particles and trajectories are calculated for each particle. This is particularly suitable for flows where a discrete phase is introduced to a continuous flow from an inlet.

When a Taylor bubble rises through a pipe, there is a distinct interface between the large air bubble and the fluid, and both phases are continuous. Hence, it would seem logical to use an Euler-Euler approach in preference to any of the other methods.

In recent years, CFD studies using the Volume of Fluid (VOF) model have been shown to be capable of replicating the behaviour observed in experimental studies, such as bubble rise rate and wake behaviour (Ndinisa et al., 2005; Taha and Cui, 2004; James et al., 2008; Araujo et al., 2012). This method is also widely available as part of commercial CFD software.

Other multiphase schemes have been used to model the gas-liquid interface. For example, Suckale et al. (2010) developed a numerical model using a level set method. Their results suggested that a stable bubble could not be sustained with a Reynolds number of more than 100. This corresponds to a maximum pipe diameter of under 0.01 m for a water-air system which is contradicted by many experimental studies. James et al. (2011) questioned whether this is the result of a physical instability or a numerical instability and pointed out that the simulation durations were limited by numerical divergence.

Another recent study has used a front tracking method. This tracks the interface explicitly with the velocity at the front of the bubble being interpolated from the finite difference in the grid (Kang et al., 2010). They used this front tracking method to successfully simulate the rise of Taylor bubbles in 2D axi-symmetrical pipes. However, no studies have used this method to simulate 3D Taylor bubbles. Lu and Prosperetti (2009) also simulated axisymmetric Taylor bubbles rising through liquids in a vertical tube. Their model neglected the flow in the gas, and tracked the interface between the gas and liquid phases using a set of marker points which were linked by cubic splines. Again, this method of interface tracking has not been used to perform 3D simulations.

The VOF method has produced reliable results in both 2D axi-symmetric and 3D geometries

and will be used in this study. The details of this method and its implementation can be found in Chapter 3.

2.3.2 Implementation

There are a number of different ways to implement interface tracking methods in the solution of CFD models. One approach is to use a single grid containing the entire domain. This method has been used to successfully model the rise of Taylor bubbles in many studies (Gupta, 2009; James et al., 2008). For situations in which it is required to model the behaviour of the whole system – such as if the atmospheric liquid-gas surface is required, or bubble behaviour changes as it rises in the pipe – this is an effective approach to take. However, this method can be extremely computationally expensive with a large domain.

An alternative modelling method, known as the “moving wall” approach, involves moving the walls of the domain vertically downwards around the rising bubble. Here a velocity inlet is placed ahead of the bubble and an outlet behind it, the walls move at the same velocity as the inlet conditions (Taha and Cui, 2004; Kawaji et al., 1997; Araujo et al., 2012). This method is much more computationally efficient as the size of the domain required is smaller. However, the main disadvantage of this method is that the full domain is not modelled. This means that this approach does not take into consideration the hydrostatic pressure differential in the pipe or include the effects of the top surface of the liquid column. These factors make it an ideal method to use to study the effect of parameters on characteristics which are independent of the presence of gas-liquid surface, such as the wake behaviour and film thickness (Araujo et al., 2012). An example of the computational domain for this method is shown in Figure 2.19.

Another modelling process involves using a periodic boundary condition at the inlet and outlet of the domain (Clarke and Issa, 1997; Shao et al., 2009). This is not, however, recommended for practical use by commercial CFD code manufacturers (CD-ADAPCO, 2011; ANSYS FLUENT).

This method has the same advantages and disadvantages of moving walls approach, which delivers a shorter computational time, but with limits placed on what can be modelled. One further note with this method is that the wake of one bubble may interact with the front of the following bubble, which, depending on the flow regime being modelled, could be either an advantage or a disadvantage. For example, if modelling a single bubble rising in a vertical pipe, these interactions could influence the behaviour of the bubble and hence would not be a realistic representation of the flow. However, if slug flow is being modelled, Taylor bubbles may well encounter the wake of previous bubbles and so this model is appropriate. A similar domain to that shown in Figure 2.19 may be used but where the flow from the outlet boundary is used as the flow entering the inlet boundary.

A Moving Frame of Reference (MFR) approach could also be applied to this problem. The co-ordinate system in this case would be set at the centre of mass of the bubble, and would move with the velocity of the bubble. The computational domain is defined with respect to the moving frame such that an arbitrary point in the domain is located by a position vector, \vec{r} from the centre of mass of the bubble. The fluid velocities are transformed from the stationary frame to the moving frame using the relation,

$$\vec{U}_r = \vec{U} - \vec{U}_t, \quad (2.33)$$

where \vec{U}_r is the relative velocity (from the moving frame), \vec{U} is the velocity viewed from the stationary frame, and \vec{U}_t is the translational velocity of the moving frame (ANSYS FLUENT). As the bubble is rising through a hydrostatic pressure gradient, time varying pressure conditions will be required to be placed on the boundaries above and below the bubble. As discussed in Chapters 4 and 5 this may cause the bubble's rise rate to accelerate and decelerate, and so an additional term will be required in the momentum equations to account for this. This approach has very similar advantages to the previously discussed moving walls approach, in that as only

the flow around the bubble is modelled, a much shorter domain is required, substantially reducing computation times.

It can be concluded, therefore, that the approach taken should depend on the situation which is to be modelled, as each method has both advantages and disadvantages. A periodic domain will not be used due to the recommendations of the code manufacturers. In the scenarios presented in Chapters 5 and 6, the whole domain is required to be modelled, and so the moving walls or periodic boundary approaches are not appropriate.

2.3.3 Results

Many CFD modelling studies (Taha and Cui, 2004; Lu and Prosperetti, 2009; Araujo et al., 2012) have predicted Taylor bubbles with a terminal rise velocity that agree with the predictions of White and Beardmore (1962) over a wide range of conditions. The studies of Taha and Cui (2004); Kawaji et al. (1997) and Araujo et al. (2012) used the moving walls approach described in Section 2.3.2. These studies compared the effect of varying Eotvos and Morton numbers on the dimensionless rise velocity, expressed by the Froude number. An example of these solutions are shown in Figure 2.20, where CFD results of Taha and Cui (2004) are plotted against the benchmark data of White and Beardmore (1962). These studies were all 2D-axisymmetric models which drastically reduced the computational expense. Taha and Cui (2004) also include a full 3D model for some simulations where unsteady flow was present. James et al. (2008) were able to simulate Taylor bubbles which matched the predicted rise rate over a range of conditions whilst modelling the whole domain. However, for larger values of the Eötvös number, significant errors in the solutions were incurred. These errors resulted in a computed rise velocity that was 10-15 % below the theoretical predictions and experimental observations and is shown in Figure 2.21. No explanation of this discrepancy in computed rise velocity was given but this is discussed further in Chapter 5.

The computational model solutions of Kawaji et al. (1997) using a moving walls condition showed good agreement with the experimental conclusion of Taylor and Davies (1950) that bubble length does not alter the rise velocity of Taylor bubbles longer than $2.5 D$ through a stagnant liquid using a VOF method.

The first numerical simulations of the rise of a single Taylor bubble were conducted by Mao and Dukler (1991). Their method neglected the flow of the gas in the domain, solving the steady state flow of liquid around and ahead of the Taylor bubble. This enabled them to determine the shape and rise velocity of the Taylor bubble but did not model the wake of the bubble. Their simulations suggested that although the different viscosities they tested (over the range from $\mu = 0.001$ to 0.05 Pa.s) did not largely affect the rise velocity, an increase in the liquid viscosity did increase the thickness of the liquid film. Bugg et al. (1998) extended this model to include the flow in the wake of the Taylor bubble. This allowed them to simulate the rise of a Taylor bubble for a large range of conditions and to compare these results with the results of an experimental study. The velocity fields around the rising Taylor bubble were experimentally determined using a PIV method. The results of both the experimental and numerical studies suggested that the influence of a Taylor bubble on the flow field ahead of it was limited to approximately one pipe diameter.

More recent studies have shown that when using the VOF model, the computed thickness of the liquid film around the Taylor bubble compares well with experimental data (Taha and Cui, 2004; Ndinisa et al., 2005; Araujo et al., 2012). Araujo et al. (2012) also validated their work against the studies of Brown (1965); Campos and Carvalho (1988); Viana et al. (2003) . This validated model was then used to conduct a numerical study with the Eotvos number over the range 6 to 900 and the Morton number from 4.72×10^{-5} to 104. They developed empirical models to estimate the length and volume of the wake, which were shown to be comparable to the experimental results of Campos and Carvalho (1988),

$$\frac{L_w}{D} = 0.25[0.555 - 7.793 \times 10^{-3} \ln(M)] \cdot \ln\left(\frac{Eo^3}{M}\right) - 2.133 + 8.046 \times 10^{-2} \ln(M), \quad (2.34)$$

$$\frac{V_w}{D^3} = 1.365 \times 10^{-1} \cdot \left(\frac{L_w}{D}\right)^2 + 2.176 \times 10^{-1} \cdot \left(\frac{L_w}{D}\right) - 2.919 \times 10^{-1}. \quad (2.35)$$

A flow map of the behaviour of the tail is presented in Figure 2.22, showing at which conditions the shape of the tail turns from convex to concave and a wake becomes prevalent (Araujo et al., 2012).

The PIV experiments of Bugg and Saad (2002) are used by Lu and Prosperetti (2009) to validate the solutions of their axisymmetric, moving wall model. This study was conducted for Eötvös numbers over the range of 15 to 100, across which surface tension is an important factor. They observed that as the effects of surface tension decreased, an increase in the unsteady behaviour was observed. Waves appeared in the liquid film, which eventually led to the shedding of bubbles at the tail of the bubble. These waves can be seen in Figure 2.23 where the interface shapes observed are plotted for a range of times during one simulation.

Kang et al. (2010) formulated an empirical model for the film thickness based on the results of a numerical study. However, this expression was subsequently confirmed by Llewellyn et al. (2011) only to be valid for an extremely limited range of values Figure 2.24. Zheng et al. (2007) and Feng (2008) showed that the development length of the liquid film depended on the value of the Reynolds number, but for turbulent flow this was between 1.5 to 2.1 pipe diameters in length. These results were comparable to the experimental observations of Nogueira et al. (2006a).

Results from Kang et al. (2010) have shown that the density and viscosity ratios have little effect on the shape of the bubble or the length of the wake. The Eötvös and buoyancy Reynolds numbers both have a large effect on the shape of the tail of the bubble and the wake left behind it, and increases in either of these numbers result in a longer wake length. An increase in the

Eötvös number also gives shorter and wider bubbles and hence reduces the size of the liquid film. An increase in Re_B produces the same effect. This is as the surface tension governs the shape of the bubble, the prolateness of the nose and oblateness of the tail both increase as the surface tension increases (Taha and Cui, 2004). These effects can be seen in Figure 2.25.

Clarke and Issa (1997) used an iterative scheme to determine the Taylor bubbles shape and rise velocity, along with the flow surrounding it. Again, the flow in the gas was neglected, and so only the liquid flow field was calculated. At each iterative step, a new mesh was generated to account for the change in bubble shape, with a boundary applied at the liquid-gas interface. Periodic boundary condition were imposed on the domain. This creates a regime similar to slug flow where some small bubbles may be dispersed in the flow.

Recently, Yan and Che (2010) addressed the problem of small dispersed bubbles in slug flow by applying a coupled system of equations. This allows different length scales to be resolved for the different regimes, one length scale for the Taylor bubble, modelled using a VOF model, and a different length scale for the much smaller, dispersed bubbles in the wake. These small bubbles are modelled using a mixture model, commonly used to model bubbly flow. An example of the results generated by the use of this model are shown in Figure 2.26.

The study of James et al. (2008) is the only one to include a compressible gas phase. This model allows the gas bubble to expand as it rises through the liquid. Their work, validated by experimental data, shows a rise of the liquid surface due to bubble expansion, as it moves into regions of lower hydrostatic pressure. Slug oscillations are mentioned to occur when an initial overpressure is used, however no further detail is provided. James et al. (2008) also detail a rapid expansion of the bubble near to the atmospheric surface of the liquid. A scaling up of this simulation is carried out to determine the behaviour of a gas bubble rising in a volcanic conduit of diameter 2 m with a highly viscous liquid phase. However, little explanatory detail is provided to detail the changes in the numerical scheme made to overcome the challenges faced by this

increased scaling. To the author's knowledge, this is one of the only studies where the results produced air bubbles in water for a pipe of diameter greater than 0.1 m have been presented in the literature. Most of the previous studies only increased pipe diameter in order to be able to neglect the effects that surface tension have on the bubble rise rate, normally not over 0.05 m giving an Eötvös number in the region of 100. The volcanic conduit flows studied by James et al. (2008) and the experiments which form the driver for this project have much greater diameters than this. In addition, the behaviour of bubbles within fluids of higher viscosities are not normally considered, and so extension to higher viscosity flows is also an area of potential novel work.

One model feature not tackled widely in the literature is the use of alternate geometries other than vertical, cylindrical pipes. Taha and Cui (2004) presented the results of a study which used an inclined pipe at 30° to the vertical, Figure 2.27. The PhD thesis of Hernandez-Perez (2011) also investigated this geometry, conducting both experimental and numerical studies. It was shown that 3D CFD simulations could replicate the behaviour of Taylor bubbles in inclined pipes. No numerical work, and very little experimental work, has been conducted on the rise of Taylor bubbles through changes in pipe geometry. One reason for the lack of CFD work in these areas is the requirement to employ a full 3D model, which is much more computationally expensive than the axisymmetric models widely employed in the literature. This is also true for vertical pipes in which flow is highly turbulent. The particular case of an expansion in pipe diameter is a gap in the literature which is investigated in Chapter 6.

2.3.4 Other applications

A lot of previous research has analysed Taylor bubbles in small diameter pipes, particularly in micro-channel and capillary flow. Despite the extremely small scale of these problems (diameters of the order of 10^{-4} m), the work does provide useful insight, particularly from the perspective

of the methodology used. Gupta (2009) uses both a VOF model with geometric reconstruction (Youngs, 1982) using FLUENT and a level-set model (Osher and Sethian, 1988) in TransAT, to obtain very similar results for a Taylor flow in a micro-channel with heat transfer. As the flow is very stable, an axisymmetric model can be used in both cases, in agreement with Taha's use of an axisymmetric model to represent these conditions (Taha and Cui, 2004). The inlet condition used, an annular flow with a small initialised bubble, shown in Figure 2.28, is very similar to one that could be used, for example, to model slug flow in a short tube filled with glycerin at the University of Nottingham. A VOF approach, employing the commercial code CFX (Shao et al., 2009), was used to model this phenomena and concluded that an increase in gas velocity gave a larger bubble, and that surface tension had the largest effect on the size of the bubble produced, which was in agreement with Taha and Cui (2004).

2.4 Conclusions

The work presented in this chapter details a critical review of the background literature on gas-liquid flows, in particular the rise of Taylor bubbles. Previous studies have shown that the rise of Taylor bubbles may be described by a number of non-dimensional parameters, namely the Froude, Eötvös, Morton and buoyancy Reynolds numbers. Furthermore, the rise rate, film thickness and wake behaviour can all be estimated using theoretical or empirical models if these parameters are known.

From an analysis of the background literature it is concluded that there are a number of areas upon which insufficient experimental work has been published. Notably, there is a lack of experimental work in both large diameter pipes (over 0.12 m) and in high viscosity fluids (over 5 Pa.s). This conclusion is used as the motivation for the work presented in Chapters 4 and 5, which are summaries of investigations that study the flow of Taylor bubbles in larger diameter

pipes.

Many studies have shown that Taylor bubbles are not only commonplace in the oil and gas, nuclear and chemical industries, but also prevalent in the natural world, in particular being the driving force behind the eruption of Strombolian volcanoes. These bubbles rise of gas through the magma and burst at the surface. Magmas in these systems have viscosities which can be in the order of hundreds of Pa.s ($O(100)\text{Pa.s}$). Although conduits are normally modelled as vertical, cylindrical pipes, this is often not the case and conduit inclinations and changes in conduit diameter often occur. The rise of Taylor bubbles through changes in pipe diameter are the focus of the numerical studies presented in Chapter 6.

A number of conclusions were drawn from previous work conducted using numerical models to study the rise of Taylor bubbles which influenced the choice of the models adopted for the numerical studies presented in this thesis. To account for the presence of two fluids, the VOF model has been shown to be an accurate and robust method when used to simulate the rise of Taylor bubbles in vertical pipes. This method is investigated in more detail in Chapter 3. Although many studies have used shortened domains with either moving walls or periodic boundary conditions, it was concluded that the whole domain was required to be modelled in the studies presented in this thesis. Although this is computationally expensive, the behaviour of the atmospheric liquid–air surface or expansion of the bubble would not have been able to modelled otherwise.

An analysis of the theoretical Reynolds numbers (based on buoyancy of the bubble) showed that in many scenarios, turbulent flow would have to be modelled. The $k-\epsilon$ turbulence model has been shown in previous studies to adequately model the turbulent wake and thin film behaviour (Taha and Cui, 2004).

An analysis of the results of published numerical studies of Taylor bubbles show that few previous investigations considered either compressible Taylor bubbles or ones possessing a high

Eötvös number (≥ 500). There were also no published numerical studies that have considered changes to the cross section of the pipe geometry. These model and parameter changes provides the motivation behind the numerical studies presented in Chapters 5 and 6.

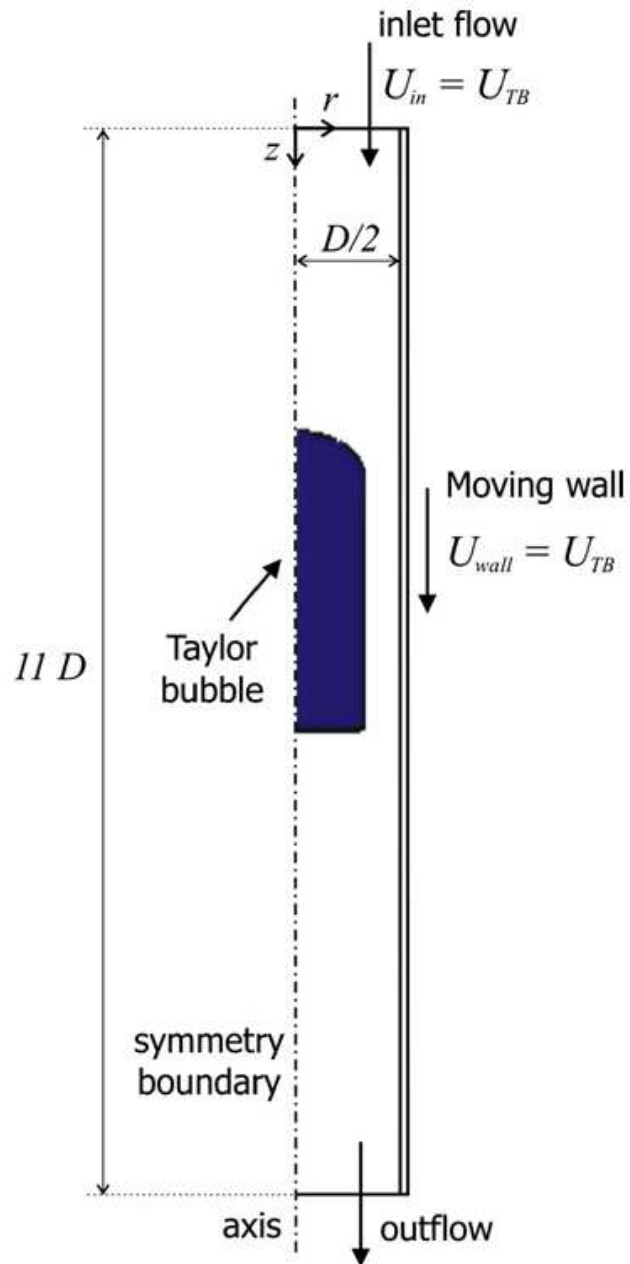


Figure 2.19: A diagram showing the computational domain when using a moving wall method, (Araujo et al., 2012). The walls move downwards vertically at the same velocity as the Taylor bubble.

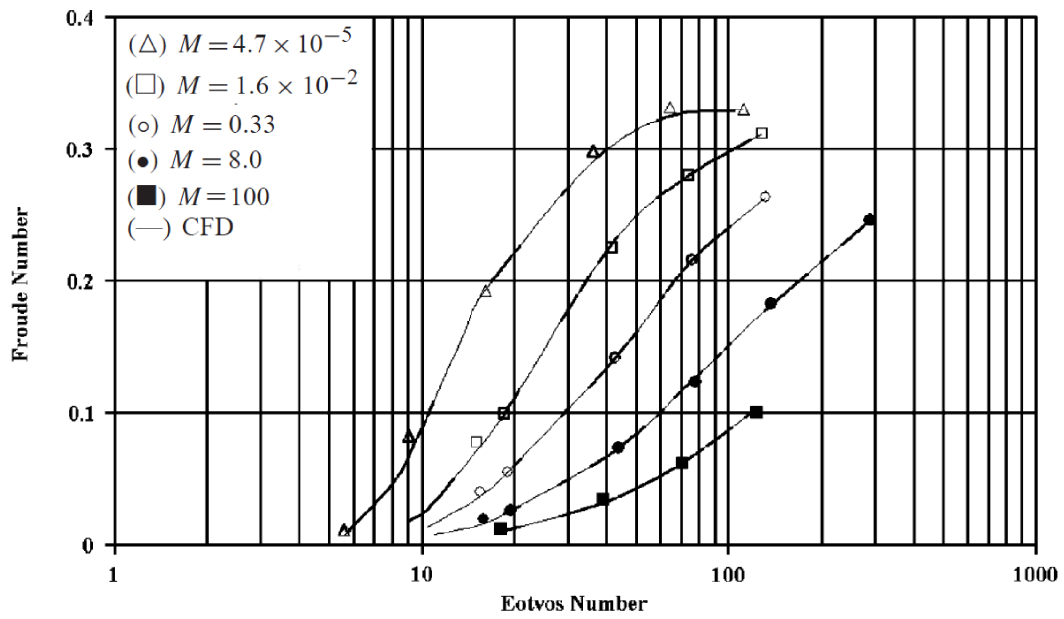


Figure 2.20: Comparison of the empirical models of White and Beardmore (1962) (symbols) with the CFD results of Taha and Cui (2004) (lines).

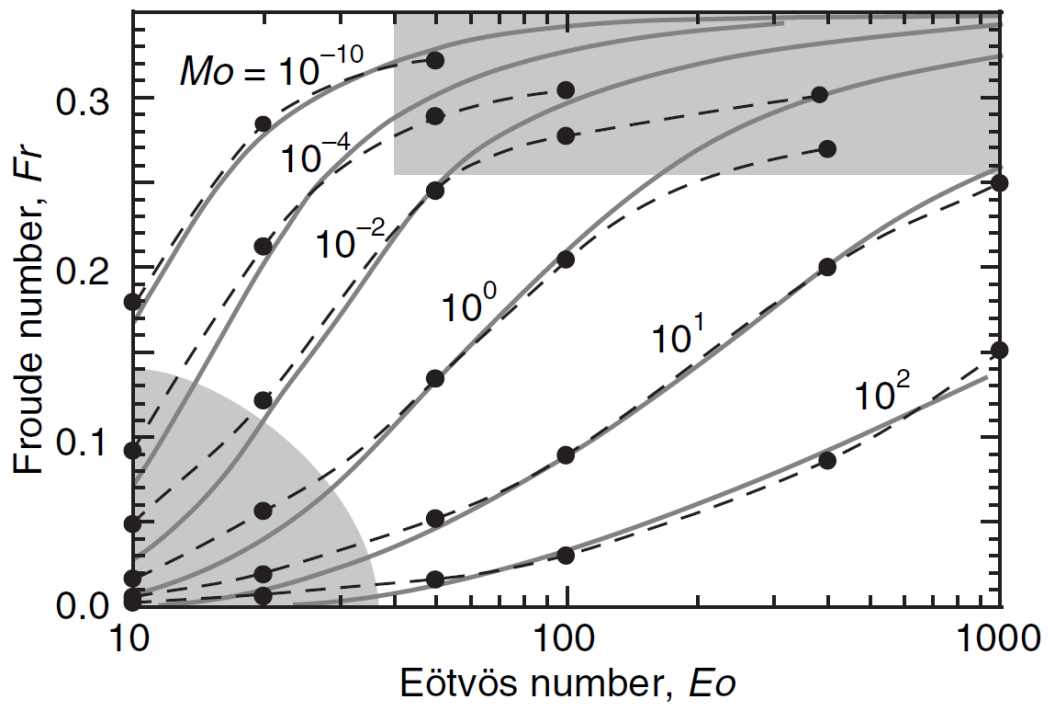


Figure 2.21: Comparison of the empirical models of White and Beardmore (1962) (filled lines) with the CFD results of James et al. (2008) (dashed lines and filled circles).

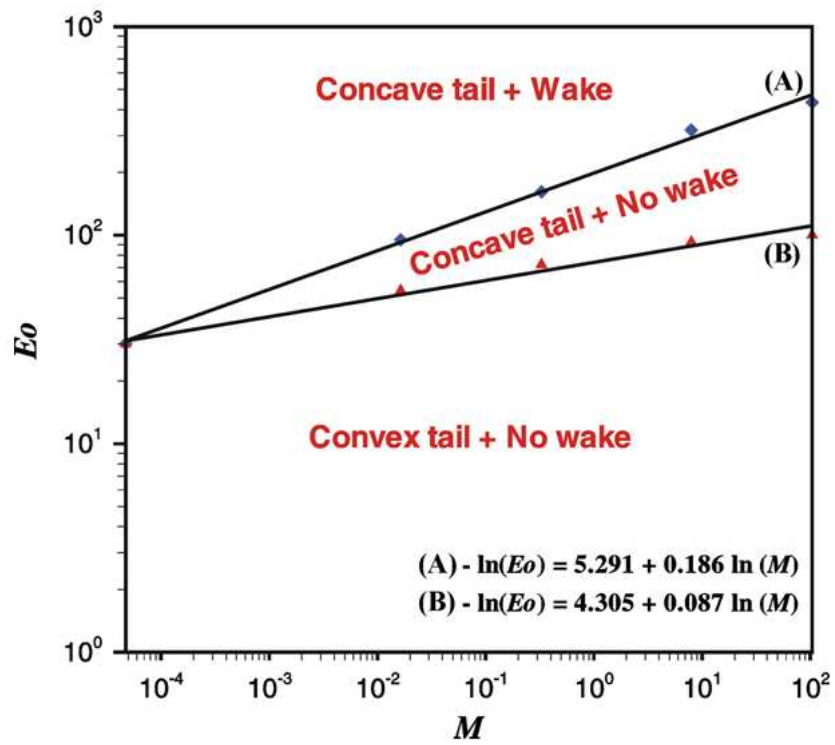


Figure 2.22: A flow map indicating the behaviour of the tail and presence of a wake behind the Taylor bubble Araujo et al. (2012).

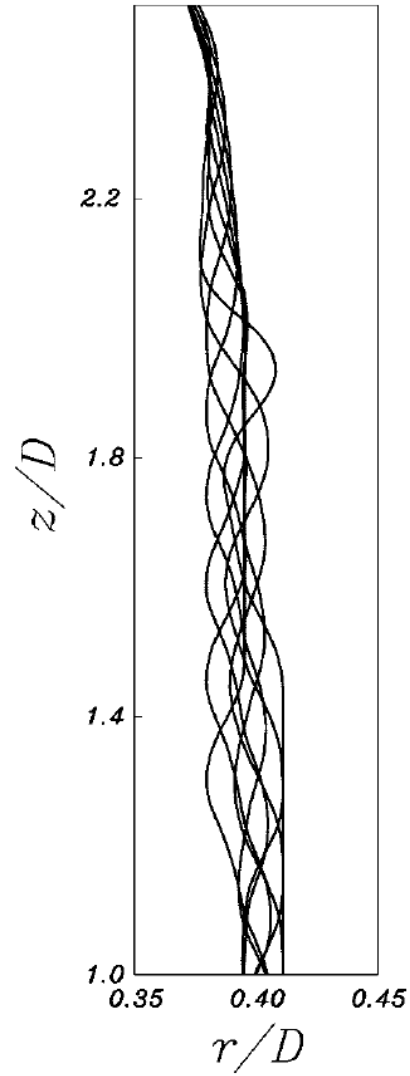


Figure 2.23: Depiction of waves in the thin film of a Taylor bubble from the work of (Lu and Prosperetti, 2009). Interface shapes are plotted at a range of different times throughout one simulation.

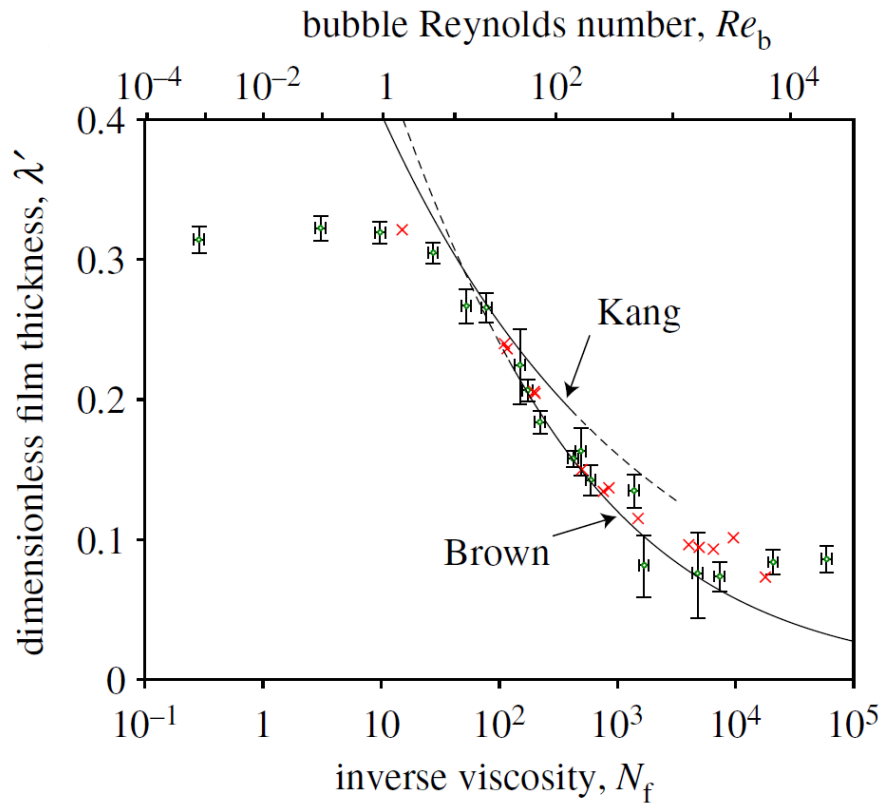


Figure 2.24: The limited range of values for which the model of Kang et al. (2010) is valid, (Llewellyn et al., 2011).

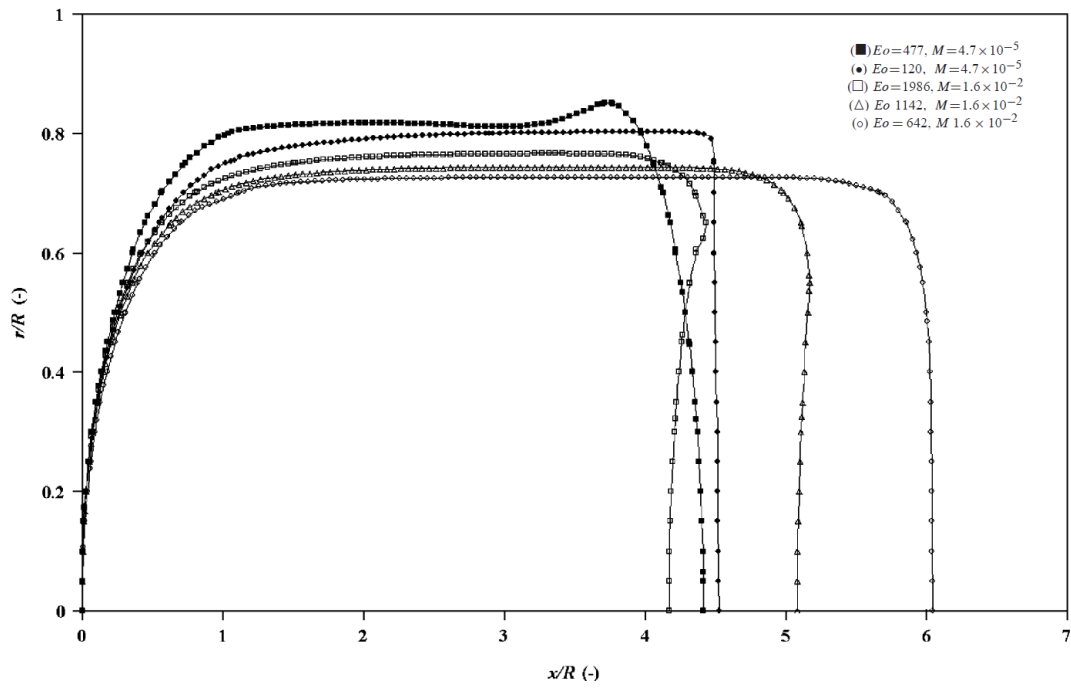


Figure 2.25: The change in shape of a Taylor bubble for varying conditions, using a fixed initial volume, (Taha and Cui, 2004). The Taylor bubble is rising to the left. An increase in the Eötvös number gives shorter and wider bubbles and hence reduces the size of the liquid film.

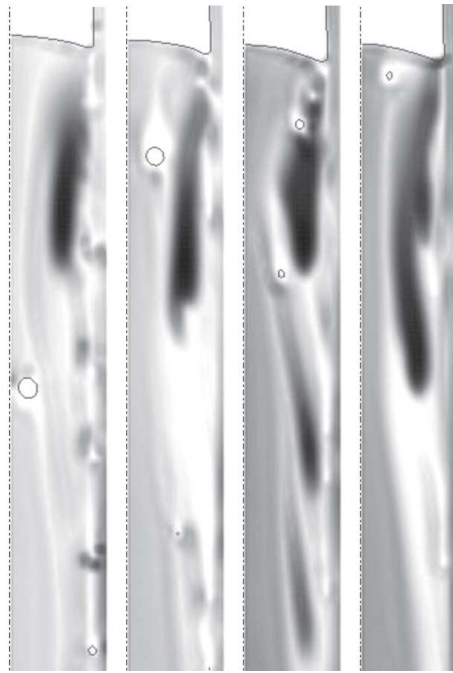


Figure 2.26: Flow in the near wake of a Taylor bubble using a coupled VOF and mixture model (Yan and Che, 2010).

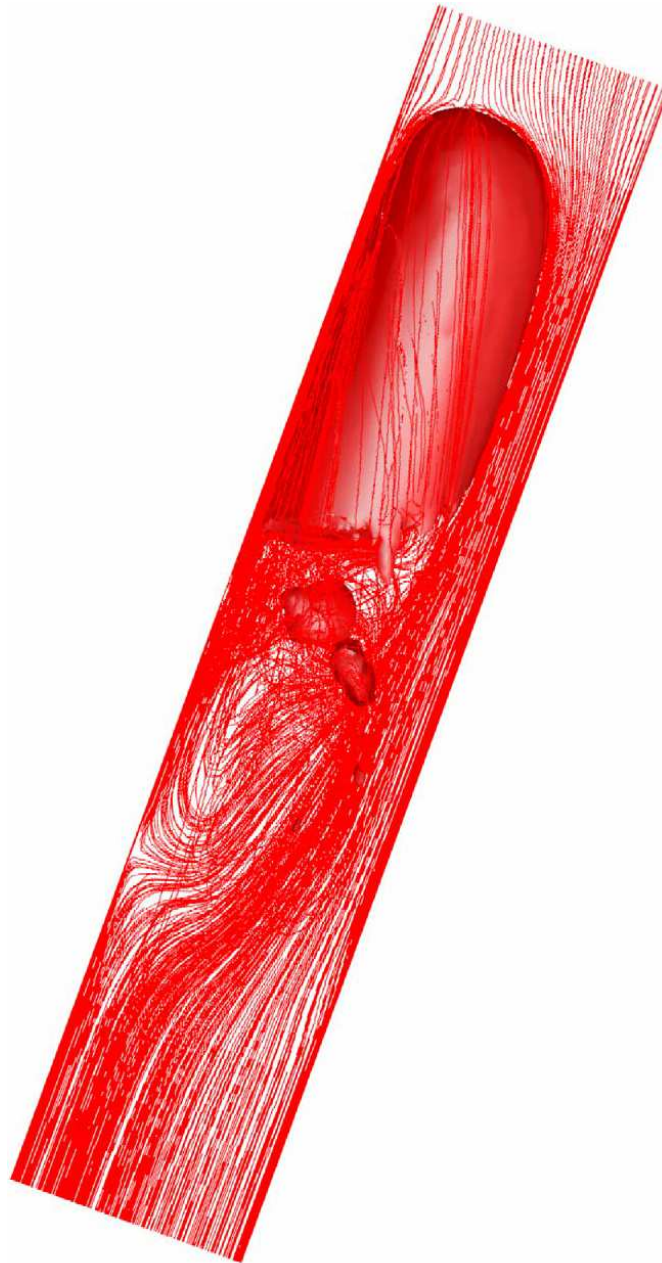


Figure 2.27: Streamlines around a Taylor bubble rising in a pipe inclined at 30° to the vertical (Taha and Cui, 2004).

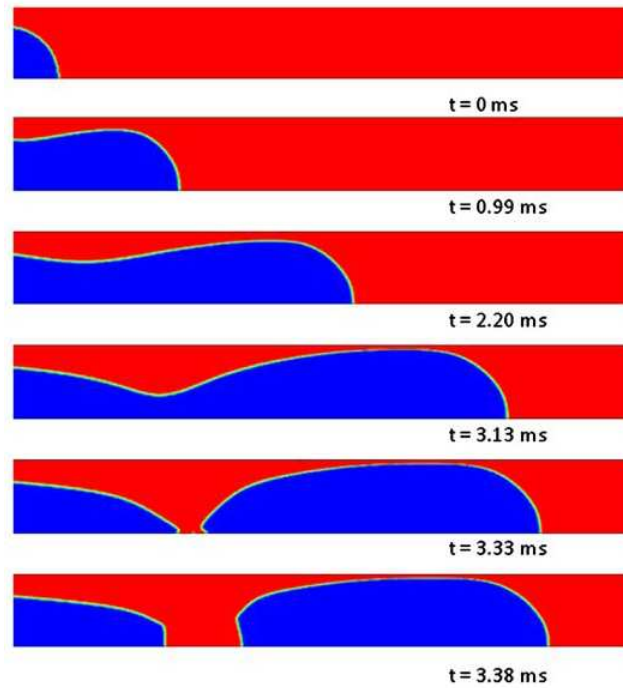


Figure 2.28: Images showing the development of slug flow in a micro channel, with gas injected at the left hand side (Gupta, 2009). In this set of images, the gas phase is blue and the liquid phase is red.

3.1 Numerical Model

3.1.1 Governing Equations

The computational studies reported in this Thesis, employed a commercial CFD solver, ANSYS FLUENT 12.1, to model the rise of a Taylor bubble. This solves the momentum and continuity equations using a finite volume method. The continuity equation is derived by applying conservation of mass to a finite volume while the momentum equations (Navier-Stokes Equations) are derived by applying Newton's Second Law. This constraint requires that the rate of change of momentum acting on the particle is equal to the sum of the forces acting upon it. In many situations, due to the turbulent nature of the flow in the thin film of liquid surrounding the Taylor bubble and in its wake, the Reynolds Averaged Navier Stokes (RANS) equations are used. These are given by

$$\frac{\partial \bar{p}}{\partial t} + \nabla \cdot (\rho \bar{\mathbf{u}}) = 0, \quad (3.1)$$

$$\frac{\partial}{\partial t}(\rho \bar{\mathbf{u}}) + (\bar{\mathbf{u}} \cdot \nabla) \rho \bar{\mathbf{u}} = -\nabla \bar{p} + (\mu + \mu_t) \nabla^2 \bar{\mathbf{u}}, \quad (3.2)$$

where $\bar{\mathbf{u}} = (\bar{u}, \bar{v}, \bar{w})$ is the ensemble average velocity, \bar{p} is the pressure, μ and μ_t are the dynamic and turbulent eddy viscosity respectively. In the RANS equations, the quantities of the Navier-Stokes equations, such as pressure, velocity and density, are split into mean and fluctuating components, which are then time averaged. Consequently, this introduces an additional term which is required to represent the effects of turbulence in the flow and to close the equations. Previous studies have shown the family of $k - \varepsilon$ models (Shih et al., 1995) is the most suitable to use for this application due to its accuracy and computational efficiency. For the studies reported in this Thesis, the Realisable $k - \varepsilon$ model was used, which has two transport equations, one for the turbulent kinetic energy, k , and one for the dissipation rate, ε ,

$$\frac{\partial}{\partial t}(\rho k) + \mathbf{u} \cdot \nabla(\rho k) = \nabla \cdot \left[\left(\mu + \frac{\mu_t}{\sigma_k} \right) \nabla k \right] + \mu_t S^2 - \rho \varepsilon, \quad (3.3)$$

$$\frac{\partial}{\partial t}(\rho \varepsilon) + \mathbf{u} \cdot \nabla(\rho \varepsilon) = \nabla \cdot \left[\left(\mu + \frac{\mu_t}{\sigma_\varepsilon} \right) \nabla \varepsilon \right] + C_1 \varepsilon S - \rho C_2 \frac{\varepsilon^2}{k + \sqrt{\nu \varepsilon}}, \quad (3.4)$$

where S is the modulus of the mean rate of strain tensor, ν is the kinematic viscosity and σ_k and σ_ε are the turbulent Schmidt numbers. In this model, C_1 is given by

$$C_1 = \max \left[0.43, \frac{\eta}{\eta + 5} \right], \quad (3.5)$$

here $\eta = Sk/\varepsilon$. The remaining model constants, C_2 , σ_k and σ_ε have been determined empirically and have values of 1.9, 1.0 and 1.2 respectively. The eddy viscosity is given by, $\mu_t = \rho C_\mu k^2/\varepsilon$. In this Realisable model C_μ is not constant but is calculated using the mean strain rate and the rates of rotation, as described in (Shih et al., 1995). This method has been shown to predict strong shear flows, such as jets, more accurately than the standard $k - \varepsilon$ model. As this characteristic flow behaviour is observed in the rise of Taylor bubbles, the Realisable $k - \varepsilon$ model was used. Details of other turbulence models may be found in Section 3.1.2 and further evidence to support the applicability of this model is presented in Section 5.1.4.

To satisfactorily replicate the rise of Taylor bubbles, the model requires a distinct interface between the gas and liquid phases. To determine the location of this interface, the Volume Of

Fluid (VOF) method is used. This is one of the most commonly used methods to represent the slug flow regime using CFD. The method tracks the interface by solving a continuity equation for the gas volume fraction, α_G , present in each cell,

$$\frac{\partial \alpha_G}{\partial t} + \nabla \cdot (\alpha_G \mathbf{u}) = 0, \quad (3.6)$$

where α_G is the volume fraction of gas (Hirt and Nichols, 1981) and where the overbars that indicate time averaged quantities have been omitted. It is assumed that there is no mass transfer between the phases. The liquid volume fraction present in each cell is then calculated by observing the constraint

$$\alpha_G + \alpha_L = 1, \quad (3.7)$$

where α_L is the volume fraction of liquid, which must be satisfied to conserve mass.

The surface tension force, \mathbf{F}_S , at the liquid–gas interface is approximated by the Continuum Surface Force (CSF) model (Brackbill et al., 1992) which is calculated using

$$\mathbf{F}_S = \sigma \kappa \mathbf{n}, \quad (3.8)$$

where σ is the surface tension coefficient, κ is the radius of curvature and \mathbf{n} is the unit normal of the interface, which in terms of the volume fraction, α is

$$\mathbf{n} = \nabla \alpha_G, \quad (3.9)$$

and κ is given by

$$\kappa = \nabla \cdot \frac{\nabla \alpha_G}{|\nabla \alpha_G|}. \quad (3.10)$$

As compressible effects are also considered, an appropriate equation of state must be used, and which, in this case, is the Ideal Gas Law,

$$\rho = \frac{p_{op} + p}{\frac{R}{M_w} T}, \quad (3.11)$$

where p_{op} is the operating pressure, p is the local pressure, R is the universal gas constant, M_w is the molecular weight and T is the temperature.

As it is assumed that temperature effects are negligible, an isothermal model is employed which defines a constant value of temperature throughout the fluid removing the need to explicitly solve the energy equation.

3.1.2 Turbulence Models

As detailed in Section 3.1.1, to solve the RANS equations, a turbulence model is required to provide closure. The complexity of these models can range from an empirical formulation represented by a single equation through to a coupled set of six equations. The turbulence model employed in the computational models presented in this Thesis, the Realisable $k - \varepsilon$ model, is described in Section 3.1.1 but there are many other possible turbulence models which were considered. A number of examples of common turbulence models are presented in this section; this is, however, not an exhaustive list.

The Spallart Allmaras (SA) model is a popular one equation turbulence model. This model is not commonly used for applications outside of aerodynamics and has been shown to produce large errors for other flow regimes including jet flows, which are seen in the near wall region around Taylor bubbles. For this reason, the use of this model is not considered in the simulations presented in the following chapters.

The standard $k - \varepsilon$ model (SKE) (Launder and Spalding, 1974) uses two equations to close the RANS equations, one for the turbulent kinetic energy, k and one for the dissipation rate ε ,

$$\frac{\partial}{\partial t}(\rho k) + \mathbf{u} \cdot \nabla(\rho k) = \nabla \cdot \left[\left(\mu + \frac{\mu_t}{\sigma_k} \right) \nabla k \right] + \mu_t S^2 - \rho \varepsilon, \quad (3.12)$$

$$\frac{\partial}{\partial t}(\rho \varepsilon) + \mathbf{u} \cdot \nabla(\rho \varepsilon) = \nabla \cdot \left[\left(\mu + \frac{\mu_t}{\sigma_\varepsilon} \right) \nabla \varepsilon \right] + C_{1\varepsilon} \frac{\varepsilon}{k} \mu S^2 - \rho C_{2\varepsilon} \frac{\varepsilon^2}{k}, \quad (3.13)$$

This is one of the most popular turbulence model for industrial applications due to its accuracy, robustness and relative lack of computational expense. Two variations of the SKE model have been developed in an attempt to improve the performance of the model, these are the Re-Normalised Group (RNG) $k - \varepsilon$ model and the Realisable $k - \varepsilon$ model, described in Section 3.1.1. The RNG model is derived from the Navier-Stokes equations using Re-Normalisation Group methods (Yakhot et al., 1992). This method again uses transport equations for k and ε

$$\frac{\partial}{\partial t}(\rho k) + \mathbf{u} \cdot \nabla(\rho k) = \nabla \cdot \left[\left(\mu + \frac{\mu_t}{\sigma_k} \right) \nabla k \right] + \mu_t S^2 - \rho \varepsilon, \quad (3.14)$$

$$\frac{\partial}{\partial t}(\rho \varepsilon) + \mathbf{u} \cdot \nabla(\rho \varepsilon) = \nabla \cdot \left[\left(\mu + \frac{\mu_t}{\sigma_\varepsilon} \right) \nabla \varepsilon \right] + C_{1\varepsilon} \frac{\varepsilon}{k} \mu_t S^2 - \rho C_2 \frac{\varepsilon^2}{k} - R_\varepsilon. \quad (3.15)$$

However, this formulation includes an additional term in the ε equation which is given by

$$R_\varepsilon = \frac{C_\mu \rho \eta^3 (1 - /\eta_0) \varepsilon^2}{1 + \beta \eta^3} \frac{1}{k}. \quad (3.16)$$

This additional term has the effect of improving the accuracy in highly strained flows. It should also be noted that the values of the constants are derived analytically in this model, with the exception of β . The values of these constants are $C_\mu=0.0845$, $\sigma_k=0.7194$, $\sigma_\varepsilon=0.7194$, $C_1=1.42$, $C_2=1.68$, $\eta_0=4.38$, $\beta=0.012$.

Another commonly used two equation turbulence model is the $k - \omega$ model of Wilcox (1988). This model defines one equation for the turbulent kinetic energy, k and one for the specific dissipation rate ω , which may be considered of as the ratio of ε to k ,

$$\frac{\partial}{\partial t}(\rho k) + \mathbf{u} \cdot \nabla(\rho k) = \nabla \cdot \left[\left(\mu + \frac{\mu_t}{\sigma_k} \right) \nabla k \right] + \mu_t S^2, \quad (3.17)$$

$$\frac{\partial}{\partial t}(\rho \omega) + \mathbf{u} \cdot \nabla(\rho \omega) = \nabla \cdot \left[\left(\mu + \frac{\mu_t}{\sigma_\omega} \right) \nabla \omega \right] + \alpha \frac{\omega}{k} \mu_t S^2. \quad (3.18)$$

where the coefficient α governs the production of ω and $\mu_t = \rho \frac{k}{\omega}$. The model constants σ_k and σ_ω . This model has been shown to be effective in regions of low Reynolds numbers such as in

wall boundary layers and is also able to automatically adapt for problems with low Reynolds numbers.

Reynolds Stress models (RSM) (Launder et al., 1975) provide an alternative method of achieving closure of the RANS equations. This approach introduces a set of six partial differential equations which are solved to obtain the Reynolds stresses. This leads to an additional 22 unknowns which are required to be modelled, which are estimated using a calibration method. McDonough (2007) concludes that this does not improve the modelling of the underlying physics, but rather give a model in which coefficients can be altered, so that results match the observed behaviour. This method is also clearly more computationally expensive than two equation models which reduces its feasibility for practical application.

A further set of turbulence models may be derived using an alternate approach to the RANS method. Large Eddy Simulation (LES) methods are transient (or unsteady) models that filter the Navier Stokes equations to resolve only the eddies whose scales are larger than the filter width or grid spacing (Smagorinsky, 1963). The smaller eddies are then modelled using what are known as subgrid scale models. This method does require very fine grids, particularly in near-wall regions. This lead to the development of hybrid RANS-LES models, known as Detached Eddy Simulation (DES) models. DES methods model the near-wall regions using a RANS approach and model the rest of the domain in an LES manner as first demonstrated by Shur et al. (1999). These approaches to turbulence modelling are much more computationally expensive than solving the RANS equations due to both their transient nature and the increased grid resolution required to accurately resolve the flow fields and hence were not employed in the computational studies presented in this Thesis.

The characteristics of the flow close to the wall of the pipe in turbulent conditions must also be considered. At a wall boundary, a no slip condition is applied, meaning that there is zero velocity at this boundary. This results in a thin layer of laminar flow very close to the wall where

viscous effects dominate; this is commonly referred to as the viscous sublayer. Above this there is a layer in which the viscous effects near the wall and the turbulent effects of the main flow are of similar magnitudes. Outside of these layers, the turbulent effects of the mean flow dominate and the flow is not affected directly by viscous effects (Versteeg and Malalasekera, 2007).

Two dimensionless groups can be defined to characterise the flow in the boundary layer,

$$u^+ = \frac{U}{U_\tau}, y^+ = \frac{\rho u_\tau y}{\mu}, u^+ = f(y^+) \quad (3.19)$$

where $U_\tau = \sqrt{\tau_w/\rho}$ is known as the friction velocity, and in which τ_w is the wall shear stress.

The viscous sub-layer is very thin and normally limited to y^+ values of below 5. In this layer, it can be shown that a linear relationship between u^+ and y^+ exists,

$$u^+ = y^+. \quad (3.20)$$

Outside of the viscous sub-layer, for y^+ values of between 30 and 500, it can be shown that the velocity profile fits a logarithmic relationship with the wall distance. In the model presented, the Standard Wall Function approach of Launder and Spalding (1974) was used, in which the layer of cells adjacent to the wall are assumed to be in this layer. This log-law is given by

$$u^+ = \frac{1}{\kappa} \ln(Ey^+), \quad (3.21)$$

where κ is the von Karman constant and E is a constant with empirically determined values of 0.4 and 9.8 respectively. In the simulations presented, y^+ values were at the lower end of this range, typically between 15 and 35.

The above RANS models were developed for single phase flows and their applicability to multiphase flows should be considered. Due to the large difference in densities between the

two fluids, there is a high density ratio in the vicinity of the interface. This results in the the assumption of zero velocity divergence, used in the derivation of the turbulent kinetic energy equation, no longer being valid. Sawko and Thompson (2010) derived expressions for turbulent kinetic energy and turbulence dissipation which are not dependent on this assumption. This method has been shown to significantly increase the accuracy of a VOF simulation modelling two phase stratified flow and should be considered for use in future simulations.

3.1.3 Mesh

For the finite volume method to be used to solve these equations, the flow domain must be sub-divided into a number discrete control volumes (commonly referred to as cells) to form a mesh (or grid)

This process of sub-dividing the domain is known as mesh generation, and is an important part of the CFD process, as the density and distribution of a computational mesh can greatly affect the accuracy of the solution. There are a number of cell types into which a domain may be split. A 2D domain may be sub-divided by quadrilateral or triangular elements, while a 3D domain may be sub-divided into hexahedral, wedge, tetrahedral, pyramid or more recently, polyhedral (n-side polygon) volumes. The corners of these cells will be referred to as nodes and the 3D sides of the cells referred to as faces.

A computational mesh can be classified as either structured or unstructured, based upon their topology. Each type has its own advantages and disadvantages which must be assessed according to the requirements of the simulation.

A structured mesh has a regular topology which can be expressed as an array, which allows an ease of data store and access. However, the structure of the grid must be maintained at all times. This means that single extra nodes may not be added to the grid, but rather an extra line in 2D, or plane in 3D, of nodes must be added to maintain the structure. However, this can lead

to the addition of cells which are not required. Consequently, 2D structured grids are restricted to the use of quadrilateral cells, and 3D grids to the use of hexahedral.

There are three main subcategories of structured grid topology, O-grid, C-grid and H-grid, examples of which are shown in Figure 3.1. The O-grid may also map a circular shape onto a rectangular, or vice versa. The use of this grid configuration is commonly seen in a wide array of scenarios, particularly in pipe flow where it allows refinement of the mesh close to the wall of the pipe. The C-grid topology is often employed to model the flow around airfoils as it allows refinement of the mesh close to the airfoil and in the wake region, whilst enabling larger cells further away from areas of interest. A H-grid topology is the collective name given to the other structured meshes which are not of the C or O type.

Unstructured grids are not subject to the same number of constraints as structured meshes. This does mean that refinement or coarsening of the mesh can be made in any location, and triangular (in 2D) and prism, pyramid and tetrahedral (in 3D) cells may be used. This means it is much easier to mesh more complicated domains, or those that require a large amount of local refinement. One of the main disadvantages of these methods is that the data is not stored in a structured array, and hence the cell connectivity information must be stored separately, which will require more memory in order to be stored and thus may be slower to run. However, modern CFD solvers, such as ANSYS Fluent, treat any mesh as unstructured. The basic mesh topology is that a face has two cells either side of it (or just one at a boundary).

The quality of a mesh may be assessed by a number of criteria, which include cell skewness, cell aspect ratio, cell area/volume, cell maximum/minimum angle and cell size growth factors. Some of these criteria will overlap, for instance, if a triangular cell has a high aspect ratio, it is also likely to have a small minimum angle. Examples of poor quality cells due to these factors are shown in Figure 3.2.

For all of the computational models created to study the rise of Taylor bubbles presented in

this Thesis, a block-structured grid with an O-Grid topology was used, as described in Section 3.3.5.

3.1.4 Spatial Discretisation

In order to solve the governing equations numerically, they need to be converted from continuous partial differential equations to discrete finite difference equations. The discrete values of a scalar quantity, ϕ , are stored at the cell-centroids, but face values, ϕ_f , are required and must be interpolated from the values at the cell centroid. There are many discretisation schemes that could be used to calculate these face values, and a number of the most common schemes are introduced in this section.

First-Order Upwind (FOU) methods assume that the values of a variable at the cell centroid are representative of an average value throughout the cell. This means that when a FOU method is used, the face value of a variable is equal to the cell centroid value of that variable in the upwind cell. This method is uncomplicated but only first order accurate.

The Second-Order Upwind (SOU) scheme uses a Taylor series expansion of the cell centred solution about the cell centroid to obtain the face values. This means the face value, ϕ_f is given by,

$$\phi_{f,SOU} = \phi + \nabla\phi \cdot \vec{r}, \quad (3.22)$$

where $\nabla\phi$ is the gradient of the cell centred value in the upstream cell and \vec{r} is the displacement vector from the upstream cell centroid to the face centroid.

The Quadrilateral Upwind Interpolation for Convective Kinematics (QUICK) scheme is based on a weighted average of second order upwind and central interpolations of variables. For face e in Figure 3.3, the face value is given by,

$$\phi_e = \theta \left[\frac{S_d}{S_c + S_d} \phi_P + \frac{S_c}{S_c + S_d} \phi_E \right] + (1 - \theta) \left[\frac{S_u + 2S_c}{S_u + S_c} \phi_P - \frac{S_c}{S_u + S_c} \phi_W \right]. \quad (3.23)$$

In this scheme the weighting variable θ is set to be 1/8 by default.

3.1.5 Temporal Discretisation

For a transient simulation, the time domain is also subdivided into a number of discrete elements, called time steps, Δt . This temporal discretisation involves the integration of all of the terms in the Navier-Stokes equations over a time step. The continuous expression for the time evolution of a variable, ϕ , is given by

$$\frac{\partial \phi}{\partial t} = F(\phi). \quad (3.24)$$

This may be discretised using a number of different methods. A backward differencing scheme, to first order accuracy gives this to be

$$\frac{\phi^{n+1} - \phi^n}{\Delta t} = F(\phi), \quad (3.25)$$

and to second order accuracy,

$$\frac{3\phi^{n+1} - 4\phi^n + \phi^{n-1}}{2\Delta t} = F(\phi), \quad (3.26)$$

where n is the value at the current time step, t , $n + 1$ is the value at the next time step, $t + \Delta t$, $n - 1$ is the value at the next time step, $t - \Delta t$.

After the time derivative has been discretised, $F(\phi)$ may then be calculated using an implicit or explicit time integration scheme.

The implicit time integration scheme evaluates $F(\phi)$ at the next time step,

$$\frac{\phi^{n+1} - \phi^n}{\Delta t} = F(\phi^{n+1}), \quad (3.27)$$

which gives

$$\phi^{n+1} = \phi^n + \Delta t F(\phi^{n+1}). \quad (3.28)$$

This implicit equation is solved iteratively for each time step. This has the advantage of being stable regardless of time step size.

The explicit time integration is given by

$$\frac{\phi^{n+1} - \phi^n}{\Delta t} = F(\phi^n), \quad (3.29)$$

which gives

$$\phi^{n+1} = \phi^n + \Delta t F(\phi^n). \quad (3.30)$$

This is referred to as an explicit method as ϕ^{n+1} is explicitly expressed in terms of ϕ^n . Unlike the implicit method, this scheme is not unconditionally stable.

An alternative method is the Crank Nicolson scheme. This is a partially implicit scheme which can be defined using

$$\frac{\phi^{n+1} - \phi^n}{\Delta t} = [\theta F(\phi^{n+1}, t^{n+1}) + (1 - \theta)F(\phi^n, t^n)], \quad (3.31)$$

where $0 \leq \theta \leq 1$. When θ is 0, the scheme is simply the fully explicit scheme defined in Equation 3.29. Similarly, when θ is 1, this gives the fully implicit scheme, shown in Equation 3.27. For the Crank-Nicolson scheme, $\theta = 0.5$ is most often used. Like the implicit scheme, the Crank Nicolson method is unconditionally stable, but has the advantage of being second order accurate (Versteeg and Malalasekera, 2007).

The computational models presented in this Thesis employ the implicit time integration method due to its stability. There is a restriction on the value of the time step that can be applied to an explicit method, given by the Courant-Freidrich-Lewy (CFL) condition

$$\text{Cr} = \frac{u\Delta t}{\Delta x} \leq 1, \quad (3.32)$$

which must hold throughout the domain and where Cr is the Courant number. In the simulations presented in this thesis, although an implicit temporal discretisation was used, an explicit VOF model, described in Section 3.1.7 was used. For this reason the CFL condition was still required to hold. CFL numbers were typically around 1 for simulations in which a bubble was rising in

a stable manner. This could rise to approximately 2-3 for simulations in which a bubble was undergoing a breakage.

3.1.6 Pressure-Velocity Coupling

The discretised Navier-Stokes equations have a coupling between the pressure and velocity terms. These equations may be solved sequentially (in a segregated manner) or as part of a coupled system. There are a number of solution algorithms which handle this pressure-velocity coupling, of which the SIMPLE, PISO, and NITA methods are described here.

The SIMPLE algorithm (Patankar and Spalding, 1972) uses a relationship between velocity and pressure corrections to enforce mass conservation and to obtain the pressure field. To apply this algorithm, an initial first guess is made for the pressure field and this is used to solve the momentum equation. The resulting face flux does not satisfy the continuity equation, and so a correction term is added. This correction term is then substituted into the continuity equation to obtain an equation for the required pressure correction. The pressure-correction equation is then solved using the Algebraic MultiGrid (AMG) method. Once a solution is obtained, the cell pressure and the face flux are corrected using an under-relaxation factor for pressure. The corrected face flux satisfies the discrete continuity equation identically during each iteration. This process is iterated until the magnitude of this correction is within a specified tolerance.

The Pressure Implicit with Splitting Operators (PISO) (Issa, 1986) scheme is closely related to the SIMPLE scheme but applies a “neighbour correction” iteration within the solution stage for each iteration. This term corrects the velocities to more closely satisfy the continuity and momentum equations. This means that the PISO algorithm takes more computational time per iteration, but often requires fewer iterations to converge. For this reason it is particularly recommended for use with transient simulations (ANSYS FLUENT). The PISO scheme also includes the option of using a skewness correction which can decrease the number of iterations

required for a converged solution on a highly skewed mesh. This works by recalculating the pressure correction gradient after solving the pressure-correction equation, and this is used to update the mass flux corrections.

Non-Iterative Time Advancement (NITA) (Issa, 1986) is a transient scheme that is used to advance in time without iterating the whole solution. Instead, inner iterations are used to ensure convergence of each set of equations, as shown in Figure 3.4. This can significantly decrease the amount of computation expense in a transient calculation.

Finally, the coupled solver solves the momentum and pressure based continuity equations simultaneously. This can provide a more stable and robust solution for supersonic flows, flows with rotating machinery or internal flows with complex geometries. However, with this comes a large computational expense. This is not appropriate for the scenarios being simulated throughout the course of this Thesis.

3.1.7 VOF

To determine the location of the interface between the phases, a continuity equation for the volume fraction must be solved

$$\frac{\partial \alpha_G}{\partial t} + \nabla \cdot (\alpha_G \mathbf{u}) = \rho_q S_{\alpha_q} + \sum_{p=1}^n (\dot{m}_{pq} - \dot{m}_{qp}) + S_{\alpha_q}, \quad (3.33)$$

where \dot{m}_{pq} is the mass transfer from phase p to phase q , similarly, \dot{m}_{qp} is the mass transfer from phase q to phase p and S_{α_q} is a source term. The constraint in Equation 3.7 must also hold. This continuity equation can be implicitly or explicitly discretised in time in order to be solved.

The implicit discretisation is given by

$$\frac{\alpha_q^{n+1} \rho_q^{n+1} - \alpha_q^n \rho_q^n}{\Delta t} V + \sum_f (\rho_q^{n+1} U_f^{n+1} \alpha_{q,f}^{n+1}) = \left[\sum_{p=1}^n (\dot{m}_{pq} - \dot{m}_{qp}) + S_{\alpha_q} \right] V, \quad (3.34)$$

where $n + 1$ is the new (current) time step, n is the previous time step, $\alpha_{q,f}$ is the face value of the q^{th} volume fraction, computed using one of the methods described in Section 3.1.7.1, V is the

volume of the cell and U_f is the volume flux through the face. In all of the simulations conducted in the present work, it will be assumed that there is no mass transfer between the liquid and gas phases, and no source terms are used. Hence, the implicit scheme may be simplified to,

$$\frac{\alpha_q^{n+1} \rho_q^{n+1} - \alpha_q^n \rho_q^n}{\Delta t} V + \sum_f (\rho_q^{n+1} U_f^{n+1} \alpha_{q,f}^{n+1}) = 0. \quad (3.35)$$

In the explicit formulation of the VOF model, the finite-difference interpolation schemes are applied to the volume fraction values from the previous time step (as opposed to the time step being calculated in the implicit formulation). This can be represented, in simplified form, by

$$\frac{\alpha_q^{n+1} \rho_q^{n+1} - \alpha_q^n \rho_q^n}{\Delta t} V + \sum_f (\rho_q U_f^n \alpha_{q,f}^n) = 0. \quad (3.36)$$

3.1.7.1 Interface Reconstruction

In its basic form, the volume fraction, being a scalar, gives no information about the location of the interface within a cell, as shown in Figure 3.5. The accuracy of the results obtained by using the VOF model can greatly differ depending on the method used to determine the location of the interface between the two phases. When using the explicit formulation, there are several possible schemes to resolve the interface between the two phases. One of the most commonly used is called the ‘‘geometric reconstruction’’ scheme, based on the ‘‘piecewise linear interface calculation’’ (PLIC) method (Youngs, 1982). This method assumes that the interface between the fluids has a linear slope within each cell and this is used to calculate the flow through the cell. The scheme initially calculates the position of the interface relative to the centre of all partially filled cells. Then the flux through each face can be found using this calculated interface along with the velocity field. Finally, the volume fraction is calculated using a balance of the fluxes from the previous calculations. This scheme has been shown to produce a high quality interface, and is recommended as the scheme which produces the sharpest interface by ANSYS

Fluent (ANSYS FLUENT).

The Donor-Acceptor approach uses the standard interpolation schemes whenever a cell is completely filled with one phase. Near the interface, however, the Donor-Acceptor scheme is used to calculate the amount of fluid advected through the face. One cell acts as a donor for an amount of one phase and this is transferred to a neighbour (acceptor) cell which in turn advects the same amount of the other phase into the donor cell. The major limitations of this approach are that the interface shape may be significantly different to the actual shape, as shown in Figure 3.6 and that it can only be applied to meshes with quadrilateral or hexahedral cells.

Other explicit schemes include the Compressive, HRIC, QUICK and First Order Upwind schemes. The Compressive scheme is a second order reconstruction scheme based on a slope limiter method. The face VOF value, ϕ_f is given by

$$\phi_f = \phi_d + \beta \nabla \phi_d \quad (3.37)$$

where ϕ_d is the donor cell VOF value, β is the slope limiter value and $\nabla \phi_d$ is the donor cell VOF gradient value. The slope limiter value is bounded between 0 and 2.

The High Resolution Interface Capturing (HRIC) method (Muzaferija and Perić, 1997) uses a non-linear blend of upwind and downwind differencing. The normalised face value of the volume fraction $\overline{\phi}_f$ is calculated using the normalised cell value of volume fraction, $\overline{\phi}_c$,

$$\overline{\phi}_c = \frac{\phi_D - \phi_U}{\phi_A - \phi_U} \quad (3.38)$$

where U refers to the upwind cell, A to the acceptor cell and D to the donor cell and $\overline{\phi}_f$ is given by

$$\overline{\phi}_f = \begin{cases} \overline{\phi}_c & \text{if } \overline{\phi}_c < 0 \text{ or } \overline{\phi}_c > 1, \\ \frac{\overline{\phi}_c}{2} & \text{if } 0.0 \leq \overline{\phi}_c < 0.5, \\ 1 & \text{if } 0.5 \leq \overline{\phi}_c \leq 1. \end{cases} \quad (3.39)$$

This scheme along with the QUICK and First Order Upwind schemes, described in Section 3.1.4, are used to calculate the face fluxes for all cells and hence do not interpolate the position of the interface separately. The HRIC method is more accurate than the upwind schemes but less computationally expensive than the Geo-Reconstruct algorithm. Unlike the Geo-reconstruct scheme these methods can all also be applied using the implicit formulation of volume fraction.

One limitation of the explicit formulation, however, is that it is not compatible with a second order discretisation in time, and therefore a first order method must be used. It should be noted that all simulations are therefore 1st order accurate. 2nd order accuracy schemes are still used where available to minimise the error in the simulations.

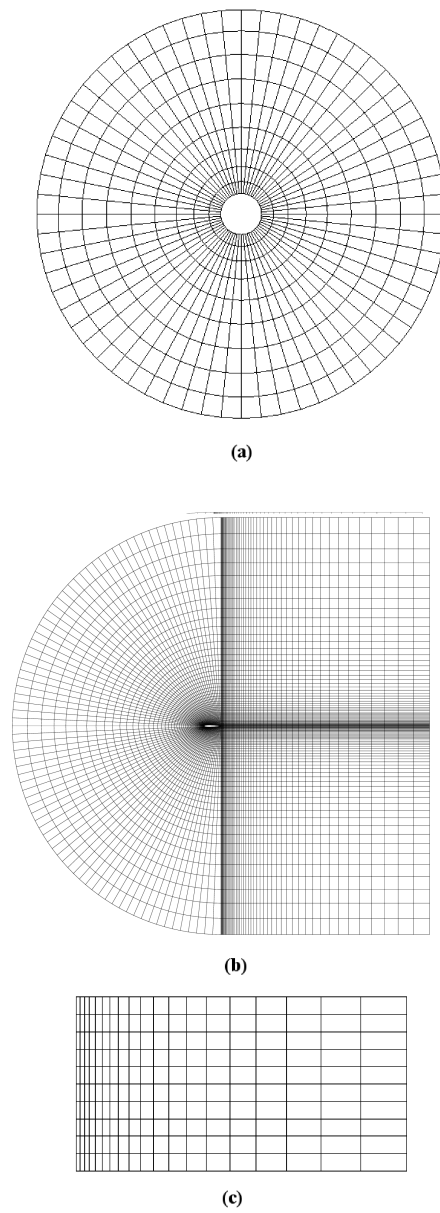


Figure 3.1: Diagram of different types of structured grid, showing (a) an “O-Grid” which is often used in pipe flow simulations (b) a “C-Grid” type mesh, often used for flow around aerofoils and (c) a “H-Grid” used in many different applications where a structured grid is required.

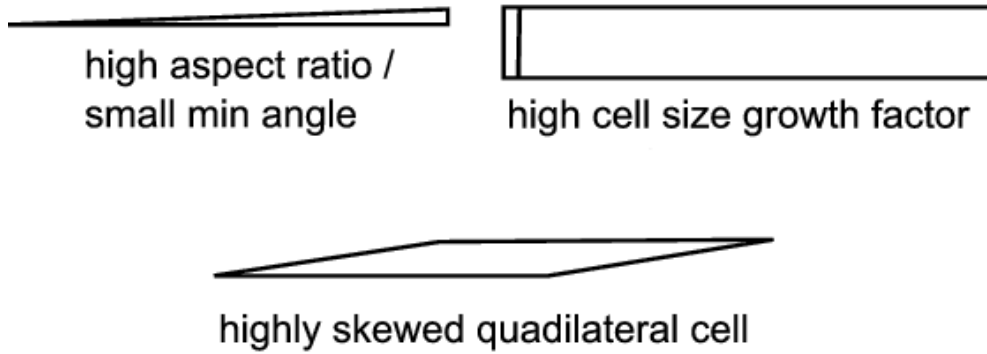


Figure 3.2: Diagram illustrating different criteria of poor cell quality (a) high aspect ratio or small minimum angle cell, (b) a cell with a high growth factor and (c) a highly skewed quadrilateral cell.

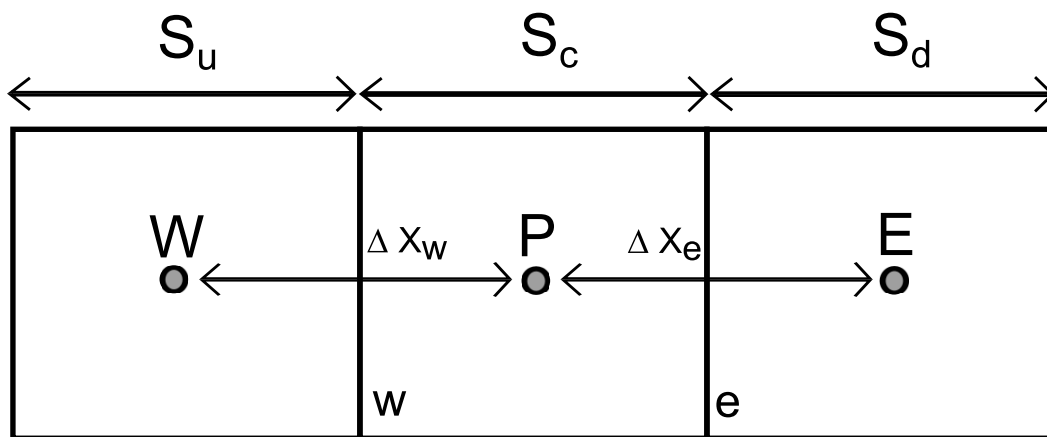


Figure 3.3: A diagram illustrating the QUICK scheme. For face e , the face value is given by Equation 3.23

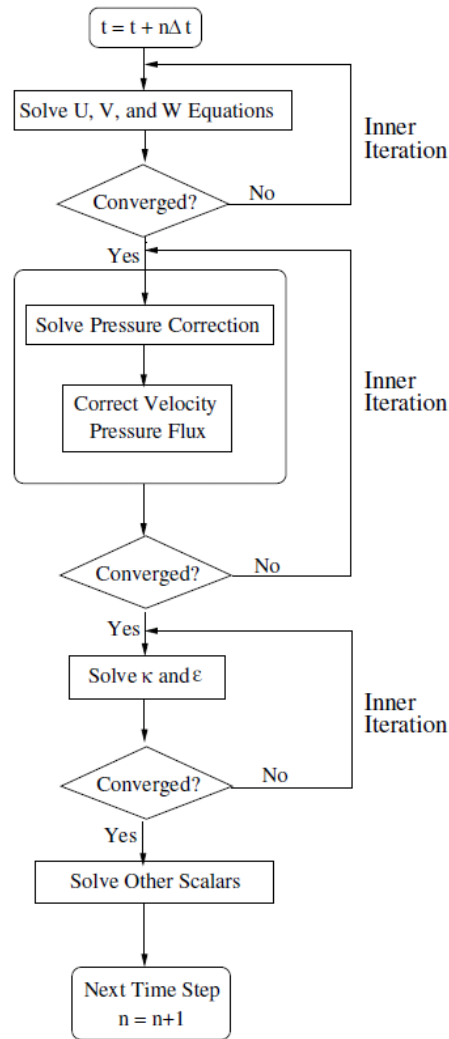


Figure 3.4: A diagram illustrating the steps in the NITA scheme (ANSYS FLUENT). Each set of equations is iterated to convergence individually to reduce the computation time required.

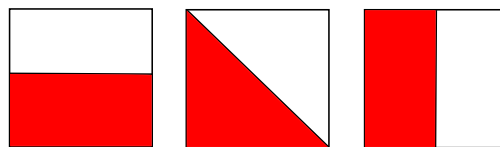


Figure 3.5: A diagram illustrating three cells each with a volume fraction of 0.5.

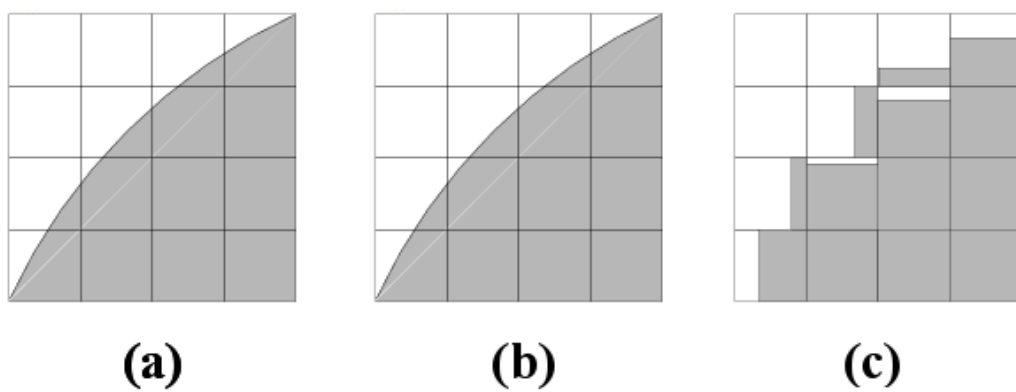


Figure 3.6: A diagram illustrating the results obtained by using the Geo-Reconstruct (b) and Donor-Acceptor (c) algorithms in comparison to the real solution, (a) (ANSYS FLUENT). As can be observed from this image, the Geo-reconstruct gives a much sharper interface shape than the Donor-Acceptor method.

3.2 Verification

Two important parts of any numerical study are the verification and validation stages. The verification of a numerical model ensures that the level of error introduced by solving equations using numerical methods is minimal (and preferably quantifiable). Validation studies ensure that the equations used appropriately model the real world physics. In the following sections a verification study is provided along with a number of initial validation studies. Further validation for specific cases are provided in Chapters 5 and 6.

3.2.1 Error and Uncertainty

When conducting a verification study it is important to consider the difference between uncertainty and error, which in some circumstances may be confused. Uncertainty is defined as,

A potential deficiency in any phase or activity of the modelling process that is due to the lack of knowledge (AIAA, 1998).

Whereas error is defined as,

A recognisable deficiency in any phase or activity of modelling and simulation that is not due to lack of knowledge (AIAA, 1998).

Errors may be classified into one of the following categories:

1. Spatial discretisation error,
2. Temporal discretisation error,
3. Iterative convergence error,
4. Computer round off error,

5. Computer programming error, and
6. Usage error.

The purpose of a verification study is to quantitatively evaluate these errors and minimise them if possible. The following sections describe this process, and these methods that are used during the development and solution of the computational models presented in this work.

An example of uncertainty is in the choice of turbulence models. As described in Section 3.1.2 there are many different turbulence models which may be used to model a scenario, however there is no way to ascertain the level of error introduced by using them. However, sensitivity analyses may be performed to ascertain the level of uncertainty. Running the same simulation multiple times with a number of different turbulence models to see the effect on the solution would be one example of this. An analysis of the results of a series of such model sensitivity studies is presented in Section 5.1.4.

3.2.2 Spatial discretisation error

Spatial discretisation errors may be introduced when the domain is sub-divided into control volumes. Celik et al. (2008) suggest a procedure for estimating the error introduced by spatially discretising a domain based on the work of Roache (1998). This five step procedure is summarised here, and is known as the Grid Convergence Index (GCI) method (or the Richardson extrapolation method):

1. A representative cell size, h , is defined.
2. Three significantly different grid sizes should then be defined, coarse, intermediate and fine.

Simulations should be performed to determine the value of a key variable Φ . Celik et al. (2008) define the refinement factor, r , as $r = h_{coarse}/h_{fine}$ and suggest that this should be in excess of 1.3. This value is based on their experience and not on any formal definition.

3. Let $h_1 < h_2 < h_3$ and $r_{21} = h_2/h_1$, $r_{32} = h_3/h_2$. The apparent order of the method, p , is given by

$$p = \frac{1}{\ln(r_{21})} |\ln |\epsilon_{32}/\epsilon_{21}| + q(p)|, \quad (3.40)$$

$$q(p) = \ln \left(\frac{r_{21}^p - s}{r_{32}^p - s} \right), \quad (3.41)$$

$$s = 1. \operatorname{sgn}(\epsilon_{32}/\epsilon_{21}), \quad (3.42)$$

where $\epsilon_{32} = \Phi_3 - \Phi_2$, $\epsilon_{21} = \Phi_2 - \Phi_1$ and $\operatorname{sgn}(a)$ is the sign of a value a . If r is constant, then $q(p) = 0$.

4. The extrapolated values can then be calculated from

$$\Phi_{ext}^{21} = (r_{21}^p \Phi_1 - \Phi_2)/(r_{21}^p - 1), \quad (3.43)$$

and similarly for Φ_{ext}^{32} .

5. The following estimates of error may then be computed.

The approximate relative error,

$$e_a^{21} = \left| \frac{\Phi_1 - \Phi_2}{\Phi_1} \right|, \quad (3.44)$$

The extrapolated relative error

$$e_{ext}^{21} = \left| \frac{\Phi_{ext}^{12} - \Phi_1}{\Phi_{ext}^{12}} \right|, \quad (3.45)$$

The fine-grid convergence index, GCI,

$$GCI_{fine}^{21} = \frac{1.25e_a^{21}}{r_{21}^p - 1}, \quad (3.46)$$

This method has been used to evaluate the error introduced by spatial discretisation in the simulations presented in Chapters 5 and 6 and for the validation study described in Section 3.3.2.

3.2.3 Temporal discretisation error

A transient solution requires the definition of discrete time steps to describe the time dependent transition from one solution to the next. Much like with the grid spacing, the solution should be independent of the time step. The level of error introduced by discretising this time step can be estimated using the same GCI method described for the spatial discretisation detailed in Section 3.2.2.

3.2.4 Convergence

As detailed in Section 3.1.6 the numerical solutions to the finite difference equations are computed iteratively. The differences between the computed values of any variables and the values required to satisfy conservation of that variable is known as the residual. This is summed over all the computational cells, giving an “unscaled residual”, and then averaged to give a “globally scaled residual”. The scheme will iterate until this residual reaches a pre-determined value for each of the equations being solved. For all of the numerical solutions presented in this Thesis, this convergence criterion value was set as a reduction of three orders of magnitude within each timestep. An example of the residuals from the base case simulation of a bubble rising in water in a 0.3 m pipe, fully described in Section 5.2.1, is shown in Figure 3.7. This image is taken while the bubble is mid way through its rise through the pipe, 4.75 s from the start of the simulation. At this time, the residuals of the continuity equation is 3.8×10^{-5} , the x , y and z momentum equations 4.5×10^{-6} , 4.45×10^{-5} and 5.5×10^{-6} respectively, the residuals for the k and ε equations are 2.4×10^{-7} and 3.9×10^{-7} , and the energy equation 7.45×10^{-8} .

3.2.5 Computer round off error

The round off error is the error incurred by the computer when rounding. For a standard floating point number, the precision is 7 digits, hence $1 = 0.9999999$, while a double precision number is typically stored to 19 digits.

3.2.6 Computer programming error

As a full version of the commercial CFD code, ANSYS FLUENT, is being used for simulations, computer code error verification has not been conducted. Code verification is conducted by ANSYS before the full release of any software (ANSYS FLUENT). Using a stable release of a popular CFD code means that users have had time to identify errors over time. However, no computer code is error free but users have little control over this particular error.

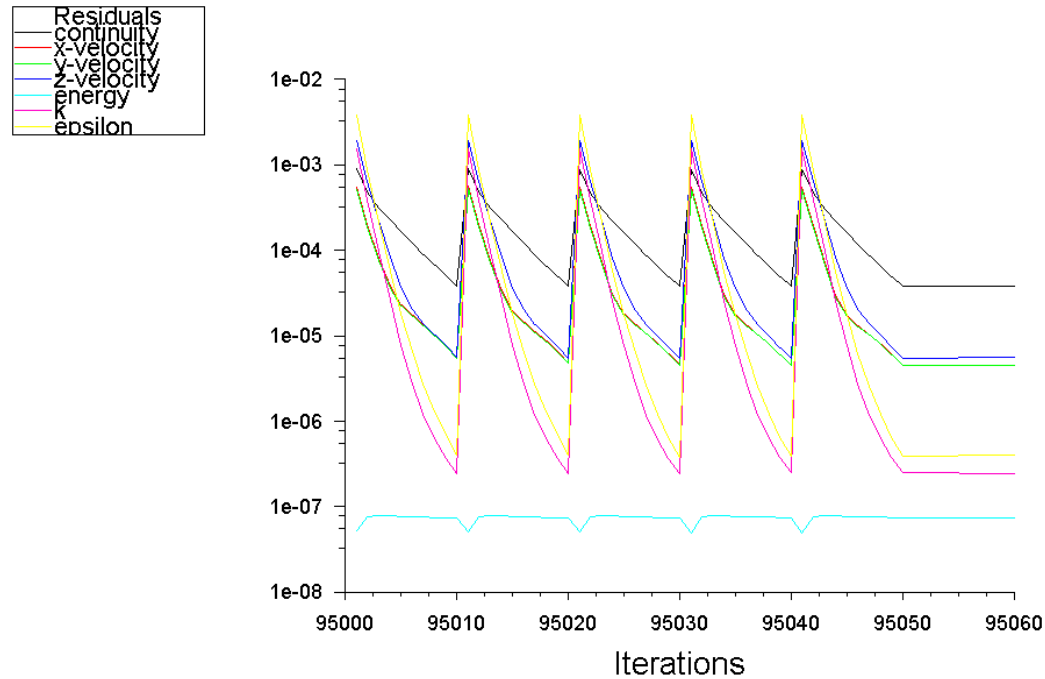


Figure 3.7: An example of the residuals from the base case simulation of a bubble rising in water in a 0.3 m pipe. This image is taken while the bubble is mid way through its rise through the pipe, 4.75 s from the start of the simulation. At this time, the residuals of the continuity equation is 3.8×10^{-5} , the x , y and z momentum equations 4.5×10^{-6} , 4.45×10^{-5} and 5.5×10^{-6} respectively, the residuals for the k and ϵ equations are 2.4×10^{-7} and 3.9×10^{-7} , and the energy equation 7.45×10^{-8} .

3.3 Validation

In the following sections, the results of three validation studies are presented. The solutions obtained from these models are compared against published benchmark studies. The first of these studies uses the widely acknowledged empirical correlations of White and Beardmore (1962) to validate CFD model over a range of non-dimensional parameters commonly used in both experimental and numerical studies (Viana et al., 2003; James et al., 2006; Araujo et al., 2012). For the second validation study considered, the results of a set of PIV experiments (van Hout et al., 2002) are used to compare real flow fields around a Taylor bubble, with those simulated using the CFD model. In the final study presented, the empirical correlations of Viana et al. (2003) are extended and used to validate the CFD model at conditions beyond the original experimental limitations.

To introduce these studies, the development and solution of a base case model is described. This model was subsequently adapted in each of the validation studies, in order to more accurately represent the problem. Details of these adaptations can be found in the corresponding sections.

3.3.1 The base case model

3.3.1.1 Boundary and Initial conditions

The base case model assumes 2D axisymmetric laminar flow. A representation of this domain (not to scale) is shown in Figure 3.8. For this 2D axi-symmetric domain, the flow is assumed to flow from left to right, the x-axis is defined as the vertical axis of symmetry, and so gravity must be set in the negative x-direction. As the flow is laminar, no turbulence model is required. A 3D case was also created for direct comparison using a vertical, cylindrical domain. The length to diameter ratio of these domains is set to $L/D = 10$ to ensure the solution produced was not affected by the base of the pipe or the outlet of the domain.

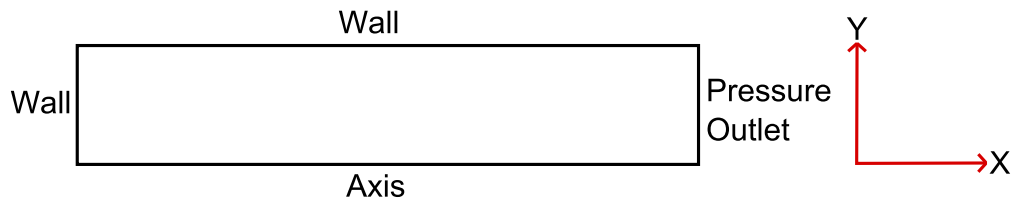


Figure 3.8: Diagram of the boundary conditions for a 2d axis-symmetric flow simulation. The x and y axes are also indicated, with gravity in the negative x direction.

At the wall boundary, a no slip condition is applied. At the outlet, a pressure outlet condition is applied. The gradient of variable normal to the boundary is zero at this boundary and zero average static pressure is enforced across the faces.

3.3.1.2 Spatial Domain

For the 2D axisymmetric model a structured rectangular mesh is used. As the flow is laminar no additional refinement of the mesh is required near to the walls in order to resolve the turbulent boundary layer. However, some additional refinement near the wall was added to ensure that the thin film surrounding the Taylor bubble was adequately resolved. A 3D mesh was also created. A cross section through the 3D mesh in the xy plane is shown in Figure 3.9. In the 3D model, the z axis is now aligned with gravity, which acts in the negative z direction. A block-structured O-Grid hexahedral mesh was chosen as this allows refinement close to the pipe walls whilst retaining a relatively coarse mesh in the centre of the pipe. Hence, this mesh configuration can accurately capture the flow field behaviour in the liquid film. This feature makes the mesh suitable for the modelling of slug flow applications, and consequently the rise of single Taylor bubbles (Abdulkadir et al., 2011).

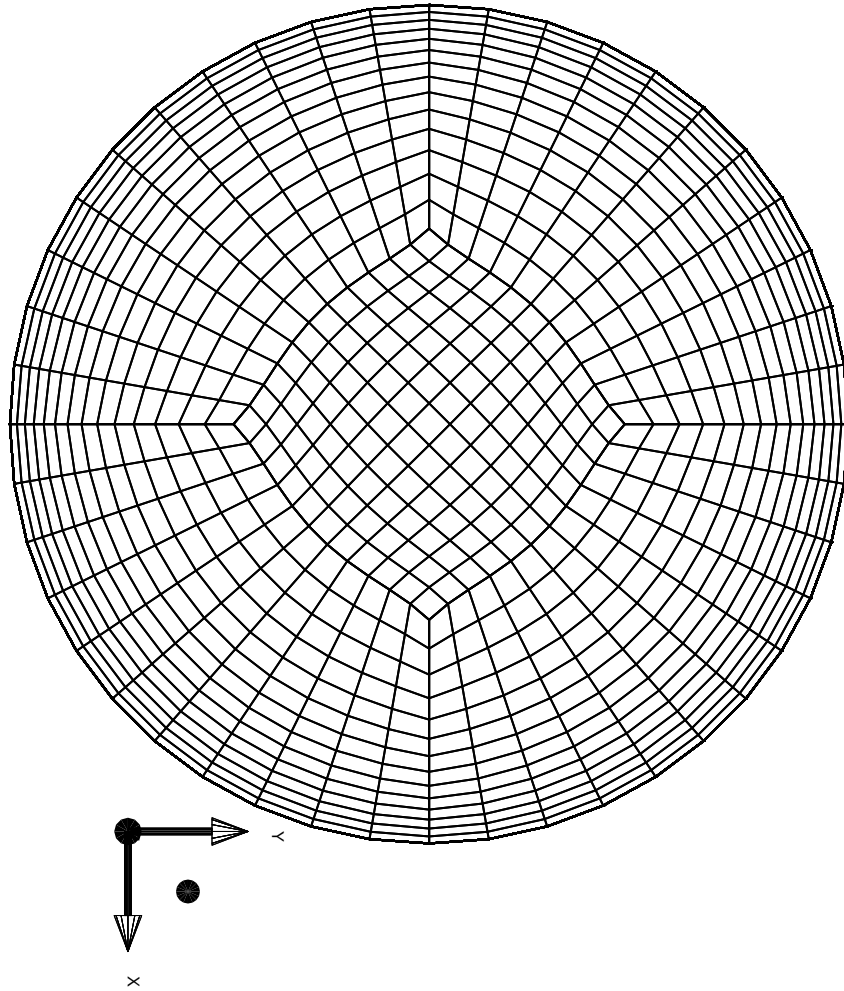


Figure 3.9: Example of a cross section in the xy plane of a 3D O-Grid mesh used in the simulations.

3.3.1.3 Initial conditions

At $t = 0$ s, the initial volume fraction of the phases within the domain must be specified. An initial bubble shape must be specified, the geometry of the bubble shape chosen has a hemisphere on top of a cylinder of radius equal to the bubble radius. When modelling the surface of the liquid column, an area (2D) or volume (3D) of gas must also be specified at the top of the pipe. This process is called patching in Fluent. A back-flow boundary condition is applied to the pressure outlet where the volume fraction of the mixture is specified to be the gas phase, to account for the fact the upper most cells will be filled with air for the duration of the simulations. An initial internal pressure inside the bubble needs to be specified. The pressure throughout the bubble was set at a constant value matching the hydrostatic pressure at the nose of the bubble. In addition the velocity components are all set at 0 ms^{-1} .

3.3.2 Verification

During the execution of these studies, a verification stage was conducted to quantify and then minimise the errors introduced by the numerical model. The errors introduced were estimated using the schemes summarised in Section 3.2.

3.3.2.1 Spatial Discretisation Errors

A series of three simulations were computed with different mesh resolutions. The static bubble was released and allowed to rise in a quiescent fluid. The terminal velocity for each bubble was recorded for each mesh size. The GCI method described in Section 3.2.2 was used to estimate the error introduced by spatial discretisation on 2D meshes of 16000 (400 in the x direction \times 40 in the y direction), 4000 (200×20) and 1000 (100×10) cells. This method estimates the values of given variables at an infinitely small grid size to provide an approximate discretisation error. For these calculations, the simulated rise speeds of the Taylor bubbles were used to compare

the performance of the three meshes. For the finest mesh, cells the error given by the GCI was 0.19% and for the intermediate mesh this was 0.77%. This procedure was also performed for the 3D meshes of 205000, 100000 and 50000 cells with a GCI error of 0.41% for the 205000 cell mesh and 2.45% for the 100000 cell mesh. It was concluded that for all subsequent simulations the 16000 and 205000 cell meshes should be used as these minimise the error introduced by the mesh. Figure 3.10 shows graphically an example of the results of the GCI method, for the 2D case the terminal velocity computed for each mesh is plotted against the average cell size

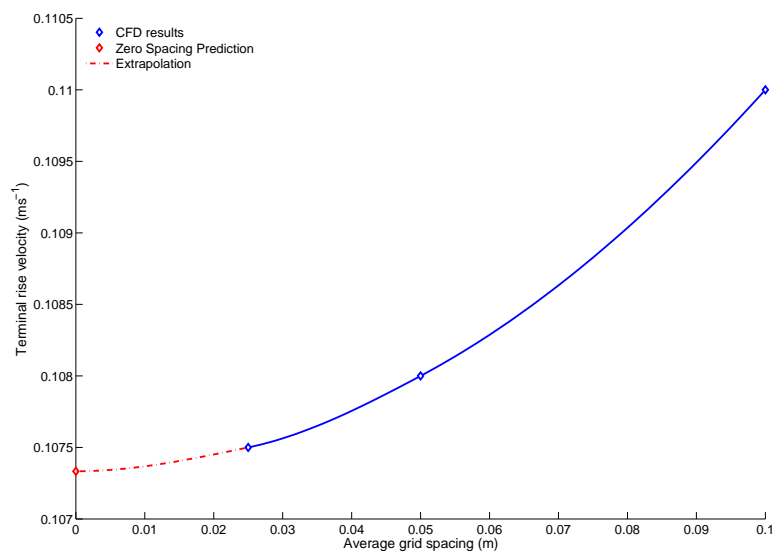


Figure 3.10: The velocities computed on the 2D meshes of 1000 cells (average size of 0.1 D), 4000 cells (0.05 D) and 16000 cells (0.025 D) along with the extrapolated value for an infinitesimally small average cell size.

3.3.2.2 Temporal Discretisation Errors

A series of simulations were also conducted using three different time-step sizes. Similar to the spatial discretisation, the method introduced in Section 3.2.2 was used to estimate of the error

introduced by temporal discretisation using time-steps of 0.0001 s, 0.0005 s and 0.001 s. Again, for these calculations, the rise speed of the Taylor bubble was used to provide a comparison of the simulation performance provided by the three different time-step sizes. For the smallest time step of 0.0001 s the error given by the GCI was 0.09% and 0.16% for the time step of 0.0005 s. These values along with the extrapolated prediction are shown on Figure 3.11. It was concluded that for the following simulations the time-step of 0.0005 s should be used as this provides a good balance between error and computational efficiency.

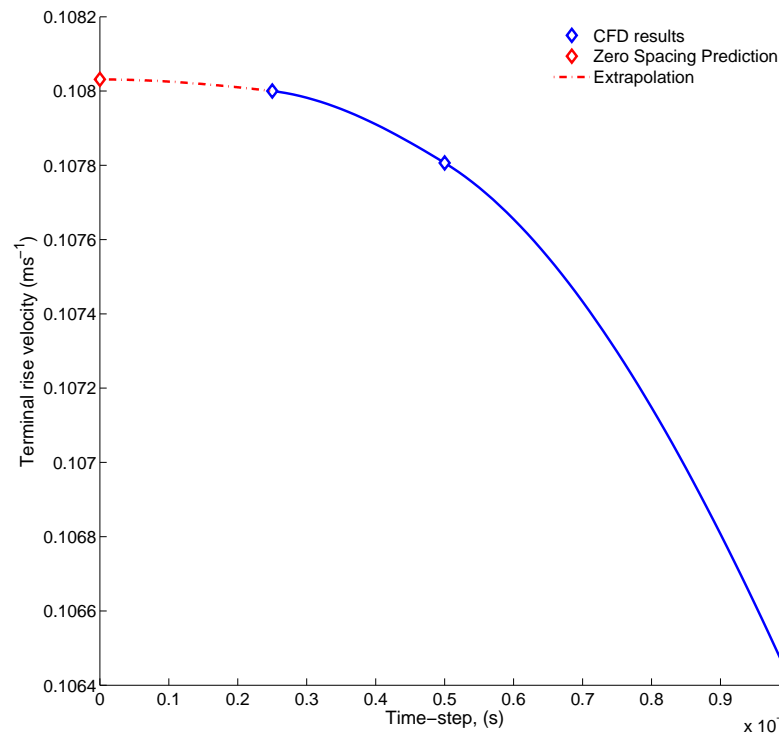


Figure 3.11: The velocities computed using time-steps of 0.0001 s, 0.0005 s and 0.001 s along with the extrapolated value for an infinitesimally small time-step.

3.3.2.3 Iterative Convergence

The simulations were seen to be convergent in fewer than 10 iterations per time-step, as per the guidelines in the Fluent manual. A decrease of three orders of magnitude in the normalized residuals of the continuity equation was confirmed, and six orders of magnitude for the x , y and z component momentum equations.

Figure 3.12: Example of a residual graph from showing the convergence of the continuity equation, x , y and z component momentum equations as well as the k and ε equations.

3.3.3 Validation Study 1: White and Beardmore (1962)

White and Beardmore (1962) conducted a series of experiments which investigated the rise of single Taylor bubbles and which were used to determine the Froude number of Taylor bubbles with various Morton ($10^{-11} < M < 10^6$) and Eötvös ($10^0 < M < 10^3$) numbers. To study these non-dimensional parameters, the flow of a range of fluids in glass pipes of diameters ranging from 0.005 m to 0.0387 m was studied. The fluids ranged in viscosity from 0.001 Pa.s to 20.9 Pa.s, in density from 803 kgm^{-3} to 1420 kgm^{-3} and in surface tension coefficient from 0.0228 to 0.0777.

Single air bubbles were introduced to the base of the pipe and the time taken for the bubbles to rise between two heights, approximately 0.6 m apart was recorded. This enabled the velocity, and hence Fr, to be calculated. The experiments were repeated “a sufficient number of times” to enable the average velocity to be determined within a 1% error (White and Beardmore, 1962).

Their results were also compared with other published experimental work, and the majority of data collapsed onto a curve fitted to their experimental data, as can be observed in Figure 3.13. The only data points do not lie on this curve are those of Gibson (1913), which was one of the first studies on Taylor bubbles. White and Beardmore (1962) suggest the discrepancy could be due to Gibson’s use of larger diameter pipes and the lack of video equipment, which makes the accurate measurement of rise velocity difficult. Correlations were developed using the full range of experimental results and White and Beardmore suggest that these are used for future comparisons. The results of these experiments were also used to create a flow regime diagram (shown previously in Figure 2.1 which determines for what conditions particular forces can be neglected).

The 2D axisymmetric CFD model described in Section 3.3.1 was used to model these experiments. The domain (and hence the mesh) was scaled to give different pipe diameters, and hence a range of Eötvös numbers. The liquid viscosity was also varied (whilst keeping the liquid

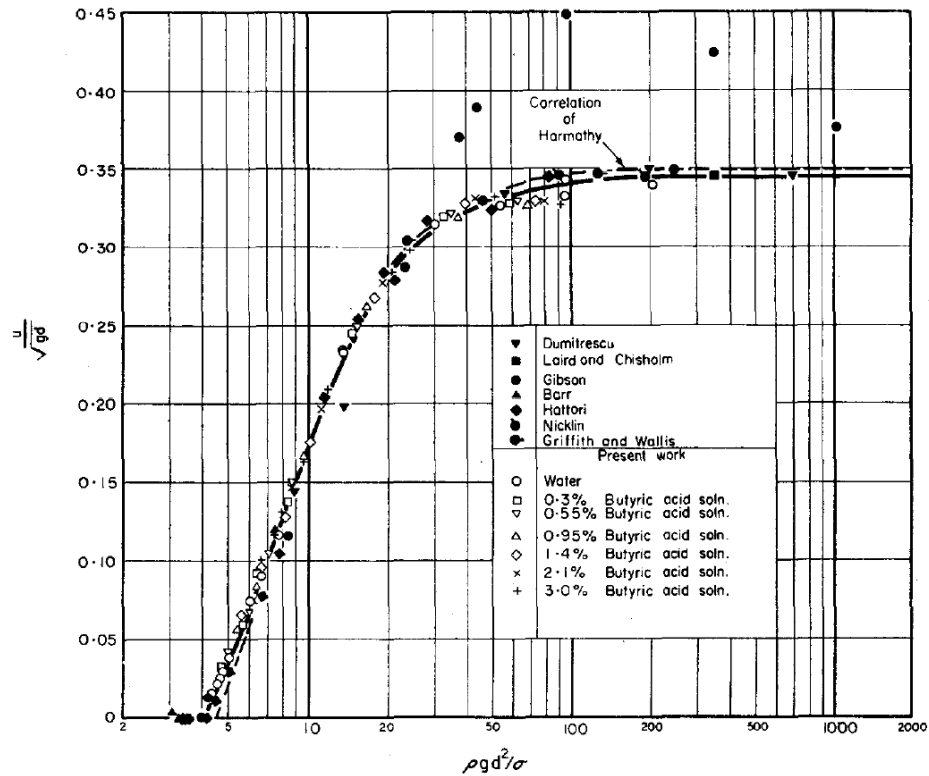


Figure 3.13: Comparison of the results of the experiments of White and Beardmore (1962) with other experimental studies.

density and surface tension coefficient constant throughout at 1000 kgm^{-3} and 0.074 kgs^{-2} respectively) in order to produce a variation in the Morton number without changing the Eötvös number. These parameter changes produced CFD solutions at Morton numbers of 10^{-11} , 10^{-4} , 10^{-2} , 10^0 , 10^1 , 10^2 and 10^4 , and Eötvös numbers of approximately 13, 19, 25, 53, 104 and 331.

Figure 3.14 shows the solutions of the simulations plotted against the empirical correlations developed by White and Beardmore (1962) for their experimental results. An analysis of this data concludes that the results of the simulations closely match the experimental correlations for higher the Morton numbers considered. However, the errors between the empirical and simulated results increase with a decrease in Morton number, particularly with a high Eötvös number. The

results for the fluid with the smallest Morton number (10^{-11}) show the greatest relative error ($\approx 6\%$). This may have been due to the flow in these simulations becoming turbulent and hence the laminar model no longer being applicable. This will be discussed in more detail in Section 3.3.4 and also later in Chapter 5 where much larger Eötvös number flows are considered.

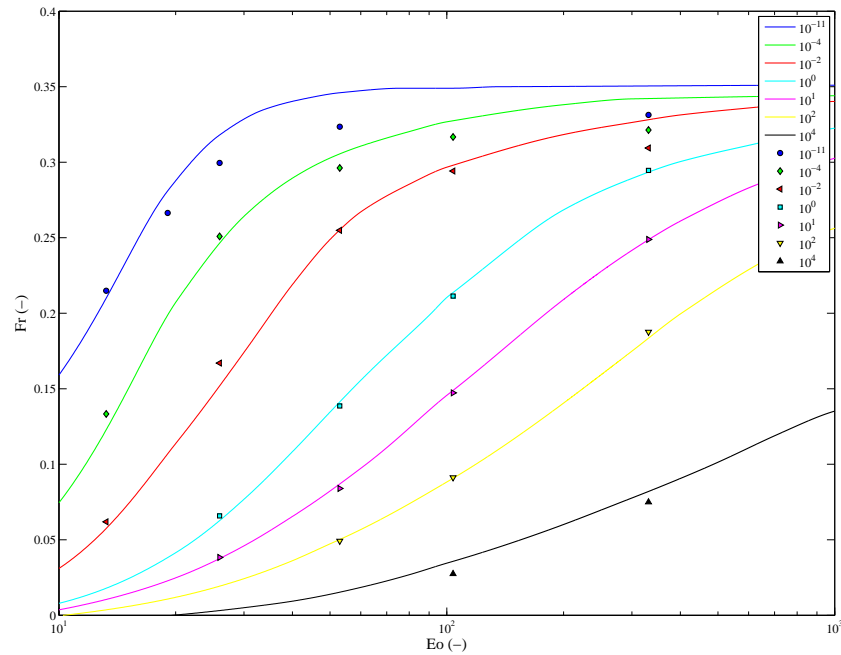


Figure 3.14: Comparison of the correlations of White and Beardmore (1962) (line) with the results from the CFD model (symbols) for various values of the Morton Number. This shows that the results of the simulations closely match the experimental correlations for higher the Morton numbers considered. However, the errors between the empirical and simulated results increase with a decrease in Morton number, particularly with a high Eötvös number.

3.3.4 Validation Study 2: van Hout et al (2002)

A validation study was conducted in which the solutions from the numerical model were compared against the experimental studies of van Hout et al. (2002). van Hout et al. (2002) used Particle Image Velocimetry (PIV) methods to investigate the flow around a single Taylor bubble rising in a vertical, 4 m long pipe filled with quiescent water. The diameter of the pipe used in these experiments was 0.025 m, which gives a $M= 10^{-11}$, $Eo= 80$ and a theoretical $Fr= 0.35$ using the correlation of Viana et al. (2003). The selection of this geometry and fluid properties should ensure that the rise velocity of single Taylor bubble should be independent of surface tension. The Reynolds number, Re , for this flow is 4350 meaning the flow in the film and wake regions will be turbulent. Consequently, to model these experiments, a 3D CFD model with a Realisable $k - \varepsilon$ turbulence model was used. The justifications for the choice of this model were discussed in Section 3.1.2 and a comparison between this and other turbulence models is presented in Section 5.1.4.

van Hout et al. (2002) et al injected bubbles through the base of the pipe via a computer controlled injection valve at a pressure of 0.4 bar. In their study, the average length of the Taylor bubbles was $3.6D \pm 0.3D$. As the nose of the bubble passed a determined point of the pipe, the PIV equipment was triggered. This trigger height was approximately 2 m from the air inlet and surrounded by a transparent Perspex box filled with water, in order to reduce image distortion of the high definition camera.

As described in Section 2.1.3, PIV uses a vertical laser sheet created across the domain to illuminate fluorescent particles that have been dispersed in the liquid phase. This laser sheet is pulsed with a set time interval, and the positions of the illuminated particles are recorded by a camera triggered at the same frequency. The resulting images are then analysed to determine the successive positions of the individual particles in order to generate instantaneous velocity

fields (van Hout et al., 2002; Nogueira et al., 2003). In their study, a Nd:YAG MiniLase III PIV-15 laser was used, which produced a laser sheet of thickness 1 mm. The laser produced a pair of 5-7 ns pulses at a wavelength of 532 nm, which is green light. The camera used to record the images was a KODAK ES 1.0 CCD, with a resolution of 1008×1018 pixels. This was operated in a double exposure mode, which allowed a pair of single frames at a short time interval to be captured. An optical sensor along with an external synchroniser unit was used to control the system. The optical sensor, placed just upstream of the measurement section, triggered the camera and the laser at a specified time delay between the laser pulses. As the fluorescent particles used emit light at 572-594 nm, which is a yellow/orange colour, a high pass filter of >550 nm was used on the camera to filter out the laser light and only show the location of the particles. Using this method it was possible to take a number of consecutive images, limited only by the RAM of the computer being used. The velocity magnitudes in the flow fields of this investigation ranged from $O(10^{-3}) \text{ ms}^{-1} - O(1) \text{ ms}^{-1}$. The time delay between the laser pulses was chosen in such a way that the maximum displacement of a single particle did not exceed 16 pixels.

A plot of the averaged measured PIV and CFD velocity fields are presented in Figure 3.15. An examination of these plots concludes that there is a good qualitative agreement between the two sets of data. In particular, the flow field ahead of the bubble and the flow behaviour in the wake are observed to be very similar, Figure 3.15.

The axial velocity profiles within the liquid film region surrounding the Taylor bubble are shown in Figure 3.16, adjusted by position. The adjustment is such that a measurement read at $z/D = 2$ with a downward velocity of 1 ms^{-1} would give a reading of -3 ms^{-1} as in van Hout et al. (2002). The outline of the Taylor bubble is also shown here. At the entrance to the film at the top of the bubble the velocities are small, but as the film decreases in size, the liquid is observed to accelerate. The velocity reaches a maximum value of approximately $0.95\text{-}1 \text{ ms}^{-1}$,

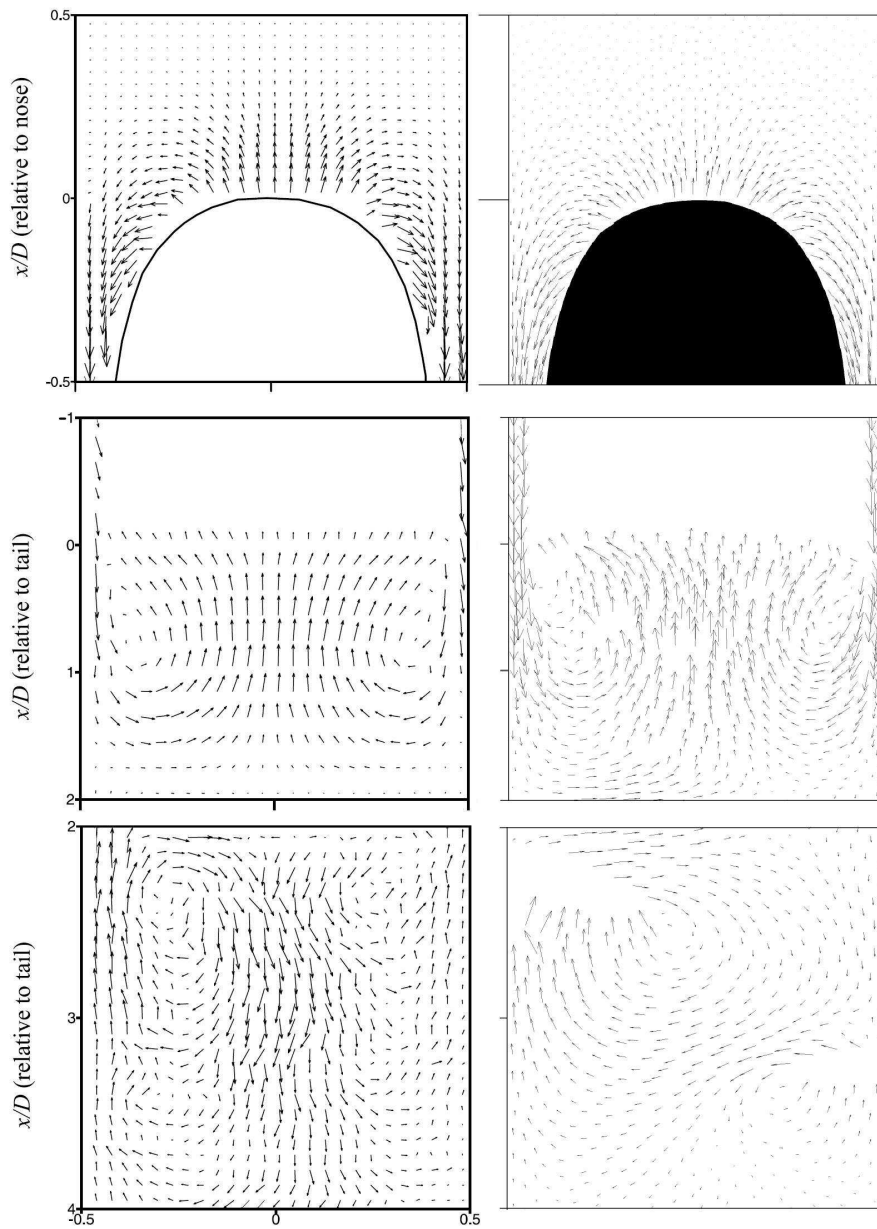


Figure 3.15: Velocity vectors around a fully developed Taylor bubble. On the left, PIV results of van Hout et al. (2002) averaged over 100 experimental runs, and on the right, instantaneous CFD results. At the top, from 0.5 D above to 0.5 D below the nose of the bubble; in the middle, from the tail of bubble to 2 D below it; and at the bottom, from 2 D to 4 D below the tail of the bubble.

close to the exit of the liquid film at the base of the bubble. This predicted maximum velocity is 5 % below the experimental value. The liquid film thickness of the simulations at the exit are 0.0114 and 0.0113 m as compared to 0.0117 m in the experiment. In the simulation, the thicker liquid film results in smaller velocities in the film. In the near wake region behind the tail of the bubble there are strong similarities in the flow behaviour between the numerical solutions and the experimental data. Within two pipe diameters of the bubble a strong vortex is observed in which the axial velocity is positive at the centre line of the pipe. Near to the wall, the axial velocity profiles are similar to those of a downward flowing annular jet. Behind this region the wake reverses in direction, exhibiting a positive axial flow near the walls and a negative flow directed towards the central region of the pipe, as can be observed in Figure 3.15. The CFD simulations also replicate well the behaviour of the trailing wake observed experimentally behind the Taylor bubble. Figure 3.17 shows a comparison between the velocity in the vertical, z , direction along the centreline of the pipe in the z direction.

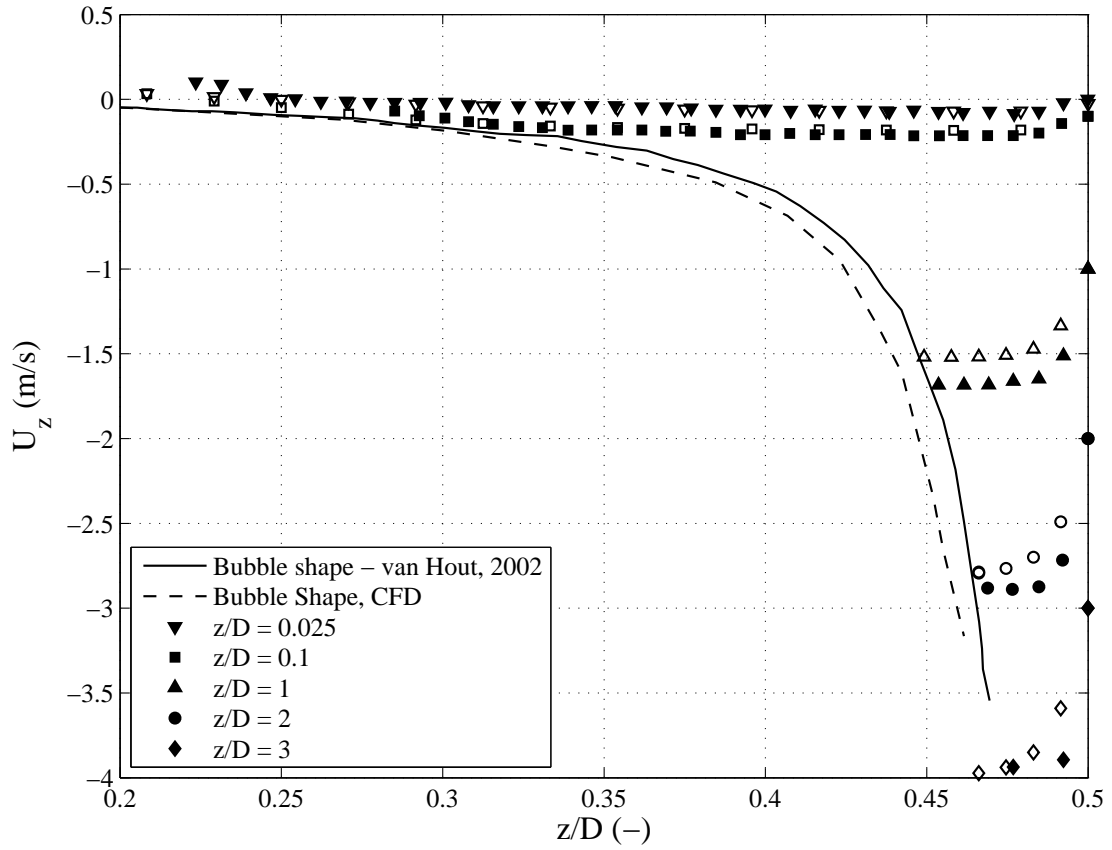


Figure 3.16: Comparison of the outline of the bubble, along with velocity measurements adjusted by position for the experimental measurements van Hout et al. (2002), filled line and filled markers, and the CFD validation case, dashed line and empty markers. The adjustment is such that a measurement read at $z/D = 2$ with a downward velocity of 1 ms^{-1} would give a reading of -3 ms^{-1} as in van Hout et al. (2002).

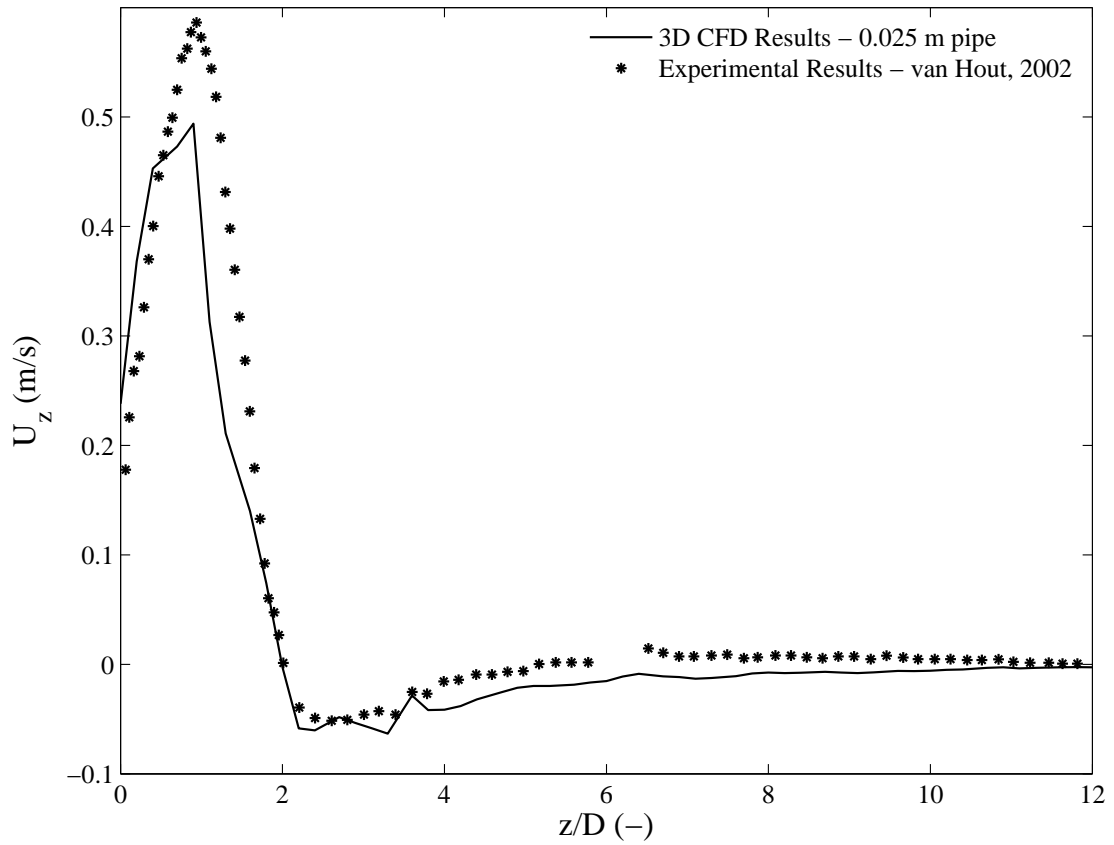


Figure 3.17: Comparison of the centreline velocity behind the tail of the bubble for the experimental measurements of van Hout et al. (2002) (*), and the CFD validation case (solid line).

3.3.5 Validation Study 3: Viana et al, 2003

The work of Viana et al. (2003) adds to and summarises a large collection of data from experimental studies performed to investigate the rise velocity of Taylor bubbles in quiescent liquids of varying viscosities. This makes it an ideal validation case study and a base case for further investigations. A numerical model was constructed to produce simulations to match the same non dimensional flow regimes as the experimental work. As described in Section 2.1.2, the study of Viana et al. (2003) was restricted to fluids with a maximum viscosity of 4 Pa s and to a maximum pipe diameter of 0.12 m. The simulations presented in this section extend the range of these values whilst maintaining a comparable non-dimensional range.

3.3.5.1 Variation of Buoyancy Reynolds number

The computational models were used to investigate the effect of Re_B on the terminal velocity and shape of a single Taylor bubble. It was expected that for higher viscosities, a greater buoyant force would be required to overcome the larger viscous force (due to friction), and hence with the same buoyant force, the velocity of the bubble would be smaller.

The viscosity of the liquid phase was varied from 5 Pa s to 200 Pa s to produce a range of Buoyancy Reynolds numbers from 1 to 146, Morton numbers ranging from $10^4 - 10^{10}$ and an Eötvös number of 10^4 . Viana et al. (2003) collated the results of a large number of experimental studies to produce formulations for the Froude number. These were split into 3 distinct regimes by Re_B ,

$$Fr = \frac{9.494 \times 10^{-3} R^{1.026}}{(1 + (\frac{6197}{E\sigma^{3.06}}))^{0.5793}}, \text{ If, } Re_B < 10, \quad (3.47)$$

$$Fr = \frac{0.34}{(1 + (\frac{3805}{E\sigma^{3.05}}))^{0.58}}, \text{ If, } Re_B > 200. \quad (3.48)$$

In between these two regimes, the following correlation is used to estimate Fr.

$$Fr = L[R; A, B, C, G] = \frac{A}{1 + (R/B)^C)^G}, \quad (3.49)$$

$$A = L[Eo; a, b, c, d], B = L[Eo; e, f, g, h], C = L[Eo; i, j, k, l], G = m/C \quad (3.50)$$

and the parameters (a, b, \dots, m) are

$a=0.34, b=14.793, c=-3.06, d=0.58, e=31.08, f=29.868, g=-1.96, h=-0.49, i=-1.45, j=24.867,$
 $k=-9.93, l=-0.094, m=-1.0295.$

These expressions may be used to give an estimate of the terminal velocity of a single Taylor bubble rising in a pipe of given diameter in a fluid of given properties. The experiments on which this approximation is based upon have an upper viscosity limit of 3.9 Pa.s. Thus the terminal velocity may be estimated by a rearrangement of these expressions, and the use of the Froude number determined from the Buoyancy Reynolds number

$$v_t = Fr \sqrt{gD_t(\rho_L - \rho_g)/\rho_L}. \quad (3.51)$$

An analysis of the computed CFD model simulations and the experimental data conclude that there is a strong agreement for Fr in the low Re_B range, as shown in Figure 3.18. A variation in the pipe diameter between 0.128 m and 0.3 m for the same range of Re_B showed no difference in Fr. This was expected as a variation the pipe diameter, whilst keeping the Re_B constant produces a change only in Eo (from 1.57×10^4 to 4.24×10^4). This has previously been shown not to affect the rise velocity for these flow conditions ($Eo > 80$). With higher Re_B , and hence higher Fr, the agreement between empirical results and simulated data was still strong but with larger errors for the 2D axi-symmetric simulations. When simulations were conducted with a 3D model, a much closer fit to the empirical rise rate values was observed, as shown in Figure 3.19. The error from the predicted values to the simulated values falls within 5% of the theoretical

value. The size of these errors increases to approximately 20% at higher Fr numbers, which has been observed in other numerical simulations of Taylor bubbles James et al. (2008).

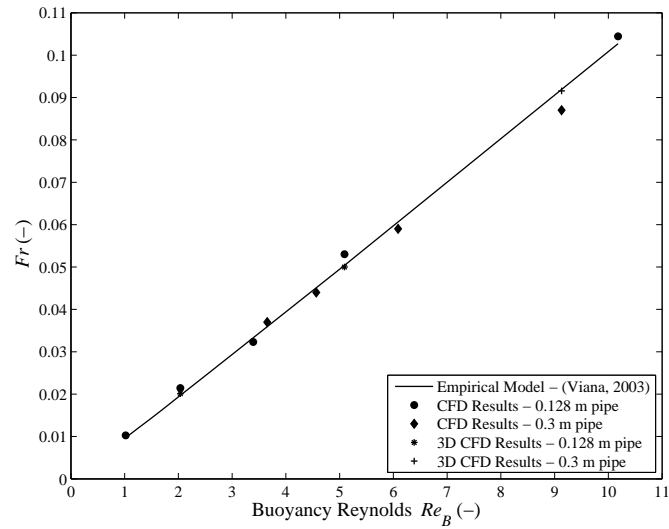


Figure 3.18: Froude number varying with Re_B for $Re_B < 10$. The simulated and predicted Froude numbers match closely in this range of values.

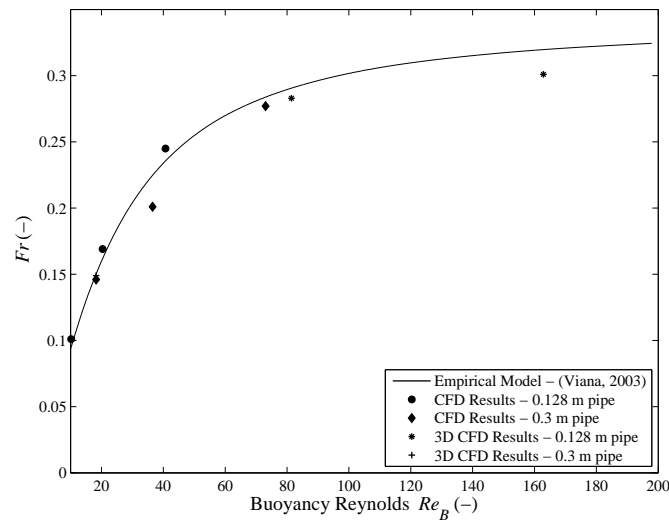


Figure 3.19: Froude number varying with Re_B for $Re_B > 10$. The difference between the simulated Fr and the predicted F increases with increasing Re_B .

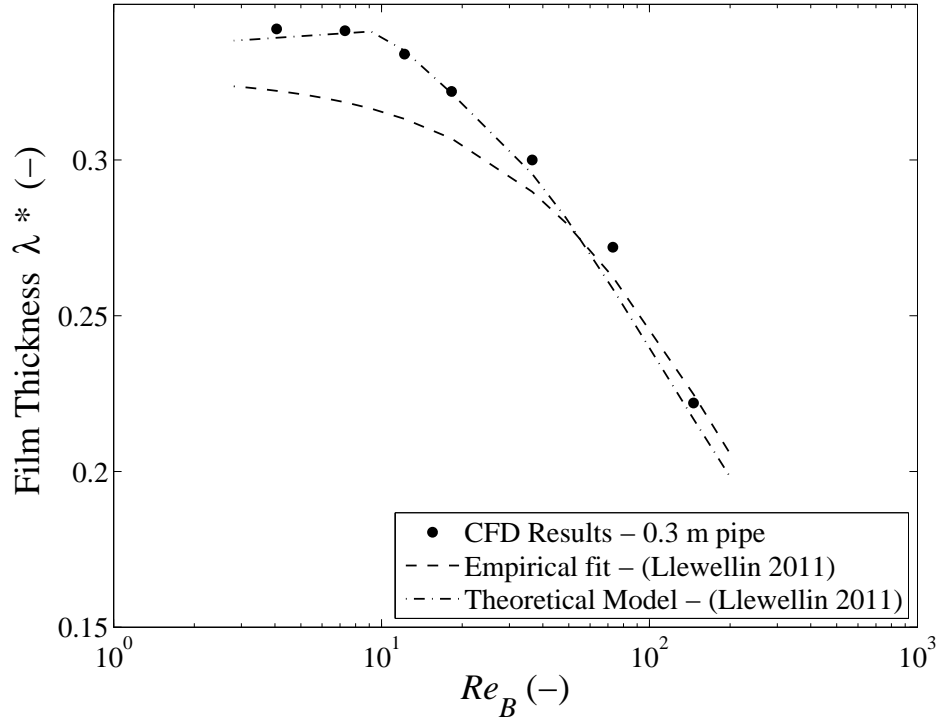


Figure 3.20: Comparison of film thickness in CFD to the results of Llewellyn et al. (2011). The results of the CFD simulations match within 5 % of the theoretical model.

The thickness of the simulated fully developed liquid film around a rising Taylor bubble was compared against the model of Llewellyn et al. (2011). This theoretical model for film thickness around a Taylor bubble was introduced in Section 2.1.4 and is given by

$$\lambda' = \frac{\sqrt[3]{b^2} - \sqrt[3]{12a}}{\sqrt[3]{18b}}, \quad (3.52)$$

$$\text{where } b = 9a + \sqrt{12a^3 + 81a^2}. \quad (3.53)$$

A comparison between the CFD values, this theoretical model of Llewellyn et al. (2011) are shown in Figure 3.20. As can be observed from an analysis of these results, the numerical results

closely match the theoretical film thickness values for the low Fr regime, with a maximum relative error of 5 %.

3.3.6 Conclusions

These validation studies show that the CFD model presented is capable of reproducing the quantitative and qualitative behaviour observed experimentally for the rise of Taylor bubbles. For the low Re_B regime defined by Viana et al. (2003) ($Re_B < 10$), results from a laminar 2D axisymmetric CFD model provide a strong agreement with published experimental and theoretical data for both rise velocity and film thickness. For higher Re_B , a 3D RANS CFD model with a Realisable $k - \varepsilon$ turbulence model results in good qualitative agreement with experimental data but with larger quantitative errors.

Rise of Taylor bubbles in vertical pipes - Experimental

4.1 Experimental Arrangement

This chapter presents the methodology, results and analysis of a series of laboratory experiments performed within the laboratories of the Department of Chemical and Environmental Engineering at the University of Nottingham in collaboration with Dr Chris Pringle. The experiments detailed in this chapter investigate the behaviour of Taylor bubbles rising through a vertically mounted cylindrical pipe with an internal diameter of 0.29 m. This pipe was partially filled with water that was open to the atmosphere at the upper surface and left to become quiescent. The results from the experiments conducted using this pipe were used in conjunction with published theoretical work to validate the results of the simulations presented in Chapter 5.

The diameter of the pipe used in these experiments is significantly larger than those employed in previous studies. The use of such a pipe diameter allows the investigation of a wider non-dimensional parameter space to be explored that has not previously been possible. The results of a number of these studies have been presented and discussed by Pringle et al. (2014).

4.1.1 Experimental Apparatus

A series of experimental studies were performed in a vertical, cylindrical plexiglass pipe of height 9.3 m and internal diameter 0.29 m. The pipe is constructed from a series of conjoined 1 m pipe sections which have a flat flange joint at each end. This allows the length of the pipe to be varied, or for sections to be replaced should they become damaged.

Compressed air may be injected into the base of the pipe from a main compressed air line via a system of twenty five inlet nozzles, with each nozzle having an internal diameter of 0.005 m. The inlet nozzles are connected to the mains compressed air supply through a manifold. The nozzles are formed into five groups of five nozzles. The air may be independently introduced to each of the five batches of nozzles by a dedicated manual flow control valve.

The pipe sections are accessible to researchers at four observation levels along the length of the pipe. Figure 4.1 shows a schematic view of the experimental apparatus. The base of the pipe is located on the first level, which is located in a sump below the ground floor of the laboratory. The sump permits access to the drainage valve (used to drain the fluid from the pipe), the compressed air inlets to the pipe, and to the interconnecting gate valve. This area is directly connected to the main water drainage system of the laboratory. As it is below ground level, it also enables longer pipes to be studied than would otherwise be possible in a building of this height.

The control valves regulating the air inlets are located on the second level, which are located on the ground floor of the laboratory. The mains air supply entering the manifold feeding the individual flow regulator valves is controlled by the mains control valve. A photograph of the air inlet regulation system is shown in Figure 4.2.

An observation platform provides direct access to both pipes on the third level, which is located at a height of 2.3 m above the base of the pipe. A high speed camera was positioned on

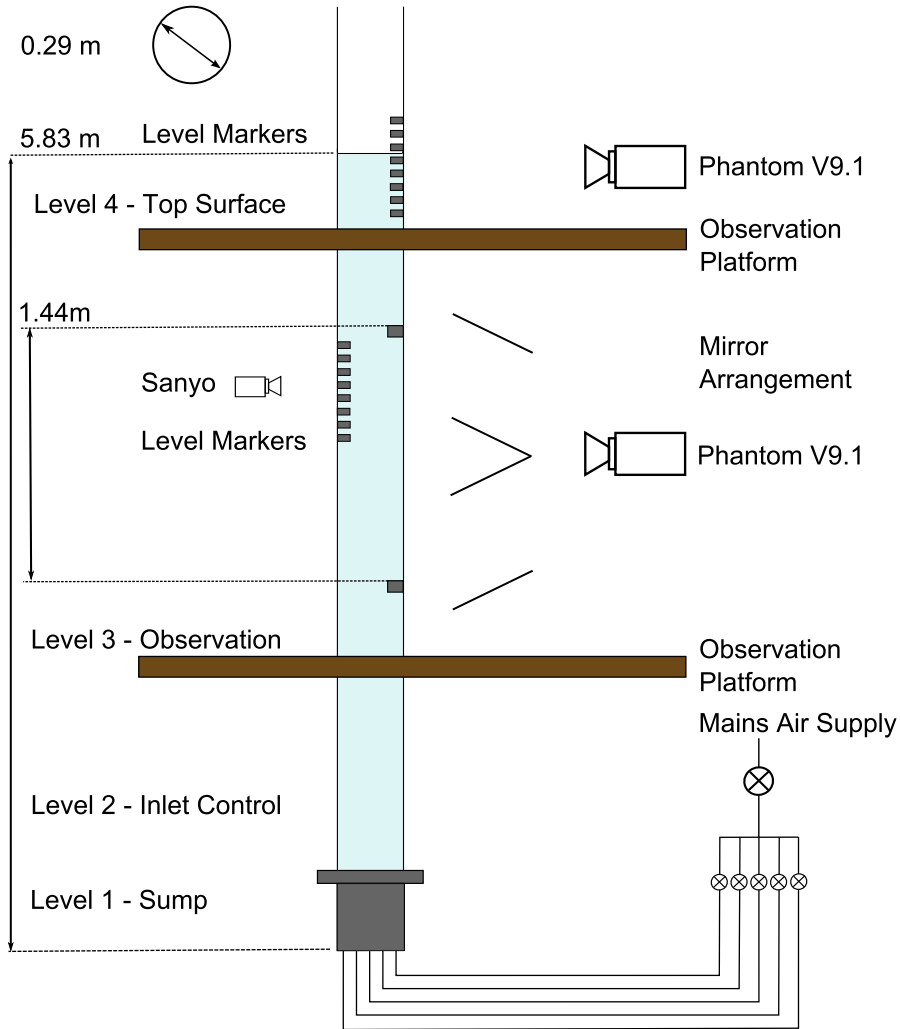


Figure 4.1: A 2D schematic side elevation view of the experimental apparatus. Air is supplied to the 0.29 m diameter pipe filled to a depth of 5.83 m with water via a mains air supply. The rise of the bubble is monitored using a Phantom V9.1 video camera in one of two locations and a Sanyo video camera.

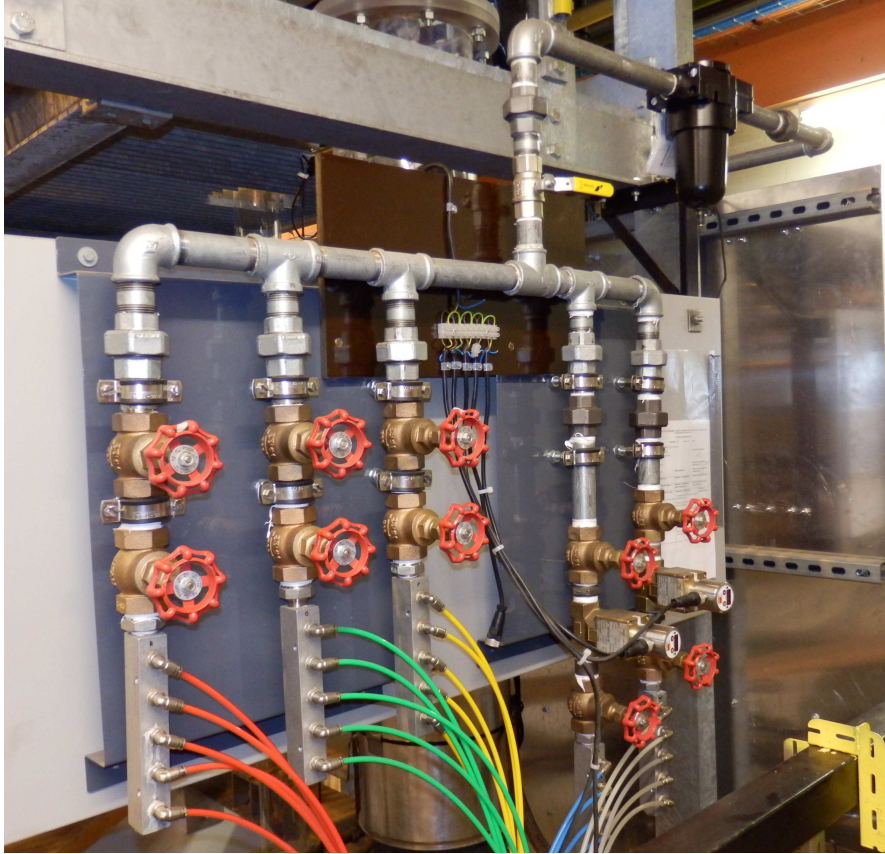


Figure 4.2: A photograph of the air inlet injection system used in these experimental studies. The yellow lever at the inlet to the flow manifold is the mains compressed air control valve and the red rotational valves allow the fine control of the flow delivered to each batch of five injection nozzles.

this level to record the observed rise velocity of the Taylor bubbles introduced at the base of the pipe. The camera used was a Phantom V9.1 high speed camera (Vision Research, 2014). This camera is capable of recording video images at a rate of 1000 frames per second with a maximum resolution of 1632×1200 pixels. However, the speed of the frame rate selected was chosen to balance the exposure time required to maintain adequate resolution images given the level and quality of the background lighting available. In addition, the recorded viewing window was cropped to a resolution of 400×900 pixels to reduce storage memory. This allows the recording of still frame images where each pixel represents approximately 0.0008 m. Black sheeting was mounted to a frame behind the pipe to enhance the contrast, sharpness and clarity of the images recorded. The camera was connected via an ethernet cable to a laptop computer running the PhantomTM video software to record the images. The software provides an interface which allows the user to control the resolution of the image, the frame rate and exposure of the video recordings. A double periscope mirror arrangement, shown in Figure 4.3, was used to observe two separate locations along the length of the pipe at the same time. An example of such a dual view frame recorded during an experiment is shown in Figure 4.4. The brightness and contrast of this image have been increased for greater clarity. This method allowed the time at which the nose of the bubble passed two marked heights on the pipe to be recorded within an accuracy of 0.01 s when using a frame rate of 100 fps. The experimental uncertainty and measurement errors introduced by the use of this method are discussed in Section 4.2.

A Sanyo Xacti AVC/H.264 camera was used to provide a video recording of a larger vertical length of the pipe. A subsequent analysis of these images allows an estimation of the length of the bubble for each experiment performed. This camera was mounted on a tripod approximately 2 m away from the pipe section being studied. Level markers were made on the pipe with a vertical separation of 0.05 m to provide a reference scale against which to estimate the length of the rising bubble. The errors introduced by using this method are discussed in Section 4.2.



Figure 4.3: A photograph of the mirror system used in conjunction with the high speed camera to record multiple viewing windows along the length of the pipe. This system allows two different locations of the pipe to be monitored in a single frame of the video recording.



Figure 4.4: An example of a still frame recorded by the Phantom. This image shows the bubble passing the marker viewable through the upper periscope. The lower marker is 1.44 m below the upper marker, and so the time taken and hence rise velocity of the bubble can be calculated.

Table 4.1: The physical properties of the fluid, the subscript L refers to the liquid phase, G to the air.

ρ_L	ρ_G	σ	μ_L	ν
998.1	1.184	0.074	0.001	1×10^{-6}

The top observation level (at a height of 4.8 m above the base of the pipe) provides access, via a ladder, to the top section of the pipe, which is open to the atmosphere. The pipe may be filled with water using a hose connected to the water main. The hose was securely fastened at a number of locations to ensure a safe working environment for other users of the laboratory. The Phantom V9.1 high speed camera was subsequently used to record images of the movements observed at the upper surface of the fluid following a separate set of experiments. Further level markers were placed at intervals of 0.05 m along the vertical length of the pipe above a known height to provide a reference scale with which to determine the vertical height of the top level of the fluid. To provide an accurate estimate, the camera must be focused on the height at which the liquid column is expected to rise to once a bubble is injected. For the experiments conducted and detailed in this Chapter, tap water was used as the liquid phase and compressed air from the mains line used as the gas phase. The physical properties attributed to these fluids are given in Table 4.1 and the computed theoretical non-dimensional properties for the flow systems are given in Table 4.2. In Table 4.2 the Froude number is the predicted value from the empirical relation proposed by Viana et al. (2003). However, an analysis of the results of experiments conducted to provide an estimate of the value of this parameter are presented in Section 4.4.



Figure 4.5: An example of a still frame recorded by the Sanyo camera to determine the length of the rising bubbles.

Table 4.2: Table of non-dimensional parameters determined for the rise of Taylor bubbles

D (m)	Re_B	Eo	M	Fr
0.29	4.88×10^5	1.11×10^4	2.42×10^{-11}	0.351

4.2 Experimental Design

4.2.1 Objectives

From an analysis of the literature presented in Chapter 2, it was concluded that stable Taylor bubbles should exist in the experimental apparatus used in these studies (Batchelor, 1987). The initial objective of these experimental studies was to confirm that Taylor bubbles do exist and can be repeatedly produced in a pipe of diameter 0.29 m. The secondary initial objective was to quantitatively and qualitatively study the behaviour of these bubbles.

4.2.2 Preliminary studies

4.2.2.1 Introduction of liquid phase

Prior to any experimental studies being undertaken, the pipe was first filled with water to a specified level. As the upper surface of the water was sufficiently below the top of the pipe for the duration of the experiment, and the base of the pipe was sealed, the volume of water within the pipe remained constant throughout the duration of the experiments. The surface level of the water at the top of the pipe was marked by the placement of marker tape (with the top of the tape aligned with the upper surface). This allowed for the periodic emptying and refilling of the column with fresh water to maintain the quality of the water in the pipe during the execution of a series of experiments. The level height of the surface of the water above the base of the pipe was set at 5.83 m. This height was chosen so that the top surface was visible during the rise of a

Taylor bubble through the viewing window of the Phantom V9.1 when the camera was located on the top observation level.

4.2.2.2 Introduction of gas phase

Air is injected to the pipe through 0.005 m tubes connected to the mains line as shown in Figure 4.2. The jets of air introduced at the base of the pipe through the nozzles produced small diameter bubbles which mix and subsequently coalesce in a turbulent zone. This method has previously been used to successfully create Taylor bubbles in a 0.24 m diameter pipe by Pioli et al. (2012). As the base section of the pipe is opaque and constructed of metal (approximately 0.5 m in height), the coalescence process is not directly visible to the eye. However, above this level, in the first acrylic section of pipe, a large, pipe-filling, bubble was observed to form. Due to the location of the apparatus, with the base being in a sump below ground level and surrounded by other equipment, video recording of the flow near to the base of the pipe was not possible. During the execution of the experiments it was observed that not all of the small air bubbles injected coalesced to form the single large Taylor bubble, but formed a cloud of smaller bubbles which rises in the wake of the large bubble. The bubbles observed in this wake appeared to be approximately uniform in size and have a diameter of approximately 0.005 m.

The length of the Taylor bubble formed is dependent upon the flow rate of the gas which is injected into the pipe. A higher injection flow rate was observed to produce Taylor bubbles of greater length. During a period of continuous flow, the bubble will rise at a rate governed by both the flow rate of the gas being injected and the force of buoyancy. When the injection is curtailed by the closure of the mains valve, the Taylor bubble will rise due to buoyancy alone. The rate of this rise is determined by its Froude number, which can be estimated from empirical correlations (Viana et al., 2003).

Due to the use of a faulty rotameter, the accurate measurement of the quantity and flow

rate of the air injected was not possible. Varying the aperture of the individual gas supply valves affects the flow rate at which the gas enters the pipe, which in turn affects the length of bubble. For this reason to reproduce experiments with bubbles of approximately equal size, the aperture of these valves was kept constant. To assist the reproducibility of the air flow injected, alignment markers were introduced to the regulating valve wheel. The volume of gas injected was controlled by manual adjustment of the mains valve. When the nose of the bubble passed a level marker located approximately 1.3 m above the base of the pipe, the mains valve was closed and the bubble allowed to rise under buoyancy alone. From an analysis of the results of these preliminary experiments, it was concluded that the use of two of the five inlet valves would allow the introduction of reproducible Taylor bubbles of lengths up to 0.7 m dependent on the aperture of the valve. The use of this manual method influences the reliability of the length of the bubble produced, and so for each experimental run the length of the bubble had to be recorded.

When the mains valve is rapidly rather than smoothly closed, the rise of the resultant Taylor bubble is observed to be unsteady rather than smooth. In particular, the length of the bubble is observed to oscillate from the nose forward, whilst the upward motion of the tail remains steady. An example of this oscillatory bubble behaviour may be observed from an analysis of the images presented in Figure 4.9, which show a series of still frames extracted at regular time intervals from a video recording of an experiment taken with the Sanyo camera. The oscillation observed at the nose of the rising bubble causes the surface of the water at the top of the pipe to oscillate. Thus, the frequency and amplitude of oscillation of the rising bubble may be estimated by measuring the oscillatory behaviour of the surface of the water at the top of the pipe. These oscillations reduced in amplitude and were no longer noticeable when the mains valve was closed smoothly. The mains valve is closed smoothly in the following experiments unless specified otherwise.

In addition to this, when introducing the first bubble in a set of experiments, a resetting procedure must first be completed. The two regulation valves that were to be used in the

experiment to introduce air to the pipe were initially opened by a quarter turn and the mains valve was then fully opened for a period of five to ten seconds. This procedure was required as the first bubble released was observed to be much smaller and less consistent than all following bubbles in preliminary experiments. This could have been due to a leakage of air and subsequent loss of pressure maintained between the mains valve and the regulation valves.

4.3 Stability of Taylor bubbles

4.3.1 Experimental Design

The first experimental objective stated in Section 4.2.1 was to confirm that stable Taylor bubbles could be produced in a pipe of diameter 0.29 m.

Initial studies had confirmed that given a quiescent fluid, stable Taylor bubbles could be formed. However, if a second bubble was then introduced to the pipe in the wake of the preceding bubble, or into the de-aerated fluid following the wake, the following Taylor bubbles were observed to break up as they rose through the pipe. Bubble break is reported to be due to the growth of an instability past a critical size before it is washed into the film surrounding the bubble (Batchelor, 1987). These instabilities on the surface of the bubble may be caused by turbulent eddies present in the surrounding fluid which is not completely quiescent. A break of a bubble was defined in this study to be one that splits any part of bubble from the main mass of the bubble. An example of a bubble break is illustrated in Figure 4.6.

The length of the Taylor bubbles was to be recorded. However, many of the bubbles were observed to break up in the section of the pipe in which the length of the bubble is recorded. Consequently, as the length of bubble could not be accurately determined it was not measured for this set of experiments. Bubbles were injected in a manner that, were it not for break up, would have led to a bubble whose length was approximately 0.45 m had it been stable.

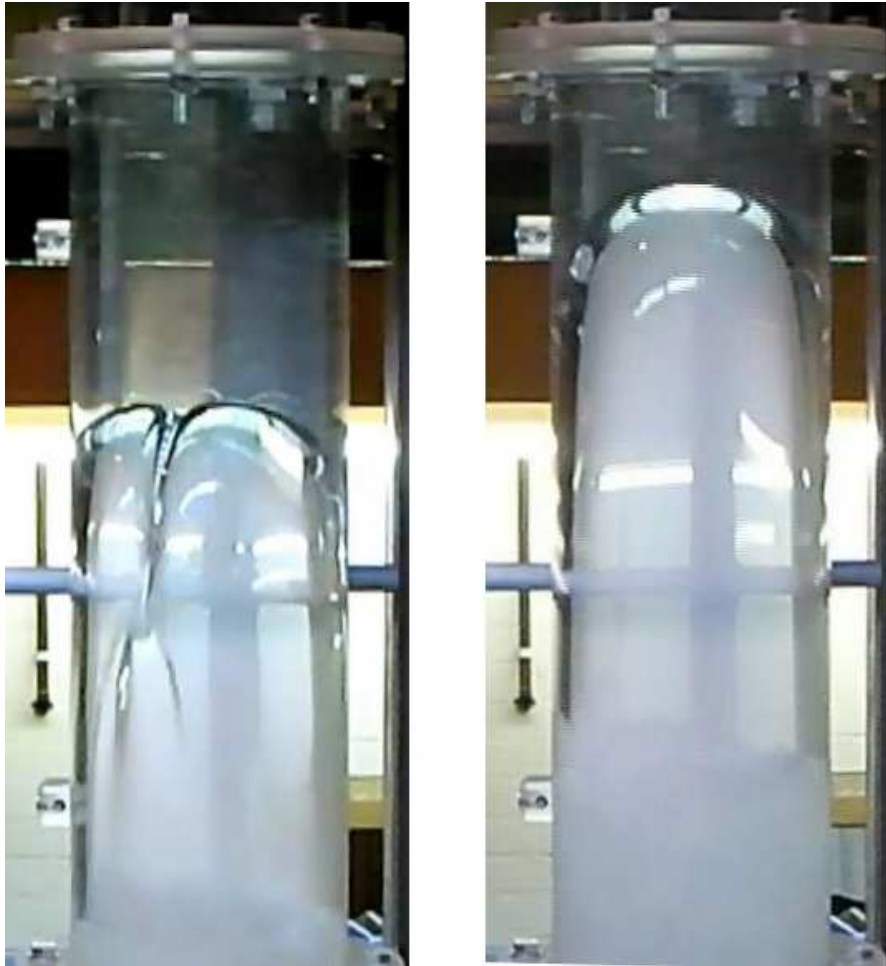


Figure 4.6: Two examples of still frames taken from the Sanyo camera showing two Taylor bubbles, the left bubble is undergoing a break while the right bubble is rising smoothly. The instability causing the bubble on the left to break up is the result of the fluid not being completely quiescent before the bubble was released.

To determine the likelihood of bubble break the following procedure was adopted. Once the bubbly wake trailing a rising Taylor bubble was observed to pass a level marker approximately 4.8 m from the base of the pipe, a set period of time was allowed to elapse before the release of the next bubble. This time period was measured using a stopwatch and so is accurate (both at the start and the end of measurement) only to the reaction time of the user. A conservative estimate for the error introduced to the measured time would be ± 1 s. The stability of the bubble was determined over a test section of 2 m of pipe from 3.3 m to 5.3 m from the base. Below this lower height, the bubble may still be developing from the initial formation, and above this upper height was not directly viewable from the second level. As the bubble ascended through this test section, the stability of the Taylor bubble was recorded. This length of time was varied in order to ascertain the length of time required for the water to return to a quiescent state.

4.3.2 Results and Discussion

These experiments were repeated twenty times for each time period. From an analysis of the results of these studies, a function of the probability of the stability of the bubble at each time period was determined, which is plotted in Figure 4.7. For a settling period of 120 s, all of the observed rising bubbles were determined to be stable. The settling period was then reduced to determine the length of time at which bubbles would become unstable. The results of this showed that there is no critical value for the settling period. Instead, there is a steady drop off over a period of approximately 50 s in which the bubbles transition from being almost certainly stable to certainly unstable. The probabilistic nature of this transition is due to the chaotic nature of the decaying turbulent eddies which trigger break up. In addition to this, due to the experimental methodology each bubble released was of slightly different length, as was the volume of the bubbly wake behind it, causing further differences between runs.

The vertical error bars on Figure 4.7 are calculated by assuming a binomial distribution to

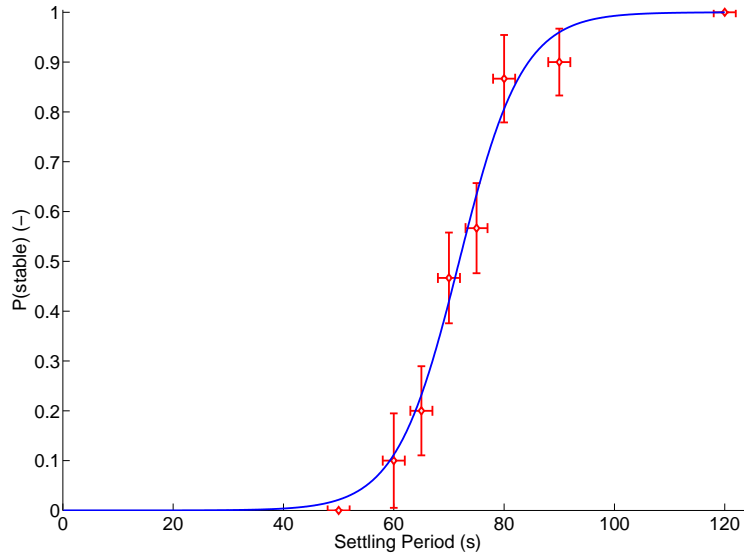


Figure 4.7: The probability of a Taylor bubble breaking up within a 2 m observation window in the 0.29 m pipe. If the settling period is below 50 s, all bubbles will break up. If the settling period is longer than 120 s all bubbles observed will rise in a stable manner. Between these values the bubble will break up with decreasing likelihood as the settling period increases from 50 s to 120 s.

the data's repeated runs and represent one standard deviation. This accounts for the error due to having a finite number of experimental runs at each settling time and could hence be reduced by conducting more experimental runs. The horizontal errors represent the error introduced by the measurement of the settling time. This is estimated from the error due to the reaction time of the user at both the start and end of the measurement period along with the uncertainty in the start time. The settling time is defined as the time from which the bubbly wake leaves the test section to when the next bubble is released.

As the bubble was consistently stable at settling times of over 120 s, it was concluded that given a quiescent liquid, Taylor bubbles are stable within the 0.29 m pipe. This conclusion

is consistent with the theoretical prediction of Batchelor (1987), which concluded that Taylor bubbles in pipes with a diameter of less than 0.46 m will be stable. This delay time was applied between the execution of all further experiments.

4.4 Rise velocity of Taylor bubbles

4.4.1 Experimental Design

Given that stable Taylor bubbles were shown to exist in the experimental apparatus, a further set of experiments was designed to characterise the behaviour of these Taylor bubbles. One key characteristic of Taylor bubbles is their rise velocity, governed by the Froude number, and so this was investigated.

In these experiments the water in the pipe was left to settle for a period of time (120 s, determined from the results of the stability experiments) so that the fluid could be assumed quiescent. When the top surface of the liquid is open to the atmosphere, bubble rise velocity is known to vary with bubble length (White and Beardmore, 1962), hence bubble length was recorded in these experiments. Figure 4.5 shows a still photograph extracted from a video recording using the Sanyo camera that record the rise of a typical Taylor bubble in the 0.29 m diameter pipe. From an analysis of this image, it may be concluded that the tail of the Taylor bubble under these flow conditions is not well defined. Consequently, it was necessary to estimate the location of the tail to determine the length of the bubble. It was concluded that the use of this method introduces an error of ± 0.025 m to the estimation of the bubble length. A measurement error is also introduced on conversion of the still images from video recordings from pixels to meters. However, this error is much smaller than that accrued by the estimation of the tail length of the bubble. The average velocity of the bubble is determined from an analysis of the consequent still frames recorded by the high speed camera and mirror arrangement, described in

Section 4.1.1. An analysis of these images allows the determination of the time taken for the nose of the bubble to rise between two markers along the length the pipe, spaced 1.44 m vertically apart.

To determine the rise velocity of a single Taylor bubbles in this apparatus, measurements of 54 bubbles were taken with the high speed camera and mirror system. As the nose of the bubble passed level markers on the pipe, the corresponding times were recorded and the rise velocity calculated from these values and the measured distance between the markers.

4.4.2 Results and Discussion

If the top surface of the liquid is open to the atmosphere, a Taylor bubble will expand as it rises. This expansion will cause an increase in velocity of the nose of the bubble, and hence in the liquid directly above the bubble (Santos et al., 2008; Sousa et al., 2006). The rise rate of the nose of the bubble is hence given as

$$U = U_b + \dot{L}, \quad (4.1)$$

where U_b is the rise rate of a non-expanding bubble and L is the bubble's length. If the bubble expands as an ideal gas, it can be concluded that

$$\dot{L} \propto L/H, \quad (4.2)$$

where H is the depth of the bubble below the surface (White and Beardmore, 1962; Pringle et al., 2014). As discussed in Section 4.2 the tail of the bubble can be ambiguous and hence was not used for measurement.

As the rise velocity of the bubble varies with bubble length, a number of different length bubbles were investigated to determine an expression for the non-dimensional rise velocity. The measurement error of the distance between the two markers on the pipe is ± 0.002 m ($\pm 0.14\%$). Images were recorded by the Phantom camera at a frame rate of 100 fps, giving a temporal

measurement error of ± 0.01 s on the time taken for the bubble to rise between the markers. The time taken for a Taylor bubble to rise between the markers was typically approximately 2.45 s, which would give the error at $\pm 0.4\%$. The propagated errors are then calculated individually. As previously described, the length of the Taylor bubbles was determined using a video camera focused on a section of the pipe between 3.5 and 4.5 m from the base of the pipe. This method of estimating the length of the Taylor bubbles introduced an error of ± 0.025 m.

Froude numbers for 54 bubbles of varying lengths were calculated using this methodology. Considering the measurement of bubble length was accurate only to ± 0.025 m, it was decided to group and average the repeated results for each length. These averaged results are shown in Figure 4.8. As expected from the theoretical work of White and Beardmore (1962), the rise rate of the bubbles varies linearly with bubble length. Extrapolating the data to a theoretical bubble of zero length gives the rise rate of bubble rising without the effect of expansion. This corresponds to a Froude number of 0.342, consistent with the published experimental and theoretical values (Dumitrescu, 1943; Taylor and Davies, 1950; Viana et al., 2003).

The rise velocity of the bubbly wake was also measured for a number of runs. This was observed to have a slower rise velocity than that recorded for the Taylor bubble (approximately 0.21 ms^{-1} as opposed to approximately 0.6 ms^{-1} for the bubbles). These rise speeds were estimated by determining the rise speed of the tail of the wake using the same method as was used to determine the rise speed of the nose Taylor bubble, but with measurements taken from the lowest point of the bubbly wake as opposed to the nose of the bubble.

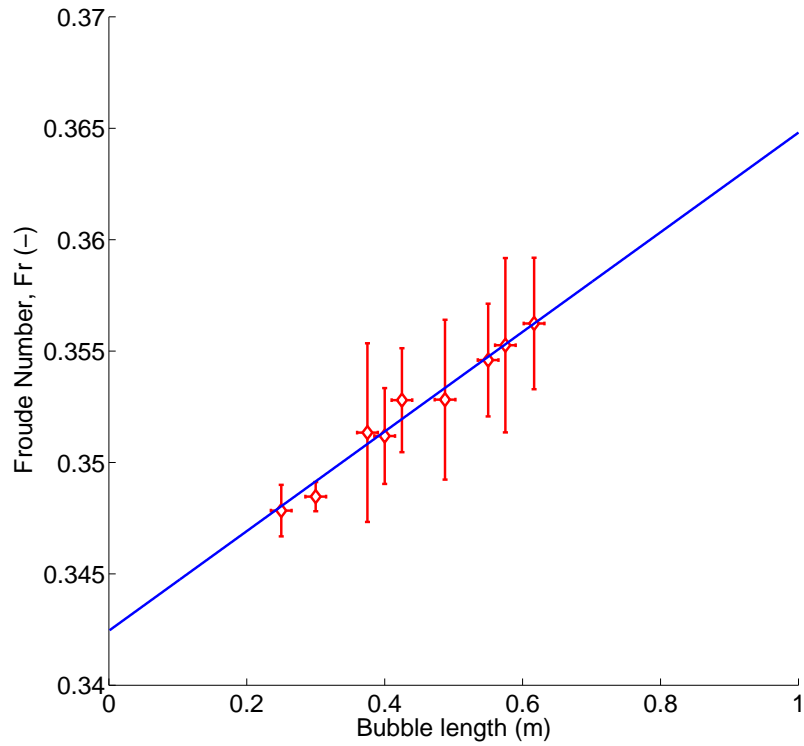


Figure 4.8: The Froude numbers of the observed Taylor bubbles in the 0.29 m pipe varying with bubble length. The Froude numbers increase with increasing bubble length due to the effect of the bubble expanding as it rises.

4.5 Oscillatory behaviour

4.5.1 Experimental design

Behaviour similar to the oscillatory behaviour observed in Section 4.2.2.2 has been discussed previously in the literature (James et al., 2004; Vergnolle et al., 1996). Vergnolle et al. (1996) proposed a model to replicate the oscillation of a volume of gas compressed by a denser fluid above it. This model was proposed to explain observed field readings of the pressure oscillations thought to be caused by a rising Taylor bubble in a volcanic conduit. James et al. (2004) observed pressure oscillations when studying the rise of a Taylor bubble in a pipe of diameter 0.038 m. However, no physical oscillation of bubble length or detectable oscillation of the top surface level was observed. In the present work, a further set of experiments were designed to investigate this phenomenon.

For these experiments the mains gas injection valve was shut quickly following the injection of a bubble, in contrast to the smooth valve shut off used during the previous sets of experiments. This abrupt valve closure was observed to initiate an oscillatory motion in the nose of the bubble. As the water is essentially incompressible, the oscillations induced in the bubble are transmitted through the liquid to the top surface, where they can be observed. The position of the surface will also undergo a mean rise due to the bubble expanding due to decompression as it ascends the pipe. These surface oscillations were recorded by a camera which was approximately level with the surface of the fluid (following the injection of a bubble). A constant depth of water in the pipe was maintained at the start of each experiment. Level markers were placed at intervals of 0.05 m along the vertical length of the pipe above a known height to provide a reference scale against which to determine the vertical height of the top level of the fluid. These markers were an average of 91 (± 2) pixels apart which results in each pixel representing 0.00055 (± 0.00001 m). The use of these images to determine the height of the fluid therefore introduces a measurement

error of approximately ± 0.00055 m.

For these experiments the recording frame rate of the Phantom Camera was set at 20 fps. Whilst this is sufficient to capture both the qualitative and quantitative frequency of the rising oscillating bubble with respect to time, the combination of the observational and the calculation errors introduced may be significant. It is recommended that to reduce these errors, a further series of experiments should be performed that employ a significantly increased number of recording frames per second. An additional potential source of error may have been introduced to the images recorded was the flicker frequency of the background laboratory strip lighting. As the lighting flicker frequency was determined as 50 Hz, a compromise video frame rate of 20 fps was selected. In recordings taken with frame rates significantly above this rate, the still images were too dark. It was not possible during the experimental programme to resource specialist lighting sources to minimise further the measured and observational errors.

From an analysis of the literature in Section 2.4 it was concluded that the frequency of oscillation of a Taylor bubble will theoretically vary with bubble length (Vergnolle et al., 1996). Consequently the experiments were designed to enable an estimation of the bubble length in order to test this hypothesis. The aforementioned uncertainty and error introduced to the measurement of bubble length is increased when one considers that the bubble also oscillates in length. To include this additional uncertainty, the bubbles were grouped into two average sizes, one at $0.45 \text{ m} \pm 0.05 \text{ m}$ and one at $0.55 \text{ m} \pm 0.05 \text{ m}$.

4.5.2 Results and Discussion

The location of the top surface of the fluid was tracked using the Phantom v9.1 high speed camera, along with video analysis software. An example of frames taken from the video showing the oscillation and rise of the top surface of the fluid is shown in Figure 4.9. The location of the surface from these video data were then plotted against time as shown in Figure 4.10. This

shows the oscillatory behaviour of the top surface, which reflects the behaviour of the bubble. The mean rise of the top surface can also be observed by an analysis of this figure. A predicted mean surface height is calculated assumed the bubble expands as an ideal gas and is also shown on this figure.

The peak values of these oscillations were used to estimate the frequency of oscillation. The frequency of the bubble oscillations were determined from the upper water surface height data using MATLAB. The maxima were extracted using the `findpeaks` function and frequencies are calculated from the inverse of the peak-to-peak time. The experimental results for the frequency of oscillation were compared to the theoretical proposed by Vergnolle et al. (1996) and Pringle et al. (2014). The predicted frequency from the Pringle model is

$$f = \frac{1}{2\pi} \sqrt{\frac{\gamma}{L} \left[g + \frac{P_{atm}}{\rho_L H_L} \right]}. \quad (4.3)$$

The experimental results compared to these models were averaged over a number of runs for two different length bubbles. The first set of ten bubbles had an average length of 0.45 ± 0.05 m as they passed through the measurement window, the second set of six bubbles had an average length of 0.55 ± 0.05 m. As described in Section 4.2, there are significant errors in both the estimation of bubble length and the process of measurement of the surface height. These factors introduce the resultant errors in the estimated frequency of oscillation.

Figure 4.11 shows a comparison of the experimental results plotted against the theoretical predictions of Pringle et al. (2014); Vergnolle et al. (1996). As the bubble ascends the pipe, the frequency of oscillation increases due to the decrease in mass of water above the bubble, which is confirmed by these results. The predicted model behaviour compares well to the experimental results whilst the bubble is far away from the surface. However as the bubble approaches the surface, the relative volumes of the fluid above the bubble and that going around the bubble's nose become comparable. The result of this is that the differences between the predicted model

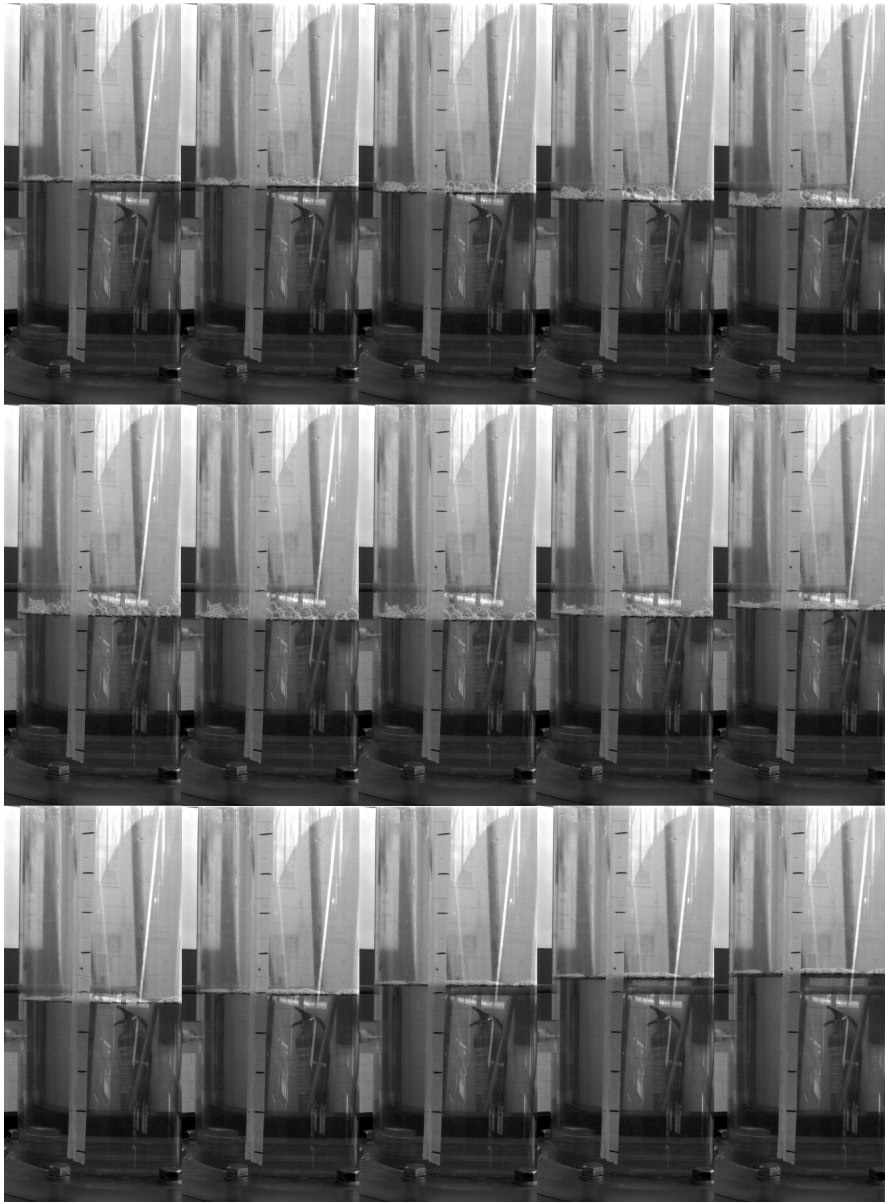


Figure 4.9: Read row by row from left to right. Still frames taken at 0.05 s intervals showing the variation in surface height. The surface level decreases on the first row, remains relatively constant on the second row and increases significantly on the third row.

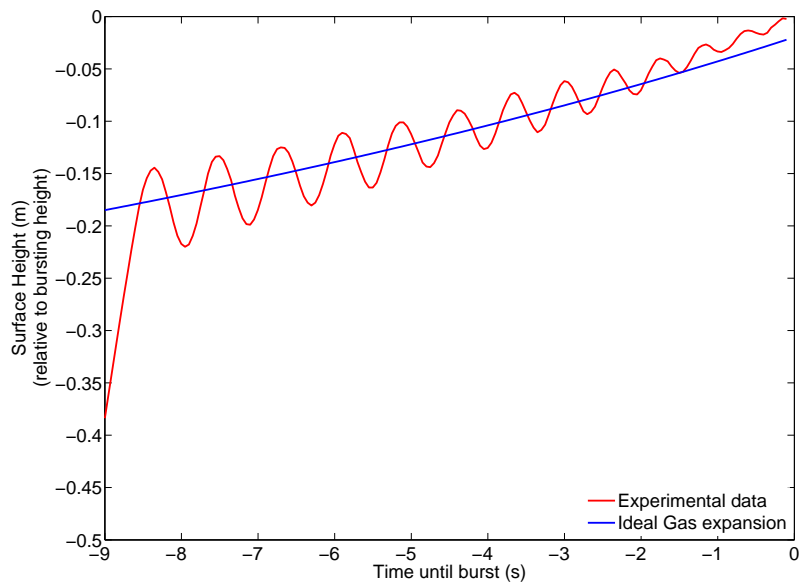


Figure 4.10: The evolution of the height of the water surface. The red line is taken from the rise of a bubble initially 0.55 m long. The green line shows the predicted mean surface rise and has been calculated by assuming the bubble expands as an ideal gas obeying $pV = nRT$. Time is measure from when the bubble bursts at the surface.

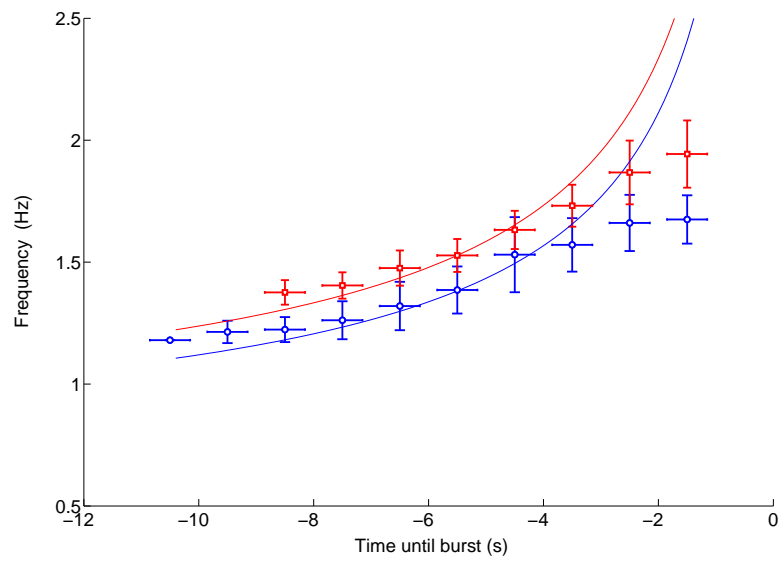


Figure 4.11: The frequency of oscillating bubbles as they rise up the pipe for two different mean lengths of bubble (blue is 0.55 m, red is 0.45 m). The points represent the average of experimental data taken from ten runs in the case of the longer bubble and six in the case of the shorter bubble. The lines come from the theoretical model of Pringle et al. (2014), where the polytropic exponent has been taken to be 1. Time is measured prior to the bubble bursting at the surface.

behaviour and the experimental results rapidly increases. In this figure, the time given is the time until the bubble bursts at the top surface of the liquid. The conclusion drawn from an analysis of the results of these experiments is that the observed oscillations in the rise rate of the Taylor bubbles are replicated by the theoretical models while the bubble is far from the surface. While signals from pressure transducer had previously suggested at this behaviour at smaller scales (James et al., 2004), oscillations of this kind had not been physically observed before. These results will provide experimental data to validate a base case of the simulations presented in Chapter 5.

4.6 Conclusions

From an analysis of the results of the experiments conducted in this chapter a number of conclusions may be drawn.

Firstly, Taylor bubbles rising in quiescent water, in a pipe of diameter 0.29 m, are inherently stable. This agrees with the theoretical work of Batchelor (1987) who predicts Taylor bubbles will be stable up to a maximum diameter of 0.46 m. Prior experimental work had never been conducted at this scale, although unpublished work of James et al. (2011) had suggested the existence of stable bubbles within a pipe of diameter 0.25 m. It was not possible to generate a further Taylor bubbles with a continuous flow of gas, due to the large instabilities introduced in the injection process and present in the wake of the preceding Taylor bubble. In order for the fluid in the pipe to be assumed to be quiescent, a settling period of 120 s needed to be left before the release of any further Taylor bubbles.

Taylor bubbles left to rise under the force of buoyancy (without a continuous flow of gas) would rise at a rate which is dependent on their length. This is expected due to surface of the liquid being open to the atmosphere and hence able to expand as it rises. The Froude numbers

determined for the bubbles compare well to those of previous experimental and theoretical studies (Taylor and Davies, 1950; Dumitrescu, 1943; Viana et al., 2003).

Given a sudden curtailment of the gas injection, oscillations were observed in both the rise rate of the surface of the liquid, and in the rise rate and length of the bubble. These oscillations display similar behaviour to that of a simple harmonic oscillator as in the models of Pringle et al. (2014); Vergniolle et al. (1996).

The results of these experiments will provide valuable experimental data with which to validate a base case of the simulations presented in Chapter 5.

Rise of Taylor bubbles in vertical pipes - Numerical

5.1 Introduction

The model introduced in Chapter 3.1 was adapted in order to model the experimental studies described in Chapter 4. These adaptations are required due to the scaling of the domain and are detailed in Section 5.1.1. Once verified and validated, as was demonstrated in Sections 3.3.2 and 3.3, using a numerical model may allow a greater scope in the parametric analyses that may be performed than in experiments. Studies which may not otherwise be feasible in the laboratory, such as a wide ranging variation of viscosity, are able to be performed with relative ease. In this example, many technical and logistical issues arise when attempting to vary viscosity in the experimental studies of Chapter 4.

Previous CFD studies have successfully reproduced the observed behaviour of single rising Taylor bubbles in pipes with diameter < 25 mm, as detailed in Section 2.3. It is widely accepted that surface tension forces do not have an effect on rise velocity when the Eotvos number is above a critical value of around 100, and hence surface tension is assumed to be negligible. However, with an increase of Eotvos number, CFD simulations using low viscosity fluids have been seen to show an increase in error of rise velocity with increasing pipe diameter (James et al., 2008).

This could be due to the more turbulent nature of the flow in these regimes, and the complexities involved in modelling this.

5.1.1 Adaptations to Numerical Model

In order to ensure that the scaling in domain size from the simulations presented in Chapter 3 does not affect the accuracy of solutions, a further set of verification studies were undertaken after a new mesh was created. This included a mesh independence study and a temporal independence study. As the flow in the wake of the bubble is observed to be turbulent from the experiments of Chapter 4, a turbulence model is included in the numerical model. Various turbulence models were assessed and the results were compared against those of the experimental studies in Chapter 4 to ascertain the optimal turbulence model for this study. This is detailed in Section 5.1.4.

The chosen numerical model was first validated against the experimental data and then a parametric study was completed. This included varying the initial conditions, such as the initial pressure of bubble, the length of the bubble, its starting depth and the fluid properties, such as viscosity, as well as testing the stability of the bubble over a range of conditions.

5.1.2 Domain and Mesh

A 3D CFD model was constructed in ANSYS FLUENT using a grid created in the meshing software ANSYS ICEM-CFD. The domain is a vertical cylinder of height 9.5 m and internal diameter 0.3 m, Figure 5.1a. The domain was subdivided into volume elements with a structured, O-Grid topology as shown in Figure 5.1b and described in detail in Section 3.3.1.2. This choice of meshing strategy permits the specification of a fine refinement close to the pipe walls whilst retaining a relatively coarse mesh near the centre of the pipe. This allows the model to more accurately capture the flow field behaviour in the thin liquid film between the gas bubble and the pipe wall that is present for Taylor bubbles rising in water.

A further series of verification studies to those in Section 3.3.2 were undertaken to evaluate the level of error introduced. To ensure minimal discretisation errors in the spatial domain, a grid convergence study was undertaken by using the Grid Convergence Index (GCI) method of Roache (1998). As detailed in Section 3.3.2, the GCI method uses a set of three grids, which decrease in average spacing, to estimate the value of a solution at a grid with zero spacing. An error can be calculated from the simulation results to estimate the zero spacing solution. Temporal convergence was computed in a similar manner, with the time-step value replacing mesh spacing. The rise velocity of the bubble was used to compare cases against each other. The application of the GCI method concluded the error introduced by spatial discretisation was found to be 0.411% for the fine grid. This had an average z grid spacing of 0.008 m, with a spacing at the wall of 0.0023 m rising to 0.014 m in the centre. These spacings correspond to 1175 cells in the z direction, and a with spacing of $D/129$ at the wall rising to approximately $D/21$ in the centre of the pipe. This method was also used to determine the error introduced by temporal discretisation. This gave an error of 0.175% away from the estimated zero time spacing solution with a time step of 0.0005 s. Simulations using this mesh took approximately 8 days

to complete on a compute node of a parallel cluster, using 2 x 4-core 2.3 GHz Opteron processors.

Figure 5.2 shows a plot of the mesh spacing size against the simulated rise speed of a fully developed Taylor bubble. An analysis of this figure concludes that the solution converges towards the zero spacing prediction with decreasing mesh spacing.

5.1.3 Initial and Boundary Conditions

In the base case simulation, the model pipe was initially filled with water to a depth of 5 m with 4.5 m of air above this. A bubble of air was then introduced close to the base of the pipe by specifying the volume fraction of air to be unity in an appropriate region. This process will be referred to as “patching” the bubble into the domain. The initial size and shape of the bubble was varied to represent the range of different laboratory experiments performed. Typically the bubbles initial shape is that of a hemisphere attached to a cylinder (Taha and Cui, 2004; James et al., 2008) both of whose radii were 0.14 m. This can be observed in Figure 5.3a.

This method of introducing the air phase is clearly significantly different to the formation of the bubble in the experimental studies presented in Chapter 4. As described in Section 4.1.1, air is introduced to the pipe through a series of twenty-five 5 mm nozzles at the base of the pipe. Many small bubbles are generated during the formation of the bubble, which coalesce to form a Taylor bubble in a turbulent mixing zone within 1.5 m from the base of the pipe. Many of these small bubbles are left behind and do not join with the main bubble, but instead form part of the wake behind it. These small bubbles at the base of the pipe and in the wake are estimated to have a diameter of approximately 5 mm, and so are could not be resolved in the numerical model without an extremely refined mesh. Grid spacings of under 2 mm would be required throughout the domain in order to resolve these bubbles. This would give a conservative estimate of 3000 cells in each cross section in the z direction, giving a total domain of over 15 million cells. With a

Table 5.1: Flow conditions of the base case simulation.

\mathbf{Re}_B	\mathbf{Fr}	\mathbf{Eo}	\mathbf{M}
5.1×10^5	0.351	1.2×10^4	2.4×10^{-11}

mesh this refined, the time-step would also need to be significantly reduced in order to maintain the same Courant number, as described in Section 3.3.1.2. This would result in the overall computational time increasing dramatically and hence it was not feasible in the scope of this thesis to conduct such a simulation.

The hydrostatic pressure value at the height of the nose of the bubble was set as a constant value that defined the pressure throughout the bubble. An example of the initial conditions after the first time step are shown in Figures 5.3a and 5.3b. Figure 5.3b shows the gauge pressure (pressure above atmospheric) in the domain. The reference pressure was set as atmospheric pressure (101325 Pa) and was specified at a location which was always within the gas phase above the upper liquid surface ($z = 9$ m).

These initial conditions for the base case scenario give the flow conditions as detailed in Table 5.1. Note here that the Froude number is the expected value from the experimental work of Chapter 4.

5.1.4 Turbulence model

As shown in Table 5.1 there is a high buoyancy Reynolds number associated with this flow regime. Both the flow in the thin film surrounding the bubble and in the wake trailing the bubble may be turbulent and hence a turbulence model should be applied to close the Reynolds Averaged Navier-Stokes equations, as detailed in Section 3.1.2. Due to its use in applications with jets, the realizable $k - \varepsilon$ was hypothesised to be the most suitable model for this study.

To confirm this hypothesis, the results produced by applying three different $k - \varepsilon$ models, the standard $k - \varepsilon$ (SKE) model, a Re-Normalized Group (RNG) model and the Realizable (RKE) model, were compared to the experimental results presented in Chapter 4. An analysis of the results of these simulations concluded that only the RKE model gave a “stable” Taylor bubble, with both the RNG and SKE models producing a bubble which broke up as it rose as well as giving a deformed nose shape which did not match the experimental observations. The SKE and RKE models both under-predicted the rise velocity of Taylor bubbles by approximately 15 % with a $Fr = 0.3$. However, the RNG model did produce a rise velocity slightly closer to the observed experimental value, giving a $Fr = 0.392$, which is approximately 12% over the experimental velocity. As the Realizable $k - \varepsilon$ model was the only of the three turbulence models to give a stable Taylor bubble comparable to those seen in the experiments, the hypothesis was confirmed and it was decided to use this model in all subsequent modelling.

A higher order turbulence model, the Reynolds Stress Model(RSM), was also tested and compared against the experimental results. This did result in a rise velocity slightly closer to the experimental value, giving $Fr = 0.31$, approximately 12% below the experimental value, whilst retaining the stability of the bubble. As previously described, the RSM model is a 7 equation model (in comparison to the 2 equation RKE model). The increased computational expense for this small increase in accuracy was not considered worthwhile. A full simulation - initialisation to bubble burst - would take on average twice as long to perform using a RSM model than a RKE model. This increase would mean a significant reduction in the amount of simulations that could be performed in the time-scale of the project and hence its use was discounted.

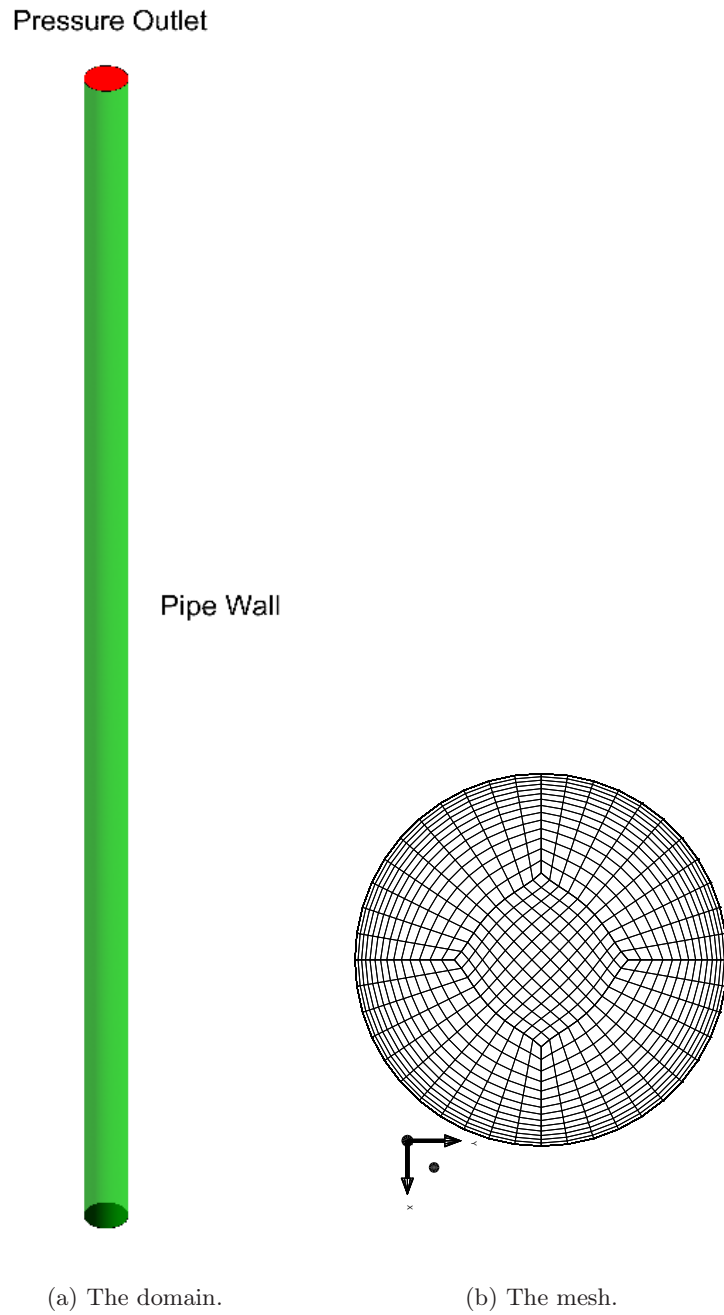


Figure 5.1: The numerical domain and the O-grid mesh used for simulations. The domain has a total height of 9.5 m and a diameter of 0.3 m. The mesh has a spacing of 0.0023 m at the wall rising to 0.014 m at the centre. The mesh is uniform in the vertical, z , direction.

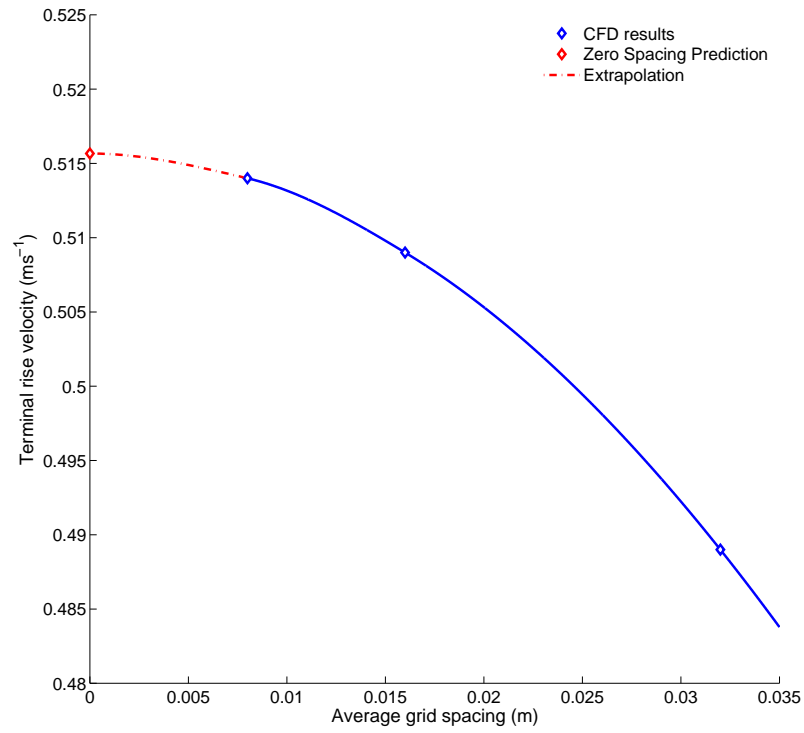
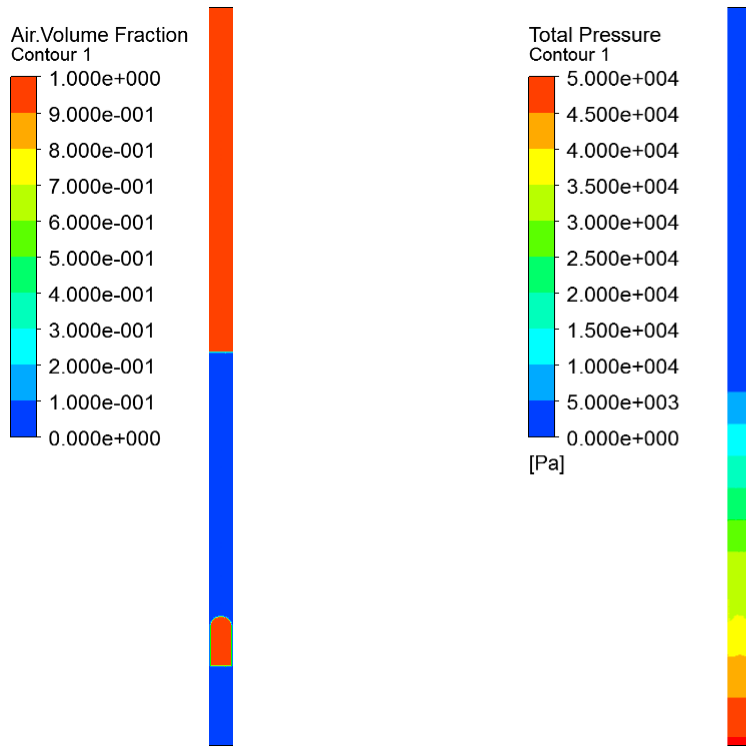


Figure 5.2: Diagram showing the independence of the grid sizing in relation to rise velocity using the GCI method. From this it was concluded that the error introduced by spatial discretisation was 0.411% for the fine grid.



(a) Contour plot of initial volume fraction, air is red and liquid is blue. (b) Contour plot of initial gauge pressure after a hydrostatic distribution has been specified.

Figure 5.3: Initial conditions imposed on the numerical domain.

5.2 Results

5.2.1 Bubble Rise and Oscillation

In the base case, the Taylor bubble is initialised with a pressure equal to the hydrostatic pressure at its nose. These are the conditions used to model to a slow injection of gas at the base of the pipe in the experiment, followed by a very gradual shut off of the delivery valve. In the experimental study detailed in Chapter 4 this produced a Taylor bubble that was not observed to oscillate during its ascent. The CFD model of this case replicates the expected behaviour – a stable rising Taylor bubble is produced, the top liquid surface rises at a constant rate until there is a rapid expansion of the bubble observed as it approaches the atmospheric-liquid surface. This effect has been previously noted for Taylor bubbles in pipes of diameter 0.025 m in the experimental studies of James et al. (2008).

For an ideal gas where temperature change is assumed to be negligible, the condition

$$p_1 V_1 = p_2 V_2, \tag{5.1}$$

holds where p is the pressure of the bubble and V is the volume of the bubble in state 1, its initial condition, and state 2 applies to it when close to the surface of the water. Given an initial hydrostatic pressure distribution, for a bubble of initial volume 0.365 m^3 , with its nose at a depth of 3.36 m, the surface will rise by 0.168 m due to expansion of the bubble. This closely matches the observed upper fluid surface rise from simulation, 0.17 m, as seen in Figure 5.4. As the pressure is specified at the nose of the bubble, this is slightly below the average pressure in the bubble. This is due to the presence of a small pressure difference in the nose region of the bubble above the thin film. This causes a small initial under pressure which results in the oscillations observed. These results are also observed for an initial depth of 4.36 m, where a surface rise of 0.218 m is expected, with simulations giving a value of 0.24 m. As the bubble

rises, it is observed to expand; however, as it sheds smaller bubbles from its tail its length remains approximately constant to within 5%. The upper liquid surface level is tracked in the simulation by a User Defined Function (UDF) that determines the maximum level of the water surface at each time-step.

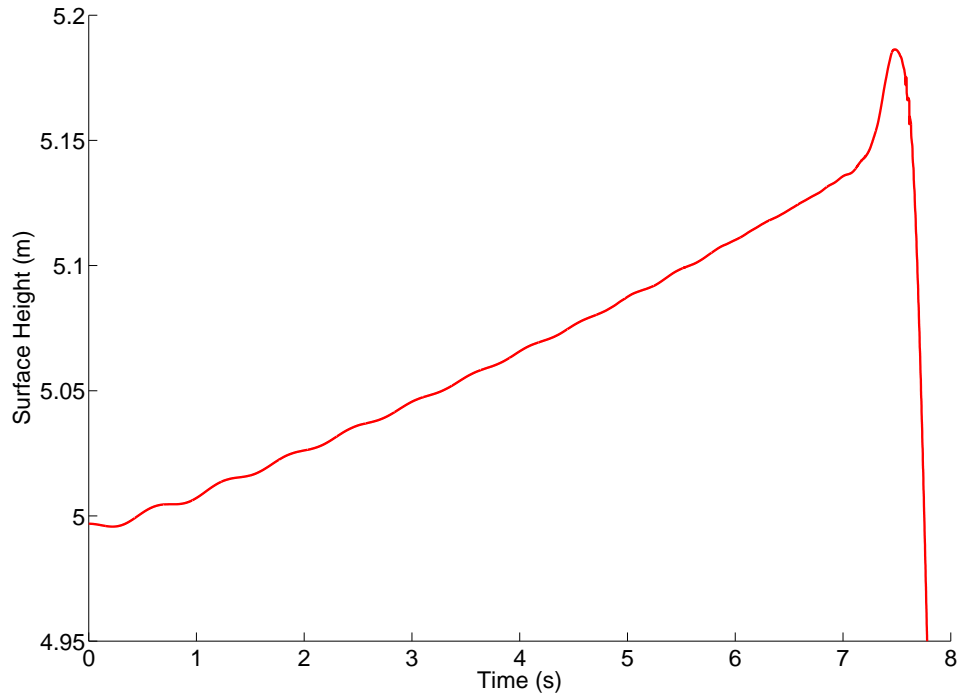


Figure 5.4: Simulated upper liquid surface rise given an initial hydrostatic pressure distribution for a Taylor bubble of length 0.64 m in a vertical, cylindrical pipe of diameter 0.3 m initially filled with 5 m of water.

There follows a brief description of the UDF, which is applied at the end of each time step. The code can be found in Appendix A. In this UDF the “fill height” is defined as the maximum vertical height of the upper liquid surface.

1. Set an initial fill height of zero and initialise the variables to be used.

2. Identify cells which have at least one adjacent cell with a volume fraction above 0.5.¹
3. Calculate the fill height of the cell, the maximum height of fluid in a cell as demonstrated in Figure 5.5 using the z coordinates of the base and top of the cell, and the volume fraction, α .
4. If this fill height, $z_{fill} = z_{min} + \alpha(z_{max} - z_{min})$, is larger than the previous maximum fill height, store this value.
5. Step through all the cells in mesh, comparing the fill height value with the maximum fill height.
6. If running the simulation in parallel, it is necessary to find the maximum fill height over all of the nodes over which the domain is partitioned.
7. Write the maximum fill height for this time value to a specified file.

Due to the observed oscillatory behaviour of the bubble rise, a continuous tracking of the bubble position is required to compute rise velocity accurately. Theoretical predictions and experimental results suggested a non-dimensional rise rate of between $Fr = 0.34 - 0.35$. However, the base case CFD model simulation computed a lower rise velocity of $Fr \approx 0.29$. At higher Froude numbers, previous CFD studies have also displayed a similar under-prediction of the rise velocity (James et al., 2008). Measurements were taken at the nose of the bubble, as the position of the base is difficult to track continuously due to the shedding of smaller bubbles. Estimates of this base velocity have been recorded and are comparable to the nose velocity, with the exception of the rapid expansion region at the liquid surface. Measurements were taken at the nose of the bubble, as the position of the base is difficult to track continuously due to

¹This is necessary because above the top surface of the water there are some cells with very small values of water volume fraction due to numerical errors which can give a false indication of the top surface.

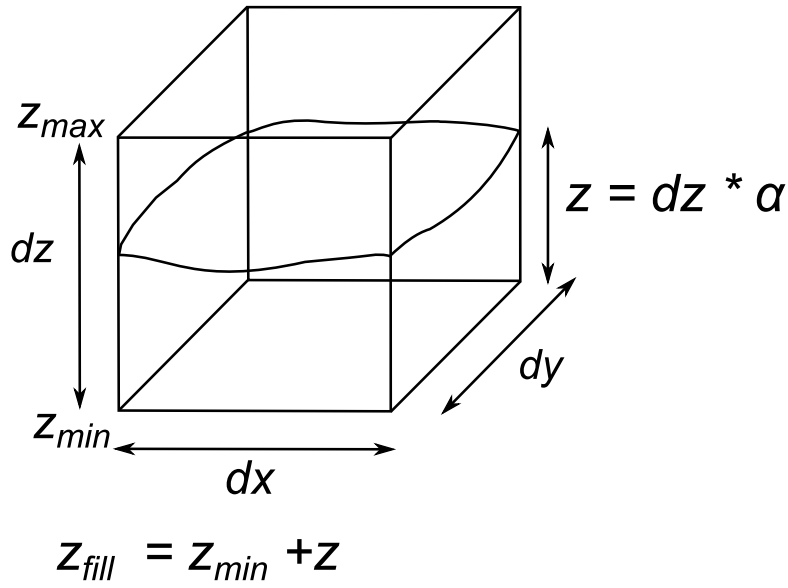


Figure 5.5: Diagram showing the determination of the fill height in the User Defined Function.

the shedding of smaller bubbles. Estimates of this base velocity have been recorded and are comparable to the nose velocity, with the exception of the rapid expansion region at the liquid surface.

Figure 5.6 shows a bubble mid-way through the rise given base case conditions, along with images showing the turbulent flow properties in the region around the bubble, turbulent kinetic energy, k , turbulent eddy dissipation, ε and eddy viscosity, μ_T . As can be observed from these images, k and ε are largest at the tail of the Taylor bubble where small bubbles are shed.

5.2.2 Pressure Oscillations

The gauge pressure is recorded in the simulations using a monitor located at a height of $z_0 = 1.5$ m at a cell next to the wall of the pipe. The oscillations in pressure at this location are correlated to the top surface oscillations, with the pressure inside the gas bubble being at a maximum when the upper air–water surface is at its lowest level. This is due to the compression of the bubble

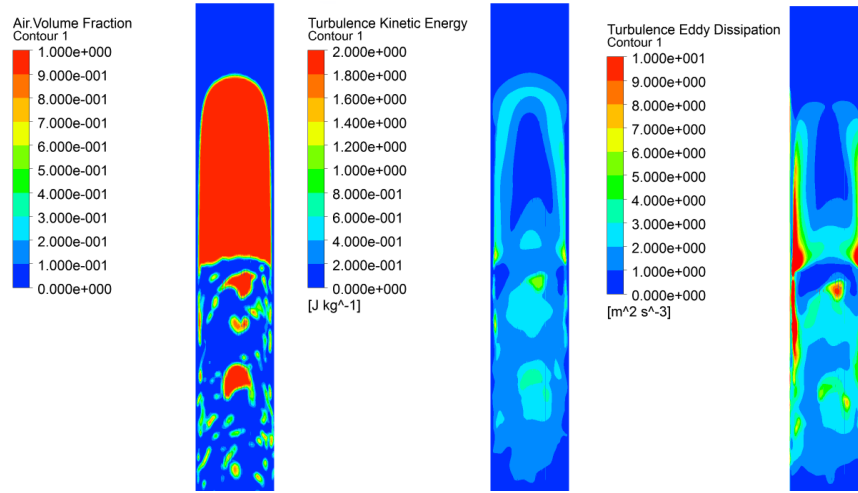


Figure 5.6: Images showing, top left, a bubble mid-way through the rise given base case conditions, centre, the turbulent the turbulent kinetic energy, k , in the area surrounding the bubble at the same time, and right, the turbulent eddy dissipation, ε .

which increases the pressure inside it, which in turn increases the pressure within the adjacent thin liquid film and hence at the wall of the pipe. An example of this is shown in Figure 5.7 for an initial quiescent water level of 5 m with an initial bubble overpressure of 20 kPa. In this simulation, the pressure has been shown to oscillate around a value of approximately 30 kPa gauge pressure, which matches the hydrostatic value of $\rho g(z - z_o)$ where z is the height of water above the base.

5.2.3 Variation of Initial Pressure

Experimentally, the initial pressure field defined on the creation of the initial gas bubble is influenced by the method used to turn off of the air injection tap which may result in the onset of the oscillations, as described in Section 4.5. Using the numerical model, a sensitivity analysis was carried out to determine the effects of varying the initial pressure condition. For example, the specification of an initial pressure inside the bubble which is above hydrostatic means that

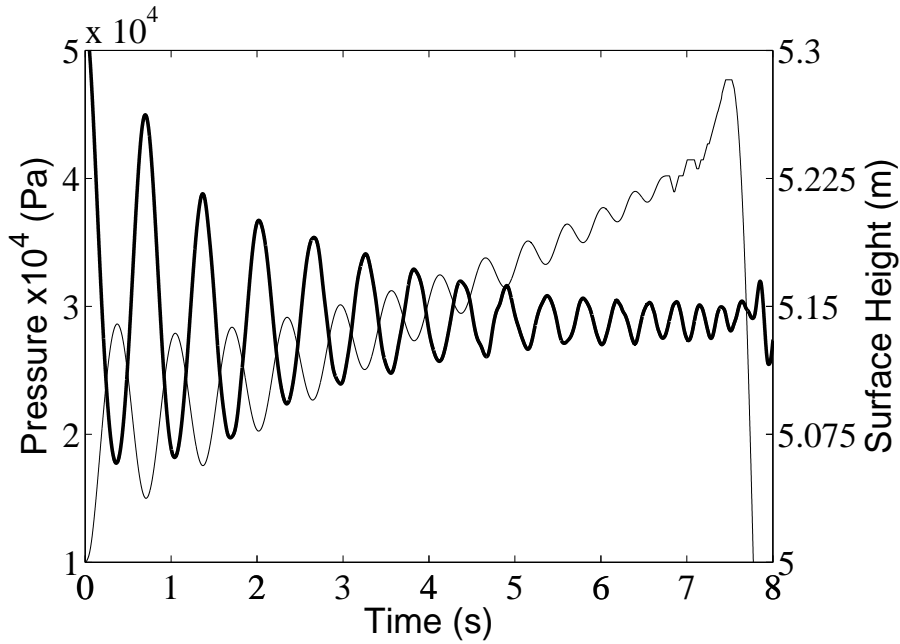


Figure 5.7: Comparison between pressure oscillations and surface oscillations with an initial over pressure of 20 kPa. The pressure is indicated by the heavy line and the location of the surface by the lighter line. The maximum pressure in the fluid corresponds to the minimum surface height, and hence the maximum compression of the bubble.

the bubble is effectively initially compressed, and so it will then expand before contracting again and so on. The expansions and contractions are damped because of the decreasing height of water above the bubble. Conversely, the setting of an initial pressure below hydrostatic means that the bubble is larger than the size it would be at hydrostatic pressure and will hence tend to compress. The magnitude of the difference in the pressure from the hydrostatic pressure at the nose of the bubble is one factor that will determine the amplitude of the resultant oscillations.

A constant initial bubble size and position (a length of 0.64 m with the nose at $z = 1.64$ m)

and a depth of water 5 m were used in this part of the investigation.

For an initial disturbance created by a similar magnitude over- or under-pressure, the resulting oscillations were initially found to be approximately equal in amplitude, at approximately 0.05 m for ± 10 kPa disturbances, 0.1 m for ± 20 kPa disturbances, and 0.15 m for ± 30 kPa disturbances, shown in Figure 5.8. However, due to the different compression/expansion regimes, the bubbles are observed to be out of phase with each other. Thus, the bubbles will have different sizes at different depths below the surface, which in turn alters the dynamics of the bubble and thus only a qualitative match in behaviour is seen.

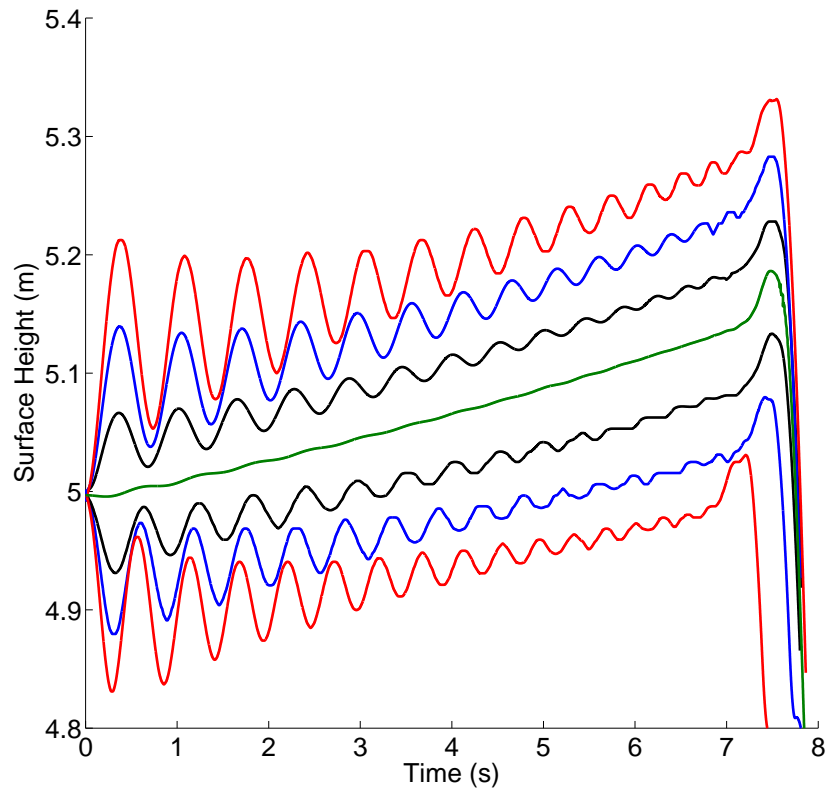


Figure 5.8: Variation of water surface height with time for various initial pressures in the bubble, ranging from a 30 kPa under pressure, shown by the lowest line, to a 30 kPa over pressure, indicated by the highest line, in increments of 10 kPa.

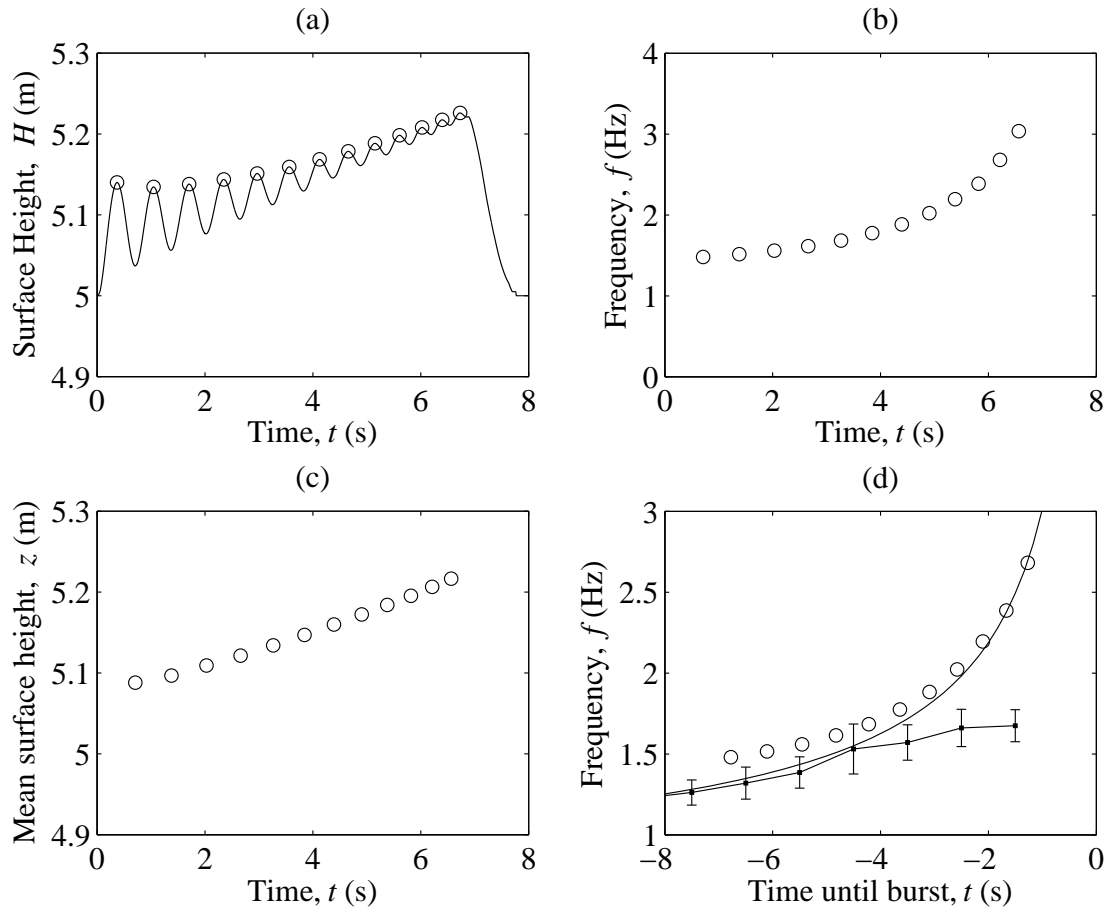


Figure 5.9: (a) Surface height plot with peaks highlighted, (b) frequency of surface oscillations, (c) mean surface height and (d) comparison against experimental data from Chapter 4, (straight lines with error bars), and model (Vergniolle et al., 1996), (smooth curve) and current simulation a 0.64 m long bubble, (circles).

In Figure 5.8, the 30 kPa under-pressure bubble is observed to burst slightly earlier than the other cases. This is due to bubble splitting into two parts which results in an acceleration in the first 0.5 s of the simulation. The bubbles are then observed to have reformed into a full Taylor bubble by 1 s and to follow the same rise rate as the other cases, and does not break up, for the remainder of its rise. The frequency of the oscillation determined for the reformed bubble does not appear to be significantly to be altered by this initial breakage and recombination phase. This is the only case for which an instability (due to the under-pressure) causes the bubble to break. Incidentally, had such behaviour been observed in the initial stages of bubble rise in the experimental study, the bubble would have been regarded as stable. However, such a large under-pressure would not be seen in the experimental studies

The frequency of the bubble oscillations were determined from the upper water surface height data using MATLAB, as described in Section 4.5 (Figure 5.9(a)). These heights were then compared against the experimental measurements from Chapter 4 and the theoretical model predictions of Pringle et al. (2014). The mean surface height was also estimated as the average height between a peak the following trough. The frequency of oscillation of the simulated Taylor bubbles is typically 10% larger than the mean value of a similarly sized experimental bubble throughout the rise, as seen in Figure 5.9(d). However, the upper limit of the standard error from the experimental measurements means that the numerical predictions fall within this error bound. The numerical error increases as the bubble approaches the surface of the liquid and is not within the error bounds for the final 3 s of the rise. This behaviour is similar to that produced by the models proposed by Pringle et al. (2014) and Vergnolle et al. (1996) which also become less accurate as the bubble approaches the water surface.

The frequency of the oscillations are observed to decrease by an average of approximately 1.5% with an increase in the initial bubble pressure of 10 kPa, as shown in Figure 5.10. It was postulated that this was due to the slight increase in the volume of the bubble produced by the

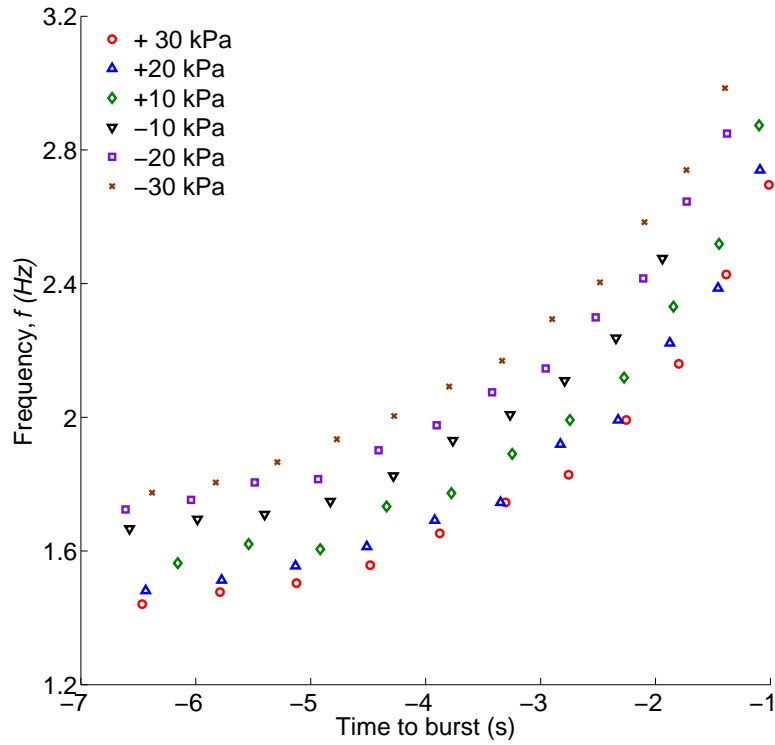


Figure 5.10: Variation in the frequency of the bubble oscillation with time for initial bubble pressures varying from -30 kPa to +30 kPa. Here the time is the time before the bubble breaks the top surface. This scale will hence be used and referred to as the “Time to burst”.

larger initial gas expansion. To test this hypothesis, the effect of bubble size on the frequency of oscillation was investigated.

5.2.4 Variation of bubble size

The initial length of the Taylor bubble in the simulation was varied across a range of values from 0.29 m to 1.04 m (1 D to 3.5 D). From the theoretical models Pringle et al. (2014); Vergniolle et al. (1996), it is predicted that shorter bubbles would oscillate at a higher frequency. Longer bubbles undergo a proportionally smaller change in volume when compressed. Consequently, the

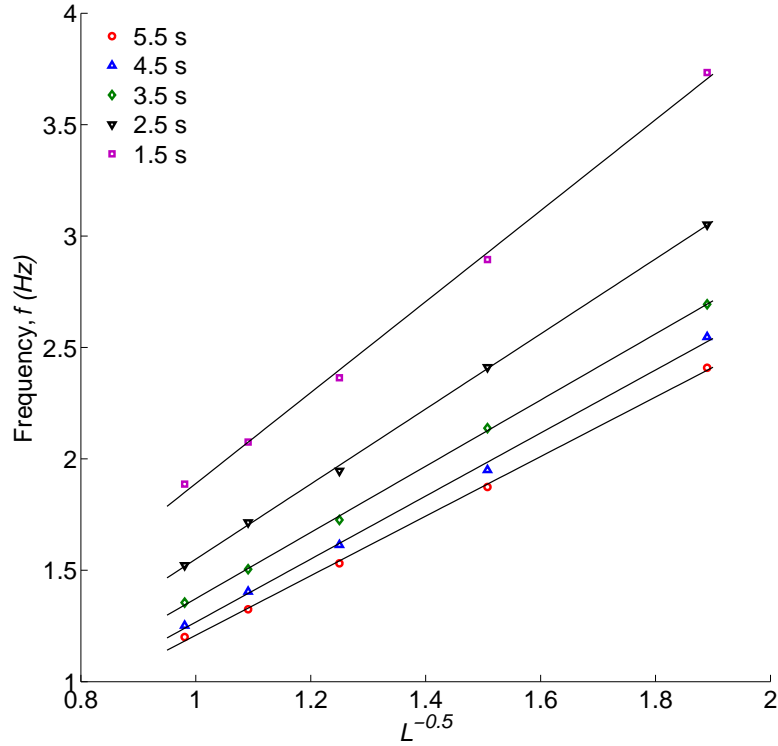


Figure 5.11: Frequency, f of the simulated surface oscillations plotted against $L^{-1/2}$ for bubbles of length, L , ranging from 0.28 m to 1.04 m. The lines correspond to various times to burst.

force required to cause this compression (or equally the force to oppose it) would therefore also be reduced. As the oscillation rate is governed by this force, larger bubbles would be expected to oscillate more slowly.

The theoretical models proposed by Pringle et al. (2014) and Vergnolle et al. (1996) predict that the frequency of bubble oscillation is proportional to $L^{-1/2}$, where L is bubble length. This trend was also observed in the experimental studies detailed in Chapter 4 – where only two bubble lengths were investigated. The simulations show good agreement with this behaviour, as observed in Figure 5.11, where the frequency, f , is plotted against $L^{-1/2}$ at set times in the rise of the bubble. To obtain the frequency at these times, data was interpolated linearly between

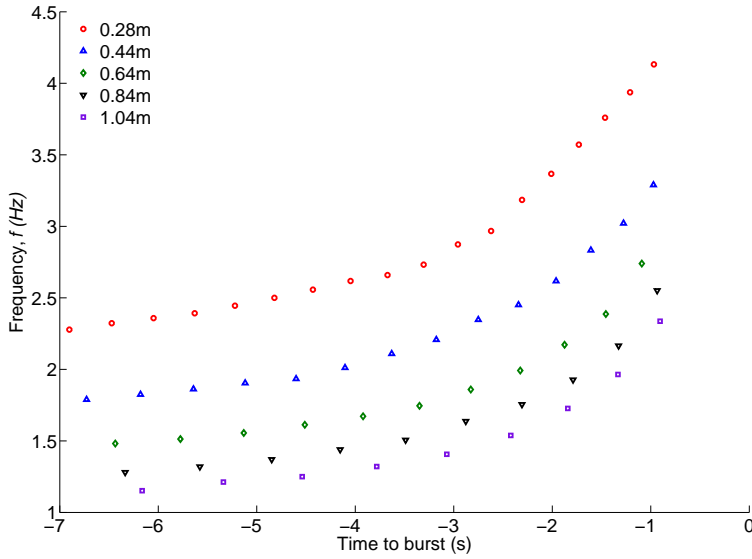


Figure 5.12: The variation in the simulated frequency of surface oscillations with time for 0.28, 0.44, 0.64, 0.84 and 1.04 m long bubbles.

the frequency values shown in Figure 5.12.

In Section 5.2.3, it was postulated that the variation in the frequency due to changes in the initial pressure was caused by the different lengths of the bubble created. The average lengths of the 30 kPa over- and under-pressure cases are 0.7 m and 0.44 m respectively, Figure 5.13. An analysis of the results of experimental studies have concluded that frequency is proportional to $L^{-1/2}$. Thus, given the frequency at one bubble length, the frequency of a different length of bubble may be estimated. Applying this principal to the 30 kPa bubble under pressure case, delivers a set of frequencies comparable to the 30 kPa over-pressure case, as shown in Figure 5.15. This shows that the change in frequency with initial bubble pressure is due to the initial bubble length. Further, it has been demonstrated that the simulation model is capable of modelling a range of bubble sizes and that any error introduced to the system does not affect the underlying physics relating to bubble size. Again, for a large variety of bubble lengths, stable bubbles were

able to be formed.

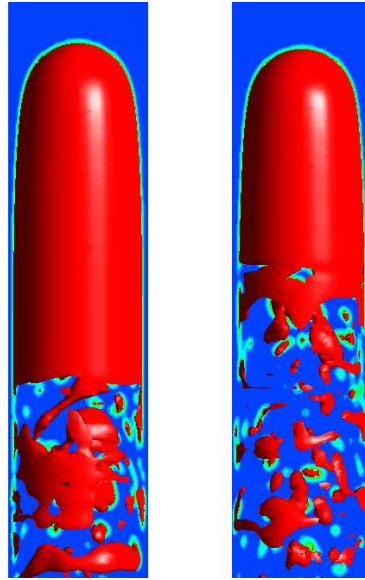


Figure 5.13: Taylor bubble with 30 kPa over pressure, left, and 30 kPa under pressure, right. A clear difference in size can be seen due to the initial expansion and compression of the bubbles. Again, the colour scale here shows the gas phase in red with the liquid phase as blue.

In Chapter 4, the effect of bubble length on rise velocity was discussed. It was concluded that the expansion of the bubble caused longer bubbles to rise with a greater velocity. Similar behaviour is also observed in the CFD results, shown in Figure 5.14, where an increase in bubble length is seen to result in an increase in Fr . An extrapolation of these results gives a prediction of the Fr of a bubble with zero length, of $Fr \approx 0.27$. This is an under prediction of approximately 18% of the Fr observed in the experimental studies.

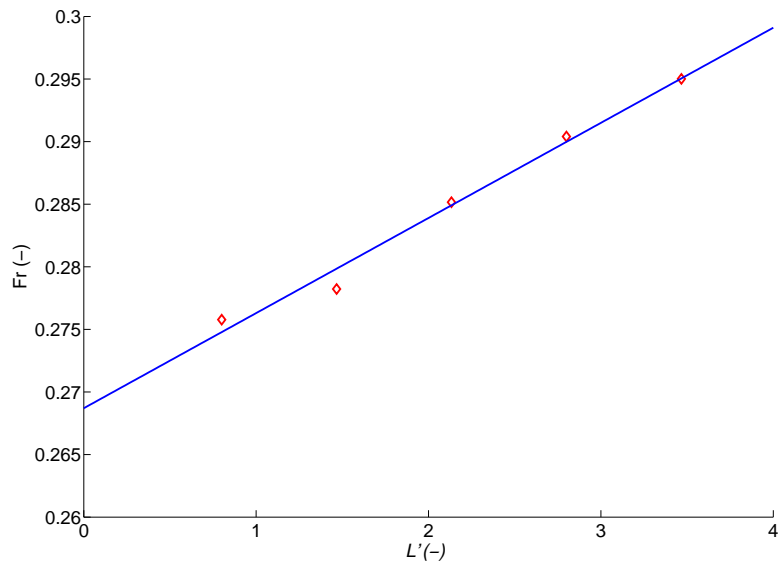


Figure 5.14: The variation of non-dimensional rise velocity, Fr , with L . An extrapolation of these results gives a prediction of the Fr of a bubble with zero length, of $Fr = 0.27$. This is an under prediction of approximately 18% of the Fr observed in the experimental studies. As in the experimental studies, the rise velocity increases with increasing bubble length as the bubble expands as it rises through the pipe.

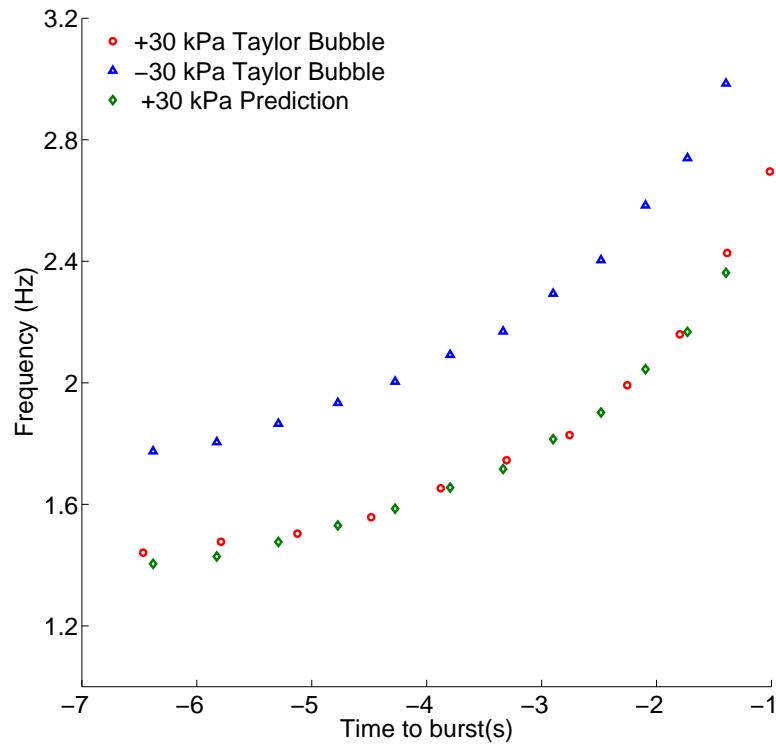


Figure 5.15: Frequency of surface oscillations of original simulations and predicted values based on correction for average bubble length. This shows the difference in frequency between the over and under pressured cases is due solely to difference in average length of the bubble.

5.2.5 Variation of initial bubble depth

The initial depth of the nose of the bubble below the water surface was varied from 4.36 m to 1.36 m. This may be interpreted as the initiation of the bubble rise simulation through a given rise height following the formation of the bubble. In this case, the frequency values should lie on top on each other when plotted against the time taken for the bubble to break the liquid surface and to burst. However, there are a number of issues that occur which preclude this ideal

outcome. Firstly, the time taken for the bubble to become fully developed (to reach its final rise velocity and shape) in comparison to the total rise time is more significant when the initial depth is reduced. The specification of the initial bubble pressure disturbance is also not a trivial calculation. Clearly, the adoption of a standard pressure value above the hydrostatic pressure value at the depth would not give analogous results, as this pressure will decrease as the bubble rises. Hence, it was decided to select a benchmark case of an over pressure of 20 kPa at a depth of 3.36 m, and use the same fraction of the hydrostatic pressure as this for each depth.

An increase in frequency is seen with decreasing initial height, as shown in Figure 5.16. The difference between the simulations can be mainly attributed to initialisation errors, with the bubble reaching a fully developed state at different times with regards to the total rise time. If the results are offset by the error from the first oscillation, a much closer agreement can be observed, Figure 5.17.

It should be noted that for the cases analogous to the initial experimental runs, the frequency values were, as expected, close together. From this it can be concluded that the initial depth does not have an effect on the frequency of the bubble oscillations. However, further investigation, both experimental and numerical may be required.

5.2.6 Variation of liquid viscosity

Vergniolle et al. (1996) reported that similar oscillatory behaviour had observed in acoustic measurements at volcanic sites, in which the fluid would be of a much higher viscosity. For this reason, the dependence of viscosity on the oscillatory behaviour was tested by varying the viscosity of the liquid phase from 0.001 to 50 Pa s. This corresponds to a variation in the buoyancy Reynolds number of $Re_B = 500000$ to 10.

A clear damping effect can be observed with increasing viscosity, the amplitude of the oscillations are observed to reduce significantly, Figure 5.18. However, the frequency of the oscillations

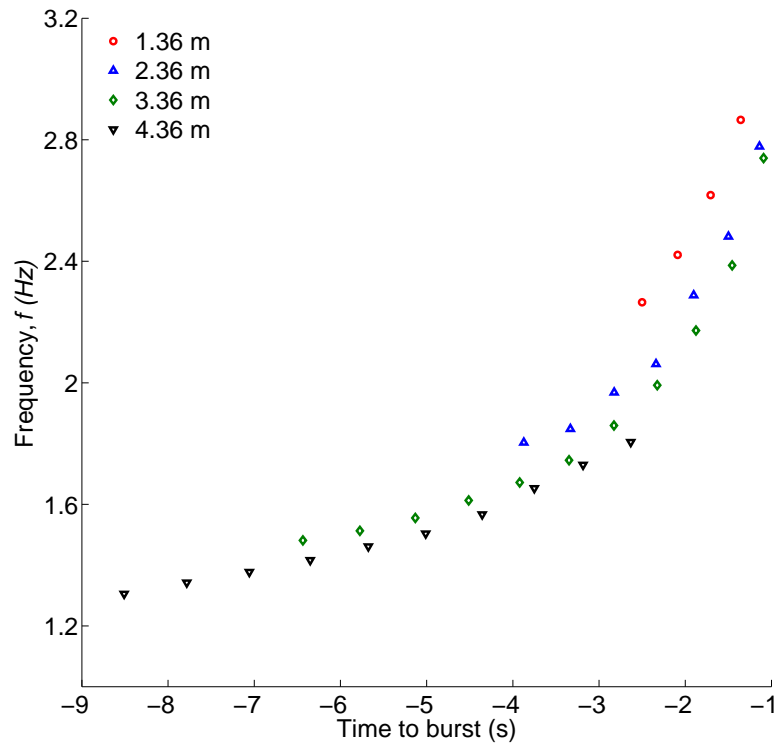


Figure 5.16: Frequency of oscillations for bubbles at different initial depths. There is a significant difference between the frequency for bubbles released at different depths below the surface.

are not significantly affected by this increase in viscosity as shown in Figure 5.19.

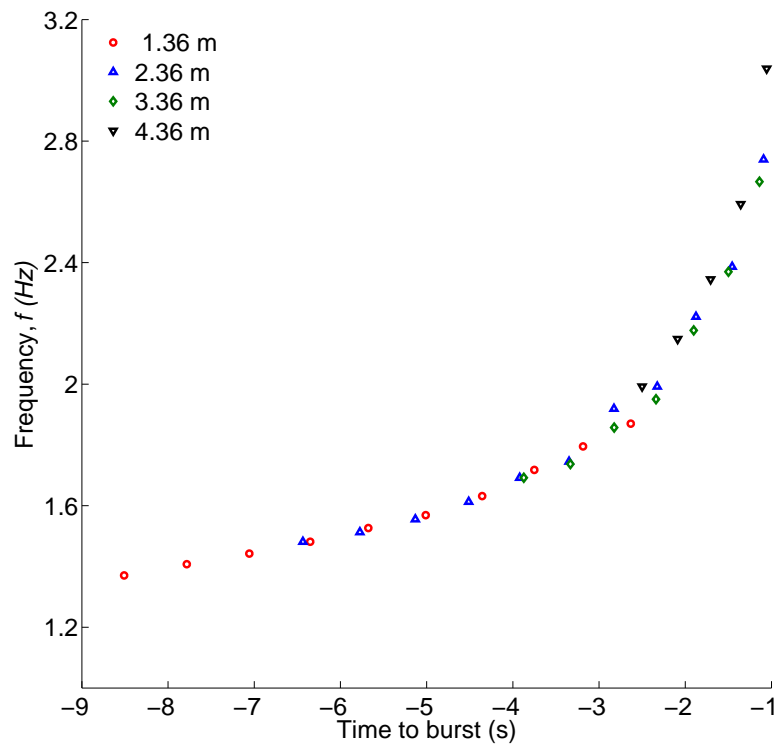


Figure 5.17: Frequency of oscillations for bubbles at different initial depths after being adjusted for initial error. This provides a much closer agreement between the different cases.

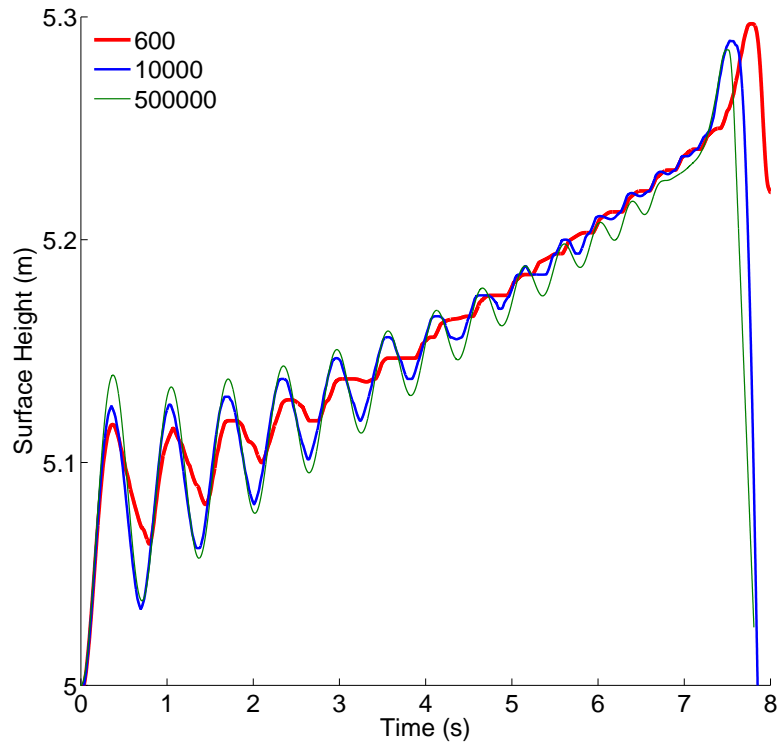


Figure 5.18: Oscillations of the surface for liquids of varying viscosity giving a range of Reynolds numbers of 600 to 500000. Further simulations were conducted but are not shown in this figure for clarity.

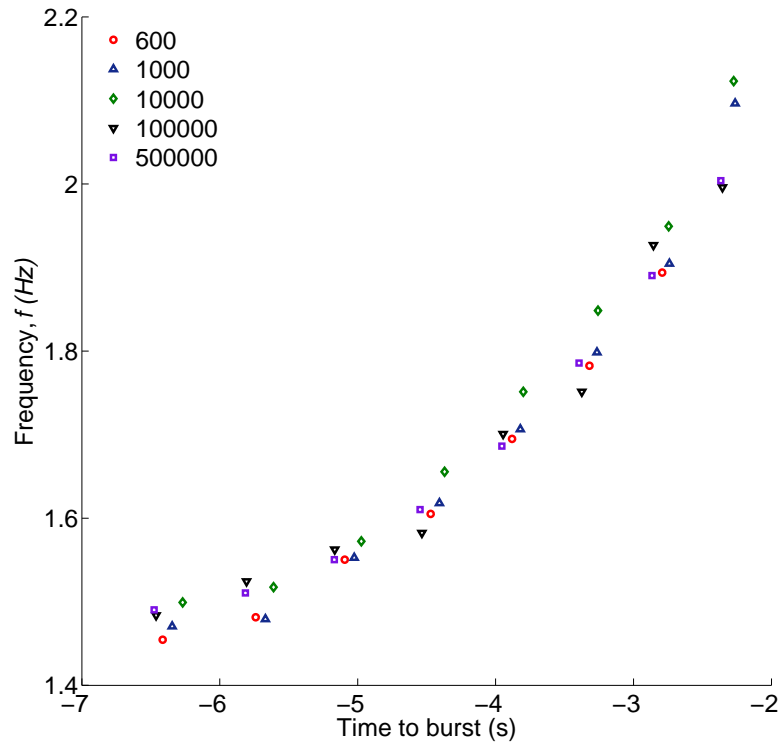


Figure 5.19: Frequency of oscillations for liquids of varying viscosity. The viscosity of the liquid phase does not significantly alter the frequency of oscillation as the bubble rises through the pipe.

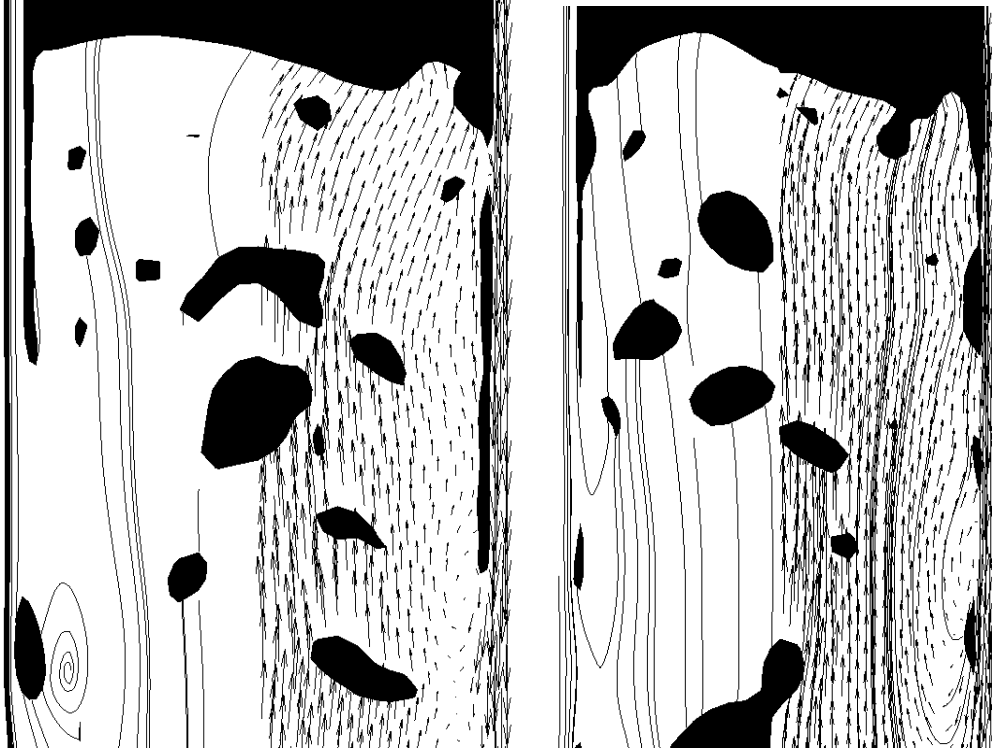
From an analysis of the simulation results, it can be observed that an increase in viscosity does slightly reduce the rise rate of the Taylor bubble - 4% lower at $Re = 600$ than at 10000. From the predictions of Viana et al. (2003) the velocity should be constant for these values of Reynolds number. A much sharper decrease in the rise velocity is expected when $Re < 200$, as the flow enters a regime where viscous forces start to influence the bubble rise more significantly (Viana et al., 2003). These trends are confirmed in the simulation results, in which a significant decrease in rise velocity is observed with $Re = 50$ and 10 which are seen to have $Fr = 0.243$ and 0.122, respectively.

With higher liquid viscosities there does not appear to be a significant effect on the frequency of oscillation, despite a reduction in the predicted bubble rise rate. However, with increasing viscosity this frequency becomes much more difficult to determine from the simulation, as surface oscillations become comparable in amplitude to the cell size used in the computational mesh. Oscillations early in the rise may still be detected through the pressure monitor. As discussed in Section 5.2.2 the pressure oscillations are correlated to the surface oscillations so even if the surface oscillations are too small to be detected, oscillatory behaviour can still be observed. At higher viscosities, $Re < 200$ these oscillations are quickly damped and could not be monitored accurately for the duration of the bubble rise. One would expect that if the oscillation rate could be measured, this high damping would reduce the frequency of oscillation, in the same fashion as a damping term in a simple harmonic motion.

5.2.7 Flow fields

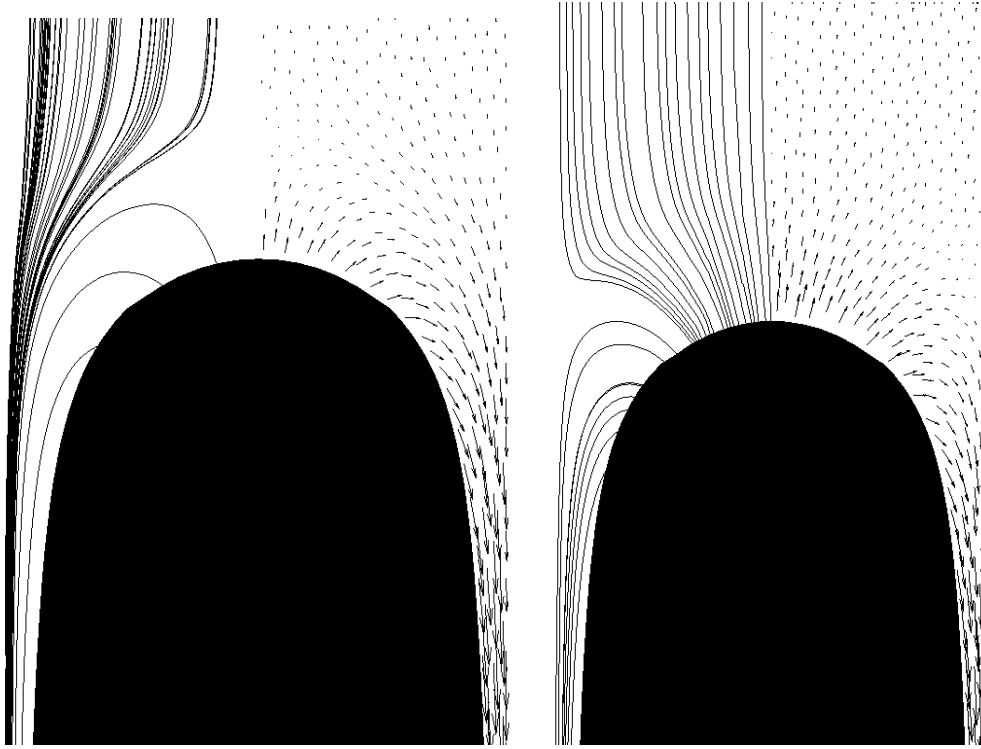
The flow field surrounding the rising Taylor bubbles were investigated, with focus on the different stages during the periods of bubble oscillation. During the expansion phases of the oscillations, the body of water ahead of the bubble is forced upwards in the pipe, causing the surface to rise. However, some of the flow is washed down the side of the bubble as the liquid film, between the

bubble and the pipe wall which then flows into the wake behind the rising bubble. This wake region is open both in compression and expansion, as opposed to an attached wake region behind the bubble observed in laminar flows (Nogueira et al., 2006b). This is shown in Figures 5.20a and 5.20b. This phenomenon is due to the large E_o number – caused by the large pipe diameter in relation to the low surface tension of the fluid used. When in compression there is a small positive velocity ahead of the bubble for approximately 0.04 m, all of which gets carried into the liquid film and wake by the fluid with a negative velocity further ahead of the bubble, as shown in Figures 5.21a to 5.21b. The qualitative behaviour observed is similar to experimental PIV (Particle Image Velocimetry) results in the literature (Nogueira et al., 2006b; van Hout et al., 2002), with clear variations observed due to the oscillatory behaviour and differing rise velocity of the bubble.



(a) Streamlines and velocity vectors around the wake of a Taylor bubble whilst in compression. (b) Streamlines and velocity vectors around the wake of a Taylor bubble whilst expanding.

Figure 5.20: Streamlines and velocity vectors in the wake of the Taylor bubble. There is little difference in the behaviour of the wake of the Taylor bubble for bubbles which are expanding and those which are in compression.



(a) Streamlines and velocity vectors around the nose of a Taylor bubble whilst in compression. (b) Streamlines and velocity vectors around the nose of a Taylor bubble whilst expanding.

Figure 5.21: Streamlines and velocity vectors around the nose of the Taylor bubble. When in compression, the flow far ahead of the bubble has a negative velocity in the vertical direction, whereas the flow far ahead of the bubble has a positive velocity when the bubble is expanding.

5.2.8 Variation of Pipe Diameter

A parametric study of the effect of varying pipe diameter on the behaviour of a rising Taylor bubble was conducted. An increase in the diameter of the pipe will lead to an increase in the Eötvös number, which may be regarded as the ratio of buoyant forces to surface tension forces. Above a value of 80 WhiteBeardmore1962, changes to this have little to no effect on the Froude number, which governs bubble rise rate. This may lead one to assume there is no value in exploring the parameter space above this value. One area that is of interest at larger Eötvös values is the stability of Taylor bubbles, which lead to the experiments described in Section 4.3. Theoretical work of (Batchelor, 1987) concluded that a single Taylor bubble would break up in a pipe with a diameter of more than 0.46 m, however no experimental work has been conducted at this diameter to verify this theory.

The base case presented in Section 5.2.1 showed a Taylor bubble rising in a stable manner in a 0.3 m pipe, in accordance with the experimental observations. The pipe diameter was then increased in order to find a critical pipe diameter at which a rising Taylor bubble ceases to be stable.

The diameter of the pipe was first doubled to 0.6 m, giving an Eötvös number of 1.19×10^4 . As with the scaling of the mesh from the simulations presented in Section 3.3.4 to 5.2.1 the solution was checked for mesh independence. A slightly finer mesh was required to give a similar number of cells in the thin film between the pipe wall and Taylor bubble. This gave a wall distance of 0.002 with a maximum cell size of 0.01 in the centre of the domain. This gave the total of number of cells to be approximately 1.3 million.

Bubbles had the same non dimensional length, $L' = L/D = 2.1$, as the base case simulations and were released from a depth of 10.7 m below the surface at a pressure equal to the expected

hydrostatic pressure at the nose of the bubble as shown in Figure 5.22. Upon release, the bubble is observed to break down the centre as shown in Figure 5.23 at a simulation time of 1 s, in contrast to the stable behaviour seen in the base case. As the bubble rises it reforms and does not break again before it bursts. A further simulation at this pipe diameter was conducted, with the bubble being released from the same depth as the base case 0.3 m pipe and hence same pressure. This was conducted to ensure that the initial breakage was caused by the diameter of the pipe and not the increased pressure exerted on the bubble at the initial depth.

However, increasing viscosity is thought to have a damping effect on the stability of the bubble. Therefore, a more appropriate non dimensional group to use in this case may be the Weber Number, a measure of effect of the inertial forces acting on a fluid in comparison to the effects of surface forces. This includes both a term for velocity, which will be affected by changes in viscosity, and terms for pipe diameter and surface tension. This is defined as,

$$We = \frac{\rho u^2 D}{\sigma}. \quad (5.2)$$

The Weber number associated with the base case is 1.47×10^3 , and that associated with the 0.6 m diameter case is 5.87×10^3 , while the Weber number of the theoretical limit for stability of Batchelor (1987) would be 3.45×10^3 .

An intermediate case, just above the theoretically critical diameter was tested in order to determine if the unstable behaviour observed at a diameter of 0.6 m was observed at this diameter. This diameter was chosen as 0.4 m, giving an Eo of 2.11×10^4 and a We of 2.61×10^3 . A further case was also carried out with a diameter of 0.35 m, between the stable 0.3 m case and the unstable 0.4 m case, with an Eo of 1.62×10^4 and a We of 2.00×10^3 .

The 0.4 m pipe diameter case showed similar behaviour to that of the 0.6 m pipe diameter case, breaking initially before reforming to rise at a constant rate in a more stable manner.

This initial breakage is shown in Figure 5.26. This contrasts to the behaviour observed in the 0.35 m pipe, which shows behaviour similar to that seen in the base case, with the bubble rising in a stable manner throughout its rise. Whilst this may not be indicative of a fully unstable regime, there is clearly a difference in stability between the 0.35 m pipe diameter case and the 0.4 m pipe diameter case so the critical diameter in the simulations is between 350-0.4 m. This difference between this critical diameter and the predicted critical diameter of Batchelor (1987) is approximately 15-20 %. This error is comparable in magnitude to the error in the velocity of the bubble. As the stability of the bubble is proposed to be determined by the speed at which disturbances are washed into the liquid film, a slower rising bubble would be more likely to break given the same pipe diameter (provided there is no damping from a higher viscosity liquid).

Further investigation is required to determine if this is a function of the Weber number, *i.e.* if increasing the viscosity in such a way that the Weber number for a case with a 0.4 m pipe is equal to that of the case with water in a pipe of diameter 0.35 m.

5.2.9 Stability of Bubbles in non– quiescent fluids

One key result of the experimental work presented in Chapter 4 was that Taylor bubbles were observed rise in a stable manner provided that the fluid in the pipe was quiescent in the 0.3 m pipe. When this was not the case, and remnants of the wake of a previous bubble were still present, bubbles were observed to break up. The CFD model has been shown to be able to replicate the stability of bubbles rising into a quiescent fluid in Section 5.2.1 and so it was decided to use the model to investigate the effect of a flow field has on a following rising bubble.

To study this, a second Taylor bubble was added to the domain, in the same fashion as the first as detailed in Section 5.1.3, after 8 s of the simulation, just after the burst of the first Taylor bubble. The pressure throughout the bubble is specified to be the pressure at the location of

the nose, in a similar fashion to that in the base case. These initial conditions are shown in Figure 5.27.

When initialised in this way the second Taylor bubble is observed to break up as it begins to rise, as shown in Figure 5.28. It is thought that this break up is caused by the turbulent velocity field left behind by the trailing wake of the leading bubble which creates an instability in the nose of the second bubble which grows and then splits the bubble down the centre. As the second bubble continues to rise, the interactions between the surface of the second bubble and the wake of the first bubble continue causing further deformation and breakage of the bubble. This does qualitatively replicate the behaviour observed in the experiments described in Section 4.3, however the breakage of the simulated bubble is less severe.

This difference between the simulation results and the experimental observations may be due to the treatment of the turbulent eddies at the interface between the liquid and gas phases. Consequently, this could cause smaller instabilities which are able to be washed into the thin film before they are able to grow enough to cause the bubble to break. Another reason for this difference between the model and the experimental observations is the presence of a large volume of bubbles in the wake of the first bubble in the experiments. These are generated during the formation of the bubble as described in Section 5.1.3. These bubbles are estimated to have a diameter of under 5 mm, and so are could not be resolved in the numerical model without an extremely highly refined mesh. A mesh capable of resolving these bubbles would result in the overall computational time increasing dramatically and hence it was not feasible in the scope of this thesis to conduct such a simulation. This is described in detail previously in Section 5.1.3.

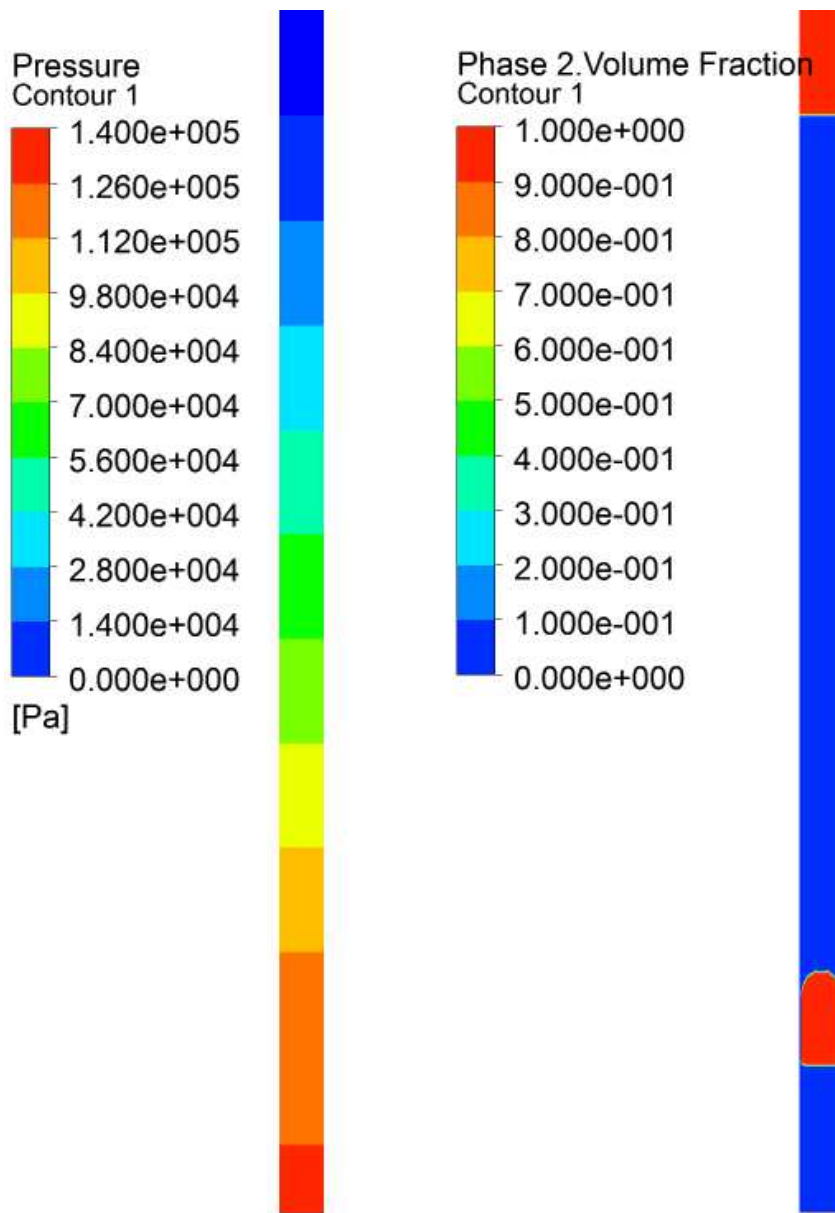


Figure 5.22: Initial conditions imposed on the numerical domain of a 0.6 m pipe. The pressure conditions are shown on the left hand side and the volume fraction on the right hand side.

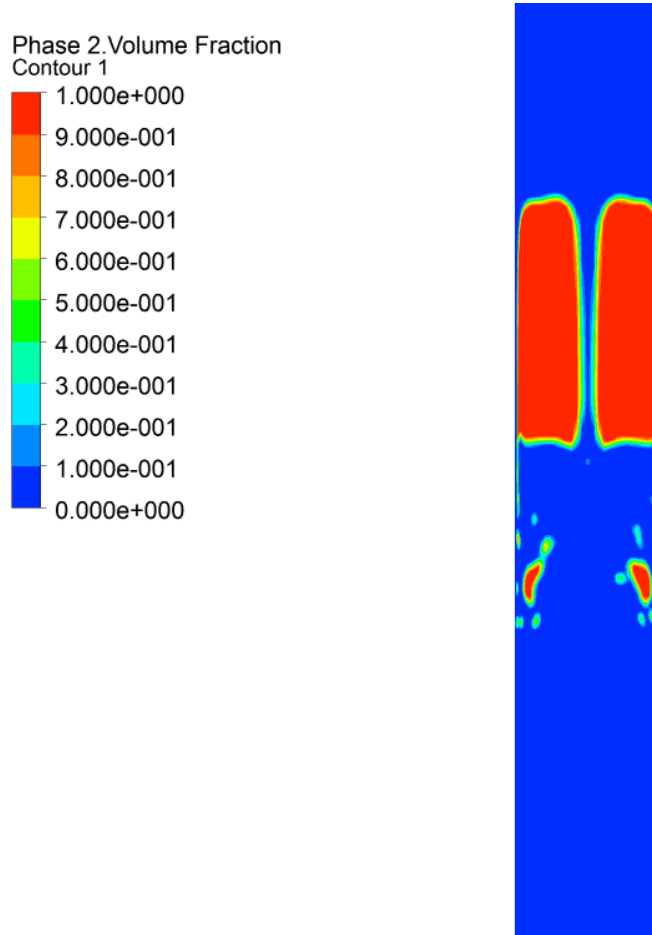


Figure 5.23: Contour plot of volume fraction of air showing the breaking of the Taylor bubble after 1 s of simulated rise.

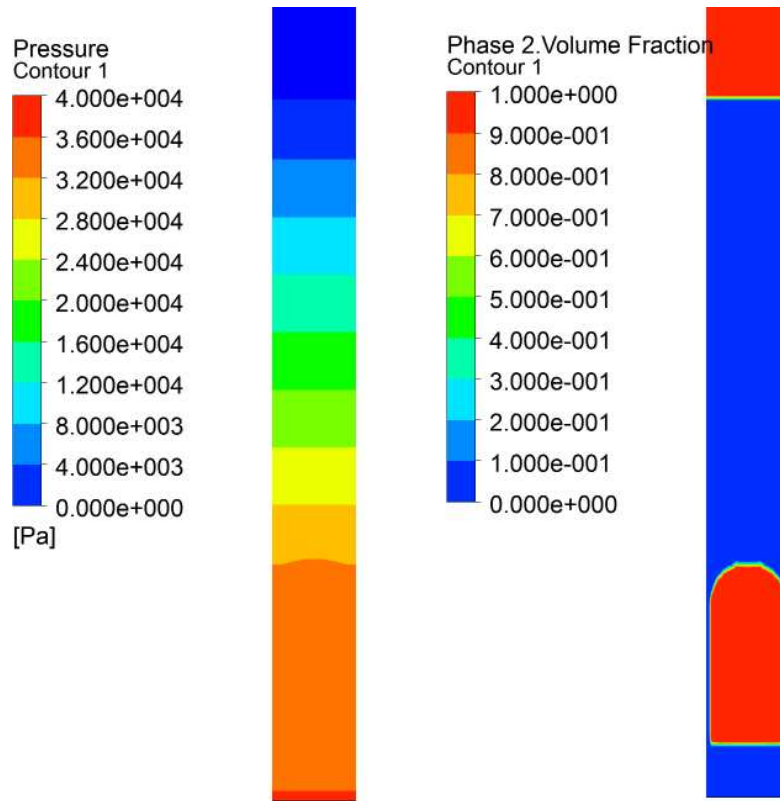


Figure 5.24: The altered initial conditions imposed on the numerical domain of a 0.6 m pipe, with the same depth of water and hence initial bubble pressure as the base case which had a pipe diameter of 0.3 m.

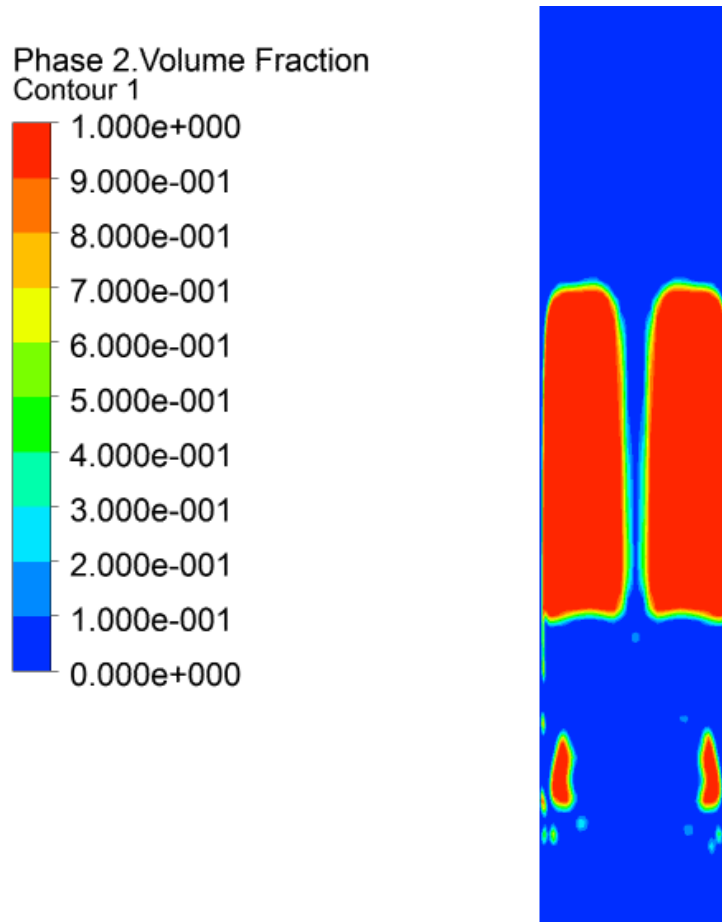


Figure 5.25: Contour plot of volume fraction of air showing the breaking of the Taylor bubble subjected to the altered initial conditions after 1 s of simulated rise.

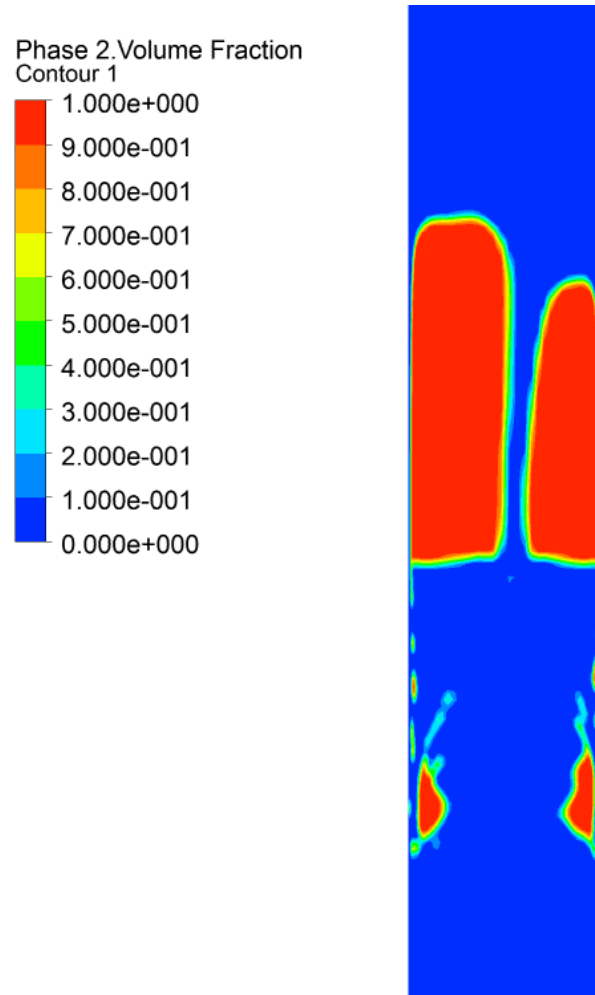


Figure 5.26: A bubble breaking in a pipe of diameter 0.4 m after 1 s of simulation. This break is noticeably different to the break observed for the 0.6 m pipe as the break is not axisymmetric.



Figure 5.27: Initial volume fraction conditions for a bubble rising into the wake of a previous bubble in a 0.3 m diameter pipe.

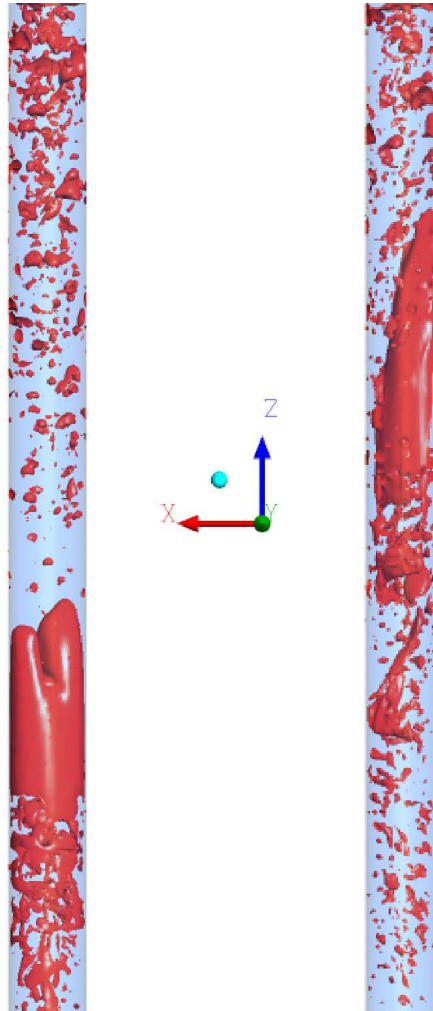


Figure 5.28: 3D iso-surface images of the breaking of a Taylor bubble when rising into the wake of a previous bubble, breaking on the left, and deforming on the right.

5.3 Conclusions

The behaviour of the rising bubbles observed during laboratory experiments was reproducible using the compressible CFD model described in Section 3.1. A stable Taylor bubble can be produced with a rise rate of the bubble was within 15% of the experimental value. The surface rise level is within 5% of the theoretically predicted value and the frequency of oscillation is approximately 10% above the experimental values. A variation in the pressure away from the hydrostatic during the creation of the bubble was shown to give oscillations with varying amplitudes but that were independent of frequency. The initial pressure disturbance produces a change in the bubble length that is dependent on the initial compression or expansion of the bubble. As the resultant oscillation frequency is dependent on this length, there is also a small change in the frequency of oscillation. This is in accordance with both the results from the experimental studies presented in Chapter 4 and the theoretical models of (Vergniolle et al., 1996) and (Pringle et al., 2014).

An increase in liquid viscosity, giving a reduction in Reynolds number reduced the amplitude of oscillations significantly. However, the effect on the frequency of the bubble was minimal up to the point at which oscillations could no longer be detected accurately. The increased viscosity has a damping effect on the oscillations and hence one would expect the frequency to decrease with increasing viscosity, if the amplitude was such that it could be measured, due to it exhibiting the same behaviour as a simple harmonic oscillator.

The stability of the bubble with increasing pipe diameter was investigated using the numerical model and shown to be comparable with the theoretical prediction of Batchelor (1987). The stability of bubbles rising into the wake of a previous bubble was also investigated. The results of the simulations showed an qualitative agreement with the observations of Section 4.3.

Further to this study the effect of using a polytropic gas law, with $\gamma = 1.1$ as suggested by Pringle et al. (2014) and Vergniolle et al. (1996) should be investigated. This would require the

development of a User Defined Function to define the density of the gas at a specified pressure. Studies of inclined pipes have shown an increased rise velocity, and the effect of changing the angle of inclination of the pipe has on the frequency and amplitude of oscillations could also be studied. Experimental studies with fluids of higher viscosity are planned to take place in future years at the University of Nottingham in the 0.29 m pipe and the results will hopefully validate this numerical study further.

It is also recommended that simulations using a LES or DES approach to model the turbulent flow be conducted and the results compared with the results of the simulations presented here. This was not able to be conducted as part of this work due to computational limitations.

Rise of a Taylor bubble through a change in geometry

6.1 Introduction

The rise of Taylor bubbles is a well-documented and well-studied phenomenon in many applied fields, from chemical reactions in micro scale systems to the eruption of volcanoes. Despite this large volume of work, there is a paucity of published experimental or numerical work that have been reported on the rise of Taylor bubbles through a pipe section of changing diameter. James et al. (2006) reported the results of an experimental investigation into the rise single Taylor bubbles through a variety of pipe expansions and contractions (using 0.038 m, 0.05 m and 0.08 m diameter pipe sections). Sugar syrup solutions of different concentrations, with viscosities of 0.001, 0.1 and 30 Pa s, were used to compare the rise behaviour across a range of Froude numbers. They observed that when a Taylor bubble encountered an expansion in pipe diameter, it rapidly expanded both vertically and laterally from the nose. This resulted in an increase in the flow in the liquid film surrounding the bubble which caused a necking or pinching of the bubble. For bubbles of sufficient length, this necking will split the bubble and generate oscillations in the measured pressure signals. The objective of this work was to compare the experimental pressure signals measured against the long period seismic data recorded at active volcanic sites. The hypothesis being that the source of pressure oscillations observed in seismic

data are caused by a gas slug rising through an expansion in the diameter of the conduit. They concluded that the pressure changes measured during in their experiments exhibited similar behaviour to those recorded in the field. Consequently, it was proposed that the expansion in conduit diameter was the source of the observed pressure changes. A more detailed analysis and discussion of the results of this study are presented in Section 6.2.

The only other study that has reported this behaviour is the conference proceeding of Kondo et al. (2002). Although the primary focus of this study was on co-current liquid gas flow, a number of experiments using single Taylor bubbles with no liquid flow were also described. In these, a Taylor bubble rises through a pipe of diameter 0.02 m which undergoes a sudden expansion into a pipe of 0.05 m. Figure 6.1 shows a still video image taken from Kondo et al. (2002) showing the bubble during the necking process. After the neck of the bubble closes, it bursts through the nose of the bubble. This process can be observed in the still video images shown in Figure 6.2. These images have been taken after the sudden expansion but are cropped to the central 0.02 m of the pipe.

A number of unpublished complementary experimental studies have recently been undertaken at the Universities of Nottingham and Bristol. The focus of these studies were to investigate the flow of Taylor bubbles through expansions in diameter of a vertical pipes.

The first of these studies was the work of Danabalan (2012). These experiments investigated the rise of Taylor bubbles through a glass pipe which expands into either a rounded glass bowl or cubic box. Two different viscous fluids were used, with viscosities of approximately 3 and 68 Pa s, which results in the non-dimensional parameters presented in Table 6.1. A known volume of air was smoothly injected into the lower section of the pipe via a syringe through a rubber bung in the base of the pipe. The bubble ascended the 0.038 m diameter pipe before rising into one of the expansion sections. The bowl had a maximum diameter of 0.162 m and the box was a cube of height 0.245 m. Both of these expansion sections were centred on the axis of rotation of the

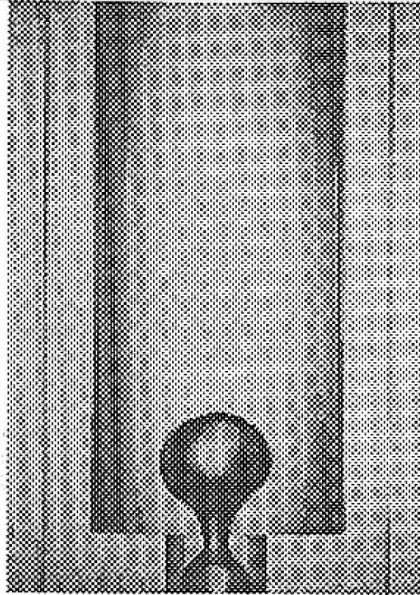


Figure 6.1: A still video image extracted from Kondo et al. (2002) which shows a Taylor bubble during the necking process while passing through a sudden expansion from a pipe of diameter 0.02 m to 0.05 m in water.

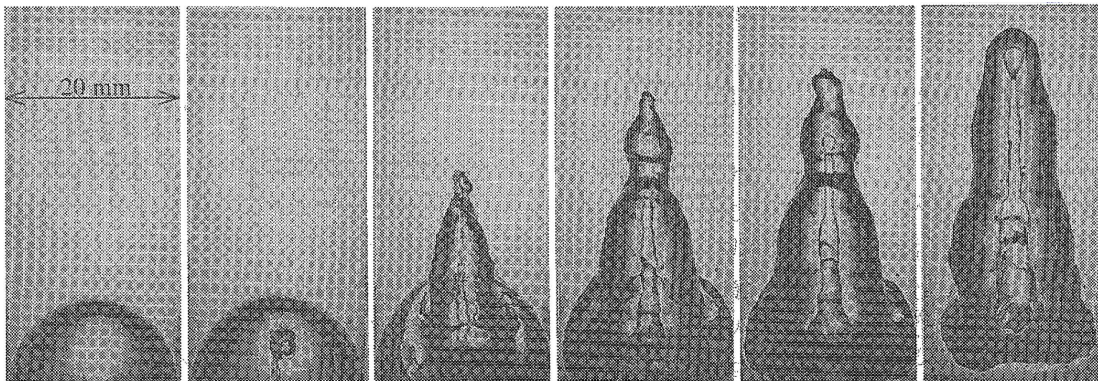


Figure 6.2: A series of still video images extracted from Kondo et al. (2002) which show a Taylor bubble which has passed through a sudden expansion from a pipe of diameter 0.02 m to 0.05 m in water (Kondo et al., 2002).

Table 6.1: Table of non-dimensional parameters determined for the rise of Taylor bubbles in the experiments of Danabalan (2012).

μ (Pas)	Re_B	Eo	M	Fr
3	7.7	191	2×10^3	0.077
68	0.3	191	5.2×10^8	0.003

pipe. The rise behaviour of the Taylor bubble was tracked by a stationary video camera adjacent to the pipe section.

A red dye was added to the glucose syrup in the lower pipe section to provide contrast to the undyed syrup initially contained within the expansion section, which can be seen in Figure 6.3 (a). As the bubble rises into the expansion section it is observed to entrain dyed fluid from the lower section of the pipe into its trailing wake, shown in Figures 6.3 (d)-(f). The motivation for this study was to replicate the behaviour of gas bubbles rising through volcanic conduits which expand into lava lakes at the surface, introduced in Section 2.2.2.4. The pipe expansions employed in the experiments were representative of the expansions in conduit diameter which result in lava lakes. The conclusion of this study was that in volcanoes, the rising Taylor bubble would entrain hot magma from a large depth and bring this in the bubble's trailing wake to the surface.

The volume of gas injected into the lower pipe was varied in 10 cm^3 increments from between 10 cm^3 to 60 cm^3 to determine the critical volume of bubble that can pass through each expansion section without the bubble splitting into two separate bubbles. An analysis of the results of these experiments showed that the critical volume is dependent on the geometry of the expansion section. From an examination of the experimental results presented in Figure 6.4 it is observed that as the diameter of the bowl expansion gradually increases, the greater the

volume of bubble that could pass through the expansion without being split than in the suddenly expanding, box section. This trend was observed in replicate experiments conducted using fluids having viscosities of 3 Pa s and 68 Pa s. For this change in viscosity, the critical volume for the box expansion remained constant; however, the critical volume for the bowl expansion is one decrement (10 cm^3) smaller. As the increments in volume are relatively large, there is a degree of uncertainty as to whether this decrease in critical volume would also be seen in the box expansion. Due to the increase in viscosity, there would be an increase in film thickness around the bubble

Further experiments were conducted which tracked particles dispersed in the syrup. An analysis of these results suggested that bubbles drive a convection process in the expanded section. Further work involving thermal gradients was suggested by the author to fully investigate this process and compare it to possible scenarios in lava lakes Danabalan (2012).

A further experimental study recently conducted by Soldati (2013) at the University of Bristol employed a quasi two dimensional Hele-Shaw cell to investigate the effect of the angle of expansion, fluid viscosity and volume of bubble may have on the observed rise characteristics. A Hele-Shaw cell is made up of two parallel plates a distance, H , apart which are sealed at the sides. A 3D CAD model of the experimental apparatus can be seen in Figure 6.5. A Hele-Shaw cell was used due to the high viscosity of the fluid and the comparatively small pipe diameter which result in a low Reynolds number flow. The use of the cell also allows the user to quickly and accurately create different angles of expansion, which would not have been possible if a traditional pipe had been used. This difficulty in producing a number of different angles of expansion in the experiments is one of the motivations behind using CFD to model this problem.

By varying the volume of air injected into the base of the apparatus, different sized Taylor bubbles were generated in the pipes. By injecting different lengths of bubbles into the pipes it was possible to find the critical volume of bubble which can pass through the expansion without

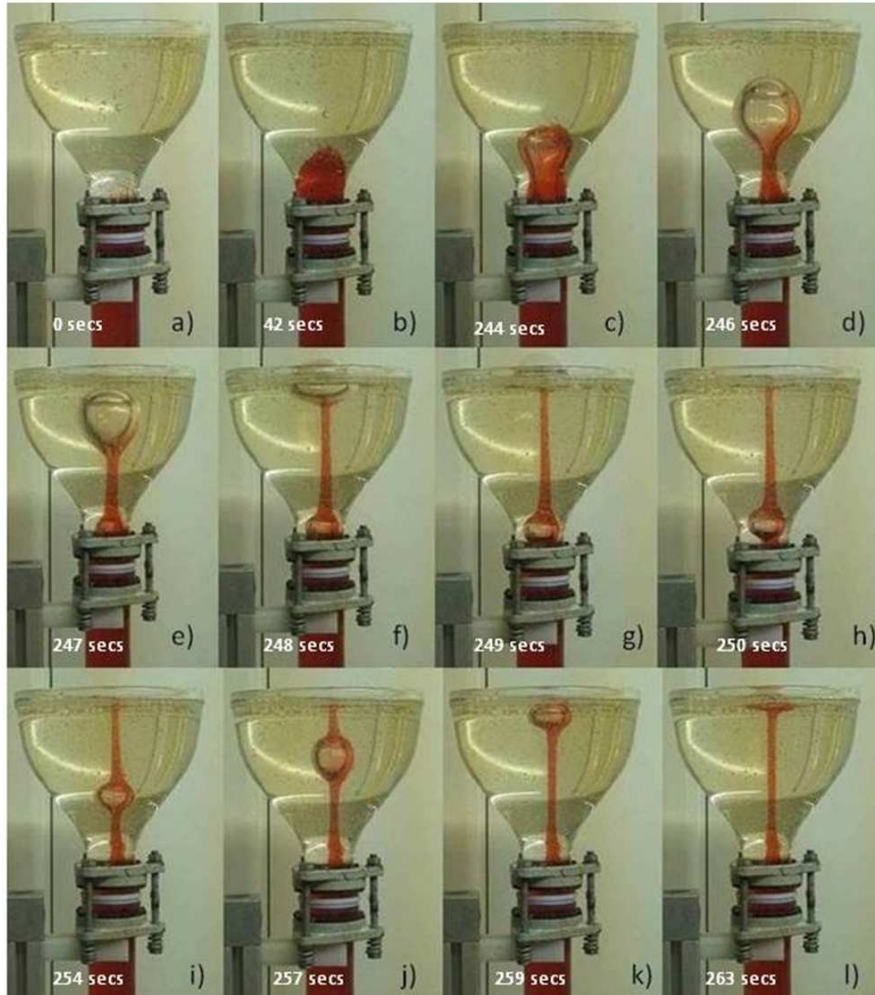


Figure 6.3: Photographic sequence in 68 Pas viscosity glucose with a 60 cm^3 bubble injected into the bowl apparatus of Danabalan (2012). The upper bowl is filled with clear glucose syrup and the lower pipe is filled with glucose syrup mixed with red dye. Images (a) to (f) show the passage of the first bubble while (g) to (l) shows secondary bubble rise (Danabalan, 2012).

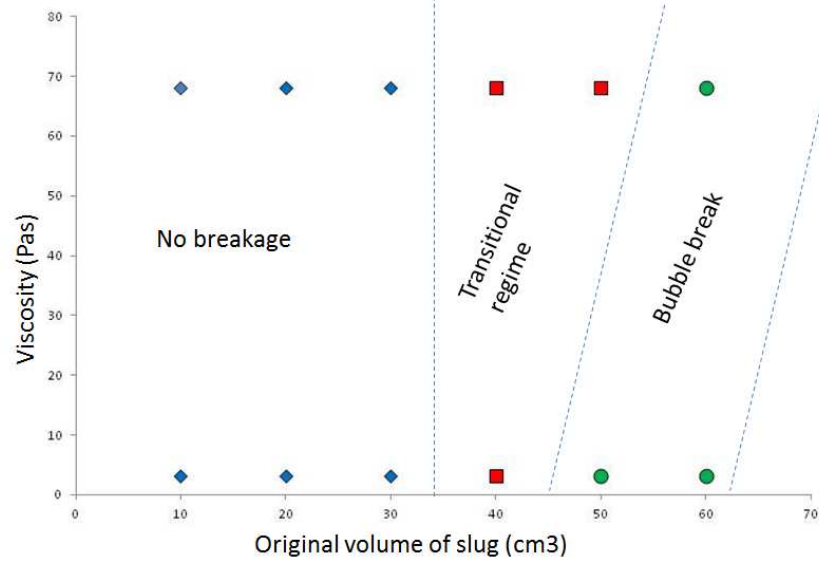


Figure 6.4: A flow regime diagram mapping the patterns of bubble breakage tendencies observed in the expansion section for different fluid viscosities and original bubble volume. The blue diamonds represent cases whereby the bubble remained intact, the red squares where the original single bubble breaks into two separate bubbles in the cubic reservoir but did not break in the bowl-shaped reservoir, the and green circles where the original single bubble broke into two separate bubbles as it entered both of the expansion geometries (Danabalan, 2012).

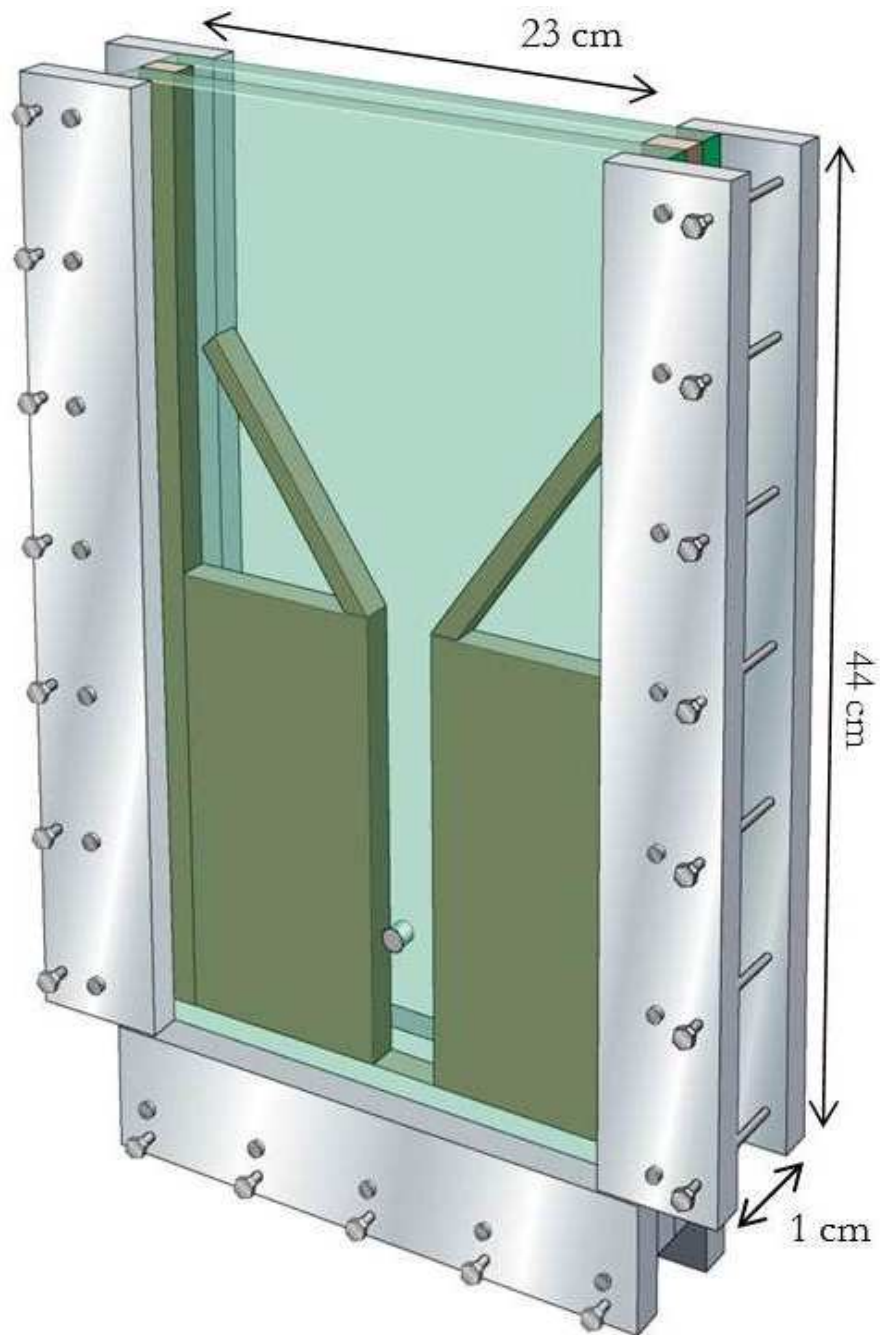


Figure 6.5: A 3D CAD image of the experimental apparatus used in the Hele-Shaw experiments conducted at the University of Bristol to study the rise of a Taylor bubble through an expansion in geometry (Soldati, 2013).

Table 6.2: Table of non-dimensional parameters determined for the rise of Taylor bubbles in the experiments of Soldati (2013).

μ (Pa s)	Re_B	Eo	M	Fr
17	0.96	119	2×10^6	0.01
47	0.35	119	2×10^8	0.003

splitting by the necking of the bubble. Two fluids of different viscosity (17 and 47 Pa s) were used in the experiments resulting in the non-dimensional parameters shown in Table 6.2. Similar to the experiments of Danabalan (2012), an exact value for the critical length could not be found, but only upper and lower bounds for it. As the volume of air injected could only be determined to the nearest millilitre, the value of the critical volume was determined to lie between two consecutive values at which the bubble passed through the expansion without breaking at the lower, but which does break at the upper.

The experiments were designed to investigate the effect of two different distance settings, H , between the parallel plates in the Hele-Shaw cell (where $H=0.005$ m and 0.01 m). An analysis of the results of these experiments shows that the upper and lower bounds of the critical volume are directly proportional to H . For example, the upper and lower bounds of the critical volumes given a 30° expansion are 14-15 ml and 7-8 ml for H values of 0.01 m and 0.005 m respectively. As the accuracy of the volume of air is hence greater for $H=0.01$ m, these results will be used for any future comparisons. This relationship suggests that the bubble length, and not the volume, is the critical factor which determines the breakup of the bubble.

An analysis of the results of the experiments of Soldati (2013) concludes that the critical length of a bubble increases as the slope of the expansion becomes steeper. This is consistent with the findings of Danabalan (2012), in which a sudden expansion gave a smaller critical length

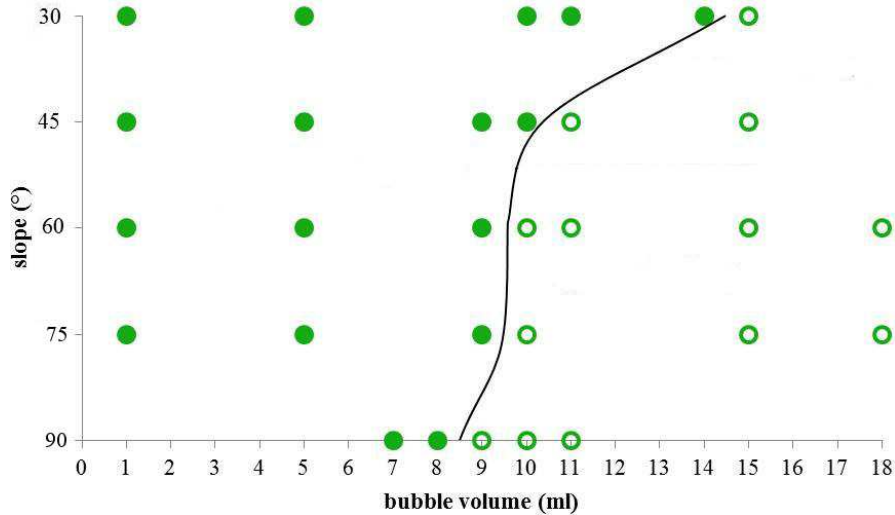


Figure 6.6: A flow regime diagram mapping the patterns of Taylor bubble breakage observed for different angles of expansion (Soldati, 2013). This shows a increase in the maximum size of bubble which could pass through the expansion given a more gradually expanding section.

than a gradual increase in pipe diameter. This result is illustrated in the flow regime diagram of Figure 6.6. The solid line indicates the expected value of the critical volume of a bubble for a given angle of expansion. The filled circles indicate the bubbles which did not split into two or more bubbles as they rose through the expansion, whilst the unfilled circles indicate those which did split.

A Sony HDR-SR5 video camera could be used record the breakup mechanism of low Reynolds number Taylor bubbles when passing through these expansions in pipe geometry. Figure 6.7, taken from Soldati (2013), shows a series of diagrams based on still photographs that clearly illustrate the different stages of this breakup mechanism. As the nose of the bubble enters the expansion section of the pipe, the nose of the bubble expands to fill the widening diameter as it is no longer constrained by the channel walls of the lower pipe section, shown in Figure 6.7 (c).

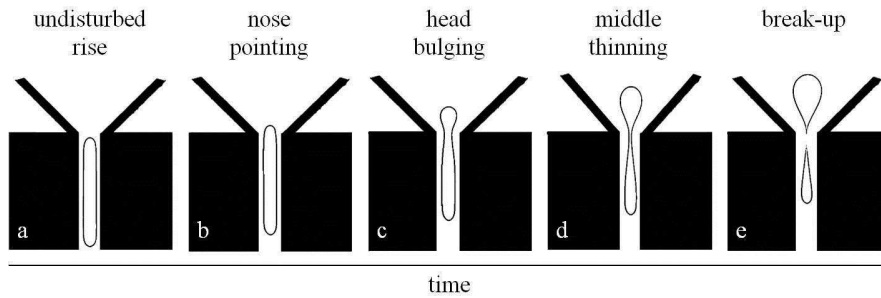


Figure 6.7: Diagrams based upon still images taken from a video recording of a Taylor bubble rising through a 75° expansion, from undisturbed rise (a) through the necking process to breakup (e) (Soldati, 2013).

As the nose of the bubble expands, the middle of the bubble thins out. If the bubble is longer than the critical length, it will break into two parts, as shown in Figures 6.7 (d) and (e).

Soldati (2013) analysed the still frames extracted from the video footage to track the position of the nose and tail of the bubble. Unlike the results of the experiments presented in Chapter 4, the tail of the bubble is distinct due to the low Reynolds number used for the design of these experiments, and the tail can hence be tracked accurately. Figure 6.8 is representative of the behaviour of a typical bubble which does not break up as it passes through the expansion section. The acceleration of the nose can be observed as the bubble passes through the expansion, as can the very rapid acceleration of the tail of the bubble as it passes through this section. The length of the bubble decreases in the upper section due to the larger confining diameter.

The work of Soldati (2013) identifies the change in flow regime as a rising bubble passes through different expansion sections. This aspect will be studied in more depth using CFD modelling later in this chapter.

A research student at University of Nottingham recently studied the acoustic signals produced by the breakup of a Taylor bubble as it rises through an expansion in the pipe diameter. The experimental apparatus used in this study consisted of a 0.01 m diameter pipe inside a longer

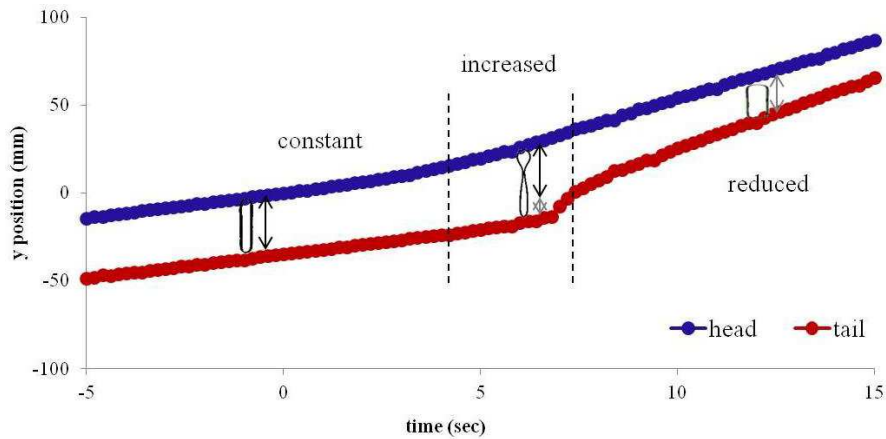


Figure 6.8: The nose and tail positions of a typical non-breaking Taylor bubble whilst rising through an expansion in pipe diameter (Soldati, 2013).

0.025 m diameter pipe. Both of these are filled with water and a specified volume of air is injected into the inner pipe via a syringe through a rubber bung located at the base of the pipe. These pipes are contained within a 0.25 m concentric pipe which can be filled with water to perform additional experiments. A high speed camera was used to record the physical behaviour of the bubbles. A high sensitivity microphone was located above the surface of the water to record the acoustic signals generated. Although no significant conclusions could be drawn from an analysis of the acoustic signals, an analysis of the high speed camera images gave further qualitative insight into the process of the breakup mechanism of a Taylor bubble passing through an expansion. A further conclusion drawn from these experiments was that the breakup mechanism is still observed to occur when the bubble is too short to be split. After the neck has thinned, the tail still bursts through the neck given a bubble length shorter than the critical length. Due to similar limitations in the experimental measurement methodology as discussed in Section 4.2, the frame rate of the recording was limited to 50 fps (with natural daylight) for the majority of the experimental runs. However, one of the experiments was recorded at a frame rate of 250 fps which enabled a more detailed analysis to be performed.

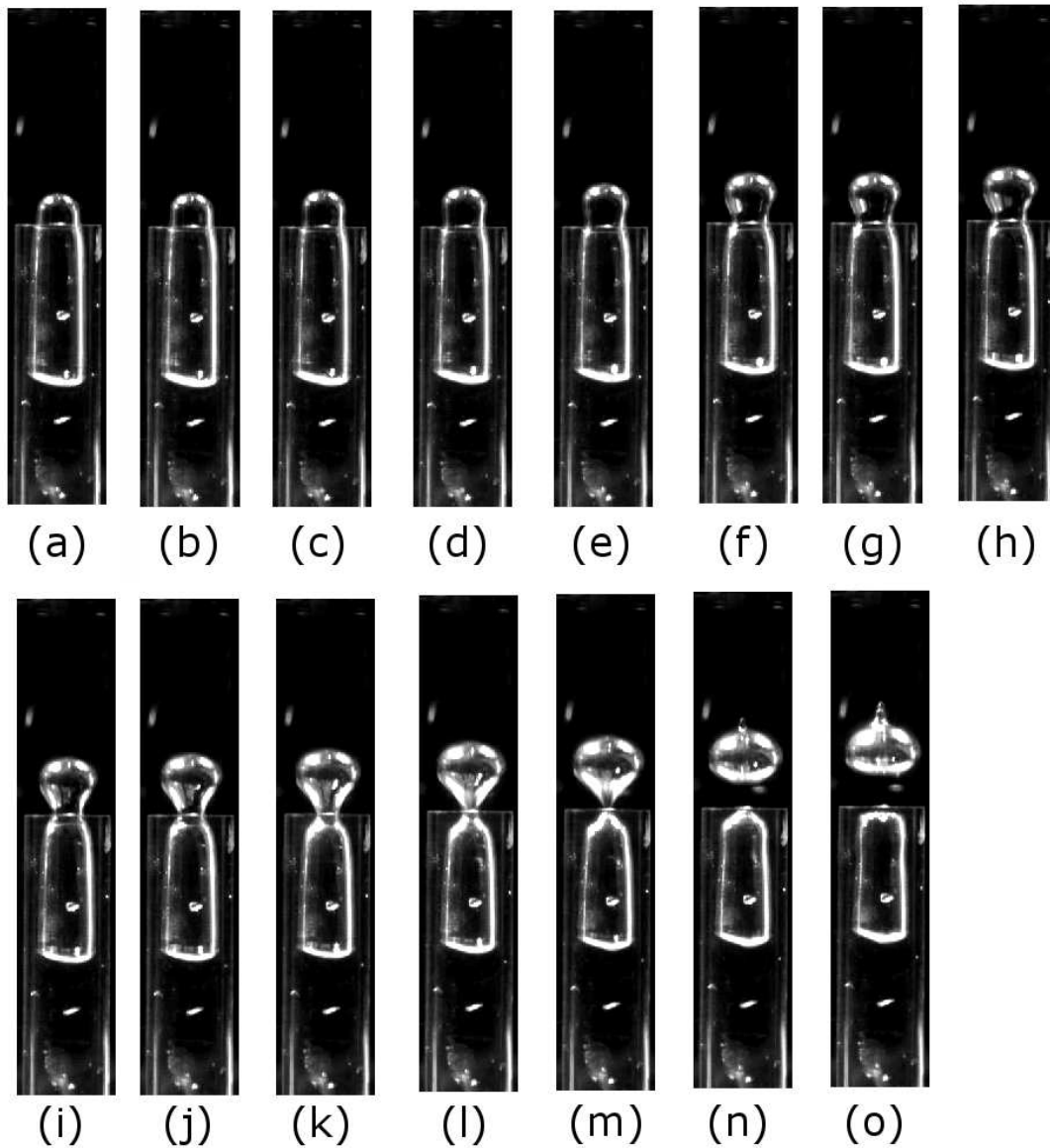


Figure 6.9: Still frames extracted from a high speed video recording of a Taylor bubble rising in water through an expansion, which show the sequential the breakup mechanism. Images (a)-(d) show the Taylor bubble approaching the top of the inner tube. The next sequence of images, (e)-(j), show the bubble starting to neck as a larger volume of water begins to enter the inner pipe at a high velocity. As the bubble continues to neck a fine central film of air is maintained, shown on images (k)-(m). Between images (m) and (n), this film breaks and is catapulted through the centre of the upper bubble. This instantaneously penetrates the nose of the bubble and water jets through this opening, which is shown in the images (n) and (o).

Still images of the progression of stages involved in a bubble breaking as it rises into the larger diameter pipe are shown in Figure 6.9. Images (a)-(d) show the Taylor bubble approaching the top of the inner tube. The next sequence of images, (e)-(j), show the bubble starting to neck as a larger volume of water begins to enter the inner pipe at a high velocity. As the bubble continues to neck a fine central film of air is maintained, shown on images (k)-(m). Between images (m) and (n), this film breaks and is catapulted through the centre of the upper bubble. This instantaneously penetrates the nose of the bubble and water jets through this opening, which is shown in the images (n) and (o). As the bubble continues to rise it is observed to reform into a spherical cap type bubble. This is not shown in these images as the 250 fps recording was curtailed before the bubble reformed.

The aim of this chapter is to demonstrate that the use CFD models can give a better understanding of the behaviour of Taylor bubbles as they rise through changes in geometry. The CFD models, introduced in Chapter 3.1, are first validated using the published experimental results of James et al. (2006). These models are subsequently used to perform a series of parametric studies to investigate the behaviour of bubbles ascending through various expansions under a range of initial conditions.

6.2 Validation

6.2.1 Experimental Apparatus

In order to have confidence in the results generated by any numerical model, the model must first be validated. To validate the model, the results of a set of simulations were compared against the experimental results of James et al. (2006). In this experimental study a single Taylor bubble rises through a vertical pipe before entering an expansion in pipe diameter. As the Taylor bubble passed through this expansion it was observed that, dependent on its length, it may split into

multiple smaller bubbles. This process was monitored in the experimental rig by a number of pressure sensors, an accelerometer, a force sensor and recorded by video camera. A diagram of the experimental apparatus used is shown in Figure 6.10, taken from James et al. (2006). Although a number of different configurations were explored in the experimental studies, the model was validated against the results of the experiments that employed the 0.038 to 0.08 m expansion in pipe diameter.

6.2.2 Experimental Results - 0.038 to 0.08 m expansion

As the bubble is observed to enter the expanding section, it rapidly expands, both vertically and laterally. James et al. (2006), hypothesised that this causes an increase in the liquid flux flowing downwards within the liquid annulus surrounding the part of the bubble still remaining in the smaller pipe. This increased flow creates a narrowing in the neck of the bubble (or pinch in the bubble), which continues until the liquid annulus closes. For bubbles of sufficient length, the neck will close before the bubble has risen through the expanding section and the bubble will hence break into two parts. However, due to a low frame rate of the video recordings and the structural elements of the apparatus shown in Figure 6.11, this could not be verified. James et al. (2006) reported that Taylor bubbles with an average length of $L' = L_B/D = 3.3$ or longer, where L_B is the length of the bubble and D is the inner diameter of the pipe, were observed to consistently break up. Bubbles that were shorter than this (having average lengths of $L' = 1.1$ or 2.2 in these experiments) were able to rise through the expanding section before the neck closed. The critical length, which was introduced in Section 6.1 would hence have a lower bound of $2.2L'$ and an upper bound of $3.3L'$.

An analysis of the pressure and force meter readings detected a number of different frequencies that were generated by the bubble passing through the expansion. Of these, there were three dominant components. For example, when $L' = 4.4$, there was a high frequency component of

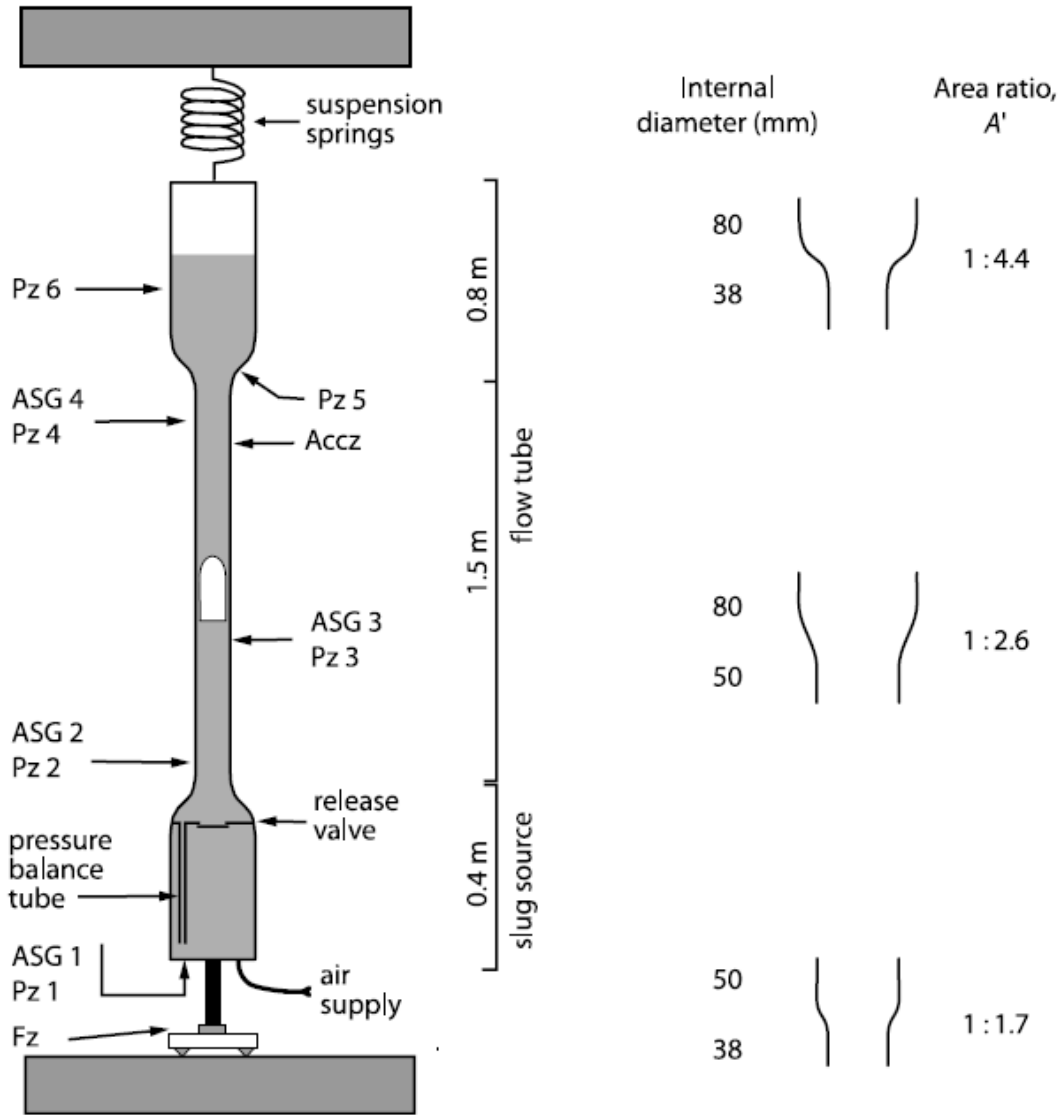


Figure 6.10: The experimental apparatus used by James et al. (2006) to study the rise of Taylor bubbles through changes in pipe diameter. The full experimental set up is shown on the left hand side and the profiles of different expansion sections are shown on the right hand side.

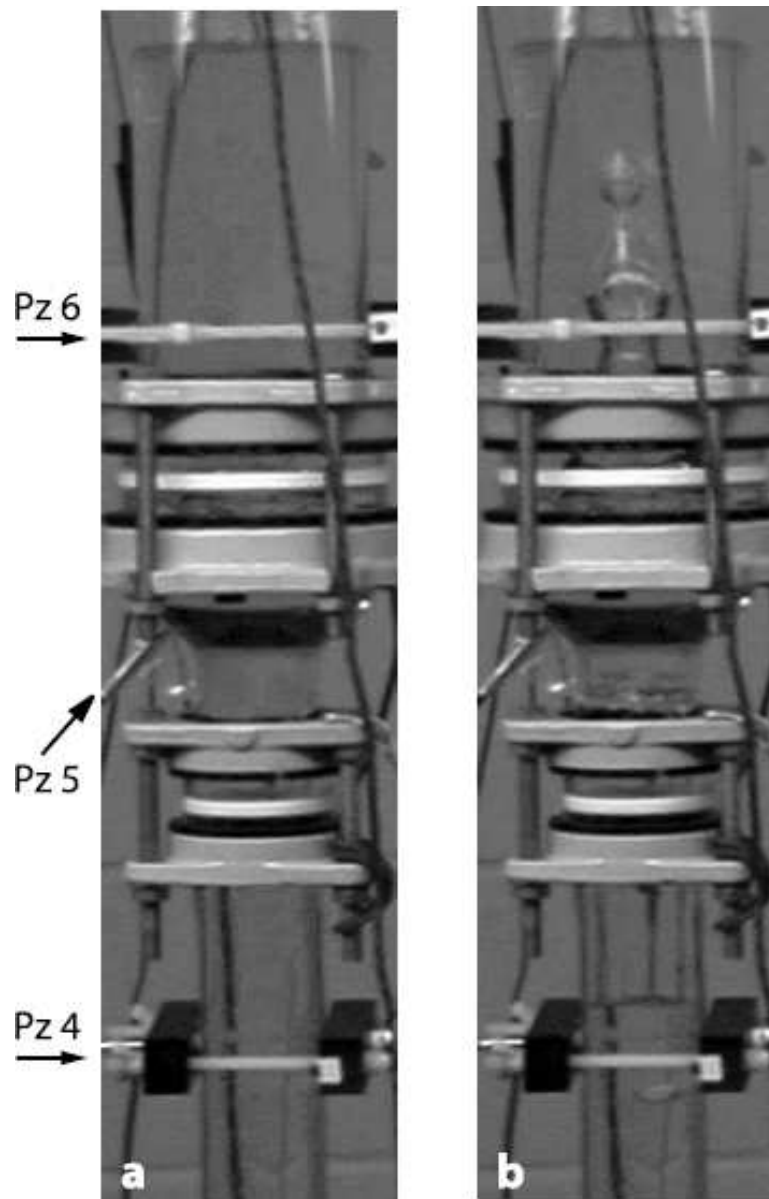


Figure 6.11: Photographs of the expansion section of the pipe showing the structural supports surrounding the pipe which obscure the video recording in the study of James et al. (2006). On the left without a bubble present (a) and on the right, (b), as a bubble has passed through the expansion.

approximately 60 Hz given and two lower frequency components one at 13 Hz and one at 6 Hz. James et al. (2006) attribute the high frequency oscillations to resonance within the fluid column caused by the deceleration of the liquid in the annulus as this closes and splits the bubble. They also hypothesise that the lower frequency oscillations are linked to the oscillation of the bubble left behind in the lower tube, in a similar fashion to those seen in Chapters 4 and 5. They also compare these to the theoretical frequency predicted by the model proposed by Vergnolle et al. (1996). The rise rates of the bubble throughout the ascent were also determined from an analysis of the video stills. In the lower pipe these velocities were constant at approximately 0.21 ms^{-1} for all bubble lengths. The average rise rate during the period of acceleration at the expansion ranges from 1 to 2.4 ms^{-1} for differing bubble lengths. The rise rate in the upper pipe varied with bubble length. This was due to the different length of bubbles formed after the expansion, with shorter initial bubbles not forming full Taylor bubbles but rather spherical cap bubbles.

6.2.3 Simulation Set-up

The CFD modelling approach which was introduced in Chapter 3 was used to simulate the experiments of James et al. (2006). The main alteration required to model the expansion was a different meshing strategy employed to account for the more complex geometry. James (by private correspondence) kindly provided additional photographs not presented in the original journal paper. These images were subsequently used to determine the geometry of the expanding section, one of these is shown in Figure 6.12. However, the thickness of the glass used to form the pipe expansion varies throughout the section, making it difficult to accurately determine the location of the inside surface of the pipe. An image analysis program, Digitizer, was used to estimate the location of a number of points on the inner surface of the pipe. A spline curve was then interpolated between these points using ANSYS ICEM software. This curve was used to define the wall boundaries of expansion section and was then connected to curves representing



Figure 6.12: A photograph of the expanding glass section used in the study of James et al. (2006) which was provided via private correspondence. This photograph was used to estimate the shape of the internal shape of the expanding section.

the upper and lower pipe sections to form a 2D axisymmetric section. This section was then swept through a rotation of 90° to generate a 3D volume. A schematic showing the stages of this process is illustrated in Figure 6.13. The figure shows, (a) the imported point data in image, (b) the 2D slice in image and (c) the 3D body in image. Subsequently, assuming a symmetrical flow regime a quarter pipe model was used to ensure mesh resolution was adequate whilst retaining important 3D effects expected when a bubble breaks as it rises through the expansion. This is discussed in more detail in Section 6.2.4.

When an internal mesh was created for a straight section of pipe, as in Section 3.3.1.2, a

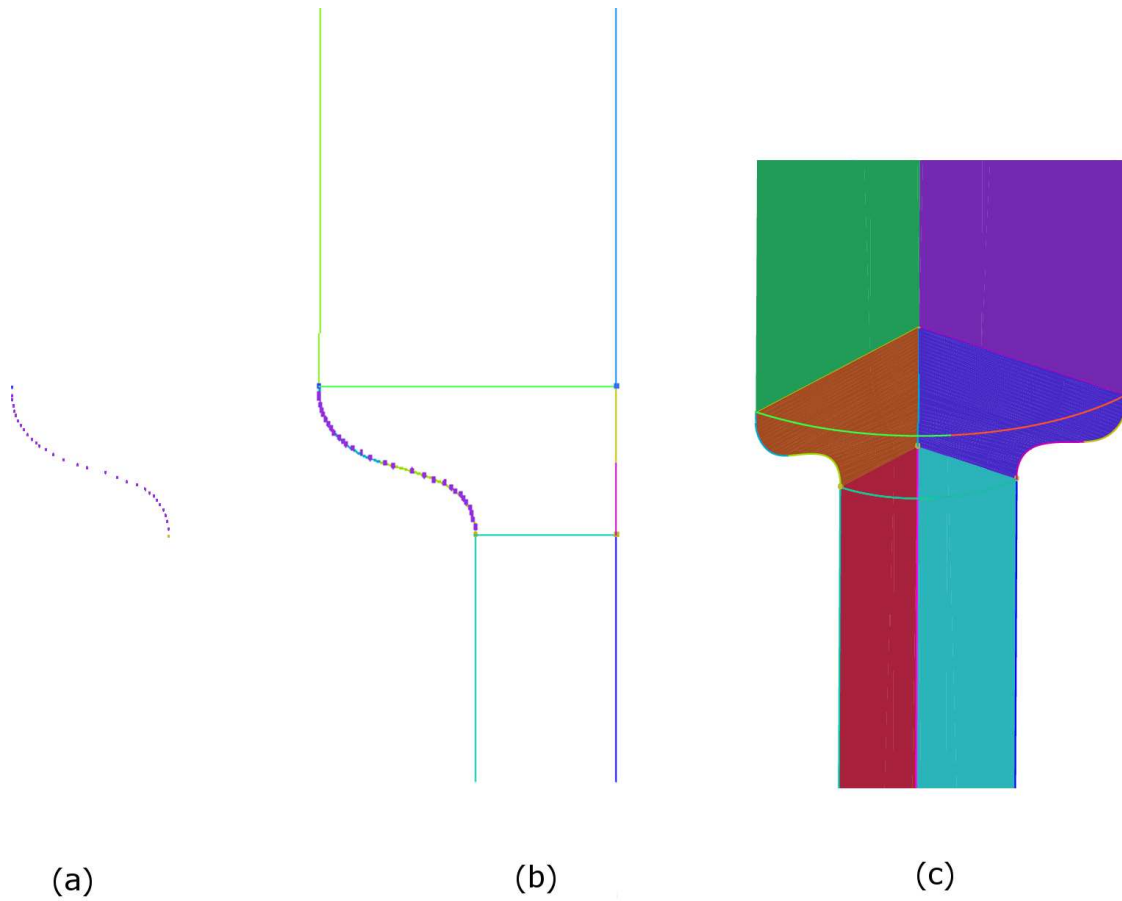


Figure 6.13: Images illustrating the model generation process. (a) The point data for the expanding section. (b) A 2D plane joining the expanding section with the rest of the domain. (c) The 3D section created by rotating the 2D plane.

surface mesh on the base of the pipe was extruded throughout the domain. When modelling a pipe which undergoes an expansion in diameter, this strategy must be altered to capture the important flow features that may be generated. Firstly, the pipe is split into three sections, the lower pipe, the upper pipe and the expanding section. The lower pipe section is meshed in the same manner as described in Section 3.3.1.2, using a quadrilateral O-grid topology. The cells at the interface between the top of the lower pipe and the bottom of the expanding section must align. If the expanding section is meshed in the same way, the shape of the expansion will result in a large number of poor quality, skewed cells. To avoid this problem, the expanding section is subdivided into four sections. Within each of these sections the spacing of the cells may be individually specified to control the shape of the mesh, to generate a higher quality mesh with fewer skewed cells. It should be noted that although the radial spacing of the cells can be altered within subdivisions of the domain, additional cells should not be added, as this would lead to the mesh becoming non-conformal. Cells can however be added in the axial direction, although this may have adverse effects on the aspect ratio of cells, and hence the quality of the cell. There is again a conformal interface between the top of the expanding section and the base of the upper pipe, from which the mesh is mapped throughout the flow volume of upper pipe.

6.2.4 Results of Validation Simulations

The vertical position of the nose of the rising bubble was recorded during the simulations. Pressure values were also recorded at each time-step of the simulations at two measurement points in the domain. These corresponded to the locations of the sensors PZ4 and PZ6 from James et al's experiments, which were located at the wall at approximately 0.65 m and 0.36 m below the top surface of the liquid. These data were then analysed using a Fast Fourier Transform (FFT) algorithm to create a power spectral density graph, from which the dominant frequencies could be determined.

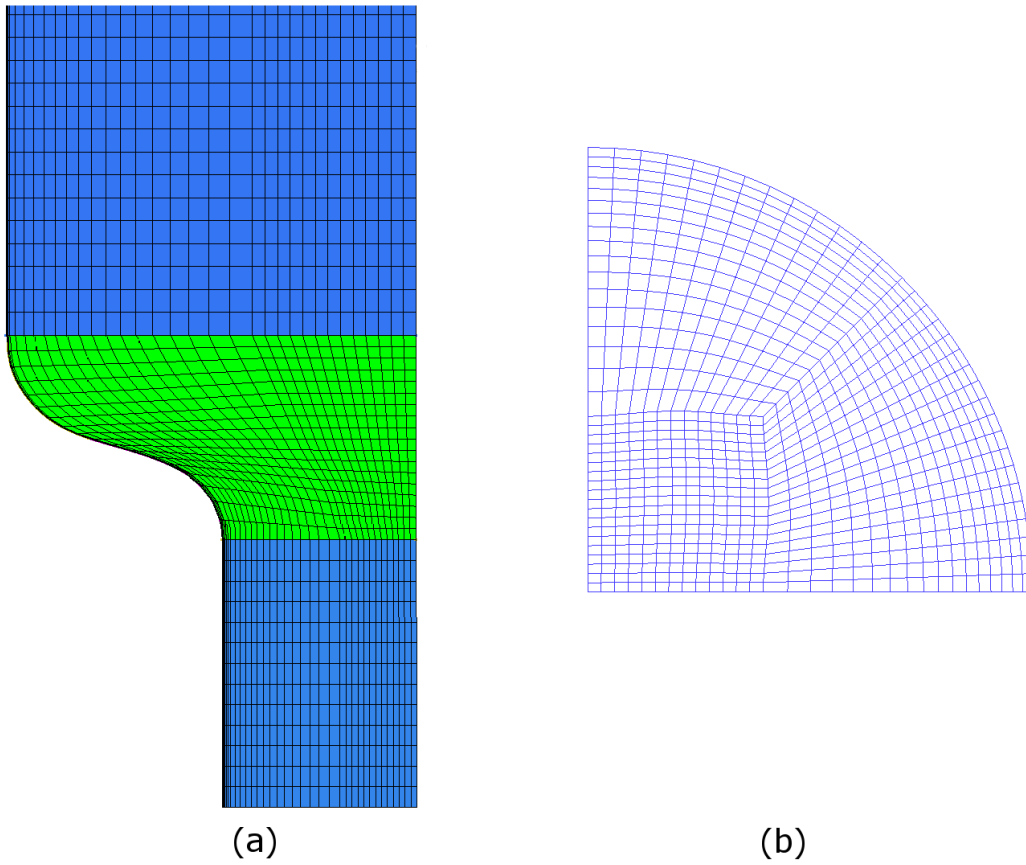


Figure 6.14: Image showing the mesh on (a) the symmetry plane (b) the outlet.

A set of simulations were conducted on grids of 3 different sizes in order to test mesh independence. In these simulations the terminal velocity in the lower pipe and frequencies generated were recorded. The GCI method, previously described in Section 3.2.2, was used to determine an estimate of the error introduced by spatial discretisation. Meshes of approximately 950000, 485000 and 250000 cells were used which gave a GCI error of 0.37% for the finest mesh and 0.57% for the intermediate mesh based on the rise velocity in the lower pipe. It was concluded that the intermediate mesh provided a satisfactory level of accuracy.

A bubble of length $4.4L'$ was introduced to the domain in the same manner as previously described. The nose of this bubble is initially 0.843 m below the top surface of the liquid, and hence 0.243 m below the start of the expanding section. The height of the expanding section was an order of magnitude smaller than the height of water above it. As the bubble ascends the lower tube, a steady rise velocity is maintained. This is followed by a rapid acceleration as the bubble enters the expanding section. The non-dimensional value of the rise velocity in the lower pipe is within 1.5% of the experimental measurements of James et al. (2006), with a Froude number of 0.355, in comparison to the experimental value of approximately 0.35.

An examination of the results of a frequency analysis show dominant frequencies at approximately 13 Hz and 56 Hz, which are comparable to the frequencies determined in the experiments of James et al. (2006) (13 Hz and 60 Hz) when the rise of a bubble of a similar length is studied. However, the low frequency component at 6 Hz which is observed in the experimental study is not replicated in the simulations.

In the experiments reported by James et al. (2006), the critical length of the bubble, introduced in Section 6.1 was bounded by $2.2L'$ and $3.3L'$. Simulations were conducted with bubble lengths of $2.2L'$ and $3.3L'$, and the results of these agreed with the behaviour observed in the experiments. A bubble of length $2.2L'$ successfully passed through the expansion before the neck closed, whereas a bubble of length $3.3L'$ was split by the pinching at the neck, which results in

a smaller bubble to be left behind in the lower pipe.

The preceding simulations were carried out using a 3D quarter pipe model with planes of symmetry. To retain the same level of spatial resolution, a full pipe 3D model would have required approximately 2 million cells. This mesh was created and used in a simulation which showed comparable results to the quarter pipe simulations with a Froude number of 0.352 in the lower pipe and dominant frequencies of 12 and 54 Hz. However, the computing power required was too great to consider this a viable option for all simulations and so the quarter pipe model was used for all following simulations.

6.3 Results

6.3.1 Variation of curvature of expansion

The expanding section used by James et al. (2006) was made of blown glass, giving a curved expansion profile. This curved profile was not used as it modelled the physical situation more accurately than a simple straight sided expanding section, but rather because it was an off the shelf part and hence readily available. As previously detailed in Section 6.2.3, the curved expansion creates additional difficulties when creating a mesh to model this domain. It also introduces difficulty when comparing sections which expand at different rates. A comparison between this curved expansion, based on the experimental blown glass pipe, and a straight sided expansion (expanding over the same height) was conducted to ascertain if the same conclusions could be drawn.

The dominant frequencies found by applying the power spectral density to the pressure readings for the straight sided expansion are very similar to those for the curved expansion. These were 13 Hz and 56 Hz for the curved expansion and 14 Hz and 59 Hz for the straight sided expansion and are shown in Figure 6.15. This suggests that the sources of oscillation are not

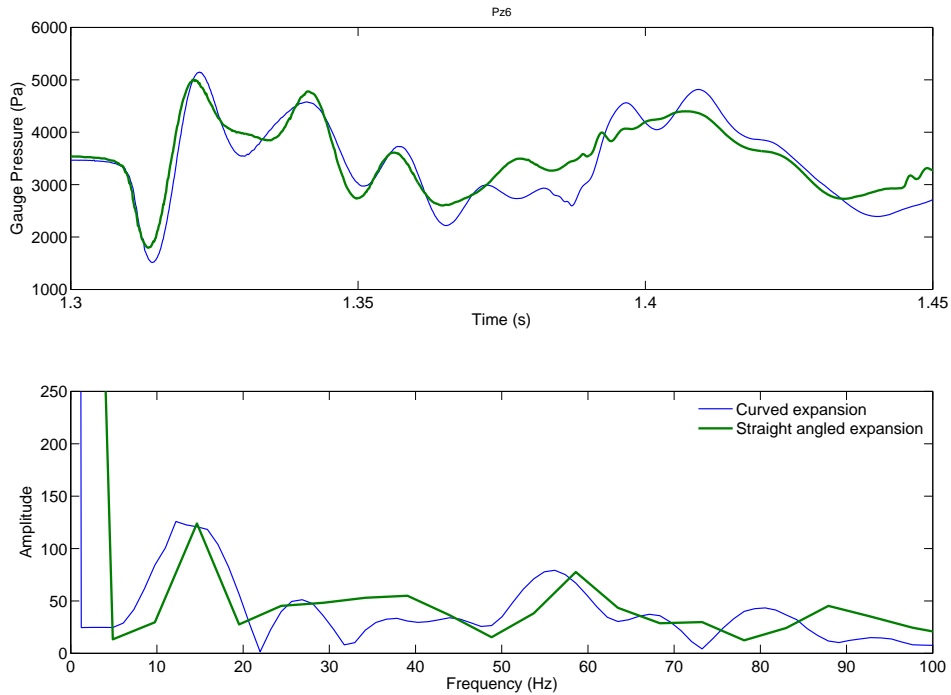


Figure 6.15: A comparison of the frequencies produced the bubbles passing through the (a) curved and (b) straight sided expansions. The dominant frequencies are similar for both the curved and straight expansion profiles indicating the sources of oscillation are not greatly by the curvature of the expansion.

affected greatly by the curvature of the expansion. This hypothesis was tested, and proven to hold, for two fluid viscosities of 0.001 and 0.1 Pa s.

The bubbles rise at approximately the same velocity throughout the lower tube, although the bubble with in the curved expansion is approximately 1% faster. The bubbles also accelerate through the expansion at a similar rate. After the bubble passes through the expanding section the liquid film caused by the closure of the neck is observed to burst through the nose of the bubble. This happens at approximately 1.3 s after the release of the bubble and leads to the

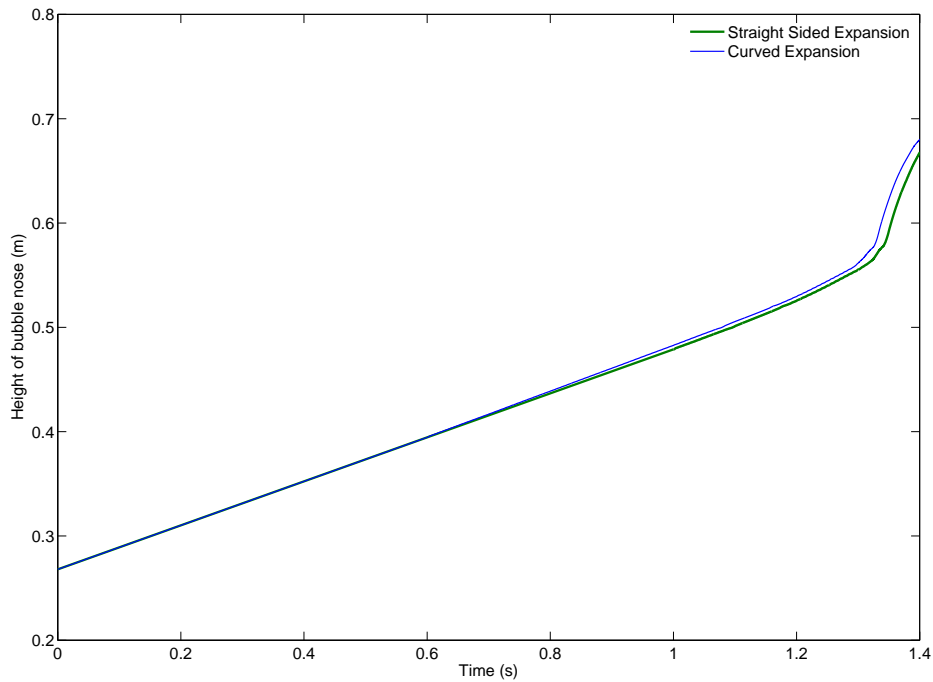


Figure 6.16: A comparison of the simulated positions of the nose of the bubbles whilst rising through pipes containing a straight sided or curved expansion. The bubbles rise through the lower pipe with rise rates within 1% of each other and exhibit similar behaviour as they encounter the expansion in pipe diameter.

large acceleration observed to occur at this time. This is shown by analysing the position of the nose of the bubbles with respect to time in Figure 6.16.

In both the experiments and simulations that involved a curved expansion profile, the critical length of bubble which could pass through the expansion before the neck closed was bounded by $2.2L'$ and $3.3L'$. Simulations were also conducted using a straight sided expansion and bubbles of length $2.2L'$ and $3.3L'$. An analysis of the results of these simulations shows that critical length of bubble is also bounded by these lengths in the straight sided expansion, and is shown

in Figure 6.17. It should be noted that although there are some small bubbles left in the lower tube for the bubble of length $2.2L'$, these are bubbles which have been shed from the tail, rather than being formed during passage through the expansion.

The major conclusion drawn from this study is that the flow behaviour of bubbles passing through straight sided and curved expansion profiles is comparable. All of the main flow features present in the original simulations remain and consequently it was decided to employ straight sided expansions as the basis of the simulation results presented for the remainder of this chapter. Straight sided expansions were used so that a systematic variation of the angle of expansion could be conducted.

6.3.2 Variation of angle of expansion

6.3.2.1 Base case

An analysis of the results of the studies of Danabalan (2012) and Soldati (2013) shows that a more gradual expansion between two pipes of differing diameter will change the behaviour of the rising bubble. A computational parametric study was conducted to assess the effect of varying the angle of expansion, θ , between 15° and 90° . This angle is defined as shown in Figure 6.26, and is equal to 90° when the direction of expansion is perpendicular to the lower pipe wall and 0° when the pipe undergoes no expansion in diameter. The length of the expansion, L_{exp} , is the distance in the z direction over which the diameter of the pipe is expanding. This increases as the angle θ decreases.

In order to model higher angles of expansion (45° and over), a further change needed to be applied to the meshing strategy. An extra block was added to the topology of the mesh for the expanding section upwards. This requires the addition of extra cells in the radial direction to maintain resolution and quality of the cells in the expanding section. Figure 6.19 shows this

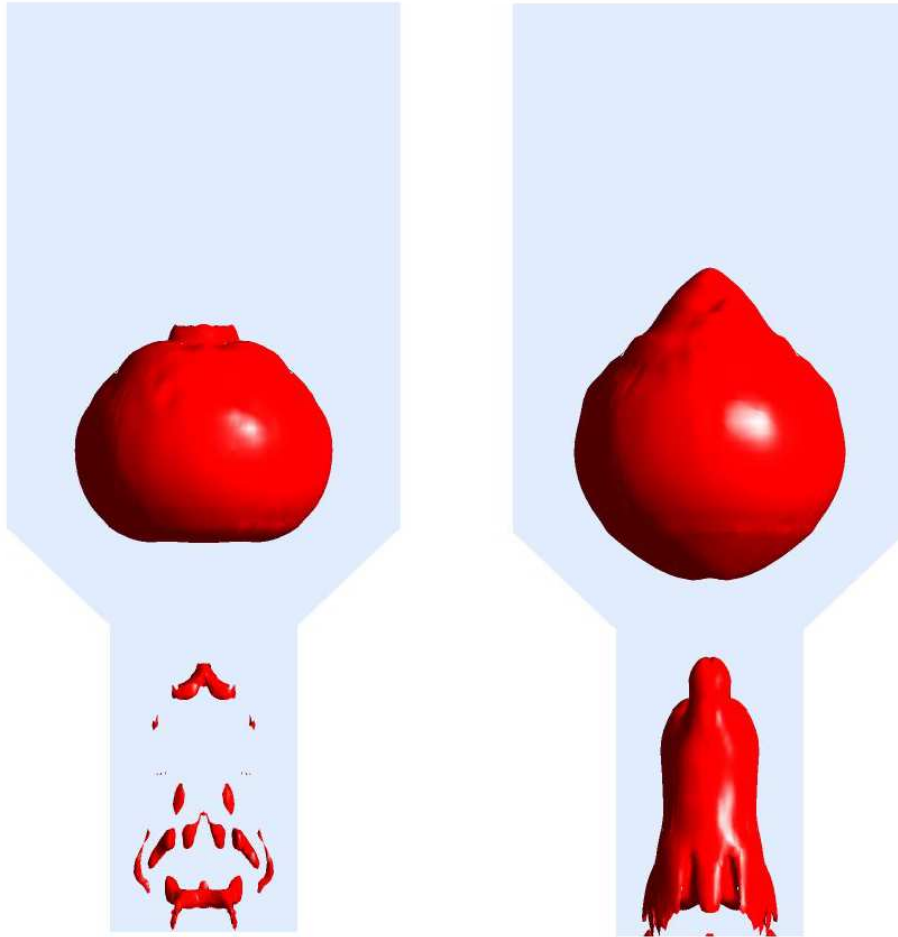


Figure 6.17: Images indicating that the critical length of bubble is bounded by lengths of $2.2L'$ (left) and $3.3L'$ (right). On the left, the only gas left in the lower pipe is that which has been shed from the tail of the bubble during the rise. On the right, the necking process has broken the longer bubble into two distinct bubbles, leaving one in the lower section of the pipe.

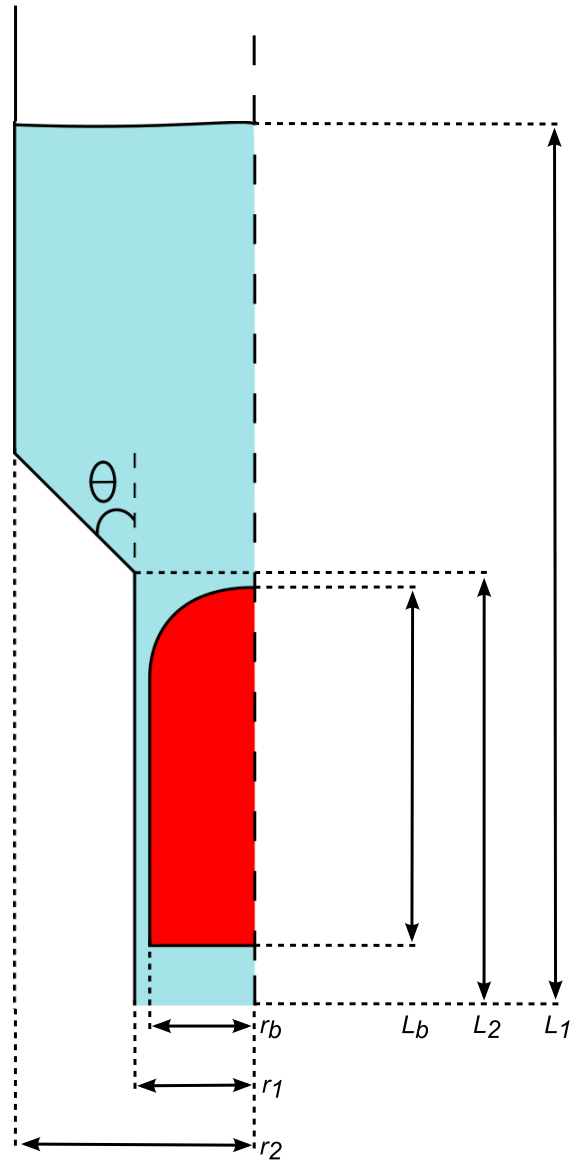


Figure 6.18: A schematic illustrating how the angle of expansion, θ , along with other quantities, are defined. Here, r_1 is the radius of the lower pipe, r_2 is the radius of the upper pipe, r_b is the radius of the bubble, L_1 is the height of the water surface above the base of the lower pipe, L_2 is the height of the start of the expansion section above the base of the lower pipe and L_b is the length of the bubble.

change in topology at the expanding section and at the outlet to the domain for the 90° expansion in diameter.

An initial set of simulations were conducted to investigate the effect of varying the angle of expansion whilst keeping all other parameters constant. Bubbles with an initial length of $4.4L'$ (0.167 m) were introduced, such that the nose is located at a depth of 0.843 m below the surface (0.233 m below the start of the expanding section) using the method described in Section 3.3.1.3.

Figure 6.20 shows a bubble during passage through the 90° expanding section, along with images showing the turbulent flow properties in the region around the bubble, turbulent kinetic energy, k , turbulent eddy dissipation, ε and eddy viscosity, μ_T . As can be observed from these images, k and ε are largest at the points where the bubble is pinching off and in the wake of the bubble where smaller bubbles had been shed.

Large qualitative differences are observed when the angle of expansion is varied. As the angle of expansion decreases, an increased volume of air is able to pass through the expansion in a single bubble, and hence the size of the bubble remaining in the lower pipe is reduced. Depending on the angle and length of bubble, the whole bubble may pass through at the same time. This length of bubble will be referred to henceforth as the critical bubble length. Figures 6.21 and 6.22 illustrate the qualitative differences in bubble behaviour when the angle of expansion is varied. A bubble passing through the 90° expands more quickly in both the lateral and vertical directions. A smaller bubble in the upper pipe is also formed given the 90° section and this hence leaves a larger volume of gas in the lower pipe than the more gradual expansions. This is most clearly observed when comparing the expansions with angles of 15° and 90° . A bubble that rises through the 15° expansion is observed to expand less quickly than the more severe 90° expansion. After a simulation time of approximately 1.1 s, the nose of bubbles in both the 90° and 15° cases enter the expanding section (at a height of 0.5 m above the base of the pipe). However, at a time of 1.3 s, the nose of the bubble in the 15° case has risen to a height of 0.55 m, whereas the

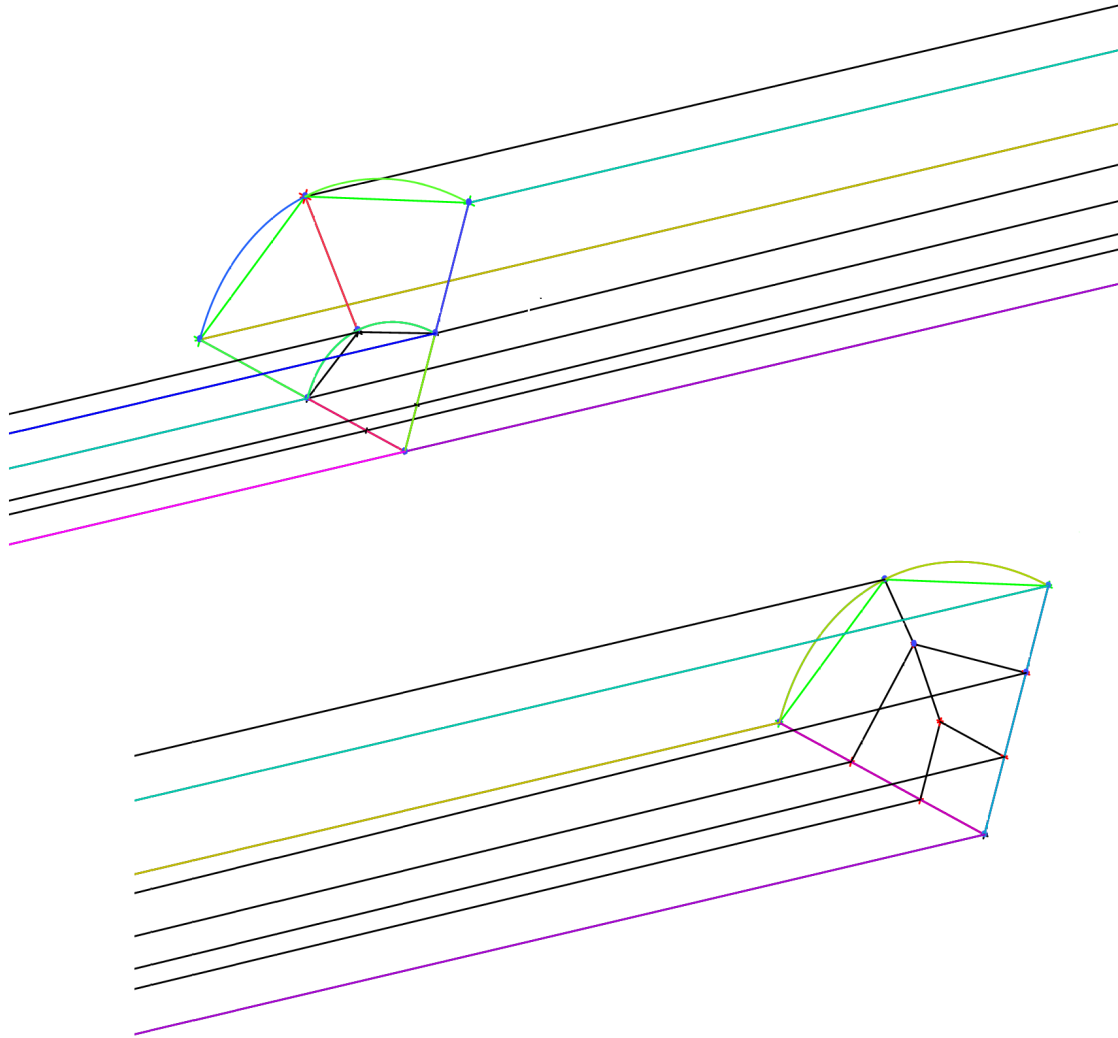


Figure 6.19: A schematic illustrating the block topology used at expanding section (above) and at the outlet (below) for the 90° expansion. An extra block was added to the topology of the mesh for the expanding section upwards. This requires the addition of extra cells in the radial direction to maintain resolution and quality of the cells in the expanding section.

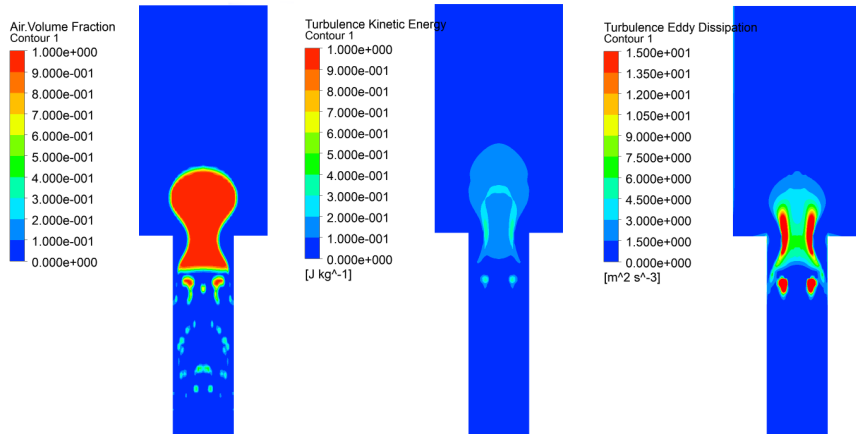


Figure 6.20: Images showing, top left, a bubble during passage through the 90° expanding section, centre, the turbulent the turbulent kinetic energy, k , in the area surrounding the bubble at the same time, and right, the turbulent eddy dissipation, ε .

nose of the bubble in the pipe with a 90° expansion is at a height of 0.568 m. This amounts to an increase of 20% in the distance travelled by the nose of the bubble over this period.

Figure 6.24 shows a comparison of the power spectral density of the signals generated by initially identical bubbles passing through expansions with angles of $\theta = 90^\circ$, 75° , 60° , 45° , 30° and 15° . An analysis of the frequency data generated by the different simulations confirms that the lower dominant frequency remains approximately constant regardless of the angle of expansion. There is an increase in the higher frequencies as the angle of expansion increases. However, the higher frequencies are not as significant as the lower ones, exhibiting much shallower peaks. It is therefore harder to identify the cause of these oscillations. However, it is noted that in the case with a 15° expansion, no dominant higher frequency is observed. This is also the only case in which none of the bubble is left in the lower pipe after the necking. One explanation could be that the higher frequency oscillations are caused by the oscillation of the portion of bubble remaining in the lower pipe, once the nose section has passed through the expansion. The lower frequency of approximately 14 Hz remains constant regardless of the angle of expansion.

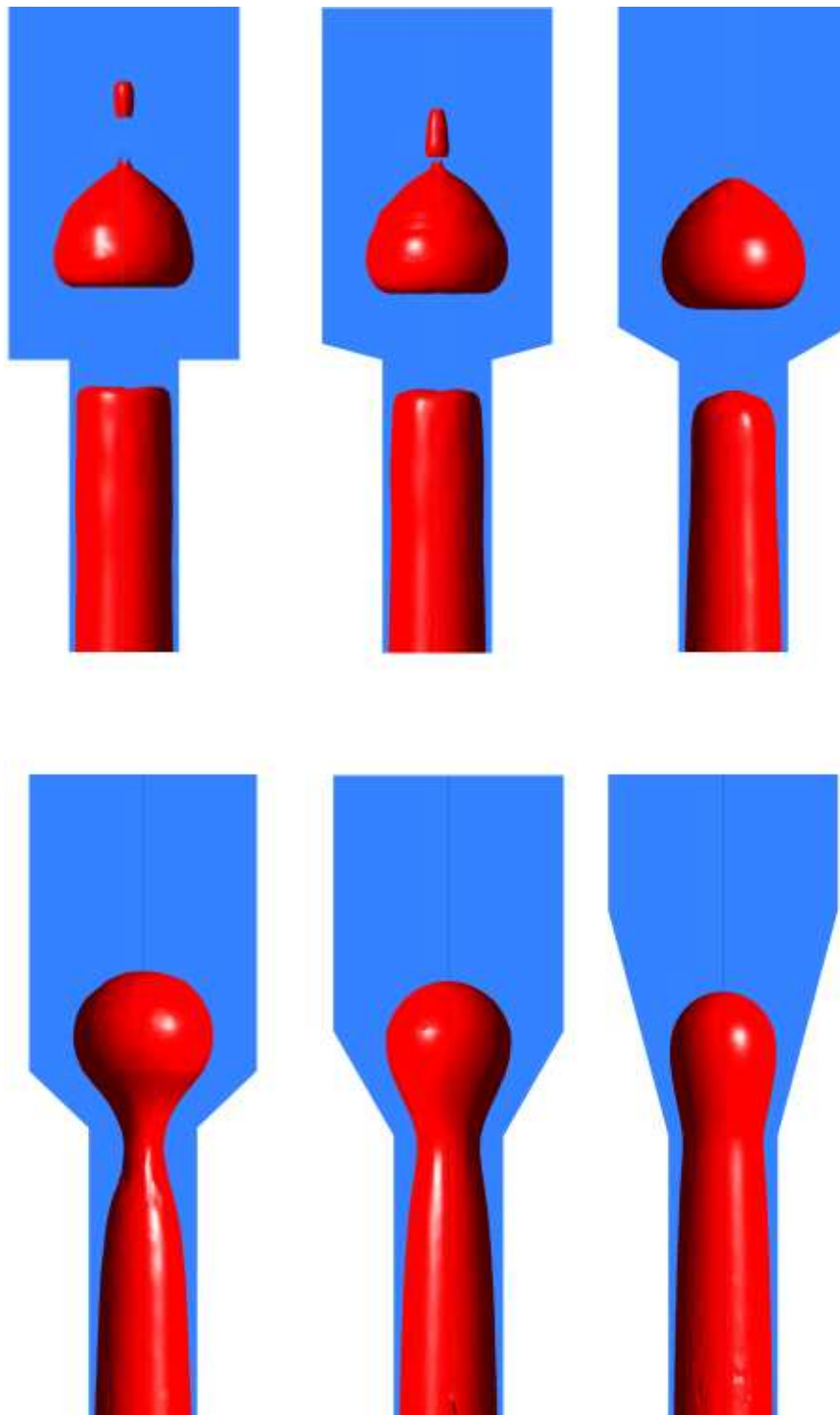


Figure 6.21: Iso-surface images indicating the location of initially identical bubbles passing through expansions with angle of expansion, $\theta = 90^\circ, 75^\circ, 60^\circ, 45^\circ, 30^\circ$ and 15° at $t=1.3$ s.

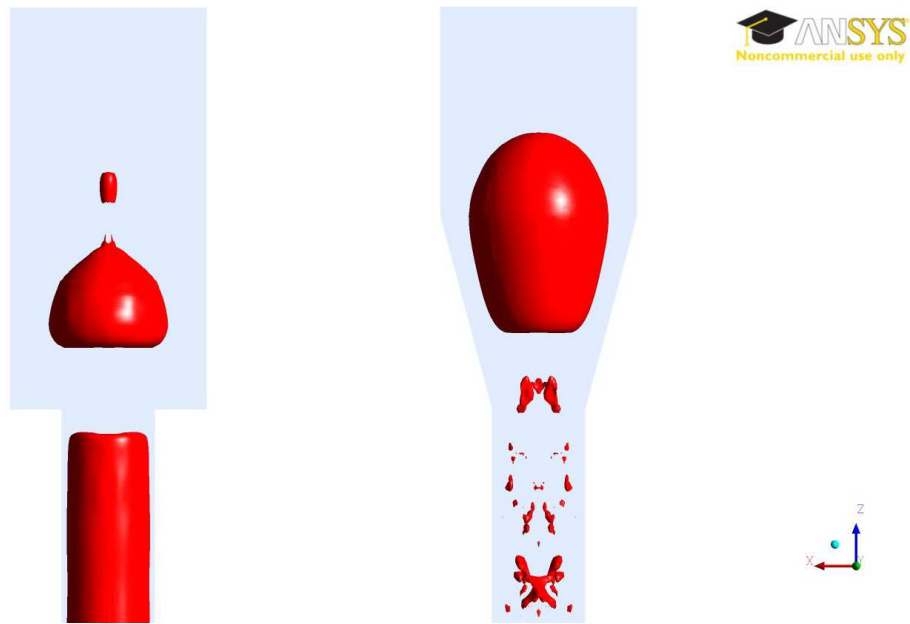


Figure 6.22: A comparison between the (a) 90° and (b) 15° cases. Each iso-surface indicates the location of the surface of the bubble after the neck has closed.

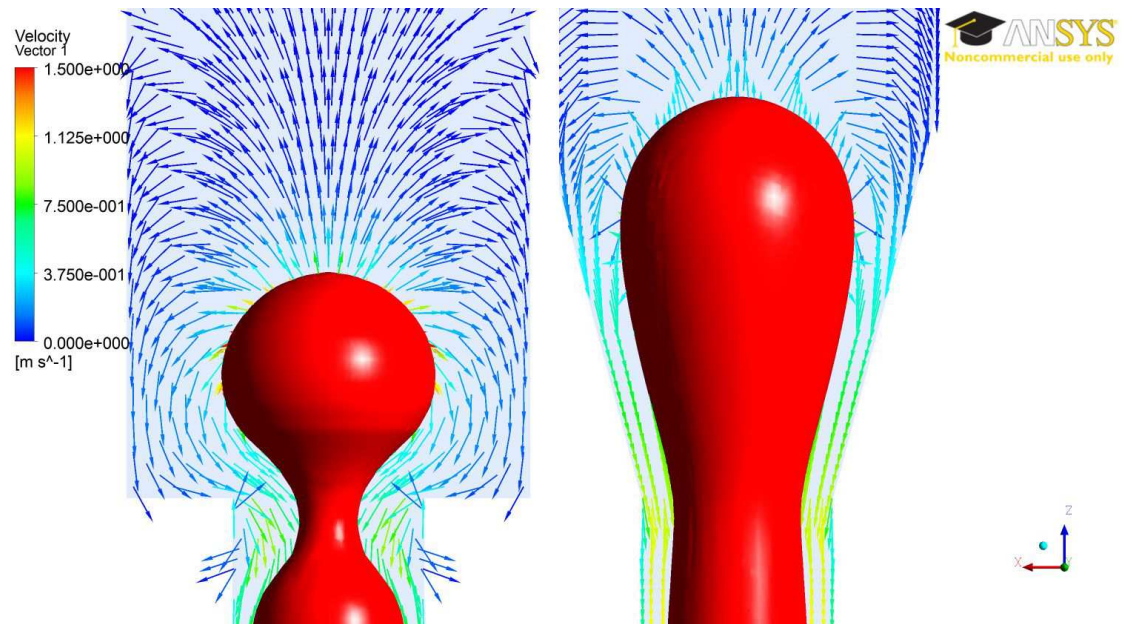


Figure 6.23: A comparison between the (a) 90° and (b) 15° cases. For each, the iso-surface indicates the location of the surface of the bubble and the vectors represent the velocity.

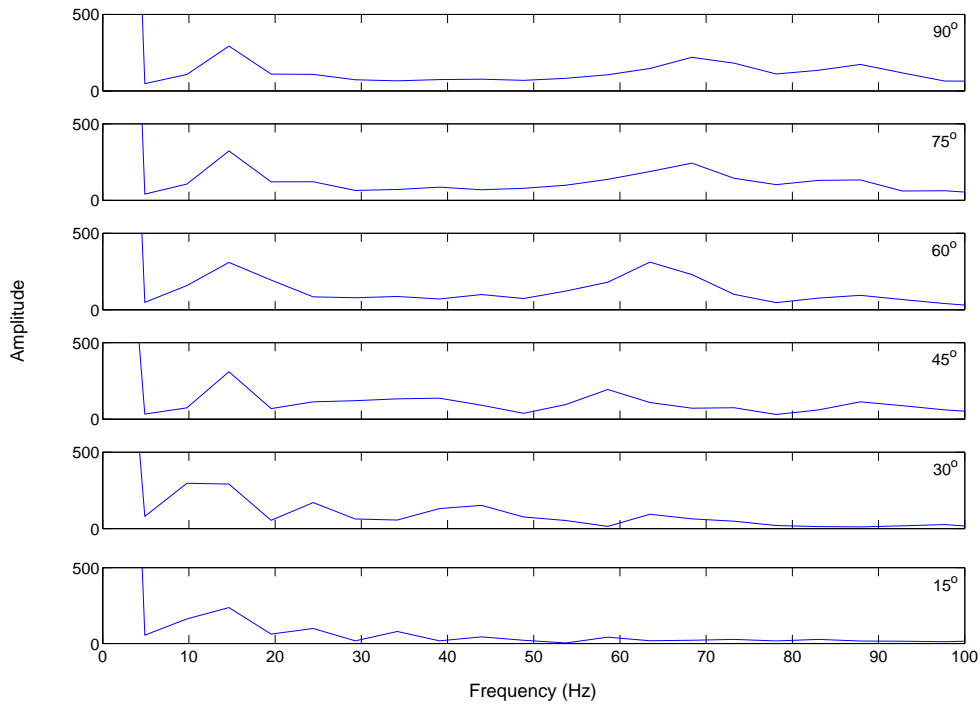


Figure 6.24: Plots showing the frequency of the signals generated by initially identical bubbles as they pass through expansions with an angle of expansion of $\theta = 90^\circ, 75^\circ, 60^\circ, 45^\circ, 30^\circ$ and 15° . The lower dominant frequency remains constant throughout while there is an increase in the higher frequencies as the angle of expansion increases.

This is consistent with the conclusion that this frequency oscillation is generated by the natural oscillation of the bubble similar to that discussed in Chapters 4 and 5. The source of any higher frequency signals from these simulations cannot be identified with any certainty. It is recommended that further work be conducted to confirm the source of these signals.

6.3.2.2 Critical Length

The qualitative conclusions drawn from both the experimental work conducted by Soldati (2013) and Danabalan (2012) and the simulations presented in Section 6.3.2.1 show that given a more

gradual expanding section, longer bubbles are able to pass through before the neck closes causing the bubble to be split into two parts.

A series of simulations were conducted to determine the critical length of a Taylor bubble in a 0.038 m pipe expanding into a 0.08 m pipe for different angles of expansion. The results of the simulations reported in Section 6.3.2.1 were used to determine initial estimates of the critical length of bubble for each angle of expansion. The initial bubble length was then refined to determine the value of the critical bubble length, L_c . The exact value of this critical length lies between an upper bound, a length at which part of the bubble is split into two parts by the closing neck, and a lower bound, a length at which the bubble was observed to pass fully through the expansion before the neck closed. Figure 6.25 shows an example of the simulated upper and lower bounds of the critical length for the 90° expansion case.

Figure 6.26 shows a plot of the results of these simulations. An analysis of these results confirms that longer bubbles are able to successfully pass through the smaller angles of expansion. However, the relationship between the angle of expansion, θ , and the critical bubble length, L_c is not linear, but increases rapidly as the angle of expansion approaches 0. Figure 6.27 shows a replot of the same data as presented in Figure 6.26, but with the $\text{cosec}\theta$ ($1/\sin\theta$) plotted against the critical bubble length. A linear regression analysis of these data concludes that a linear relationship exists between $\text{cosec}\theta$ and critical length (with R^2 values of 0.998 for the lower bound and 0.997 for the upper bound).

This confirms that the angle of expansion directly influences the flow behaviour. To investigate this finding further, the flow field around the bubble was studied. As shown in Figure 6.23, the fluid velocity fields in the film surrounding the bubble are significantly different between the extreme cases of 90° and 15° expanding sections.

To quantify this difference, the angle of the velocity relative to the vertical, z axis, were

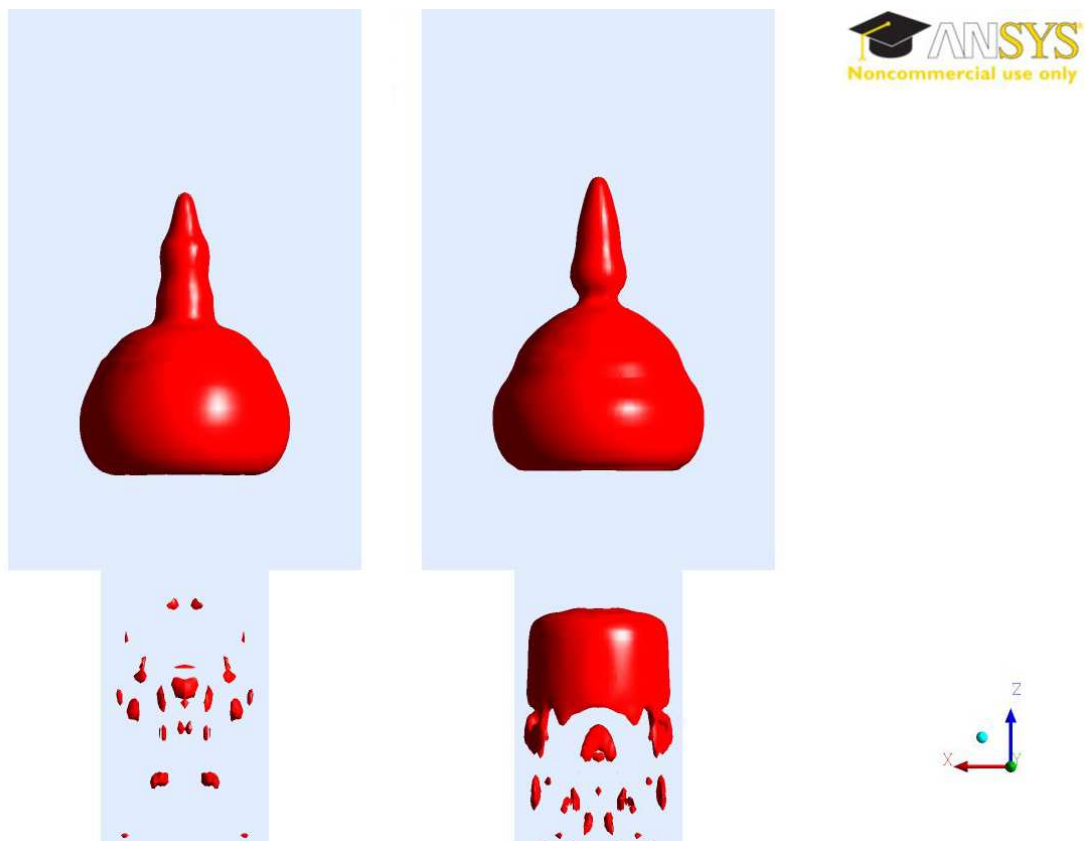


Figure 6.25: 3D iso-surfaces showing an example of the bubble at or above the upper bound of the critical length(left), and at or below the lower bound of the critical length (right) as they pass through a 90° expansion.

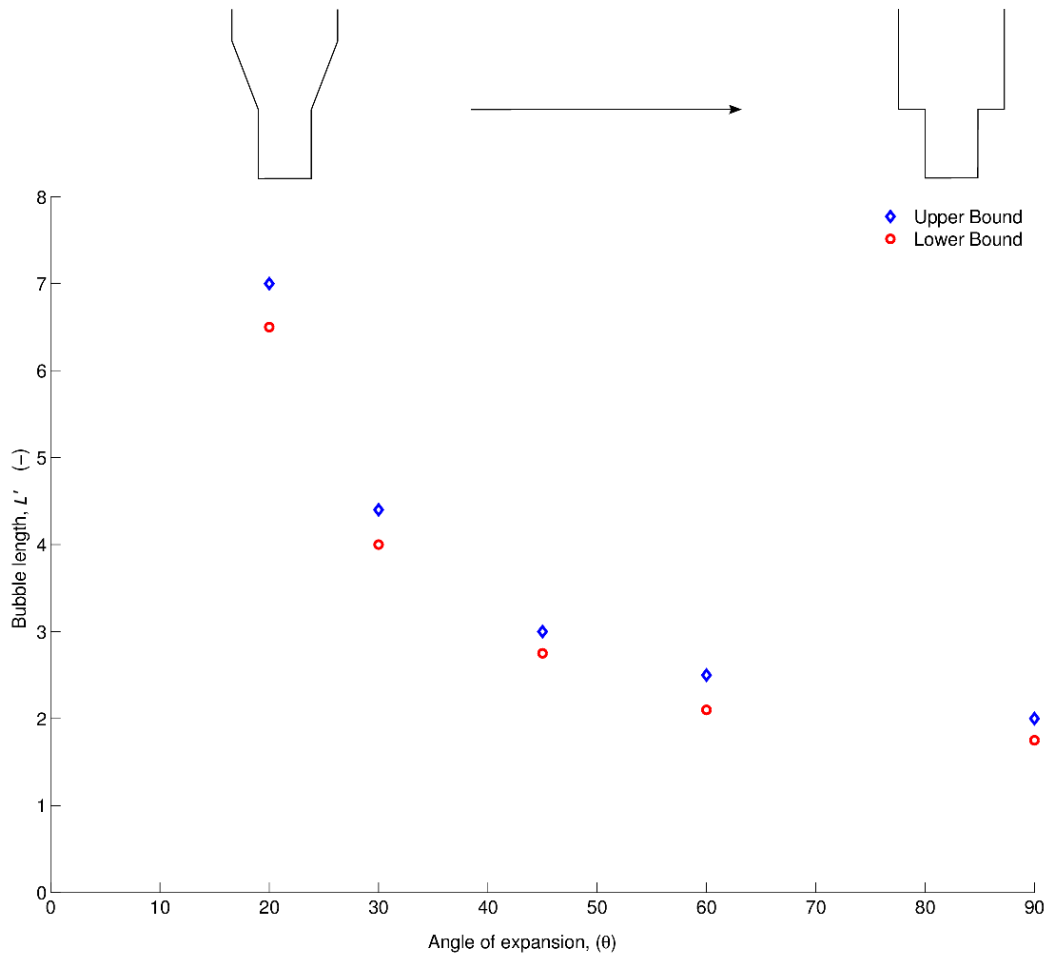


Figure 6.26: A plot of the upper and lower bounds of the critical length of bubble which can fully pass through the expansion before the neck closes against the angle of expanding section.

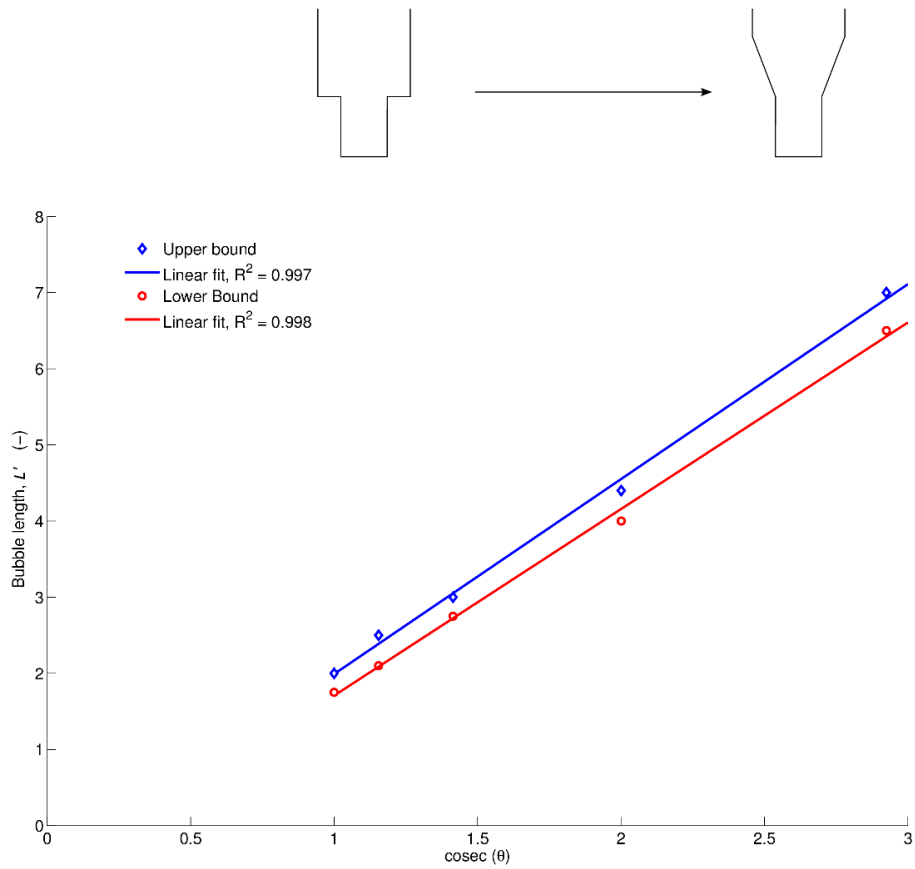


Figure 6.27: A plot of the upper and lower bounds of the critical length of bubble which can fully pass through the expansion before the neck closes against the cosec of angle of expanding section. This shows a linear relationship between L' and $\text{cosec}\theta$.

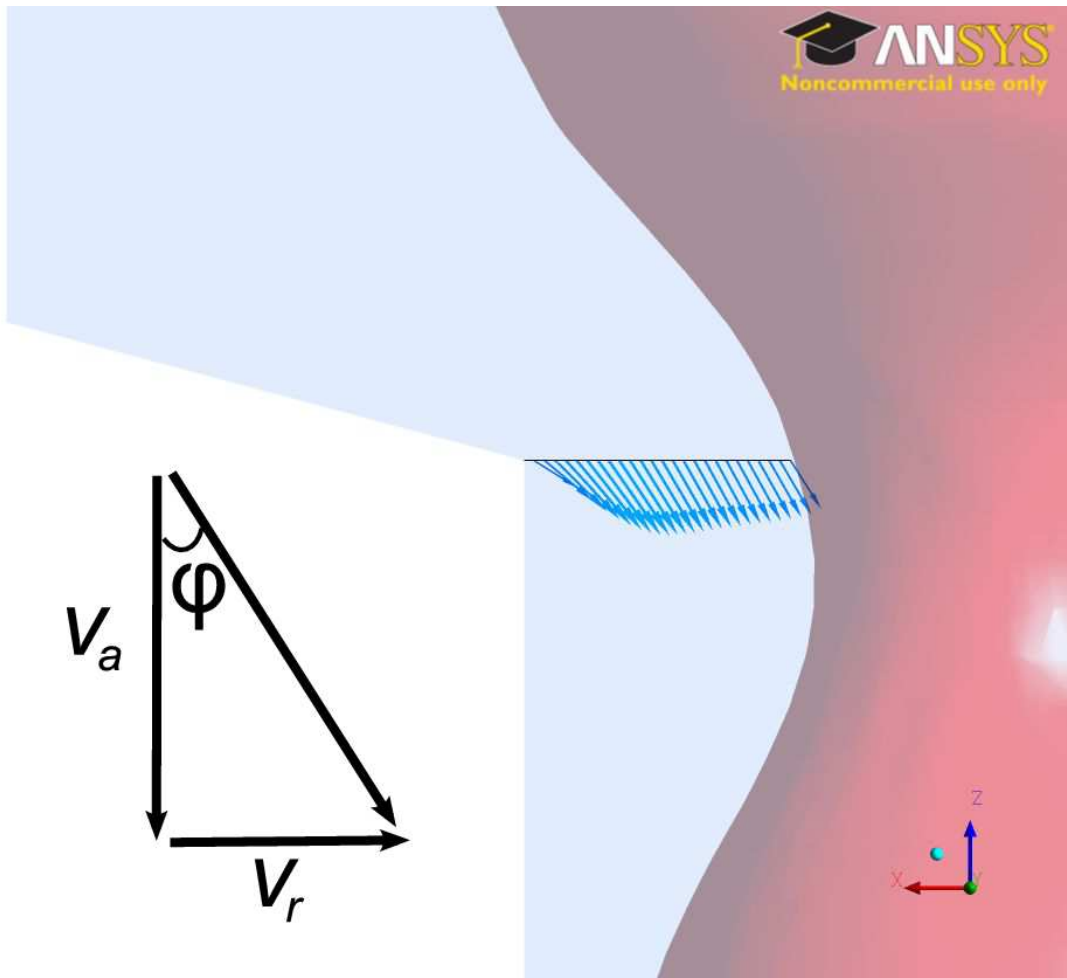


Figure 6.28: Schematic illustrating the definition of the angle ϕ .

averaged over the radius of the film. These are given by

$$\phi = \tan^{-1} \frac{u_r}{u_z} \quad (6.1)$$

where u_r and u_z are the radial and axial components of the velocity, as indicated in Figure 6.28. These were taken at the level of the base of the expansion, at a height of 0.5 m from the base of the pipe. Figure 6.29 illustrates the results of this investigation, where the angle ϕ is observed to vary in a linear fashion with θ .

One possible explanation for the relationship between the critical length of bubble and $\text{cosec}\theta$

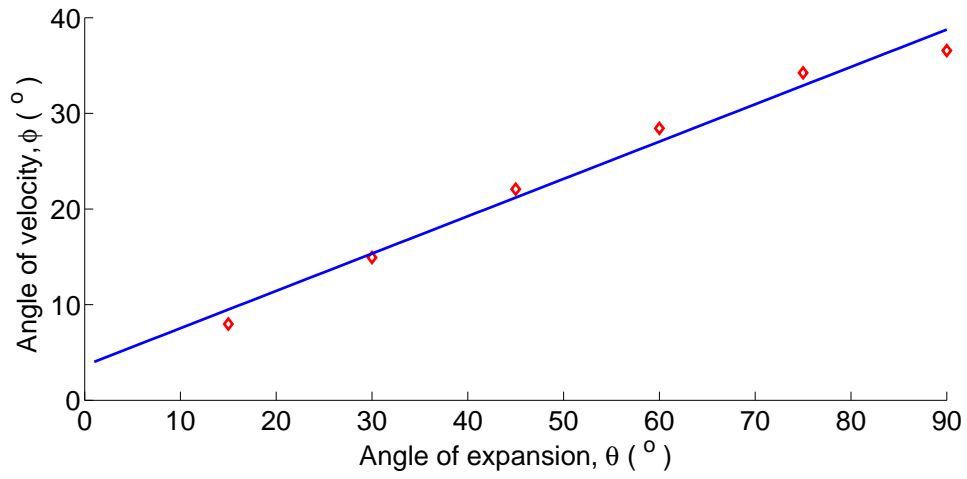


Figure 6.29: Plot showing the linear relationship between ϕ and *theta*.

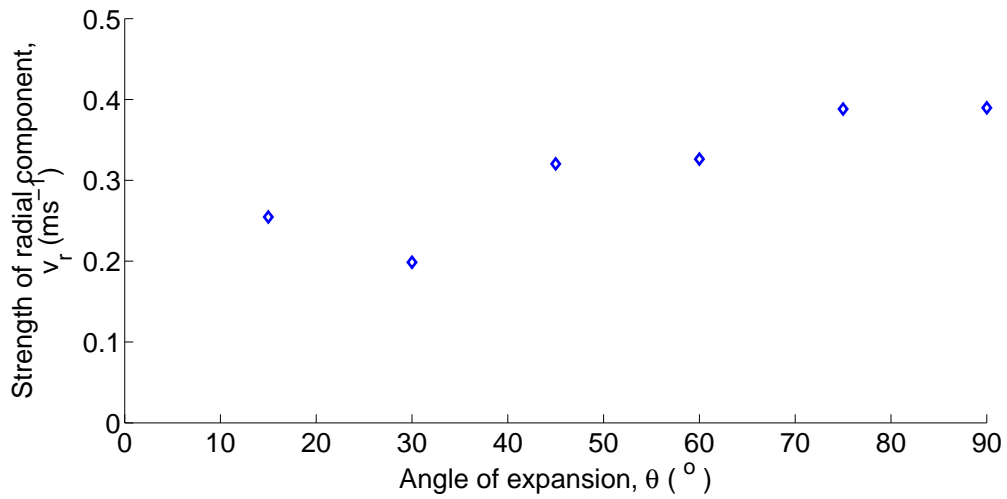


Figure 6.30: Plot showing the relationship between v_r and *theta*.

is to consider the time taken for the bubble to rise through the expansion. Assuming the bubbles with length, L' are all rising with the same velocity, u , the time, T , taken for the bubble to pass through the expansion is

$$T = L'/u. \tag{6.2}$$

While it passes through the expansion, it is being affected the radial component of a jet of strength, v_r , which is assumed to be constant (as it is shown to be approximately constant in Figure 6.30. The radial component of the jet is $v_r \sin\phi$. Assuming that jet works its way into the bubble at a constant rate, it will take

$$T = D/(2v_r \sin\phi), \tag{6.3}$$

where D is the diameter of the lower tube, to pinch off the bubble. Equating these two times and rearranging gives

$$L' = (uD/2v_r) \frac{1}{\sin\phi}. \tag{6.4}$$

As shown in Figure 6.29, ϕ is linearly related to θ , and so

$$L' \propto \operatorname{cosec}\theta. \tag{6.5}$$

The experimental results of Soldati (2013) were also analysed in the same manner for comparison, and are shown in Figure 6.31. From this it can be observed that whilst a linear relationship may exist between $\operatorname{cosec}\theta$ and L_c , its fit within experimental error is not as good as that predicted by the simulated data. In this case, a linear regression analysis leads to a coefficient of determination, R^2 of 0.95. This discrepancy may in part be due to the relatively large discrete increments between the different volumes of gas injected during the experiments.

From an analysis of the results of these simulations it was concluded that the angle of the expanding section can significantly affect the flow field around the Taylor bubble as it rises through the expansion. The variation in the direction of flow affects the necking process, which may influence the critical length of bubble which may pass through the expansion without splitting into

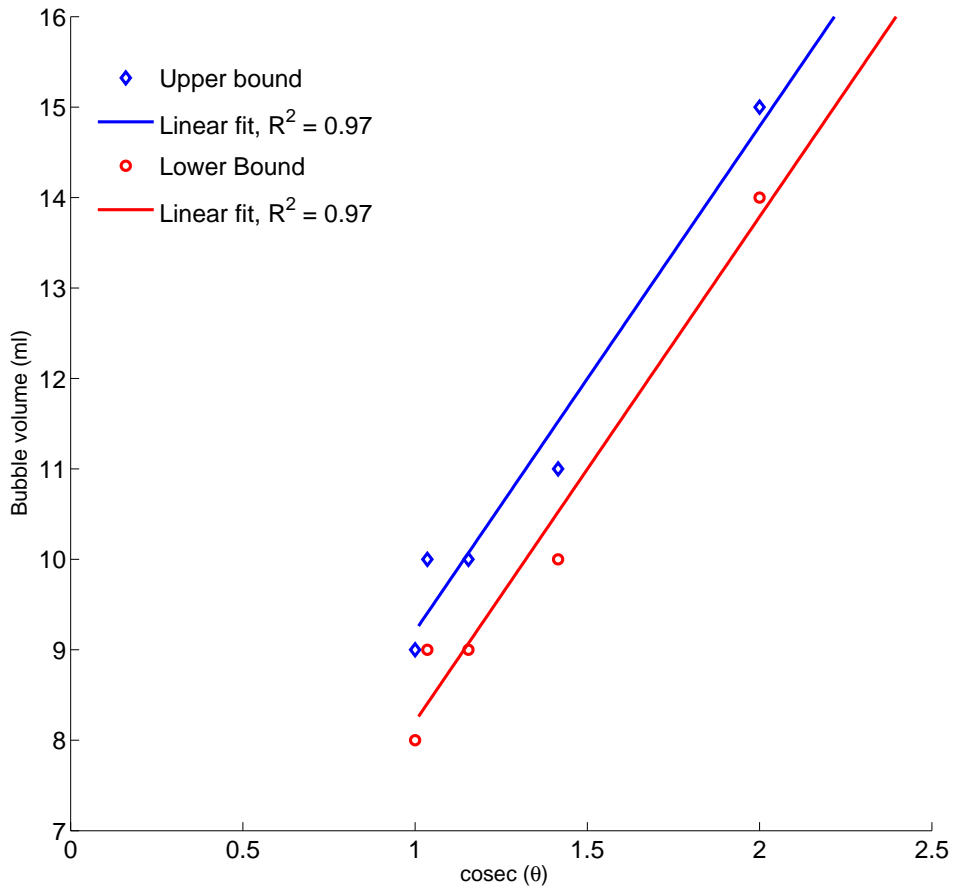


Figure 6.31: The upper and lower bounds of the critical volume of bubbles which can fully pass through the expansion before the neck closes against $\text{cosec}\theta$ for the experiments performed by Soldati (2013). This also shows a linear relationship between bubble volume and $\text{cosec}\theta$ supporting the results of the simulations.

two parts. The variations in the critical bubble lengths for both the simulations presented and the experiments of Soldati (2013) were confirmed to have a linear relationship to $\text{cosec}\theta$.

6.3.3 Variation of viscosity

A set of simulations was conducted in which the viscosity of the liquid phase was varied. The experiments of James et al. (2006) and Soldati (2013); Danabalan (2012) suggest that the necking process is governed mainly by the geometry of the expanding section, rather than the viscosity of the fluid.

In the simulations presented, the viscosity of the liquid phase was varied over 3 orders of magnitude (from 0.001 Pa s, 0.1 Pa s and 1 Pa s) to verify if the behaviour observed in Section 6.3.1 is still observed in more viscous liquids. Due to the higher viscosity, there will be an increase in the thickness of the liquid film (Llewellyn et al., 2011). For this reason, bubbles were initialised with a thicker liquid film, but equivalent lengths to those in Section 6.3.2.2. These bubbles therefore had a smaller volume of air, but all other initial conditions were kept constant. This gave a set of non-dimensional parameters as described in Table 6.3. From an analysis of the theoretical Reynolds number based on buoyancy, Re_B , and the simulated Reynolds number based on the liquid film thickness and film velocity, Re_f , it was determined that for cases with viscosity 0.1 and 1 Pa s, the flow may be considered to be laminar (Nogueira et al., 2006a; Llewellyn et al., 2011).

Simulations were initially run with an expansion angle of 90° and initial length of $4.4L'$, as in Section 6.3.1. The frequencies of the oscillations generated by the Taylor bubbles were analysed. Taylor bubbles rising in a higher viscosity liquid were observed to produce similar frequencies to the lower viscosity cases. Figure 6.32 shows the oscillations in pressure and the subsequent frequencies of these oscillations. From an analysis of this figure, a damping effect can be observed on the amplitude of the oscillations. The resulting low frequency component remains constant;

Table 6.3: Table of non-dimensional parameters determined for the rise of Taylor bubbles within fluids of viscosity 0.001, 0.1 and 1 Pa s.

μ (Pa s)	Re_B	Re_f	Eo	M	Fr
0.001	23143	4867	191	2.4×10^{-11}	0.351
0.1	231	56	191	2.4×10^{-3}	0.331
1	23	2.9	191	2.4×10^1	0.175

however, the higher frequency component is seen to decrease slightly with this damping. Further increasing the viscosity by an order of magnitude to 1 Pa s again reduces the higher frequency, while the lower frequency remains constant.

One qualitative change that can be noticed given an increased liquid viscosity is the decrease in bubbles shed from the tail of the Taylor bubble. Bubbles which are shed in the $\mu = 0.1$ Pa s case are seen to coalesce more readily than the $\mu = 0.001$ Pa s case. This is due to the closed wake structure observed behind the Taylor bubble rising in the more viscous fluid at these Reynolds numbers (Nogueira et al., 2006a). Figure 6.33 shows a comparison of streamline plots of the wake regions behind rising Taylor bubbles in liquids of 0.001, 0.1 and 1 Pa s. One consequence of this is that any parts of the bubble shed in the 0.001 Pa s case will reduce the length of the bubble, and hence bubbles may have a different length when reaching the expanding section given a different viscosity. This may account for the decrease in the higher frequency given an increase in viscosity. Another qualitative difference which can be observed is that when viscosity is increased to a level of 1 Pa s ($Re_f = 2.9$), the splitting of the bubble as it passes through the expansion does not result in the film of gas penetrating the nose of the bubble. This can be attributed to a damping effect caused by the increased viscosity.

The results of these simulations are in agreement with the conclusions of the experimental

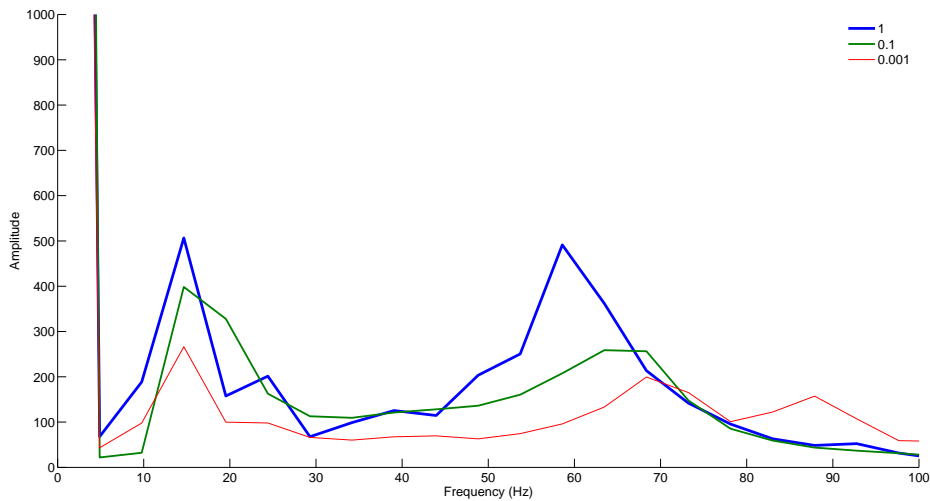


Figure 6.32: Plots of the Power Spectral Density of the signals generated by bubbles of identical initial length as they pass through a 90° expansion section for viscosities of 1, 0.1 and 0.001 Pa s respectively.

studies of James et al. (2006); Danabalan (2012); Soldati (2013). These suggest that while some damping effects may be observed, viscosity does not play a critical role in the breaking mechanism. Similar behaviour is observed in the simulations conducted at 0.001 Pa s as is observed in the experiments of Soldati (2013) at a viscosity of 70 Pa s, an increase of almost six orders of magnitude.

6.3.4 Variation of pipe diameter ratio

A set of simulations was conducted in which the diameter of the upper pipe was varied. The angle of expansion was maintained at 90° and the diameter of the lower pipe was maintained at 0.038 m during these simulations. The purpose of these simulations was to determine the effects of varying the ratio between the diameters of the upper and lower pipes on the critical length of the bubble. It was hypothesised that there would be a critical ratio at which the effect of the

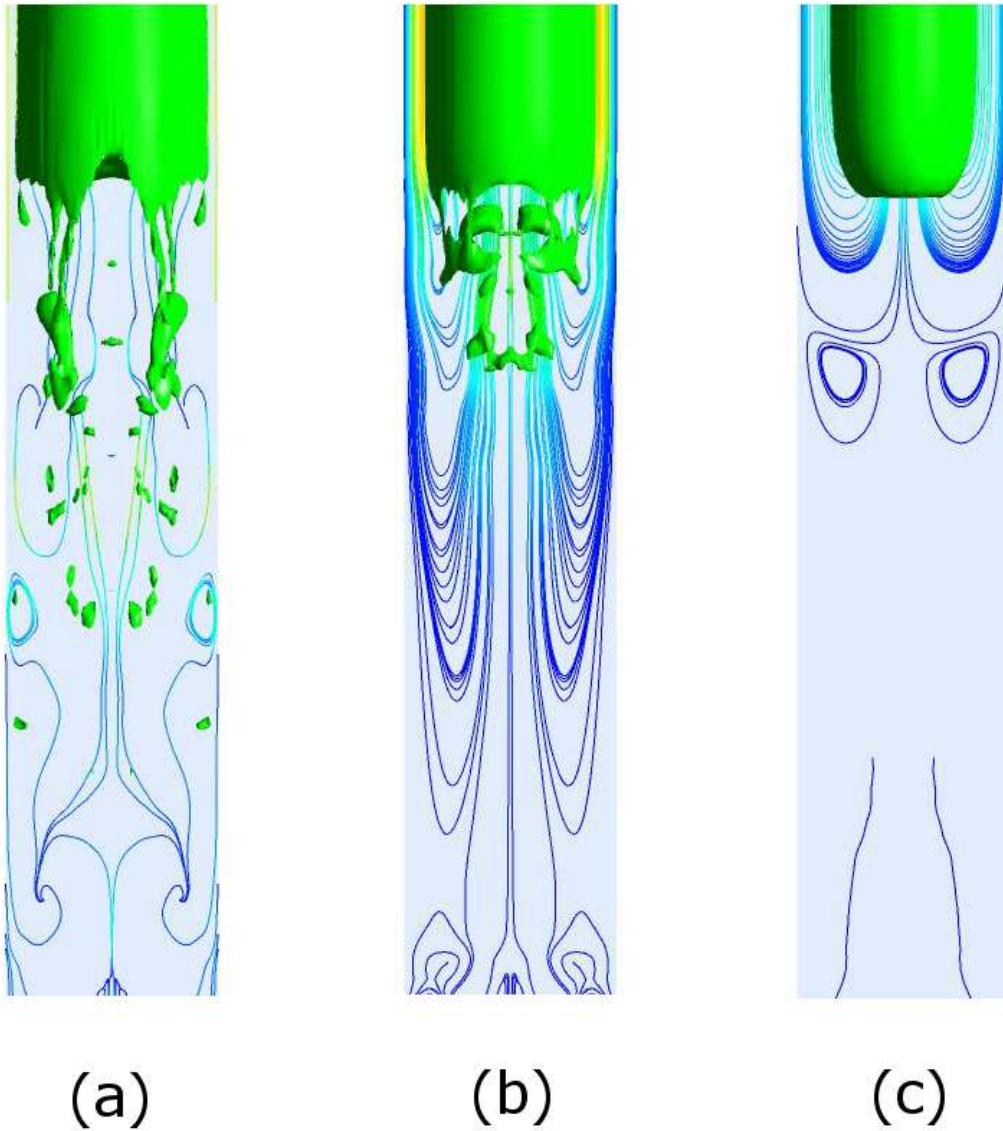


Figure 6.33: Plots of the streamlines in the wake of a Taylor bubble rising in fluids of viscosity (a) 0.001 Pas, (b) 0.1 Pas, (c) 1 Pas. Image (a) demonstrates the open wake structure associated with turbulent flow regime given $Re_B > 1500$ (Nogueira et al., 2006a) and images (b) and (c) demonstrate the closed wake structure associated with the laminar flow regime with $Re_B < 500$,

walls of the upper pipe played no role in the necking process of the bubble.

In these simulations, the diameter of the upper pipe was varied from 0.06 m to 0.14 m in increments of 0.02 m. This corresponds to a variation in upper to lower pipe diameter ratios of approximately 1.5 to 3.7. For the cases with upper pipe diameters of 0.06 m, 0.08 m and 0.1 m, the critical length of bubble was seen to decrease with increasing upper pipe diameter. However, the critical length of bubble does not vary with further increases in upper pipe diameter, which can be observed in Figure 6.34.

Although the Taylor bubbles rising through the pipes with upper diameter 0.1 m, 0.12 and 0.14 m have the same critical length, an analysis of Figures 6.36 and 6.35 shows some slight qualitative differences. Figure 6.35 shows bubbles of initial length $1.5L'$, at a time of 1.3 s from the start of the simulation, having risen into pipes of 0.1, 0.12 and 0.14 m respectively. In the cases with an upper pipe diameters of 0.1 m and 0.12 m, there is a small difference in the shape of the bubble as the tail penetrates the nose. This is not observed when comparing the bubbles in the 0.12 and 0.14 m cases. Similar conclusions can be drawn from an analysis of Figure 6.36 which shows bubbles with an initial length of $1.75L'$, which is the upper bound of the critical length. Although the bubble shapes in all three cases are similar, there are some minor discrepancies between the bubbles rising into pipes of diameter 0.1 m and 0.12 m which are not seen between the bubbles rising into pipes of diameter 0.12 m and 0.14 m.

From an analysis of the results of these simulations, it can be concluded in this case that a ratio of upper to lower pipe diameters of approximately 2.5 to 3 is required for the walls of the upper pipe to have a negligible effect on the process of Taylor bubbles passing through this expansion section.

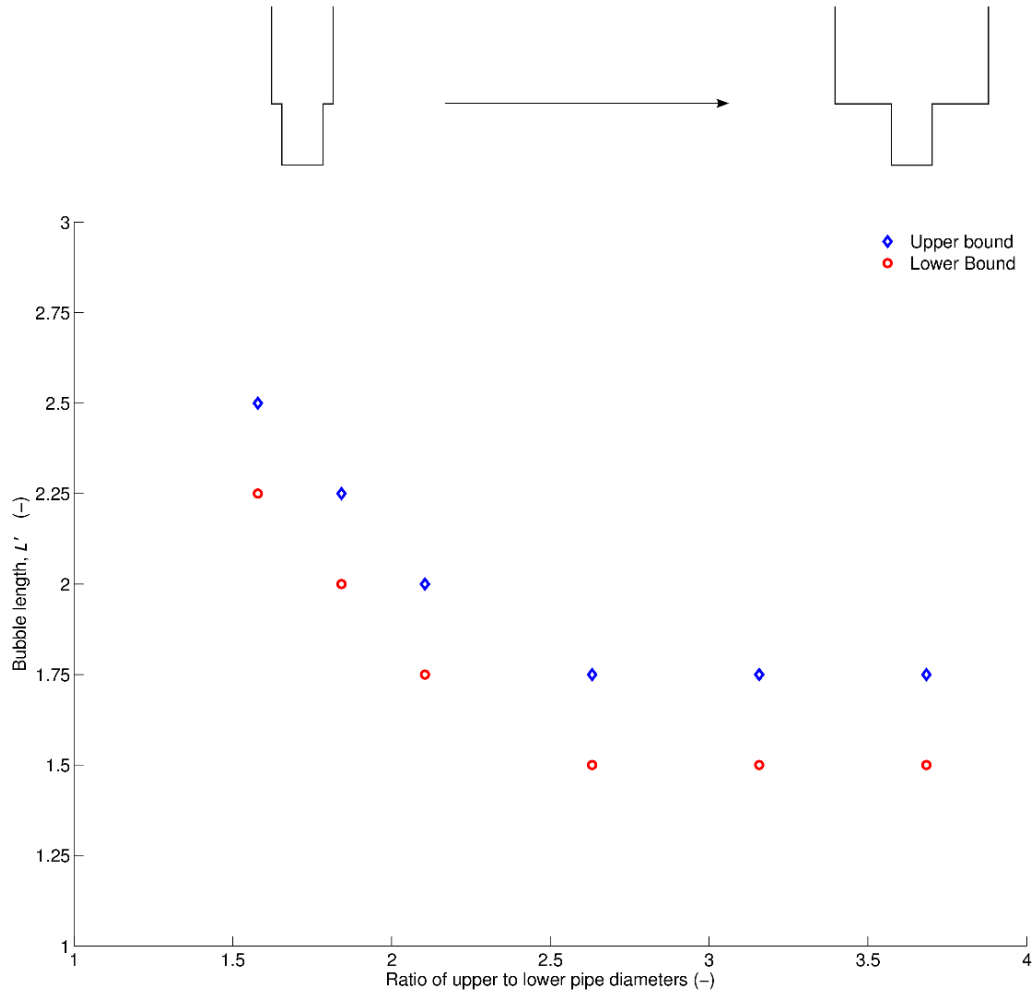


Figure 6.34: A plot of the upper and lower bounds of the critical length of bubble against the ratio of the diameter of the upper pipe to the diameter of the lower pipe. This shows that a ratio of upper to lower pipe diameters of approximately 2.5 to 3 is required for the walls of the upper pipe to have a negligible effect on the process of Taylor bubbles passing through this expansion section.

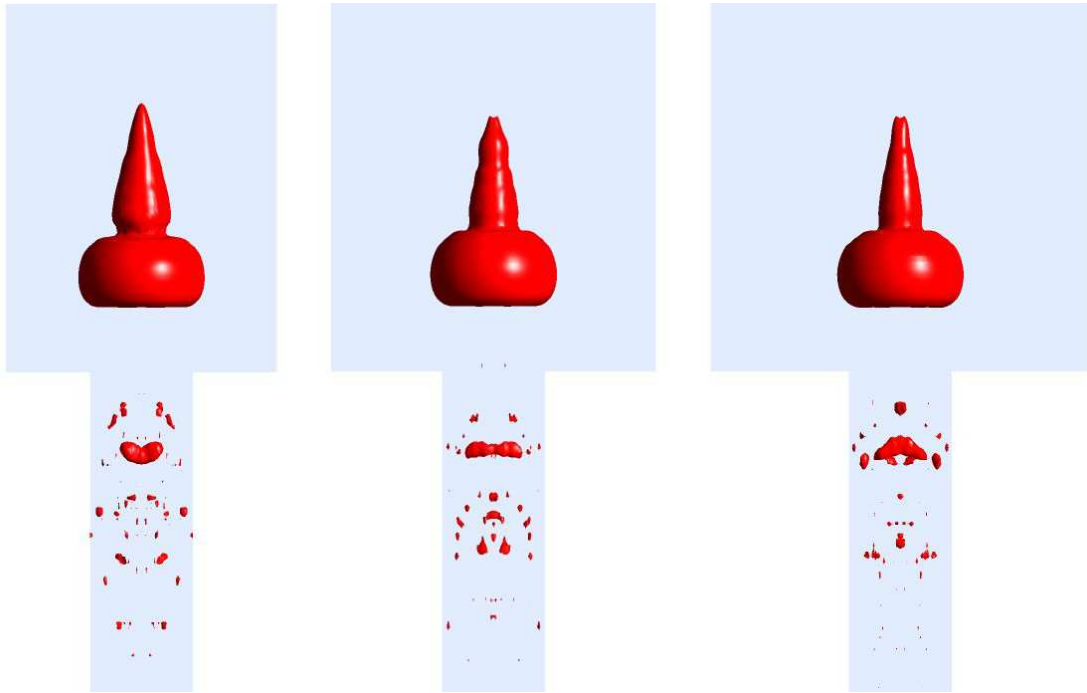


Figure 6.35: 3D iso-surfaces showing the simulated behaviour of the bubbles at the lower bound of the critical length as they pass through a 90° expansion with upper diameter 0.1 m (left), 0.12 m (centre) and 0.14 m (right). In the cases with an upper pipe diameters of 0.1 m and 0.12 m, there is a small difference in the shape of the bubble as the tail penetrates the nose. This is not observed when comparing the bubbles in the 0.12 and 0.14 m cases

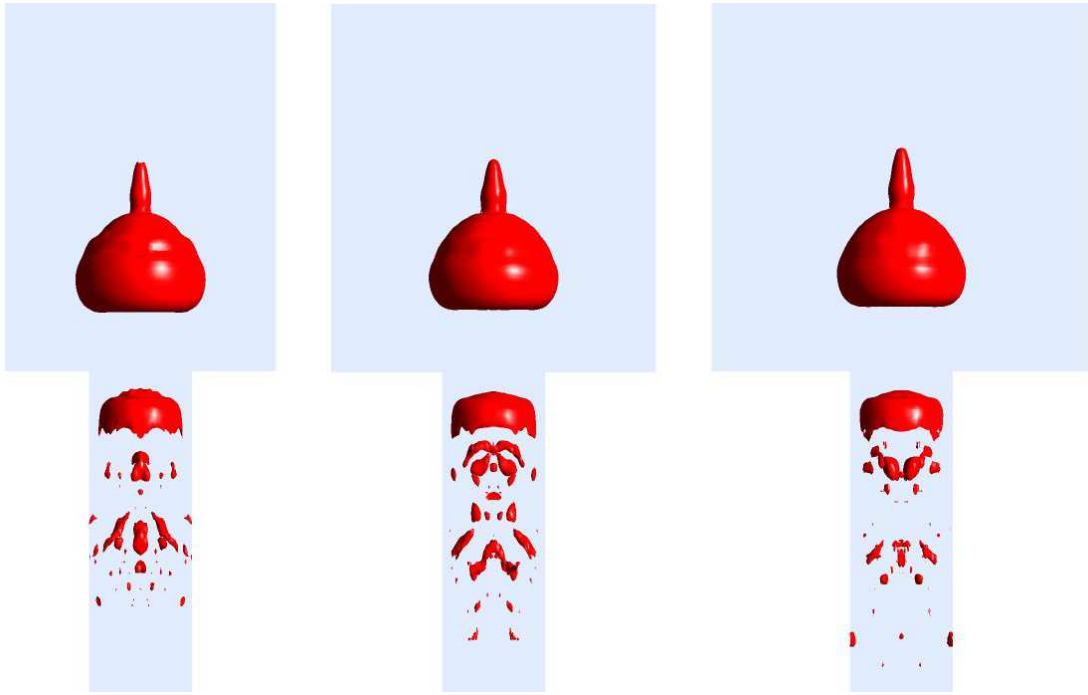


Figure 6.36: 3D iso-surfaces showing the simulated behaviour of the bubbles at the upper bound of the critical length as they pass through a 90° expansion with upper diameter 0.1 m (left), 0.12 m (centre) and 0.14 m (right). Although the bubble shapes in all three cases are similar, there are some minor discrepancies between the bubbles rising into pipes of diameter 0.1 m and 0.12 m which are not seen between the bubbles rising into pipes of diameter 0.12 m and 0.14 m.

6.4 Conclusions

The qualitative and quantitative behaviour of Taylor bubbles rising through expansions in pipe diameter observed during the laboratory experiments reported by James et al. (2006) was modelled using CFD. A frequency analysis of the results of the CFD simulations showed comparable dominant frequencies to the experimental results. The use of a CFD model also confirmed the qualitative mechanism proposed by James et al. (2006) for the breaking of a Taylor bubble as it passes through an expansion section.

A variation in the angle of the expansion, given constant upper and lower pipes of diameters 0.038 m and 0.08 m respectively, resulted in significantly different behaviour of a Taylor bubble as it passed through the expansion section. Much longer bubbles could pass through a more gradually expanding section than could pass through a sudden expansion before the neck closed. This resulted in very different flow regimes in the upper pipe given different angles of expansion. A Taylor bubble could split into numerous smaller bubbles given a sudden expansion, or remain as one bubble given a more gradually expanding section. A linear variation was found between the critical length of bubble which could pass through the expansion section before the neck closed and the cosec of the angle of expansion. When analysed in the same fashion, the results of Soldati (2013) also exhibited this trend.

Similar to the results presented in Chapter 5, an increase in liquid viscosity, giving a reduction in Reynolds number, reduced the amplitude of oscillations significantly. However, the effect on the frequency of the bubble was minimal, with a small damping effect reducing the frequency of oscillation given an increase in viscosity. A significant increase in viscosity did influence the breaking mechanism, with the film of gas from the neck of the bubble no longer penetrating the nose of the bubble

Results obtained by varying the diameter of the upper pipe suggest that the effects of the

wall on the behaviour of a Taylor bubble passing through an expansion section become negligible at a ratio of upper to lower pipe diameters of approximately 2.5 to 3.

Further investigations into the results of a variation of Eötvös number should be conducted to determine the roles of surface tension and pipe diameter on the behaviour of Taylor bubbles passing through expansions in pipe diameter. Investigations into the effect of contractions of pipe diameter are also recommended.

Conclusions and Recommendations

This chapter summarises the conclusions drawn from this study together with proposed recommendations for future work in this field.

7.1 Conclusions

The work presented in Chapter 2 details a critical review of the background literature on gas-liquid flows, in particular the rise of Taylor bubbles. Previous studies have shown that the rise of Taylor bubbles may be described by a number of non-dimensional parameters, namely the Froude, Eötvös, Morton and buoyancy Reynolds numbers. Furthermore, the rise rate, film thickness and wake behaviour can all be estimated using theoretical or empirical models if these parameters are known.

From an analysis of the background literature it is concluded that there are a number of areas upon which insufficient experimental work has been published. Notably, there is a lack of experimental work in both large diameter pipes (over 0.12 m) and in high viscosity fluids (over 5 Pa.s). This conclusion was used as the motivation for the work presented in Chapters 4 and 5, which presents a summary of investigations that study the flow of Taylor bubbles in larger diameter pipes.

Many studies have shown that Taylor bubbles are not only commonplace in the oil and gas industry, but also prevalent in the natural world, where they are, in particular the driving force behind the eruption of Strombolian volcanoes. These bubbles of gas rise through the magma and burst at the surface. Magmas in these systems have viscosities which can be in the order of hundreds of Pa.s ($O(100)\text{Pa.s}$). Although conduits are normally modelled as vertical, cylindrical pipes, this is often not the case and conduit inclinations and changes in conduit diameter often occur. The rise of Taylor bubbles through changes in pipe diameter were the focus of the numerical studies presented in Chapter 6.

A number of conclusions were drawn from previous work conducted using numerical models to study the rise of Taylor bubbles which influenced the choice of the models adopted for the numerical studies presented in this thesis. To account for the presence of two fluids, the VOF model has been shown to be capable of simulating the rise of Taylor bubbles in vertical pipes. This method is investigated in more detail in Chapter 3. Although many studies have used shortened domains with either moving walls or periodic boundary conditions, it was concluded that the whole domain was required to be modelled in the studies presented in this thesis. Although this is computationally expensive, the behaviour of the atmospheric liquid–air surface or expansion of the bubble would not have been able to modelled otherwise.

An analysis of the theoretical Reynolds numbers (based on buoyancy of the bubble) showed that in many scenarios, turbulent flow would have to be modelled. The $k-\varepsilon$ turbulence model has been shown in previous studies to adequately model the turbulent wake and thin film behaviour (Taha and Cui, 2004).

An analysis of the results of published numerical studies of Taylor bubbles show that few previous investigations considered either compressible Taylor bubbles or ones possessing a high Eötvös number (≥ 500). There were also no published numerical studies that have considered changes to the cross section of the pipe geometry. These model and parameter changes provided

the motivation behind the numerical studies presented in Chapters 5 and 6.

Chapter 3 discusses the model created using the commercial CFD solver ANSYS Fluent 12.1 to study the rise of a Taylor bubble. This solver computes a numerical solution to the momentum and continuity equations using a finite volume method.

For turbulent flow regimes ($Re_B > 1500$, (Nogueira et al., 2006b)) the realisable $k - \varepsilon$ model was applied to close the RANS equations. This closure model has been shown to produce high quality results in situations which involve jets, such as those seen in the thin film and wake trailing a rising Taylor bubble.

A critical analysis of the literature concludes that the use of the Volume of Fluid (VOF) method coupled with the Piecewise Linear Interface Construction (PLIC) scheme is capable of modelling the rise of Taylor bubbles. The use of these schemes have been shown to produce higher quality results when used in conjunction with an O-grid structured hexahedral mesh (Abdulkadir et al., 2011).

A review of potential models gave rise to the conclusion that the Quadrilateral Upwind Interpolation for Convective Kinematics (QUICK) scheme was to be used to spatially discretize the solution and the transient Non Iterative Time Advancement (NITA) scheme to temporally advance the model.

A series of verification and validation studies were also conducted and presented in Chapter 3. A quantitative method of verification, the GCI method, was used to compute error values for both the spatial and temporal discretisation stages. An analysis of the results of the CFD simulations showed a strong agreement with the empirical correlations published for rise velocity. In addition, the simulated film thickness measurements were in close agreement with the theoretical model of Llewellyn et al. (2011). The results from this study also suggest that the theoretical values for rise rate are valid over a wider range of pipe diameters and fluid viscosities than stated in the

literature. These increased ranges correspond with flow regimes which have high Morton and Eötvös numbers, similar to those which govern the flow of magma and magmatic gases within volcanoes.

The experiments detailed in Chapter 4 investigated the behaviour of a Taylor bubble rising in water within a pipe of internal diameter 0.29 m. Here the Eötvös number is significantly higher than had previously been reported in the literature. From an analysis of the results of these experiments, a number of conclusions may be drawn. Firstly, Taylor bubbles rising in quiescent water, in a pipe of diameter 0.29 m, are inherently stable. This finding agrees with the theoretical work of Batchelor (1987) who predicted that Taylor bubbles will be stable up to a maximum diameter of 0.46 m, assuming quiescent conditions. Previous experimental work had never been conducted at this scale, although unpublished work of James et al. (2011) had suggested the existence of stable bubbles at a diameter of 0.25 m. In order for the fluid in the pipe to be assumed to be quiescent, a settling period of 120 s needed to be left before the release of any further Taylor bubbles.

Taylor bubbles left to rise under the force of buoyancy (without a continuous flow of gas) will rise at a rate which is dependent on their length. This was expected due to surface of the liquid being open to the atmosphere and hence able to expand as it rises. The Froude numbers for the bubbles compare well to previous experimental and theoretical studies (Taylor and Davies, 1950; Dumitrescu, 1943; Viana et al., 2003).

Due to the injection method described in Section 4.2, a sudden curtailment of the gas injection resulted in oscillations of both the rise rate of the surface of the liquid, and in the rise rate and length of the bubble. The observed oscillations display a similar behaviour to that of a simple harmonic oscillator. Consequently, Pringle et al. (2014) and Vergniolle et al. (1996) propose the use of such a model to describe the oscillatory behaviour of such bubbles, which was shown to

closely agree with the observed behaviour.

The results of these experiments also provided data with which to validate the results of the CFD simulations which are presented in Chapter 5. These simulations successfully replicate the behaviour of the rising bubbles observed during laboratory experiments using the compressible CFD model described in Chapter 3.1.

The use of this model was able to reproduce the observed rise behaviour of a stable Taylor bubble within 15% of the measured experimental values. The simulated rise of the upper surface level was shown to be within 5% of the predicted theoretical value and the simulated frequency of oscillation is approximately 10% above the observed experimental values.

In a base case simulation, the Taylor bubble is initialised with a pressure equal to the expected hydrostatic pressure at the nose of the bubble. A variation in this initial pressure away from the hydrostatic value was shown to give oscillations with varying amplitudes but that were of the same frequency. The initial pressure disturbance produces a change in the bubble length that is dependent on the initial compression or expansion of the bubble. As the resultant oscillation frequency is dependent on this length, there is also a small change in the frequency of oscillation. This is in accordance with both the results from the experimental studies presented in Chapter 4 and the theoretical models of Vergnolle et al. (1996) and Pringle et al. (2014).

A set of parametric studies were also conducted to study the effects of a change in the liquid viscosity on the oscillatory behaviour of the bubble. Given an increase liquid viscosity, giving a reduction in Reynolds number, the amplitude of oscillations reduced significantly. However, the effect on the frequency of the bubble was minimal up to the point at which oscillations could no longer be detected accurately. The increased viscosity has a damping effect on the oscillations and hence one would expect the frequency to decrease with increasing viscosity, if the amplitude was such that it could be measured, due to it exhibiting the same behaviour as a simple harmonic oscillator.

The stability of the bubble given an increase in pipe diameter was investigated using the numerical model. The limiting value of stability was shown to be comparable with the theoretical prediction of Batchelor (1987). The stability of bubbles rising into the wake of a previous bubble was also investigated. The results of these simulations showed an qualitative agreement with the experimental observations presented in Section 4.3.

A numerical study investigating the rise of Taylor bubbles through an expansion in pipe diameter was detailed in Chapter 6. The qualitative and quantitative behaviour observed during the laboratory experiments reported by James et al. (2006) was replicated using the compressible CFD model previously described in Chapter 3.1. The results of the CFD model replicated the qualitative mechanism proposed by James et al. (2006) for the breaking of a Taylor bubble as it passes through an expansion section. James et al. (2006) observed that when a Taylor bubble encountered an expansion in pipe diameter, it rapidly expanded both vertically and laterally from the nose. This resulted in an increase in the flow in the liquid film surrounding the bubble which caused a necking or pinching of the bubble. For bubbles of sufficient length, this necking will split the bubble and generate oscillations in the measured pressure signals. Conducting a frequency analysis on the results of the CFD simulations showed comparable dominant frequencies to the experimental results.

A parametric study was conducted to assess the effect of varying the angle of the expansion, given upper and lower pipes of diameter 0.038 m and 0.08 m respectively. A variation in the angle of the expansion resulted in significantly different qualitative behaviour of a Taylor bubble as it passed through the expansion section. Much longer bubbles could pass through a more gradually expanding section than could pass through a sudden expansion before the neck closed. This could result in very different flow regimes in the upper pipe given different angles of expansion. A Taylor bubble could split into numerous smaller bubbles given a sudden expansion, or remain

as one bubble given a more gradually expanding section. A linear variation was found between the critical length of bubble which could pass through the expansion section before the neck closed and the cosec of the angle of expansion. When analysed in the same fashion, the results of Soldati (2013) also exhibited this relationship.

Similar to the results presented in Chapter 5, an increase in liquid viscosity, giving a reduction in Reynolds number, reduced the amplitude of oscillations. Again, the effect on the frequency of the bubble was minimal. A small damping effect was observed, reducing the frequency of oscillation given an increase in viscosity. A significant increase in viscosity (3 orders of magnitude) did influence the breaking mechanism, with the film of gas from the neck of the bubble no longer penetrating the nose of the bubble.

A set of simulations were conducted in which the effects of a systematic variation in the diameter of the upper pipe were investigated. An analysis of the results of these simulations suggest that the effects of the wall on the behaviour of a Taylor bubble passing through an expansion section become negligible at a ratio of upper to lower pipe diameters of approximately 2.5-3.

In conclusion, the objectives set in Section 1.2 have been met to fulfil the aim of gaining a better understanding of the rise of single Taylor bubbles in flow conditions which had not previously been studied.

7.2 Recommendations

A number of areas exist for further experimental and numerical investigations into the rise of single Taylor bubbles.

Firstly, a number of improvements to experimental method described in Section 4.2 are recommended to reduce the magnitude of the errors. The repair of the faulty rotameters would

allow more repeatable experiments, as would the introduction of an automated injection system, such as that seen in the work of Nogueira et al. (2006b). The use of pressure sensors to monitor the oscillatory behaviour, such as in the work of James et al. (2004, 2006) is also recommended to reduce the magnitude of the errors incurred in the calculation of the frequency of oscillation. The use of specialist lighting equipment would allow high speed video recording at higher frame rates than was possible, which again could reduce the magnitude error values for the frequency calculations as well as the rise rate calculations.

Future experimental work to test the theoretical limit on the stability of rising Taylor bubbles proposed by Batchelor (1987) could be conducted. For this, a vertical pipes with diameters in the region of 0.4 m 0.45 m and 0.5 m would be required. However, it is likely to be prohibitively expensive to carry out a range of experiments at this range.

Further experiments at an increased liquid viscosity using this experimental apparatus are recommended, and are due to be conducted in future projects at the University of Nottingham.

Further numerical research is also recommended in this field, in particular the use of LES (Large Eddy Simulation) or DES (Detached Eddy Simulation) to resolve the turbulent flow behaviour in finer detail. These models are significantly more computationally expensive than the RANS approach used in this work. The method of Sawko and Thompson (2010) for treating turbulence at the interface between the two phases should also be applied to the model and tested for the rise of Taylor bubbles as this has shown excellent results in stratified flows.

Further to the work presented in Chapter 5, the effect of using a polytropic gas law, with $\gamma = 1.1$ as suggested by Pringle et al. (2014) and Vergnolle et al. (1996) should be investigated. This would require the development of a User Defined Function to define the density of the gas at a specified pressure. Studies of inclined pipes have shown an increased rise velocity, and the effect of changing the angle of inclination of the pipe has on the frequency and amplitude of oscillations could also be studied.

When considering the rise of Taylor bubbles through expansions in pipe diameter, it is recommended that further investigations into the results of a variation of Eötvös number should be conducted. This study would determine the roles of surface tension and pipe diameter on the behaviour of Taylor bubbles passing through expansions in pipe diameter. Investigations into the effect of contractions of pipe diameter are also recommended.

Bibliography

- M. Abdulkadir, V. Hernandez-Perez, S. Sharaf, I. S. Lowndes, and B. J. Azzopardi. Experimental investigation of phase distributions of two-phase air-silicone oil flow in a vertical pipe. *World Academy of Science, Engineering and Technology*, 61, 2010.
- M. Abdulkadir, V. Hernandez-Perez, and B.J. Azzopardi. Grid generation issues in the CFD modelling of two-phase flow in a pipe. *The Journal of Computational Multiphase Flows*, 3(1): 242–252, 2011.
- R.J. Adrian. Particle imaging techniques for experimental fluid dynamics. *Annual review of Fluid Mechanics*, 23:262–304, 1991.
- W.H. Ahmed. Pressure recovery of two-phase flow across sudden expansions. *International Journal of Multiphase Flow*, a.
- W.H. Ahmed. Development of two-phase flow downstream of a horizontal sudden expansion. *International Journal of Heat and Fluid Flow*, b.
- AIAA. Guide for the verification and validation of Computational Fluid Dynamics simulations. *Technical Report AIAA-G-077-1998*, American Institute of Aeronautics and Astronautics, Reston, VA, 1998.

- F. Aloui, L. Doubriez, J. Legrand, and M. Souhar. Bubbly flow in an axisymmetric sudden expansion: pressure drop, void fraction, wall shear stress, bubble velocities and sizes. *Experimental Thermal and Fluid Science*, 19(2):118–130, 1999.
- ANSYS FLUENT. ANSYS FLUENT training manual.
- J.D.P. Araujo, J.M. Miranda, A.M.F.R. Pinto, and J.B.L.M. Campos. Wide-ranging survey on the laminar flow of individual Taylor bubbles rising through stagnant Newtonian liquids. *International Journal of Multiphase Flow*, 43:131 – 148, 2012.
- B.J. Azzopardi, A. Ijioma, S. Yang, L.A. Abdulkareem, A. Azzi, and M. Abdulkadir. Persistence of frequency in gas-liquid flows across a change in pipe diameter or orientation. *International Journal of Multiphase Flow*, 2014. Article in Press.
- R.W. Bartlett. Magma convection, temperature distribution, and differentiation. *American Journal of Science*, 267:1067–1082, 1969.
- G.K. Batchelor. *An Introduction to Fluid Dynamics*. Cambridge University Press, 1967.
- G.K. Batchelor. The stability of a large gas bubble rising through liquid. *Journal of Fluid Mechanics*, 184:399–422, 1987.
- E. Bouche, S. Vergnolle, T. Staudacher, A. Necessian, J.-C. Delmont, M. Frogneux, F. Cartault, and A. Le Pichon. The role of large bubbles detected from acoustic measurements on the dynamics of Erta 'Ale lava lake (Ethiopia). *Earth and Planetary Science Letters*, 295(1–2):37 – 48, 2010.
- J.U. Brackbill, D.B. Kothe, and C. Zemach. A continuum method for modeling surface tension. *Journal of Computational Physics*, 100:335 – 354, 1992.

- R. Brown. The mechanics of large gas bubbles in tubes. *Canadian Journal of Chemical Engineering*, 43:375–390, 1965.
- J.D. Bugg and G.A. Saad. The velocity field around a Taylor bubble rising in a stagnant viscous fluid: numerical and experimental results. *International Journal of Multiphase Flow*, 28:791–803, 2002.
- J.D. Bugg, K. Mack, and K.S. Rezkallah. A numerical model of Taylor bubbles rising through stagnant liquids in vertical tubes. *International Journal of Multiphase Flow*, 24(2-7):271–281, 1998.
- J. B. L. M. Campos and J. R. F. Guedes De Carvalho. An experimental study of the wake of gas slugs rising in liquids. *Journal of Fluid Mechanics*, 196:27–37, 1988.
- W. Carter. An acoustic and visual study of the ascent of a Taylor bubble through a vertical expansion. *University of Nottingham Master's Thesis*, 2012.
- CD-ADAPCO. STAR-CCM+ training manual. 2011.
- I.B. Celik, U. Ghia, P.J. Roache, C.J. Freitas, H. Coleman, and P.E. Raad. Procedure for estimation and reporting of uncertainty due to discretization in CFD applications. *Journal of Fluids Engineering, Transactions of the ASME*, 130(7), 2008.
- B. Chouet, P. Dawson, M. Martini, G. De Luca, G. Milana, R. Scarpa, and M. Cattaneo. Source mechanisms of explosions at Stromboli volcano, Italy, determined from moment-tensor inversions of very-long-period data. *Journal of Geophysical Research*, 108:2019, 2003.
- A Clarke and R.I. Issa. A numerical model of slug flow in vertical tubes. *Computers and Fluids*, 26(4):395 – 415, 1997.
- R. Clift, J. R. Grace, and M. E. Weber. *Bubbles, Drops and Particles*. Academic Press, 1978.

- D. Danabalan. New insights into bubble-driven convection in lava lakes. *University of Bristol Master's Thesis*, 2012.
- A. E. Dukler and O.P. Bergelin. Characteristics of flow in falling liquid films. *Chemical Engineering Progress*, 48:557–563, 1952.
- D T. Dumitrescu. Strömung an einer Luftblase im Senkrechtenrohr. *Zeitschrift fr Angewandte Mathematik and Mechanik*, 23(3):139–149, 1943.
- J. Fabre and A. Line. Modelling of two-phase slug flow. *Annual Review of Fluid Mechanics*, 24: 21–46, 1992.
- J. Q. Feng. Buoyancy-driven motion of a gas bubble through viscous liquid in a round tube. *Journal of Fluid Mechanics*, 609:377–410, 2008.
- Geology.com. Images available online at www.geology.com/volcanoes, last accessed 15/07/14. 2011.
- A. J. Ghajar. Non-boiling heat transfer in gas-liquid flow in pipes. *Journal of the Brazilian Society of Mechanical Sciences*, 27, 2005.
- A.H. Gibson. On the motion of long air-bubbles in a vertical tube. *Philosophical Magazine Series 6*, 26(156):952–965, 1913.
- H. L. Goldsmith and S. G. Mason. The movement of single large bubbles in closed vertical tubes. *Journal of Fluid Mechanics*, 14:42–58, 1962.
- D.F. Haynes B.S. Gupta, R. Fletcher. On the CFD modelling of Taylor flow in micro-channels. *Chemical Engineering Science*, 64:2941–2950, 2009.
- V. Hernandez-Perez. Gas-liquid flow in inclined pipes. *University of Nottingham, PhD Thesis*, 2011.

- C.W. Hirt and B.D. Nichols. Volume of fluid (VOF) method for the dynamics of free boundaries. *Journal of Computational Physics*, 39:201 – 225, 1981.
- M. Hobiger, I. Sonder, R. Büttnera, and B. Zimanowskia. Viscosity characteristics of selected volcanic rock melts. *Journal of Volcanology and Geothermal Research*, 200:27–34, 2011.
- H.M. Houghton, B.F. Gonnerman. Basaltic explosive volcanism: Constraints from deposits and models. *Chemie der Erde*, 68:117–140, 2008.
- Y.Y. Hsu and F.F.. Simon. Stability of cylindrical bubbles in a vertical pipe. *ASME Conference Paper*, 69-HT-28, 1969.
- D. Huang, Z.and Xie, H. Zhang, and H. Li. Gas–oil two-phase flow measurement using an Electrical Capacitance Tomography system and a Venturi meter. *Flow Measurement and Instrumentation*, 16:177–182, 2005.
- R.I. Issa. Solution of the implicitly discretised fluid flow equations by operator-splitting. *Journal of Computational Physics*, 62(1):40–65, 1986.
- M. R. James, S. J. Lane, and S. B. Corder. Modelling the rapid near-surface expansion of gas slugs in low-viscosity magmas. *Geological Society, London, Special Publications*, 307:147–167, 2008.
- M.R. James. Private Communication via email.
- M.R. James, S.J. Lane, B. Chouet, and J.S. Gilbert. Pressure changes associated with the ascent and bursting of gas slugs in liquid-filled vertical and inclined conduits. 129:61–82, 2004.
- M.R. James, S.J. Lane, and B. Chouet. Gas slug ascent through changes in conduit diameter: Laboratory insights into a volcano-seismic source process in low-viscosity magmas. *Journal of Geophysical Research*, 111, 2006.

- M.R. James, E.W. Llewelin, and S.J. Lane. Comment on : It takes three to tango: 2. Bubble dynamics in basaltic volcanoes and ramifications for modelling normal Strombolian activity. *Journal of Geophysical Research*, 116, 2011.
- C. Jaupart and S. Vergnolle. Separated two-phase flow and basaltic eruptions. *Journal of Geophysical Research*, 91:12842–12860, 1986.
- C. Jaupart and S. Vergnolle. The generation and collapse of foam layer at the roof of a basaltic magma chamber. *Journal of Fluid Mechanics*, 203:347–380, 1989.
- C. Kang, S. Quan, and J. Lou. Numerical study of a Taylor bubble rising in stagnant liquids. *Physical Review E*, 81, 2010.
- Fedkiw R. P. Kang, M. and X. D. Liu. A boundary condition capturing method for multiphase incompressible flow. *Journal of Scientific Computing*, 15:323–360, 2000.
- T. D. Karapantsios and A. J. Karabelas. Longitudinal characteristics of wavy falling films. *International Journal of Multiphase Flow*, 21:119–127, 1995.
- T. D. Karapantsios, S. V. Paras, and A. J. Karabelas. Statistical characteristics of free falling films at high Reynolds numbers. *International Journal of Multiphase Flow*, 15:1–21, 1989.
- M. Kawaji, J. M. DeJesus, and G. Tudose. Investigation of flow structures in vertical slug flow. *Nuclear Engineering and Design*, 175:37–48, 1997.
- J. Kitscha and G. Kocamustafaogullari. Breakup criteria for fluid particles. *International Journal of Multiphase Flow*, 15:573–588, 1989.
- K. Kondo, K. Yoshida, T. Matsumoto, T. Okawa, and I. Kataoka. Flow patterns of gas-liquid two-phase flow in round tube with sudden expansion. volume 3, pages 179–186, 2002.

- H.S. Jr. Kushiro, I. Yoder and B.O. Mysen. Viscosities of basalt and andesite melts at high pressures. *Journal Geophysical Research*, 81:6347–6350, 1976.
- B.E. Launder and D.B. Spalding. The numerical computation of turbulent flows. *Computer Methods in Applied Mechanics and Engineering*, 3(2):269–289, 1974.
- B.E. Launder, G.J. Reece, and W. Rodi. Progress in the development of a Reynolds-Stress turbulence closure. *Journal of Fluid Mechanics*, 68(pt 3):537–566, 1975.
- V. V. Lel, F. Al-Sibai, A. Leefken, and R. Renz. Local thickness and wave velocity measurement of wavy films with a chromatic confocal imaging method and a fluorescence intensity technique. *Experiments in Fluids*, 39:856–864, 2005.
- E.W. Llewellyn, E. Del Bello, J. Taddeucci, P. Scarlato, and S.J. Lane. The thickness of the falling film of liquid around a Taylor bubble. *Proceedings of the Royal Society A: Mathematical, Physical and Engineering Sciences*, 468:1041–1064, 2011.
- P.A. Lottes. Expansion losses in two-phase flow. *Nuclear Science and Engineering*, 9(1):26–31, 1961.
- X. Lu and A. Prosperetti. A numerical study of Taylor bubbles. *Industrial and Engineering Chemistry Research*, 48:242–252, 2009.
- M. Manga and H.A. Stone. Interactions between bubbles in magmas and lavas: effects of bubble deformation. *Journal of Volcanology and Geothermal Research*, 63:267–279, 1994.
- M.T. Mangan, K.V. Cashman, and S. Newman. Vesiculation of basaltic magma during eruption. *Geology*, 21:157–160, 1993.
- Zai-Sha Mao and A.E. Dukler. The motion of Taylor bubbles in vertical tubes—ii. Experimental

- data and simulations for laminar and turbulent flow. *Chemical Engineering Science*, 46(8): 2055 – 2064, 1991.
- C. S. Martin. Vertically downward two-phase slug flow. *Journal of Fluids Engineering*, 98(715): 722, 1976.
- J.M. McDonough. *Lectures in Computational Fluid Dynamics of incompressible flow: Mathematics, algorithms and implementations*. Departments of Mechanical Engineering and Mathematics, University of Kentucky, 2007.
- R. Moissis and P. Griffith. Entrance effects in a two-phase slug flow. *Journal of Heat Transfer*, 84, 1962.
- T. Murase. Viscosity and related properties of volcanic rocks at 800°C to 1400°C. *Hour. Fac. Sci.Hokkaido University, Ser VII*, 1:487–584, 1962.
- S. Muzaferija and M. Perić. Computation of free-surface flows using the finite-volume method and moving grids. *Numerical Heat Transfer, Part B: Fundamentals*, 32(4):369–384, 1997.
- N.V. Ndinisa, D.E. Wiley, and D.F. Fletcher. Computational fluid dynamics simulations of Taylor bubbles in tubular membranes model validation and application to laminar flow systems. *Chemical Engineering Research and Design*, 83:40–49, 2005.
- S. Nogueira, Sousa R.G., M.L. Riethmuler, J.B.L.M. Campos, and A.M.F.R. Pinto. Simultaneous PIV and shadowgraphy in slug flow: a solution for optical problems. *Experiments in Fluids*, 35:598–609, 2003.
- S. Nogueira, M.L. Riethmuler, J.B.L.M. Campos, and A.M.F.R. Pinto. Flow in the nose region and annular film around a Taylor bubble rising through vertical columns of stagnant and flowing Newtonian liquids. *Chemical Engineering Science*, 61(2):845 – 857, 2006a.

- S. Nogueira, M.L. Riethmuller, J.B.L.M. Campos, and A.M.F.R. Pinto. Flow patterns in the wake of a Taylor bubble rising through vertical columns of stagnant and flowing Newtonian liquids: An experimental study. *Chemical Engineering Science*, 61:7199 – 7212, 2006b.
- W. Nusselt. Die Oberflächenkondensation des Wasserdampfes. *Zeitschrift des vereines Deutschem Ingenieure*, 60:541–546, 1916.
- S. Osher and J. A. Sethian. Fronts propagating with curvature dependent speed: Algorithms based on Hamilton-Jacobi formulations. *Journal of Computational Physics*, 79:12–49, 1988.
- E.A. Parfitt. A discussion of the mechanisms of explosive basaltic eruptions. *Journal of Volcanology and Geothermal Research*, 134:77– 107, 2004.
- S.V. Patankar and D.B. Spalding. A calculation procedure for heat, mass and momentum transfer in three-dimensional parabolic flows. *International Journal of Heat and Mass Transfer*, 15(10): 1787–1806, 1972.
- Pinto and Campos. Coalescence of two gas slug rising in a vertical column of liquid. *Chemical Engineering Science*, 51:45–54, 1996.
- L. Pioli, C. Bonadonna, B. J. Azzopardi, J. C. Phillips, and M. Ripepe. Experimental constraints on the outgassing dynamics of basaltic magmas. *Journal of Geophysical Research: Solid Earth*, 117(B3), 2012.
- S. Polonsky, D. Barnea, and L. Shemer. Averaged and time-dependent characteristics of the motion of an elongated bubble in a vertical pipe. *International Journal of Multiphase Flow*, 25:795 – 812, 1999.
- C.C.T. Pringle, S. Ambrose, A.C. Rust, and B.J. Azzopardi. The existence and behaviour of large diameter Taylor bubbles. *International Journal of Multiphase Flow*, 2014. Article In Press.

- A. Rinne and R. Loth. Development of local two-phase flow parameters for vertical bubbly flow in a pipe with sudden expansion. *Experimental Thermal and Fluid Science*.
- P.J. Roache. *Verification and Validation in Computational Science and Engineering*. Hermosa, Albuquerque, New Mexico, 1998.
- L.M.T. Santos, M.T.M. Sena Esteves, and M.N. Coelho Pinheiro. Effect of gas expansion on the velocity of individual Taylor bubbles rising in vertical columns with water: Experimental studies at atmospheric pressure and under vacuum. *Chemical Engineering Science*, 63(18): 4464–4474, 2008.
- R. Sawko and C.P. Thompson. Estimation of rate of strain magnitude and average viscosity in turbulent flow of shear thinning and yield stress fluids. *International Conference of Numerical Analysis and Applied Mathematics*, 2010.
- C.M. Scarfe. Viscosity of basic magmas at varying pressure. *Nature*, 241:101–102, 1973.
- R. Seyfried and A. Freundt. Experiments on conduit flow and eruption behavior of basaltic volcanic eruptions. *Journal of Geophysical Research*, 105:23727–23740, 2000.
- N. Shao, A. Gavrilidis, and P. Angeli. Flow regimes for adiabatic gas–liquid flow in micro-channels. *Chemical Engineering Science*, page 2749–2761, 2009.
- H.R. Shaw. Rheology of basalt in the melting range. *Journal Petrology*, 10:510–535, 1969.
- T.H. Shih, W.W. Liou, A. Shabbir, Z. Yang, and J. Zhu. A new k - ϵ eddy viscosity model for high Reynolds number turbulent flows. *Computers and Fluids*, 24(3) : 227 – 238, 1995.
- H. Shinohara. Excess degassing from volcanoes and its role on eruptive and intrusive activity. *Reviews of Geophysics*, 46, 2008.

- M. Shur, P.R. Spalart, M. Strelets, and A. Travin. Detached-eddy simulation of an airfoil at high angle of attack. *Engineering Turbulence Modelling and Experiments*, 4:669–678, 1999.
- J. Smagorinsky. General circulation experiments with the primitive equations. *Monthly Weather Review*, 91:99–164, 1963.
- A. Soldati. Slug rise and break up in volcanic conduits. *University of Pisa Masters Thesis*, 2013.
- R.G. Sousa, M.L. Riethmuller, A.M.F.R. Pinto, and J.B.L.M. Campos. Flow around individual Taylor bubbles rising in stagnant CMC solutions: PIV measurements. *Chemical Engineering Science*, 60(7):1859–1873, 2005.
- R.G. Sousa, A.M.F.R. Pinto, and J.B.L.M. Campos. Effect of gas expansion on the velocity of a Taylor bubble: PIV measurements. *International Journal of Multiphase Flow*, 32(10-11): 1182–1190, 2006.
- J. Suckale, J.C. Nave, and B. H. Hager. It takes three to tango: 1. Simulating buoyancy-driven flow in the presence of large viscosity contrasts. *Journal of Geophysical Research*, 115, 2010.
- T. Taha and Z.F. Cui. Hydrodynamics of slug flow inside capillaries. *Chemical Engineering Science*, 59:1181 – 1190, 2004.
- G. I. Taylor and R. M. Davies. The mechanics of large bubbles rising through extended liquids and through liquids in tubes. *Proceedings of the Royal Society of London*, 200:375–390, 1950.
- G.I. Taylor. The criterion for turbulence in curved pipes. *Royal Society of London – Proceedings*, 124(A794):243–249, 1929.
- R. van Hout, A. Gulitski, D. Barnea, and L. Shemer. Experimental investigation of the velocity field induced by a Taylor bubble rising in stagnant water. *International Journal of Multiphase Flow*, 28:579–596, 2002.

- S. Vergnolle, G. Brandeis, and J.-C. Mareschal. Strombolian explosions 2. Eruption dynamics determined from acoustic measurements. *Journal of Geophysical Research B: Solid Earth*, 101(9):20449–20466, 1996.
- H.K. Versteeg and W. Malalasekera. *An Introduction to Computational Fluid Dynamics*. Pearson Education, 2007.
- F. Viana, R. Pardo, R. Yanez, J. Trallero, and D. Joseph. Universal correlation for the rise velocity of long gas bubbles in round pipes. *Journal of Fluid Mechanics*, 494:379 – 398, 2003.
- Vision Research. Phantom V9.1 data sheet, May 2014. URL http://www.visionresearch.com/uploads/Docs/Products/DS_v91.pdf.
- G.B. Wallis. *One-dimensional Two-phase Flow*. McGraw Hill, 1969.
- C.C. Wang, C.Y. Tseng, and I.Y. Chen. A new correlation and the review of two-phase flow pressure change across sudden expansion in small channels. *International Journal of Heat and Mass Transfer*.
- E. T. White and R. H. Beardmore. The velocity of rise of single cylindrical air bubbles through liquids contained in vertical tubes. *Chemical Engineering Science*, 17:351–361, 1962.
- D.C. Wilcox. Reassessment of the scale-determining equation for advanced turbulence models. *AIAA journal*, 26(11):1299–1310, 1988.
- A. Williams, H. McBirney. *Volcanology*. Freeman, Cooper and Company, San Fransisco, 1979.
- L. Wilson. Relationships between pressure, volatile content and ejecta velocity in three types of volcanic explosion. *Journal of Volcanology and Geothermal Research*, 8, 1980.
- L. Wilson and J.W. Head. Ascent and eruption of basaltic magma on the earth and moon. *Journal of Geophysical Research*, 86:2971–3001, 1981.

- V. Yakhot, S.A. Orszag, S. Thangam, T.B. Gatski, and C.G. Speziale. Development of turbulence models for shear flows by a double expansion technique. *Physics of Fluids A*, 4(7):1510–1520, 1992.
- K. Yan and D. Che. A coupled model for simulation of the gas-liquid two-phase flow with complex flow patterns. *International Journal of Multiphase Flow*, 36(4):333–348, 2010.
- G.H. Yeoh and J. Tu. *Computational Techniques for Multiphase Flow*. Butterworth-Heinemann, 2010.
- D.L. Youngs. Time-dependent multi-material flow with large fluid distortion. *Numerical Methods for Fluid Dynamics*. Academic Press, New York, page 273, 1982.
- D. Zheng, X. He, and D. Che. CFD simulations of hydrodynamic characteristics in a gas-liquid vertical upward slug flow. *International Journal of Heat Mass Transfer*, 50:4151–4165, 2007.
- D. W. Zhou, T. Gambaryan-Roisman, and P. Stephan. Measurement of water falling film thickness to flat plate using Confocal Chromatic Sensing technique. *Experimental Thermal Fluid Science*, 33:273–283, 2009.

Appendices



UDF Source Code

The source code for the UDF to determine the level of the top surface in the simulations of Chapter 5 is provided below.

```
/* UDF to calculate the level of the water surface */
#include "udf.h"

/* This type of UDF gets executed at the end of each time step */
DEFINE_EXECUTE_AT_END(surfaceHeightCalc)
{
    /* The surface height that we're after */
    real surfaceHeight = 0.0;

    #if !RP_NODE

        FILE *file;          /* File pointer */

        /* Get the current time */
        real currentTime = CURRENT_TIME;

    #endif /* !RP_NODE */

    #if !RP_HOST
```

```
Domain *mixture = Get_Domain(1); /* Mixture domain*/
/* The first (ie index 0) phase should be water here */
Domain *water = DOMAIN_SUB_DOMAIN(mixture,0);
Thread *ct; /* Cell thread */
int n; /* Node/face counter */
/* Nodes need this variable */
real fillHeightMax;
/* Set maximum fillHeight to a large negative number */
fillHeightMax = -1.0E+06;
/* Step through the cell threads*/
thread_loop_c(ct,water)
{
    cell_t c;
    /* Step through the cells in each thread */
    begin_c_loop(c,ct)
    {
        /* Set the maximum and minimum extents of this cell */
        real zMin = 1.0E+06;
        real zMax = -1.0E+06;
        real dz; /* Cell extend in z-direction */
        real fillHeight = 0.0;
        int fullAdjacent = 0;
        /* Loop over the faces of the cell , checking that at least
           one adjacent cell has a volume fraction above 0.5 */
```

```
c_face_loop(c, ct, n)
{
    face_t f = C_FACE(c, ct, n);
    Thread *ft = C_FACE_THREAD(c, ct, n);

    /* Find the outer cell and thread */
    cell_t c1 = F_C1(f, ft);
    Thread *ct1 = THREAD_T1(ft);
    if ( c1 != 0 && ct1 != NULL && C_VOF(c1, ct1) > 0.5 )
        fullAdjacent = 1;
}

/* Loop over the nodes in the cell */
c_node_loop(c, ct, n)
{
    Node *node;                /* Node pointer */
    real zNode;                /* Node z coord */
    node = C_NODE(c, ct, n);
    zNode = NODE_Z(node);
    if ( zNode > zMax )
        zMax = zNode;
    if ( zNode < zMin )
        zMin = zNode;
}
dz = zMax - zMin;
```

```

        /* Calculate the "fill height" for this cell */
        if ( fullAdjacent == 1)
            fillHeight = zMin + C_VOF(c, ct)*dz;
        /* Check against the running maximum */
        if ( fillHeight > fillHeightMax )
            fillHeightMax = fillHeight;
    }
    end_c_loop(c, ct);
}

/* Can probably comment this out */
Message("Node: %6d, Max. height: %12.5e\n", myid, fillHeightMax);

#if RP_NODE
    /* In parallel, work out the max of fillHeightMax across all nodes */
    surfaceHeight = PRF_GRHIGH1(fillHeightMax);
#endif /* RP_NODE */
#endif /* !RP_HOST */

/* Pass maximum from the nodes to the host */
node_to_host_real_1(surfaceHeight);

#if !RP_NODE
    /* Write the current time and surface height to file */
    file = fopen("surfaceHeight62899.log", "a");
    fprintf(file, "%15.8e%15.8e\n", currentTime, surfaceHeight);
    fclose(file);
#endif

```

```
#endif /* !RP_NODE */  
}
```